



University of L'Aquila

Local Energy Transfer in Geophysical Fluids and Space Plasmas

Department of Physical and Chemical Sciences

PhD in Physical and Chemical Sciences – Cycle XXXV

Candidate

Raffaello Foldes

ID number 268146

Thesis Advisors

Prof. Ermanno Pietropaolo

Dr. Raffaele Marino

Dr. Emmanuel Lévêque

February 2023

Local Energy Transfer in Geophysical Fluids and Space Plasmas
Ph.D. thesis. University of L'Aquila

© 2022 Raffaello Foldes. All rights reserved

This thesis has been typeset by L^AT_EX and the uaqthesis class.

Author's email: raffaello.foldes@graduate.univaq.it



N° d'ordre NNT : xxx

**THÈSE de DOCTORAT DE L'UNIVERSITE DE LYON opérée au
sein de l'École Centrale de Lyon**

École Doctorale N° 162
Mécanique Énergétique Génie Civil Acoustique

Spécialité de doctorat :
Mécanique des fluides

Soutenue publiquement le 31/03/2023, par :
Raffaello Foldes

**Local Energy Transfer in Geophysical Fluids and
Space Plasmas**

Devant le jury composé de :

BERRILLI Francesco	Senior scientist, Professor (UNITOV, Italy)	Président du jury
LANOTTE Alessandra	Senior scientist, Professor (CNR/Nanotec, Italy)	Examinatrice
LEHNER Thierry	Researcher (CNRS/OBSPM, France)	Examinateur
PIETROPAOLO Ermanno	Senior scientist, Professor (UNIVAQ, Italy)	Directeur de thèse
MARINO Raffaele	Directeur de recherche (CNRS/ECL, France)	Co-directeur de thèse
LÉVÊQUE Emmanuel	Directeur de recherche (CNRS/ECL, France)	Co-directeur de thèse

Alle persone che rendono migliore la mia vita!

Abstract

Turbulence in geophysical fluids and space plasmas compete with internal waves in transferring the energy across scales. Evidences point to the possibility that an upscale energy transfer, resembling the case of two-dimensional turbulent flows, may develop in the atmosphere and in the oceans, under the effect of rotation, perhaps helped by the large aspect ratio of the domain. Indeed, bi-directional energy transfers (to large and small scales) have been observed in different natural contexts, in the oceans, for instance, but also in kinetic plasmas, in which magnetic fields support the propagation of waves, and magnetic reconnection contributes to make the dynamics of these flows even richer. In these frameworks, characterized by strong inhomogeneity and anisotropy, standard analysis tools can only provide partial information on how energy is distributed over the various scales. In order to achieve a more exhaustive characterization of the energy transfer, in this thesis we employed the so-called space-filtering (SF) technique to investigate the energetics of stratified turbulent flows of geophysical interest, and of plasmas in the kinetic regime, the latter being relevant to understand the dynamics of the interplanetary medium. In particular, we targeted two major phenomena, the extreme vertical drafts developing in the stratified geophysical flows, and the reconnection events observed in heliospheric and magnetospheric plasmas, always using simulation data. After further refining the SF technique, we used it to analyze a set of direct numerical simulations of stratified flows, varying the Froude number, focusing on the feedback of developing extreme vertical drafts on the energy transfer, locally in the physical and the Fourier space. We were able to verify that vertical drafts do actually inject energy, ultimately enhancing turbulence and dissipation, affecting the mixing properties of geophysical flows. The same approach was finally implemented on the outputs of hybrid-kinetic plasma simulations to assess the effects of magnetic reconnection events on the energy transfer at the sub-ion scales. Our analysis emphasized for the first time the role of reconnection as a trigger for dual energy transfers, simultaneously towards scales larger and smaller than the scales associated to the observed reconnection events.

Résumé

La turbulence dans les fluides géophysiques et les plasmas spatiaux entre en concurrence avec les ondes internes pour transférer l'énergie à travers les échelles. Des preuves pointent vers la possibilité qu'un transfert d'énergie vers les grandes échelles, ressemblant au cas des écoulements turbulents bidimensionnels, puisse se développer dans l'atmosphère et dans les océans, sous l'effet de la rotation, éventuellement aidé par le grand rapport d'aspect du domaine. En effet, des transferts d'énergie bidirectionnels (à grande et petite échelles) ont été observés dans différents contextes naturels, dans les océans par exemple, mais aussi dans les plasmas cinétiques, dans lesquels les champs magnétiques favorisent la propagation des ondes et la reconnexion magnétique contribue à rendre la dynamique de ces flux encore plus riche. Dans ces situations, caractérisées par une forte inhomogénéité et anisotropie, les outils d'analyse standards ne peuvent fournir qu'une information partielle sur la répartition de l'énergie aux différentes échelles. Afin de parvenir à une caractérisation plus exhaustive du transfert d'énergie, dans cette thèse, nous avons utilisé la technique du filtrage spatial (SF) pour étudier l'énergétique des écoulements turbulents stratifiés, d'intérêt géophysique, et des plasmas dans le régime cinétique, ce dernier étant pertinent pour comprendre la dynamique du milieu interplanétaire. En particulier, nous avons ciblé deux phénomènes majeurs, les courants verticaux extrêmes se développant dans les écoulements géophysiques stratifiés et les événements de reconnexion observés dans les plasmas héliosphériques et magnétosphériques, toujours à l'aide de données de simulation. Après avoir encore plus affiné la technique SF, nous l'avons utilisée pour analyser un ensemble de simulations numériques directes d'écoulements stratifiés, en faisant varier le nombre de Froude, en nous concentrant sur la rétroaction du développement des vents verticaux extrêmes sur le transfert d'énergie, localement dans l'espace physique et de Fourier. Nous avons pu vérifier que les courants verticaux injectent effectivement de l'énergie, renforçant finalement la turbulence et la dissipation, et affectant les propriétés de mélange des écoulements géophysiques. La même approche a finalement été mise en œuvre sur les sorties des simulations de plasma hybride-cinétique, afin d'évaluer les effets des événements de

reconnexion magnétique sur le transfert d'énergie aux échelles sub-ioniques. Notre analyse a souligné pour la première fois le rôle de la reconnexion comme déclencheur de transferts double d'énergie simultanément vers des échelles plus grandes et plus petites que les échelles associées aux événements de reconnexion observés.

Acknowledgments

I am profoundly grateful to my supervisors, Ermanno Pietropaolo (University of L'Aquila), Raffaele Marino (CNRS/École Centrale de Lyon), and Emmanuel Lévêque (CNRS/École Centrale de Lyon) for their help in the research presented on those pages and in the support they gave me in this three-year path. Everything I know about turbulence, plasma and computational physics, I owe to them and, most importantly, I benefited generous and unselfish people's time, many thanks!

I really enjoyed working on this challenging project, from the help of many colleagues and the great time spent with many friends at the University of L'Aquila, to the new ones met later at the École Centrale de Lyon, I want to thank them all and I hope this is just the beginning of a long successful journey. In particular, I would like to thank Silvio S. Cerri and Enrico Camporeale for their fundamental contributions to the research here presented. I would also like to thank Fabio Feraco for welcoming me in a new laboratory, in a new city and country as an old friend. I acknowledge the support provided by the University of L'Aquila during my 2-years stay at the École Centrale de Lyon. Finally, I wish to thank Sara, my parents, and my little sister, Federica, for their support and encouragement over the years; none of this would have been possible without them.

Contents

1	Introduction	4
1.1	Incompressible hydrodynamic turbulence	5
1.1.1	The energy cascade	5
1.1.2	Small-scale intermittency	6
1.1.3	Locality of the energy transfer	8
1.2	Geophysical Flows	8
1.2.1	Effects of rotation and stratification on turbulent flows	10
1.2.2	Modeling geophysical turbulent flows	11
1.3	General formulation of the space-filtering (SF) approach	14
1.4	The Boussinesq approximation	17
2	Dynamics and energetics of geophysical flows	22
2.1	Extreme Vertical Drafts in Stratified Turbulent Flows	22
2.2	Space-Filtering the Boussinesq equations	27
2.2.1	Energy equations of the Boussinesq model	28
2.2.2	Filtered Boussinesq equations	29
3	Space-Filtering and spectral energy transfer rate	36
3.1	Total Energy Flux	38
3.1.1	Anisotropic energy fluxes	41
3.2	Space-Filtering to investigate the anisotropic flux	42
3.2.1	Direct numerical simulations	45
3.2.2	Operative definitions of the governing parameters	47
3.2.3	Validation of the Space-Filtering technique in DNS	50

3.2.4	Stably stratified runs varying the Froude number	58
4	Local energy injection by vertical velocity drafts in stratified geophysical flows	61
4.1	Characterization of local energy injections by vertical drafts	61
4.1.1	Anisotropic energy transfer in the presence of vertical drafts (run S8)	64
4.1.2	Time variation of the cross-scale energy transfer with vertical drafts	69
4.2	Local energy transfer variation with Froude number	80
5	Link to small-scale intermittency and the buoyancy flux	89
5.1	Comparison of the kurtosis of large- and small-field components . . .	89
5.2	A mechanism for the generation of large-scale vertical drafts	92
5.3	Effect of large-scale intermittency on the mixing properties of stratified flows	96
6	Low-dimensional representation of large-scale intermittency in stratified flows	103
6.1	Statistical-Informed Convolutional Autoencoders	105
6.1.1	By-plane approach to fluid anisotropy	107
6.1.2	Statistical-aware loss function	108
6.2	SI-CAE Performance	111
6.2.1	Low-dimensional representation of extreme vertical drafts . .	114
6.2.2	Physical fields 3D reconstruction	117
7	Conclusions and discussion	120
7.1	Conclusions	120
	Appendices	125
A	Space-Filter analysis of reconnection events in 2D3V hybrid Vlasov-Maxwell simulation	126

A.1	R. Foldes et al.: Dual energy transfer driven by magnetic reconnection at sub-ion scale	129
B	Deep-FLRID: Machine Learning Algorithms for Automated Field Line Resonance Identification	139
B.1	R. Foldes et al.: Assessing machine learning techniques for identifying field line resonance frequencies from cross-phase spectra	143
C	FLAME: Fast Lattice Boltzmann Algorithm for Magnetohydrodynamics (MHD) Experiments	164
C.1	R. Foldes et al.: Efficient kinetic Lattice-Boltzmann simulation of three-dimensional Hall-MHD turbulence	167
C.2	L. Sorriso-Valvo et al.: Helios 2 observations of solar wind turbulence decay in the inner heliosphere	202
	Bibliography	211

Acronyms

CAE Convolutional Autoencoder. [104–117](#)

CDF cumulative distribution function. [69](#)

CG coarse-graining. [14, 36, 120](#)

DNS direct numerical simulation. [12, 13, 22, 23, 27, 34, 36, 43–47, 50, 51, 58, 62, 69, 80, 81, 89, 90, 103, 104, 118, 122, 123, 127](#)

EMMA European quasi-Meridional Magnetometer Array. [140](#)

FFT Fast-Fourier transform. [45](#)

FLAME Fast Lattice-Boltzmann Algorithm for MHD Experiments. [164, 166](#)

FLR Field Line Resonance. [139–142](#)

GHOST Geophysical High-Order Suite for Turbulence. [45, 166](#)

GPU Graphical Processing Units. [45](#)

Hall-MHD Hall magneto-hydrodynamics. [37, 164–166](#)

HD hydrodynamics. [5, 7, 8, 39](#)

HIT homogeneous isotropic turbulence. [21, 26, 50, 51, 53, 54, 81, 82, 94, 95, 98, 101, 104, 121](#)

K41 Kolmogorov turbulence theory 1941. [5, 10, 11, 41](#)

- KHI** Kelvin-Helmholtz instability. [94](#), [122](#)
- KHM** Karman-Howarth-Monin. [37](#)
- LB** Lattice-Boltzmann. [164](#), [166](#)
- LBM** Lattice-Boltzmann method. [12](#), [166](#)
- LES** Large-Eddy simulations. [12–14](#), [16](#), [27](#), [36](#), [38](#), [43](#), [45](#)
- LHS** left-hand side. [16](#), [32](#)
- MAPE** mean absolute percentage error. [114](#), [115](#)
- MHD** magneto-hydrodynamics. [4](#), [7](#), [8](#), [34](#), [36](#), [38](#), [164–166](#)
- ML** Machine Learning. [104](#), [142](#)
- MSE** mean squared error. [110–113](#), [115](#)
- NSEs** Navier-Stokes equations. [8](#), [10–13](#), [15](#), [17](#), [18](#), [21](#), [28](#), [36](#), [39](#), [44](#), [93](#), [104](#)
- PDF** probability distribution function. [23](#), [64](#), [65](#), [70](#), [89](#), [91](#), [97](#), [105](#), [109](#), [111](#), [115](#), [116](#)
- RANS** Reynolds-averaged Navier-Stokes. [45](#)
- RHS** right-hand side. [16](#), [29](#), [31](#), [33](#), [94](#), [95](#)
- rms** root mean squared. [6](#), [100](#)
- SF** space-filtering. [viii](#), [14–16](#), [27](#), [29](#), [34–39](#), [42](#), [44](#), [46](#), [53](#), [54](#), [56–60](#), [62](#), [64](#), [68](#), [69](#), [82](#), [96](#), [120](#), [121](#), [123](#), [126](#), [127](#)
- SI-CAE** statistical-informed Convolutional Autoencoder. [113](#)
- SOC** self-organized criticality. [71](#)
- ULF** ultra-low frequency. [141](#), [142](#)
- URANS** Unsteady Reynolds-averaged Navier-Stokes. [45](#)

VSHW vertically sheared horizontal wind. [59](#), [80](#), [94](#), [95](#), [99](#), [101](#), [118](#)

Chapter 1

Introduction

Flow turbulence is ubiquitous in nature, characterizing for instance the dynamics and energetics of the Earth's atmosphere and oceans, as well as astrophysical and space plasmas, such as the solar wind pervading the interplanetary environment.

Turbulence is a multi-scale phenomenon, involving structures across a wide range of spatial scales; in addition, in plasma turbulence different physical descriptions may be adopted at different scales (e.g., magneto-hydrodynamics (MHD), two-fluids, kinetic), therefore it can be considered also as a multi-physics process.

The various length scales ℓ of turbulent motion are well sketched in the energy spectrum $E(k)$ in Fourier space, see Fig. 1.1, where wave vectors are linked to length scale ℓ by the relation $k \sim \ell^{-1}$. In the classical description of turbulence, spatial scales are split into three ranges: the energy-containing range, the inertial range and the dissipation range (see Fig. 1.1(a)). The bulk of the energy resides in the large scales, which is therefore called the energy-containing range; on the other hand, the bulk of the dissipation is at the small-scale range, in the so-called dissipation range. The interval of scales in between is the inertial range, the most studied in turbulence theory. However, given the vast range of scales involved, the energy transfer processes usually link these scales together. The power-law spectra, observed in the atmosphere for the kinetic energy [163, 162, 118], and in the solar wind for the magnetic energy [204, 34, 136], represent one direct evidence of ranges tied together. The kinetic energy spectrum shows a power law in the inertial range, the slope steepens and finally breaks near the so-called Kolmogorov scale η . The

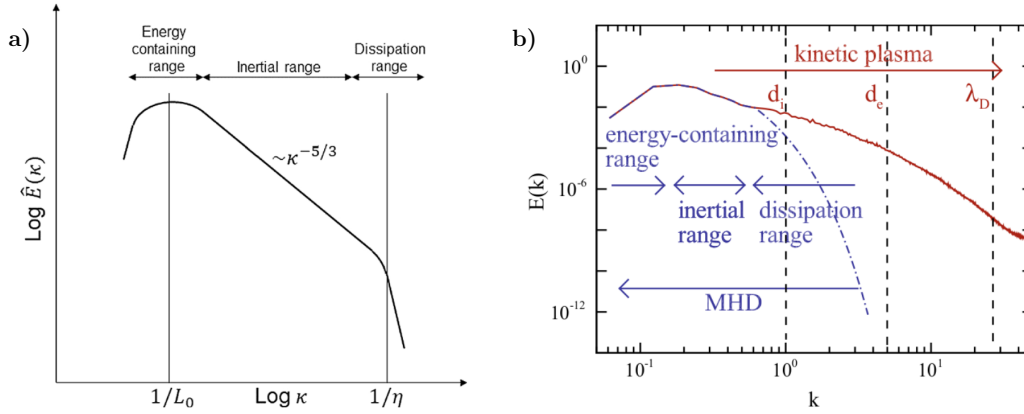


Figure 1.1. Sketch of turbulent energy spectra of kinetic energy ((a) from Kalmar-Nagy and Bak [98]), and of magnetic energy ((b) from Yang [235]), highlighting the richness of spatial scale involved.

main goal of this work is to characterize the effect of large-scale extreme events, observed in the vertical velocity, on the local energy transfer of stratified turbulent flows, in a range of governing parameters compatible with geophysical fluids. Such extreme events have been observed in both numerical simulations and observations of stably stratified flows, drawing the attention of the fluid mechanics community as well as the atmospheric physics one. For the sake of simplicity, the introduction of turbulence will be mainly given in the framework of hydrodynamics (HD), with particular attention to terrestrial flows.

1.1 Incompressible hydrodynamic turbulence

The following sections are provided to briefly review incompressible hydrodynamics (HD) turbulence, with the aim of giving a qualitative understanding of the main ideas that are involved in energy transfer processes.

1.1.1 The energy cascade

The current ideas on HD turbulence date back to the seminal work of A. N. Kolmogorov in 1941 (in short K41) [102, 103]. The classical theory [103] suggests the development of a turbulent energy cascade (introduced first by Richardson [69]),

in which energy is transferred from large to small scales at a constant rate, i.e., $\Pi_\ell \sim \epsilon$, until the energy is dissipated by viscous action at small-scales. Following Richardson's idea, the energy cascade is the result of successive generations of eddies with smaller sizes. Indeed, eddies of size ℓ have a characteristic velocity u_ℓ and energy u_ℓ^2 . It is then possible to define the so-called eddy turnover time associated with a given scale ℓ , $\tau_\ell \sim \ell/u_\ell$. Instead, the average turnover time τ_{NL} is defined using the integral length scale and the root mean squared (rms) velocity. Such a timescale can be considered as the typical time for eddies of size ℓ to be affected by significant distortions; it is also the typical time required for the energy to be transferred from ℓ to a smaller scale; so that, the energy transfer rate can be estimated as

$$\Pi_\ell \sim \frac{u_\ell^2}{\tau_\ell} \sim \frac{u_\ell^3}{\ell}, \quad (1.1)$$

therefore in the inertial range, where forcing and viscous effects can be neglected, the following relation is valid, $\Pi_\ell \sim \epsilon$, leading to

$$u_\ell \sim \epsilon^{1/3} \ell^{1/3}. \quad (1.2)$$

The energy spectra $E(k)dk$, already shown in Fig. 1.1, represents the energy in the wave vector range $k \leq |\mathbf{k}| \leq k + dk$, where $|\mathbf{k}|$ is the radius of a spherical shell in the Fourier space. By using Eq. (1.2), the Kolmogorov spectrum of kinetic energy can be written as

$$E(k) = C_K \epsilon^{2/3} k^{-5/3}, \quad (1.3)$$

where C_K is a dimensionless constant, depending on the context. Several studies in numerical simulations [139, 202, 181] and observations [162, 118] support the evidence of a Kolmogorov-like (or more in general power-law) spectrum in geophysical flows.

1.1.2 Small-scale intermittency

By using the self-similarity hypothesis suggested by the power-law spectrum, the K41 theory also encompasses the idea of small-scale intermittency. This is defined in terms of scaling behavior of the structure functions of order p , $[\delta \mathbf{u}(\mathbf{r})]^p$, being $\delta \mathbf{u}(\mathbf{r}) = \mathbf{u}(\mathbf{x} + \mathbf{r}) - \mathbf{u}(\mathbf{x})$ the velocity increments between two points separated by

r . Therefore, according to K41,

$$S_p(r) = \langle [\delta \mathbf{u}(\mathbf{r})]^p \rangle = r^{\zeta_p}, \quad (1.4)$$

with $\zeta_p = p/3$, and $\langle \dots \rangle$ denoting the ensemble average. It is worth mentioning that Eq. 1.4 assumes global homogeneity and isotropy of the system. Structure functions computed especially from experimental data give a power-law dependence on r with scaling exponents which sometimes deviate from the Kolmogorov prediction, which is attributed to the small-scale (or internal) intermittency. We refer to a quantity as intermittent, whether it is distributed sparsely in time or space, showing the rare occurrence of very strong fluctuations. For instance, the dissipation is highly intermittent, presenting local and instantaneous extreme values in small regions of the space and during fractions of time [174, 139]. Several intermittency models have been implemented as a correction to the K41 theory, such as the β -model [81], the multifractal model [81] and the log-normal or log-Levy models [174]. One of the most successful models, especially with experimental and numerical data, is the She-L ev eque formula [195]. The classical K41 theory for structure functions with $p \geq 4$ is no longer valid in presence of intermittency. However, both in HD and MHD turbulence, there exist a few exact laws derived from the dynamic equations which have been successfully applied in several context [136]. For instance, the most famous result in HD turbulence is Kolmogorovs' four-fifths law [51, 78], relating the third-order structure functions to the energy dissipation rate. This relation requires homogeneity, isotropy and the finiteness of the energy dissipation in the limit of an infinite Reynolds number, and it can be expressed as,

$$\langle [\delta u_{\parallel}(\mathbf{r})]^3 \rangle = -\frac{4}{5} \epsilon r, \quad (1.5)$$

with $\delta u_{\parallel} = \delta \mathbf{u} \cdot \mathbf{r}/r$. An analogous law for the transport of a passive scalar was established by Yaglom [155, 234], and in the context of MHD turbulence by Politano-Pouquet [178] by using the Elsasser variables $\mathbf{z}^{\pm} = \mathbf{u} \pm \mathbf{b}$ (with \mathbf{b} the magnetic field in velocity units).

1.1.3 Locality of the energy transfer

The Kolmogorov phenomenology of incompressible hydrodynamics turbulence assumes the locality in the spectral space of energy transfer, meaning that interactions, produced by the non-linear term in the Navier-Stokes equations (NSEs), occur predominately between comparable scales $\ell_1 \sim \ell_2$. In this framework, the flow motions over the inertial range are independent of the injection (large) and dissipative (small) scales, having therefore universal statistics at high Reynolds numbers. The locality of energy transfer discussed here is close to, but not exactly the same as, the concept of local (or triadic) interactions. Indeed, as suggested by Kraichnan [105, 106], triadic interactions involve wave vectors (k, p, q) satisfying $k + p + q = 0$. If the three wave numbers are of comparable size, we can talk about local energy transfer, otherwise the former is non-local. Therefore, the locality of interactions implies the locality of transfer, but the opposite is not true. The properties of energy transfer across scales in HD turbulence have been studied in great detail, being able to prove the locality for very large Reynolds numbers (see e.g., Aluie and Eyink [5], Domaradzki and Carati [63], Eyink [67]). However, in geophysical flows as well as in MHD plasmas the picture of energy transfer processes is more complicated; this happens mainly because of the presence of several energy transfer channels between different fields (and between fields and scalars), but also for the propagation of waves (gravito-inertial in the atmosphere and oceans, and Alfvén waves in plasmas). As a result, small scales may interact directly with large scales. In this thesis works, we will focus on the locality of energy transfer, and we will introduce as well the idea of locality-in-space which represent the key point for the analysis of non-homogeneous and/or anisotropic turbulent systems.

1.2 Geophysical Flows

Geophysical fluid dynamics deals with motions observed in various systems governed by similar dynamics, such as Earth's anticyclones, vortices in the Gulf Stream and Jupiters' Great Red Spot (see Fig. 1.2). Indeed, all those systems involve large-scale motions, where either the ambient rotation or density differences assume

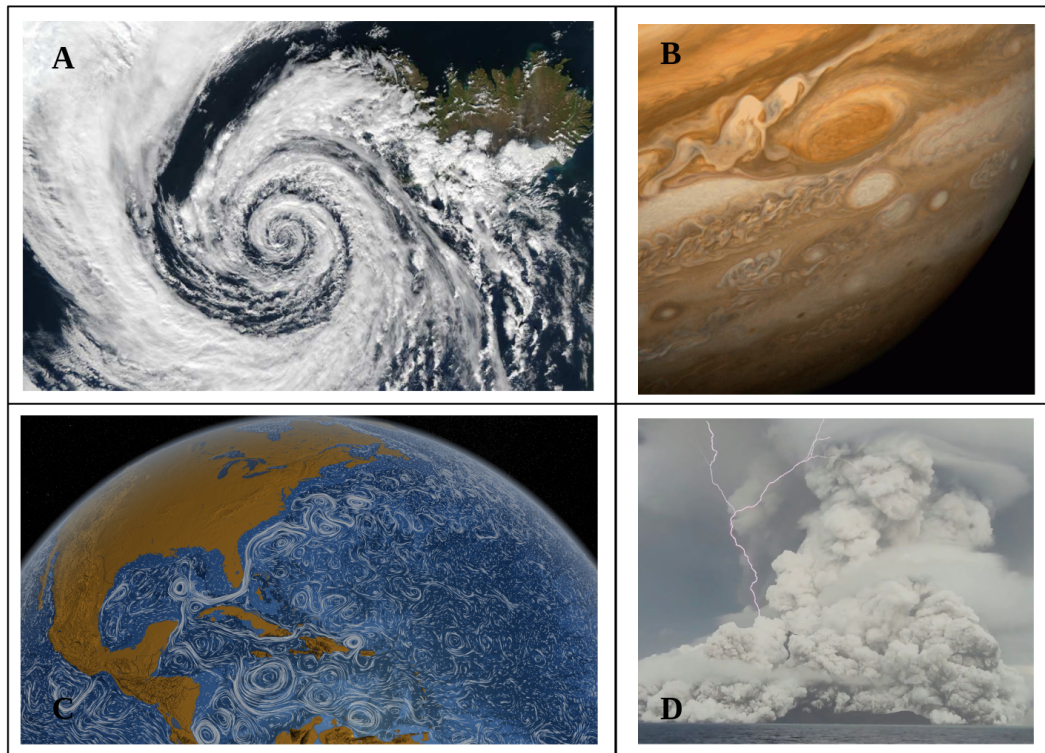


Figure 1.2. Four examples of geophysical flows, where rotation and/or stratification plays a central role: (a) evolution of an hurricane, (b) Jupiters' Great Red Spot, (c) mesoscale eddies in the ocean, (d) particle dispersion after a volcanic eruption.

great importance. In this respect, geophysical fluid dynamics comprises all naturally occurring rotating-stratified fluid motions, therefore encompassing an enormous range of spatial and temporal scales, from the vortices of a river around a stone to the global atmospheric and oceanic current systems. Speaking of geophysical flows, the terms “large-scale” and “small-scale” must be necessarily contextualized, and their definition dynamically depends on other characteristic length scales of the system. For instance, a phenomenon with a characteristic length scale of 100km can be considered small-scale for the atmosphere but large-scale for oceans. In general, however, we can refer to large-scale as those which are significantly affected by the Earth's rotation.

1.2.1 Effects of rotation and stratification on turbulent flows

The presence of the Earth's rotation introduces in the Navier-Stokes equations (NSEs) two acceleration terms that, in the rotating framework, can be viewed as forces: the Coriolis and the centrifugal force. The latter is not relevant however in geophysical flows, whereas the former is crucial in geophysical motions. The major effect of the Coriolis force is to impose vertical rigidity on the fluid, which is thus characterized by strict columnar motions. The strength of rotation is measured through the Rossby number $Ro = U/Lf$, being defined as the ratio between the characteristic time of inertial waves $\tau_{IW} = 1/f$ (with $f = 2\Omega$ the Coriolis parameter and $\Omega \approx 7 \times 10^{-5} Hz$ the average Earth's rotation) and the turnover time U/L . Strong rotation implies small Rossby, meaning that large-scale motions are slow compared to the velocity imposed by the rotation. The other key ingredient for geophysical flows is stratification, arising in nature because of fluids of different densities and of the gravitational force, which tends to lower the heaviest fluid and raise the lightest. Under the condition of hydrostatic equilibrium, the fluid develops a stable stratification, consisting of vertical layers whose extension is controlled by the so-called buoyancy scale $\ell_B = U/N$, being N ($\approx 10^{-2} Hz$ in the atmosphere) the Brunt-Väisälä frequency. As we did for the rotation, it is possible to define a dimensionless parameter controlling the intensity of stratification, this is the Froude number $Fr = U/LN$, which is defined as the ratio of the characteristic time of gravity waves $\tau_{GW} = 1/N$ and the non-linear time τ_{NL} . Indeed, the propagation of internal gravity waves in stably stratified flows, such as in the ocean and in the upper atmosphere, are produced by perturbations of the ambient density stratification. Rotation and stratification are common features accounted in geophysical fluid dynamics that strongly affects the evolution of turbulence. In particular, stratification partially inhibits vertical motions, typically leading to a $k_z \sim 3$ scaling of the vertical kinetic energy spectrum, differently from what foreseen by the K41 and observed for the horizontal spectrum ($k_{\perp} = \sqrt{k_x^2 + k_y^2} \sim -5/3$ in the inertial range). These different scaling laws make those system highly anisotropic, posing a true challenge for modeling and parameterizations. The horizontal velocity spectrum in the atmosphere was analyzed using aircraft observations by Nastrom

and Gage [162], which found a power-law with exponent around $-5/3$ in the mesoscale range; however, it is still controversial whether this is due to an upscale (inverse) cascade of energy [137] as it happens for two-dimensional turbulence [21], or a downscale (direct) cascade because of the intermittent breaking of internal gravity waves [27, 26]. Despite this discussion, the inertial range with an exponent of $\sim -5/3$ in the horizontal component has been observed by many authors using both observations [213, 145] and numerical simulations [2]. Lindborg [119] proposed a scaling analysis of the Navier-Stokes equations in the Boussinesq framework (see Sec. 2.2.2), which works pretty well for strong stratification and high Reynolds numbers, to explain the horizontal and vertical spectra observed in the atmosphere in terms of strong anisotropic 3D turbulence. Other studies, instead, claim that, since the atmosphere and oceans can be considered as shallow layers developing on a spherical frame, their vertical extension is much smaller than the horizontal one and therefore, also for this reason, their motions are strongly affected by quasi-2D dynamics, other than by rotation and stratification [118]. Generally speaking, the original picture of turbulent energy cascade and local transfer by Kolmogorov (K41) is extremely more complicated, for instance, in geophysical flows. Indeed, in this latter turbulent motions do not represent the sole mechanism of energy transfer but dynamics and energetics emerge from the interaction between waves and turbulent eddies. Whether this interplay produces either a direct or inverse (or both) energy cascade is still debated, and mostly depend on the spatial and temporal characteristic scales of the two phenomena; however, this represents a crucial question in geophysics which will help for instance for understanding the oceanic circulation closure [140] or the mechanisms of formation of large-scale structures in the atmosphere.

1.2.2 Modeling geophysical turbulent flows

Numerical simulations of turbulent process in geophysical flows are manifold, since they range from the weather forecasting to operational oceanic prediction, and climate studies. However, in many situations one is mainly interested to gain insight and understanding of a specific process, of a form of instability or of the role of shears in a particular regime of parameters. Therefore, a review of the numerical

models and methods to simulate Earths' flows is out of the aim of this paragraph, and it would probably need an entire book. In this section, instead, we focus on the use of numerical simulations for fundamental studies of turbulence processes in rotating and stratified fluids. Despite the wide number of numerical codes and different approaches, we made a simple separation in two main categories: direct numerical simulations (DNSs) and Large-Eddy simulations (LES). The difference is that, while the former solve the equations of motion from the energy-containing scale to the dissipative one. On the other hand, LES (and similar approaches) solve only a portion of the range of available scales and rely on sub-grid models to simulate the feedback of small-scale effects on the larger scales; such methods are based on the universality of small-scales at high Reynolds number (see Kolmogorov [102, 103]). In recent years, DNSs have benefited from the advent of peta- and hexa-scale computing capacity since they are computationally expensive, requiring large amounts of memory and computing hours. Turbulent flows, especially with rotation and/or stratification (see Fig. 1.5), involve many spatial and temporal scale whose dynamics needs to be resolved. The complexity in solving turbulent flows (with or without rotation and stratification) arises mainly from the non-linearity of the Navier-Stokes equations (NSEs) and, in particular, from the convective term $\mathbf{u} \cdot \nabla \mathbf{u}$, and the pressure gradient, being this latter both non-linear and non-local. For these reasons, usually, DNSs are not suitable to simulate complex geometries, including structured boundary conditions, or to take into account many different effects and phenomena (e.g, thermodynamical or radiative process) at large- and small-scales. Algorithms to perform DNSs of turbulent fluids and plasmas range from pseudo-spectral codes [189], finite volume [97] and finite difference methods [214] directly solving the equations of motion, to different approaches, such as Lattice-Boltzmann methods (LBMs) [75]. As we mentioned in the previous section, geophysical flows in general represent complex interacting systems, as those under study in condensed matter physics or biology, therefore most of the times the best approach is to seek explanations of complex phenomena by simply looking at the interactions of all the constituent parts. Nowadays, this level of information is almost achievable by DNSs from the governing equations. However, in the majority of situations, we can only

understand how those complex systems behave by means of reduced model, such as the Large-Eddy simulations (LES). Atmospheric General Circulations Models (AGCMs), Oceanic General Circulation Models (OGCMs) and coupled General Circulation Models (GCMs) are all based on the LES approach. For its versatility, the possibility of including complex geometries, boundary conditions and many different interactions allowed to these methods to significantly improve since the seminal idea of [112], then further developed by Germano [86]. The idea proposed by Germano [86] was to apply a low-pass filtering function to the NSEs at the last resolved length scale. The filtered equations present an additional term which represents the effect of the filtered small-scales on the large-scale dynamics; in the LES approach this is called Reynolds stress tensor, it is obtained by an ensemble average operation, and the performance of LES strongly relies on how sub-grid scale closures are able to reliably simulate such term (see Sec. 1.3 for a detailed derivation). Limitations of LES codes rely on the fact that, sub-grid scale turbulence closures generally suffer from the problem that the computed Reynolds stresses are of the same order as the grid truncation error; this interference may lead to computational instability or a lack of grid convergence. Several sub-grid scale models have been developed to take into account various small-scale effects, such as intermittency, velocity shears or helicity structures. Probably, the most famous is the Smagorinsky model [99], and its modified versions [124, 25], but more structured turbulence closures have been created, as those based on the eddy damped quasi-normal Markovian (EDQNM) models [160, 198]. Large-Eddy simulations definitely are based on our understanding of turbulence indeed, for instance, in the atmosphere, convection occurs on the scale of km , so it is impossible to properly capture its effects in global climate models in DNSs, and this will be for many years to come. Therefore, improved parametrization and sub-grid scale models, accounting for more and more phenomena and small-scale effects, are probably still the best option to simulate geophysical flows, but novel codes need some prior understanding on the physical system to be implemented. Indeed, the existence of complicated numerical models of complex phenomena only increases the need for understanding at a more basic level, with such understanding coming from analytical studies, but also from simplified numerical models. In this

thesis manuscript, however, we are mainly interested in the idea at the basis of Large-Eddy simulations (LES), employed by [86] for the study of turbulent systems, since it represents the starting point for the space-filtering (SF) (or coarse-graining (CG)) approach, being at the heart of this analysis of large-scale intermittent events in stratified flows.

1.3 General formulation of the space-filtering (SF) approach

In general, given any turbulent field $\mathbf{f}(\mathbf{x})$, the space-filtering (SF) technique consists in computing its convolution with a filtering function \mathbf{G}_ℓ ,

$$\tilde{\mathbf{f}}(\mathbf{x}) = \mathbf{G}_\ell * \mathbf{f} \quad (1.6)$$

or

$$\tilde{\mathbf{f}}(\mathbf{x}) = \int_V \mathbf{G}_\ell(\mathbf{x} - \boldsymbol{\xi}) \mathbf{f}(\boldsymbol{\xi}, t) d^3 \boldsymbol{\xi} \quad (1.7)$$

where the integral is computed over the entire volume V . The filtering function can be chosen as any real-valued and sufficiently smooth even function, rapidly decaying for large \mathbf{x} and normalized, so that $\int \mathbf{G}(\mathbf{x}) d^3 \mathbf{x} = 1$. To interpret (1.7) as a spatial average, the filtering function must also be positive definite ($\mathbf{G}(\mathbf{x}) \geq 0$ for any \mathbf{x}). This represents a linear operator, which can be applied to the dynamical equations of the system, commuting with space and time derivatives,

$$\widetilde{\partial_t \mathbf{f}}(\mathbf{x}) = \partial_t \tilde{\mathbf{f}}(\mathbf{x}) \quad \text{and} \quad \widetilde{\nabla \cdot \mathbf{f}}(\mathbf{x}) = \nabla \cdot \tilde{\mathbf{f}}(\mathbf{x}) \quad (1.8)$$

preserving for an incompressible flow the divergence-free condition of the filtered velocity field, $\nabla \cdot \tilde{\mathbf{u}} = 0$. Any other filtering operations, such as a simple average of adjacent values along the domain, do not satisfy these conditions resulting in filtered fields which are not suitable for analyzing the scale-to-scale dynamics [9]. The choice of the filtering kernel adopted in this technique determines the information we can derive from the filtered fields. A variety of functions is commonly used (*i.e.* Gaussian kernel, top-hat kernel, Butterworth filter and many others), and they can be classified into three categories: low-pass, high-pass and band-pass filters

(see the sketch 3.3). Low- and high-pass filters essentially describe the interaction between scales above and below the filtering scale, while band-pass filters are useful to highlight the energy exchange within a particular range of scales.

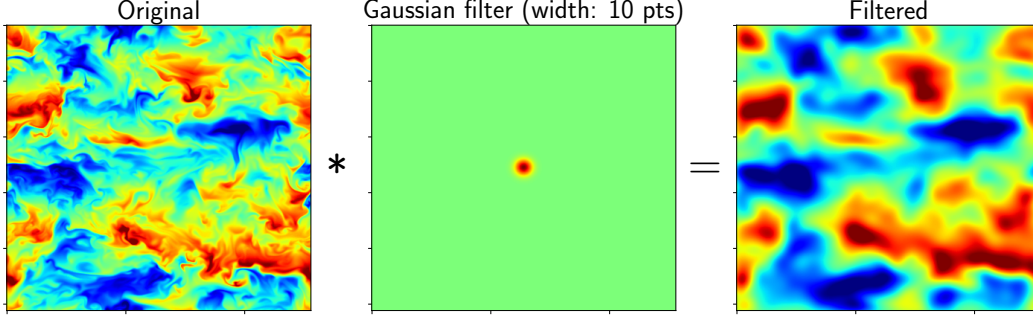


Figure 1.3. Example of the application of a Gaussian filter (center) on a 2D field of temperature θ (left).

Let us derive the general formulation of the space filtering approach for homogeneous, isotropic and incompressible fluids, as from [86]. If we consider the incompressible formulation of the Navier-Stokes equations (NSEs),

$$\partial_j u_j = 0 \quad (1.9)$$

$$\partial_t u_j + u_i \partial_i u_j = -\partial_j p + 2\nu \partial_i s_{ij} \quad (1.10)$$

where s_{ij} is the strain tensor defined as,

$$s_{ij} = \frac{1}{2} (\partial_i u_j + \partial_j u_i) \quad (1.11)$$

For a generic linear filtering operator \mathbf{G} applied to the velocity field, we obtain the following filtered equation,

$$\partial_t \tilde{u}_j + \tilde{u}_i \partial_i \tilde{u}_j = -\partial_j \tilde{p} + 2\nu \partial_i \tilde{s}_{ij} - \partial_i \tau(u_i, u_j) \quad (1.12)$$

with

$$\tau(u_i, u_j) = \widetilde{u_i u_j} - \tilde{u}_i \tilde{u}_j \quad (1.13)$$

representing the turbulent stress relative to the filtered scales. Suppose the filtering operation is obtained through an ensemble average. In that case, $\tau(u_i, u_j) = \langle u_i u_j \rangle - \langle u_i \rangle \langle u_j \rangle = \langle u'_i u'_j \rangle$, u'_i being the velocity field fluctuations, is the usual

Reynolds stress tensor which is commonly at the hearth of Large-Eddy simulations (LES). Then, multiplying (1.12) by \tilde{u}_j we can derive the equation for the rate of variation of the filtered energy. The detailed derivation follows,

$$\underbrace{\tilde{u}_j \partial_t \tilde{u}_j}_{(I)} + \underbrace{\tilde{u}_i \tilde{u}_j \partial_i \tilde{u}_j}_{(II)} = - \underbrace{\tilde{u}_j \partial_j \tilde{p}}_{(III)} + \underbrace{2\nu \tilde{u}_j \partial_i \tilde{s}_{ij}}_{(IV)} - \underbrace{\tilde{u}_j \partial_i \tau(u_i, u_j)}_{(V)} \quad (1.14)$$

We can rearrange the above equation by considering the relations,

$$(I) \quad \tilde{u}_j \partial_t \tilde{u}_j = \frac{1}{2} (\tilde{u}_j \partial_t \tilde{u}_j + \tilde{u}_j \partial_t \tilde{u}_j) = \frac{1}{2} \partial_t \tilde{u}_j \tilde{u}_j = \partial_t \tilde{\mathcal{E}} \quad (1.15)$$

$$(II) \quad \tilde{u}_i \tilde{u}_j \partial_i \tilde{u}_j = \frac{1}{2} (\tilde{u}_i \tilde{u}_j \partial_i \tilde{u}_j + \tilde{u}_i \tilde{u}_j \partial_i \tilde{u}_j) = \frac{1}{2} \tilde{u}_i \partial_i \tilde{u}_j \tilde{u}_j = \tilde{u}_i \partial_i \tilde{\mathcal{E}} \quad (1.16)$$

$$(III) \quad \partial_j (\tilde{u}_j \tilde{p}) = \tilde{u}_j \partial_j \tilde{p} + \tilde{p} \cancel{\partial_j \tilde{u}_j} \xrightarrow{0 \text{ continuity eq.}} \quad (1.17)$$

$$(IV) \quad \partial_i \tilde{u}_j \tau(u_i, u_j) = \tilde{u}_j \partial_i \tau(u_i, u_j) + \tau(u_i, u_j) \partial_i \tilde{u}_j \quad (1.18)$$

$$\tilde{u}_j \partial_i \tau(u_i, u_j) = \partial_i \tilde{u}_j \tau(u_i, u_j) - \tau(u_i, u_j) \partial_i \tilde{u}_j$$

$$(V) \quad 2\nu \partial_i \tilde{u}_j \tilde{s}_{ij} = 2\nu (\tilde{u}_j \partial_i \tilde{s}_{ij} + \tilde{s}_{ij} \partial_i \tilde{u}_j)$$

$$2\nu \tilde{u}_j \partial_i \tilde{s}_{ij} = 2\nu (\partial_i \tilde{u}_j \tilde{s}_{ij} - \underbrace{\tilde{s}_{ij} \partial_i \tilde{u}_j}_{\tilde{s}_{ij} \partial_i \tilde{u}_j}) = 2\nu (\partial_i \tilde{u}_j \tilde{s}_{ij} - \tilde{s}_{ij} \tilde{s}_{ij}) \quad (1.19)$$

$$\tilde{s}_{ij} \partial_i \tilde{u}_j = \frac{1}{2} \tilde{s}_{ij} (\partial_i \tilde{u}_j + \partial_j \tilde{u}_i) = \tilde{s}_{ij} \tilde{s}_{ij}$$

Finally, we can write the expression for the energy rate as,

$$\partial_t \tilde{\mathcal{E}} + \partial_i \left[\tilde{u}_i (\tilde{\mathcal{E}} + \tilde{p}) + \tilde{u}_j \tau(u_i, u_j) - 2\nu \partial_i \tilde{u}_j \tilde{s}_{ij} \right] = -\tau(u_i, u_j) \partial_i \tilde{u}_j - 2\nu \tilde{s}_{ij} \tilde{s}_{ij} \quad (1.20)$$

which highlights how multiple effects produce the temporal variation of the energy. The second and third terms left-hand side (LHS) in (1.20) indicate the energy transport due to the mean flow and the pressure work, respectively; the fourth term is the energy variation due to turbulent advection and finally the last term LHS is the transport of energy through the system due to viscous effects. The two terms right-hand side (RHS) indicate the energy rate (first) and the dissipation $\epsilon = 2\nu \tilde{s}_{ij} \tilde{s}_{ij}$, respectively. In particular, by the sub-grid term \mathcal{S} it is clear that the energy transport arises because of the interaction between the strain tensor $\partial_i \tilde{u}_j$ at scales greater than the filtering scale and the sub-grid stress tensor $\tau(u_i, u_j)$, pointing out how the filtering approach relates larger scale with those filtered out. This term gives a measure of any source or sink for the energy at a given scale and

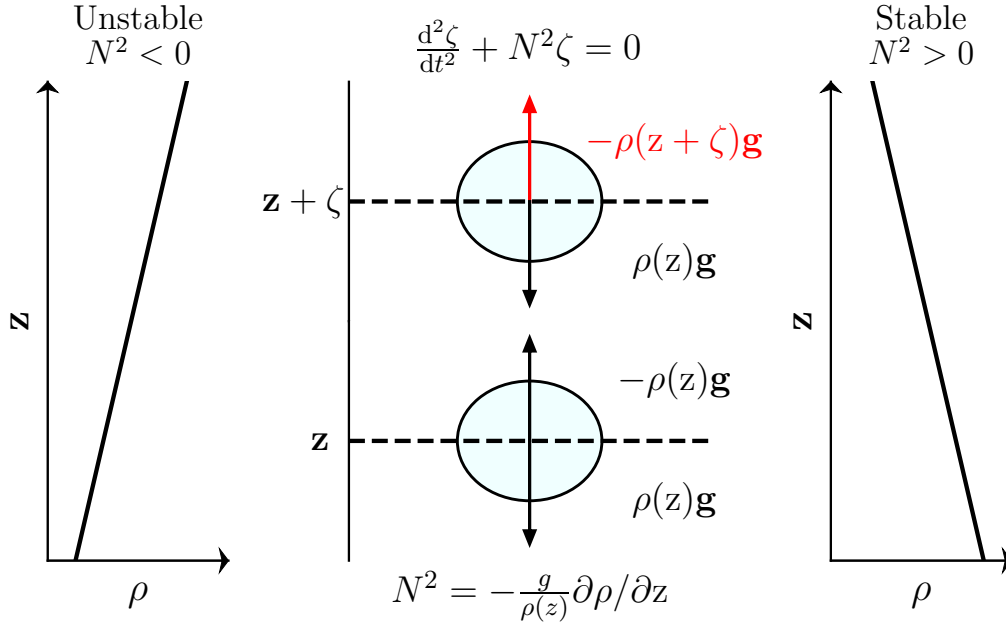


Figure 1.4. Sketch of a fluid parcel in hydrostatic equilibrium. If displaced, it oscillates around its equilibrium state with frequency N , if $N^2 > 0$. On the contrary, if $N^2 < 0$, the stratification is unstable and usually convective motions are triggered.

time, in any point \mathbf{x} within the domain. According to this, let us rewrite the rate of energy as follows,

$$\partial_t \tilde{\mathcal{E}} + \partial_i [\tilde{u}_i (\tilde{\mathcal{E}} + \tilde{p}) + \tilde{u}_j \tau(u_i, u_j) - 2\nu \partial_i \tilde{u}_j \tilde{s}_{ij}] = -\tilde{\mathcal{S}} - \tilde{\epsilon} \quad (1.21)$$

with

$$\mathcal{S} = \tau(u_i, u_j) \partial_i \tilde{u}_j \quad (1.22)$$

1.4 The Boussinesq approximation

In many cases in geophysical flows, the density variations are quite small compared to the mean density, and this evidence can be exploited to derive, starting from the NSEs. This model provides a pretty accurate description of fluid dynamics in a geophysical context. The model is known as the *Boussinesq approximation* which describes the fluid motion, with a system of equations coupling the bulk velocity with the temperature (or buoyancy) scalar field, which in this scenario is an active

scalar affecting the fluid velocity. However, even though the density fluctuations are assumed small, they are still relevant for the evolution of the buoyancy ρg and thus are taken into account in the Boussinesq model (only) when coupled with the gravity. The Boussinesq model has been successfully applied also for the study of the dynamics of the oceans as well of the upper Earth's atmosphere. A very simple derivation of the Boussinesq equations for incompressible stably stratified flows from the Navier-Stokes equations in the compressible formulation, therefore accounting for density variations, with a forcing term, acting along the z direction, due to gravity, is proposed here [175]

$$\frac{d\rho}{dt} + \rho \nabla \cdot \mathbf{u} = 0 \quad (1.23)$$

$$\frac{D\mathbf{u}}{Dt} = -\nabla p + \mu \nabla^2 \mathbf{u} + \rho g \quad (1.24)$$

where $D/Dt = \partial/\partial t + \mathbf{u} \cdot \nabla$ is the material derivative, $g = g \hat{e}_z$ is the gravity acceleration and μ the viscosity coefficient. In this framework, considering thermodynamic relationships between state variables for an ideal gas, i.e. $e = c_v T$ and $p = \rho R T$, the balance equation of thermal energy can be written in terms of temperature T as,

$$\frac{DT}{Dt} = \frac{1}{\rho c_p} \frac{dp}{dt} + \kappa \nabla^2 T \quad (1.25)$$

here c_p is the specific heat and κ the thermal diffusivity. The set of equations (1.23), (1.24) and (1.25) describes the hydrostatic balance for a fluid. Indeed if $\mathbf{u} = 0$, the conservation of momentum (1.24) reduces to $d_z p_0 = -\rho g$, indicating that the state variables (e.g. ρ , T , p) are simply a function of the vertical coordinate z , therefore the fluid is said to be in hydrostatic equilibrium. Since the Boussinesq model is valid for small density fluctuations, we can obtain the equations of motion by considering this approximation as a first-order perturbation of the hydrostatic equilibrium. Therefore, by subtracting the hydrostatic balance relation, $0 = \rho_0 \mathbf{g} - \nabla p_0$, from Eq. (1.24), then dividing by ρ_0 , we obtain,

$$\left(1 + \frac{\rho'}{\rho_0}\right) \frac{D\mathbf{u}}{Dt} = \frac{\rho'}{\rho_0} g \hat{e}_z - \frac{1}{\rho_0} \nabla p' + \nu \nabla^2 \mathbf{u} \quad (1.26)$$

where $\nu = \mu/\rho_0$ is the kinematic viscosity and $\rho' = \rho - \rho_0$. Considering small density fluctuations (i.e. $\rho'/\rho_0 \ll 1$), Eq. (1.26) reduces to,

$$\frac{D\mathbf{u}}{Dt} = \frac{\rho'}{\rho_0} g \hat{e}_z - \frac{1}{\rho_0} \nabla p' + \nu \nabla^2 \mathbf{u} \quad (1.27)$$

Indeed, as mentioned before, even if the fluctuations are weak, gravity can still make the term $\rho'g/\rho_0$ of the same order of $D_t\mathbf{u}$, and therefore it should not be neglected. It is also worth noticing that the small density variations in the Boussinesq approximation essentially imply an incompressible fluid $\nabla \cdot \mathbf{u} = 0$.

The same approach can be adopted for the thermal energy equation (1.25), considering its perturbation from the equilibrium, which gives

$$\frac{DT'}{Dt} = \frac{1}{c_p\rho_0} \frac{dp'}{dt} + \kappa\nabla^2 T' \quad (1.28)$$

The term $d_t p'/c_p\rho_0$ represents the temperature fluctuations due to the perturbation of the hydrostatic equilibrium from an isentropic state. This is in general not true in the atmosphere, however the deviation from the isentropic equilibrium can be considered small; therefore we can neglect this term, obtaining,

$$\frac{DT'}{Dt} = \kappa\nabla^2 T' \quad (1.29)$$

Equations (1.27) and (1.29) with the incompressibility condition represent the full set of Boussinesq equations. However, since the state variables are strictly linked together and to reduce the number of parameters of this set of equations, it is sometimes helpful to express the Boussinesq model in terms of (potential) temperature fluctuations θ , which is the temperature that a fluid parcel would have if moved adiabatically to some reference pressure. By recalling that for an ideal gas $d \ln p = d \ln \rho + d \ln T$, and assuming small perturbations in an adiabatic system, we can replace T from Eq. 1.29 by using the relation,

$$\tilde{T} \approx \left(-\frac{T_0}{\rho_0}\right) \left(\tilde{\rho} - \frac{\rho_0}{p_0}\tilde{p}\right) \quad (1.30)$$

where a general state variable $\tilde{q} = q_1 + q'$ represents departure from isentropic hydrostatic equilibrium. By replacing Eq. (1.30) in Eq. (1.29), after a few straightforward manipulations we obtain an equation for the density fluctuations which reads as,

$$\frac{D}{Dt} \left(\tilde{\rho} - \frac{\rho_0}{p_0}\tilde{p}\right) = \kappa\nabla^2 \left(\tilde{\rho} - \frac{\rho_0}{p_0}\tilde{p}\right) \quad (1.31)$$

which eventually leads to,

$$\frac{D\rho'}{Dt} = b\mathbf{u} \cdot \hat{e}_z + \kappa\nabla^2 \rho' \quad (1.32)$$

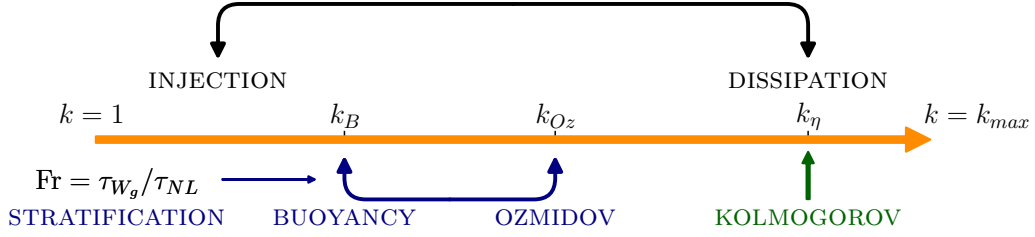


Figure 1.5. Schematic representation of the typical scales involved for a stratified turbulent flow. All the definitions are summarized in Sec. 3.2.2.

where $b = -\partial_z (\rho_1 - \rho_0 p_1/p_0)$ is the buoyancy term. In obtaining this equation, we neglected the material derivative and the Laplacian of the pressure variations p' . In many geophysical applications, this can be justified by the quasi-geostrophic and quasi-hydrostatic assumptions [175].

At this point we introduce an additional parameter, which will be particularly useful in the following for the setup of numerical simulations, the so-called Brunt-Väisälä (or buoyancy) frequency N (see Fig. 1.4). This represents the frequency of oscillation of a fluid parcel having a small density difference with respect to the surrounding flow, and it is strictly related to the fluid stratification. Indeed, if we consider a typical mean flow velocity U , the vertical extension of the strata in a stably stratified flow is inversely proportional to the buoyancy frequency, that is $L_B = U/N$. The Brunt-Väisälä frequency as well as other relations involving quantity can be used to rescale the Boussinesq equations (1.27) and (1.29),

$$\begin{aligned}
 N &= \sqrt{\frac{gb}{\rho_0}} \\
 \rho' &= \theta \sqrt{\frac{b\rho_0}{g}} \\
 p &= \frac{p'}{\rho}
 \end{aligned} \tag{1.33}$$

Therefore, the set of Boussinesq equations can be written in terms of the minimum number of free parameters as follows,

$$\nabla \cdot \mathbf{u} = 0 \tag{1.34}$$

$$\frac{\partial \mathbf{u}}{\partial t} + (\mathbf{u} \cdot \nabla) \mathbf{u} = -\nabla p - N\theta \hat{e}_z + \nu \nabla^2 \mathbf{u} + \mathbf{F} \tag{1.35}$$

$$\frac{\partial \theta}{\partial t} + (\mathbf{u} \cdot \nabla) \theta = Nu \mathbf{u} \cdot \hat{e}_z + \kappa \nabla^2 \theta \quad (1.36)$$

where we completed the momentum equation with a generic forcing \mathbf{F} . As it is commonly done in the classical framework of the Navier-Stokes equations, if we proceed with the non-dimensionalization of the equations set (1.34)–(1.36), we obtain

$$\nabla \cdot \mathbf{U} = 0 \quad (1.37)$$

$$\frac{\partial \mathbf{U}}{\partial t} + (\mathbf{U} \cdot \nabla) \mathbf{U} = -\nabla P - \frac{1}{Fr} \Theta \hat{e}_z + \frac{1}{Re} \nabla^2 \mathbf{U} + \mathbf{F} \quad (1.38)$$

$$\frac{\partial \Theta}{\partial t} + (\mathbf{U} \cdot \nabla) \Theta = \frac{1}{Fr} \mathbf{U} \cdot \hat{e}_z + \frac{1}{Nu} \nabla^2 \Theta \quad (1.39)$$

in which we defined $\mathbf{U} = \mathbf{u}/U$, $P = p/U^2$ and $\Theta = \theta/U$ as dimensionless physical units, where U and L represent some macroscopic characteristic features of the mean flow. Nu is the Nusselt number, analogously representing the ratio of convective to conductive heat transfer. However, for our applications the Prandtl number $Pr = \nu/\kappa$ is usually taken as unity, meaning that $Nu = Re$. The set of equations above depends on an additional parameter which involves the buoyancy, the Froude number $Fr = U/LN$, referring essentially to the intensity of stratification. This non-dimensional parameter indeed represents a measure of the strength of gravity waves, propagating within the domain because of the density fluctuations, with respect to the turbulent motions; in fact, it can also be defined as the ratio between the characteristic time of gravity waves τ_{W_g} and the non-linear time τ_{NL} , $Fr = \tau_{W_g}/\tau_{NL}$. For $Fr \sim 1$, meaning $\tau_{W_g} \sim \tau_{NL}$, the two phenomena have almost the same intensity. Therefore the flow is very close to the homogeneous isotropic turbulence (HIT) case, on the contrary for $Fr \ll 1$ the system is strongly stratified (and strongly anisotropic), being the characteristic time associated with inertial waves much smaller than the typical turnover time.

Chapter 2

Dynamics and energetics of geophysical flows

2.1 Extreme Vertical Drafts in Stratified Turbulent Flows

Intermittency is a hallmark of fully developed turbulence in fluids. Contrary to the predictions of Kolmogorov's original theory (K41), both experiments and numerical simulations show that dissipation exhibits intense fluctuations, localized in space and time. This phenomenon, known as small-scale (or internal) intermittency, is widely observed in the atmosphere and in the ocean in the form of highly concentrated and sporadic patches of dissipation. Intermittency, however, is not only present at the smallest scales. In the problem of mixing of a passive scalar by a turbulent flow [183], for stratified flows as in the Earth's atmosphere and in the oceans [174, 49, 58, 42], non-stationary energetic bursts at scales comparable to that of the mean flow are also observed [188, 72]. Such large-scale intermittency of vertical velocity and temperature and its relation with the mixing properties of stably stratified turbulent flows have been recently studied using both Lagrangian and Eulerian fields from DNSs of the Boussinesq equations [72], in a parameter space relevant for the atmosphere and the oceans, very close to the set of simulations adopted in this work. Over a range of Froude numbers of geophysical interest ($Fr \simeq 0.05 - 0.3$) very large fluctuations of the vertical components of the velocity and the potential temperature (diagnosed through their kurtosis of the fields $K_x = \langle x^4 \rangle / \langle x^2 \rangle$, with $x = u, \theta$) have been observed, with

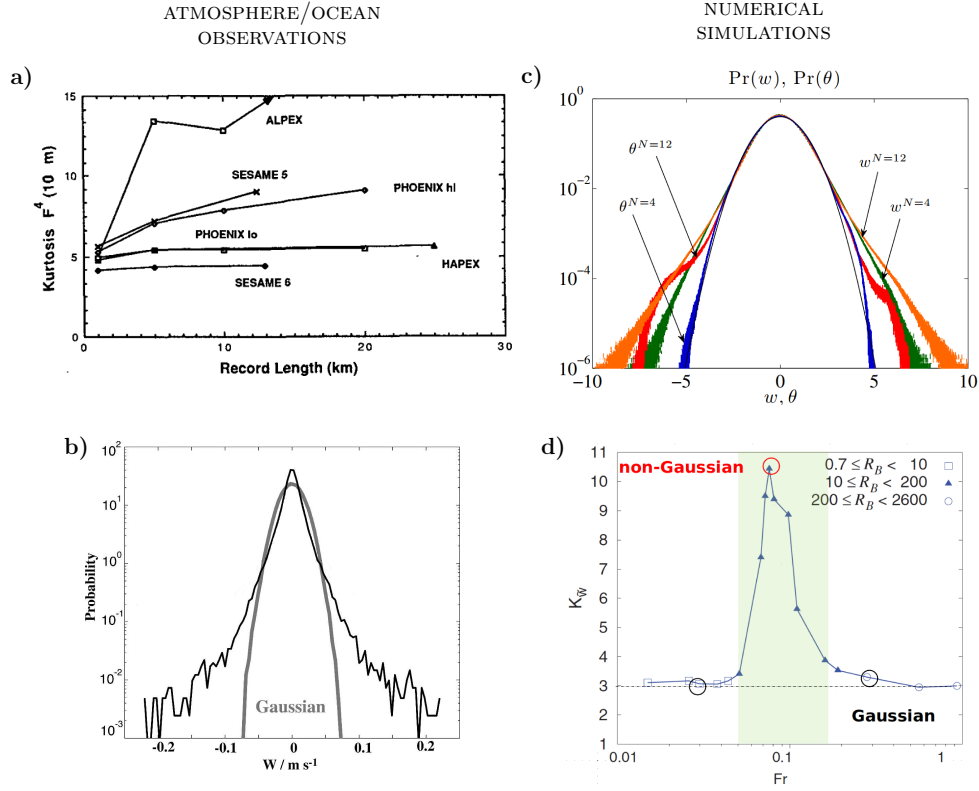


Figure 2.1. Major results regarding vertical drafts in observations and numerical simulations from: **a)** time series of the kurtosis computed from atmospheric velocity measurements obtained by aircraft [128], **b)** PDF of the vertical velocity w from floaters in the Oregon shelf (from [58]), **c)** PDF of the vertical velocity w and temperature θ fields for different levels of stratification in DNSs (from [188]) and **d)** trend of the kurtosis of the vertical velocity K_w as a function of the Froude number obtained from several DNSs (adapted from [72]).

a non-monotonic trend as a function of Fr resulting in a sharp transition from Gaussian to non-Gaussian wings of the probability distribution functions and back again, Fig. 2.1 (panel d), [72]). This behavior is also captured by a simple model, representing the competition between gravity waves on a fast time-scale and nonlinear steepening on a slower time-scale (details in [72]). The existence of a resonant regime characterized by enhanced large-scale intermittency, as understood within the framework of the proposed model, was then linked to the emergence of structures in the velocity and potential temperature fields, localized overturning diagnosed through the gradient Richardson number $Ri_g = [N(N - \partial_z \theta) \partial_z \mathbf{u}_\perp]^2$ and mixing. In the

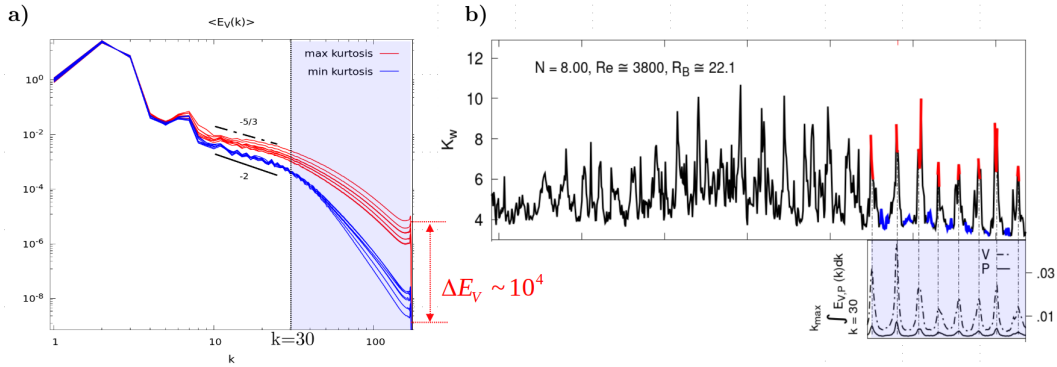


Figure 2.2. Turbulence and small-scale intermittency generation by large-scale extreme vertical drafts. Kinetic energy power density spectra in panel a) are computed over peaks (red spectra) and troughs (blue spectra), respectively (adapted from [139]). Panel b): Temporal trend of K_w for run $N = 8.0$ which shows the highest overall volume kurtosis (vertical dotted line). The bottom right inset shows the kinetic and potential dissipation integrated for $k \geq 30$ in the sub-interval with highlighted peaks (red) and troughs (blue) of K_w .

same regime, the mixing efficiency Γ exhibits a linear scaling with the Froude number and an increase of its value of roughly one order of magnitude, reaching its maximum value in correspondence with the peak in K_w . It is worth noticing that, unlike other studies on the mixing efficiency in stratified and/or rotating flows [127, 101], these flows are forced, increasing the probability of observing extreme vertical drafts intermittently developing in the simulation domain. Large-scale intermittency in stratified flows has also been linked to mixing, dissipation and anisotropy. This last, in particular, has been extensively studied with the help of velocity and temperature tensors [182] referring to the geometry of the fields (1D or 2D, 3D and axisymmetric, oblate or prolate); these tensors are equal to zero in the isotropic case. A lack of isotropy can be associated with intermittency, as well as with the long-range interactions between large-scale coherent structures and small-scale dissipative eddies. Combining these mathematical tools with dimensional analysis and estimates of the adimensional numbers it can be found that, in rotating stratified flows, a sharp increase in mixing and dissipation efficiency associated, in an intermediate regime of parameters, with large-scale anisotropy and large-scale intermittency, as observed in the vertical velocity through its kurtosis [182].

The same authors [139] extended some of the simulations of the Boussinesq equations used in [72, 73], yet with $Fr \approx 0.05 - 0.3$, for much longer times (under the action of a random forcing, isotropic in the Fourier space) observing that the temporal evolution of the volume kurtosis of the vertical component of the velocity K_w is characterized by the alternation “quite” regions, with values close to the Gaussian reference (namely 3), and very “active” regions where K_w spikes up to $\simeq 11$. Kinetic and potential energy spectra averaged (in time) over peaks and troughs show that in correspondence with the highest values of the kurtosis, small (turbulent) scales are massively generated in the fluid domain, the spectral redistribution of the kinetic energy approaching a $k^{-5/3}$ slope within the inertial range (thus at intermediate scales), compatibly with the Kolmogorov prediction for fully developed turbulence. Conversely, the spectra corresponding to the troughs in K_w are steeper and lower in magnitude (for wavevectors $k > 10$), following a k^{-2} trend at the intermediate scale, with much reduced spectral density at the smaller scales (up to four orders of magnitude) compare to what is observed in the neighbour regions of the signal (with higher kurtosis, see panels (b) and (c) in Fig. 2.2). The same happens for the potential energy spectrum which is characterized by a $k^{-5/3}$ power law behaviour inertial range in both peaks and troughs [139]. In the study presented in Marino et al. [139] the statistics of kinetic and potential energy dissipation rates ($\epsilon_V = \nu (\partial_j u_i) (\partial_i u_j)$ and $\epsilon_P = \kappa |\nabla \zeta|^2$, respectively) revealed that extreme vertical drafts feedback on ϵ_V and ϵ_P , playing a major role in the way energy is dissipated in stratified turbulence. Large-scale intermittent structures in the vertical velocity do generate small turbulent scales and dissipation, thus modulating the distribution of the kinetic energy dissipation rate (see 2.3).

A comparison between the vertical profile of $K_w(z, t)$ and $\epsilon_V(z, t)$, shown in Fig. 2.3(c)–(d) for the stratified flow with $N = 8$, also evidenced at a given time $t = T^*$ in panels (a)–(b), reveals how planes characterized by strong values of the dissipation (integrated into the horizontal, for a fixed z identifying the plane) corresponds to peaks of the by-plane kurtosis indicative of the abundance of vertical drafts at that quota along z . The correlation can be clearly appreciated visually in Fig. 2.3 showing patches of enhanced kinetic energy dissipation (larger than three

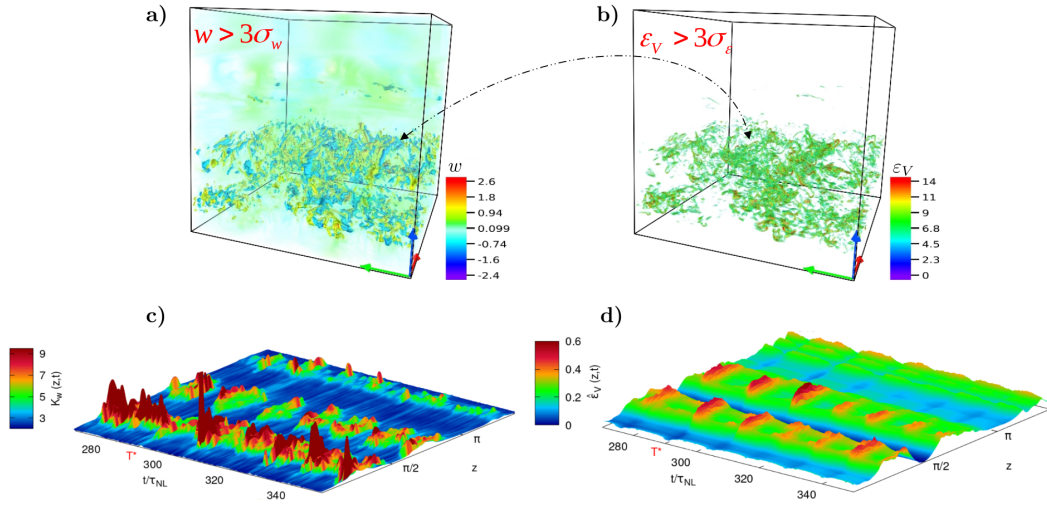


Figure 2.3. Visual comparison between extreme values of the vertical velocity (a) and of kinetic dissipation (b). Bottom panels, (c)–(d), show the variation of the vertical velocity kurtosis K_w and kinetic dissipation ε_V over time and planes (identified by the z coordinate), respectively (adapted from [139]).

standard deviations) emerging concomitantly with extreme values of w . On the other hand, regions with moderate and weak values of the integral dissipation are associated with lower values of the by-plane kurtosis. Visualizations in Fig. 2.3 (bottom panels) of the vertical profiles of the by-plane kurtosis and of the normalized kinetic energy dissipation $\varepsilon_V(z, t + \phi)$ (as a function of time) emphasize both spatial and temporal correlations between the emergent vertical drafts (detected through the amplitude of the kurtosis) and the enhancements of the kinetic energy dissipation along the z -axis. The large dissipation peaks occur immediately after the strong vertical drafts and develop in the same flow layer. Although the small temporal shift cannot be appreciated from the visualized signals, its existence results clearly and quantitatively from a cross-correlation analysis between the two signals. The latter shows how the (point-wise) correlation between the two quantities maximizes for a time delay $\phi \simeq \tau_{NL}/3$ (time lag of the forward shift of the kurtosis signal), proving causation [139]. Linked to this analysis, the authors discovered that extreme drafts are necessary, for flows with moderate-to-strong stratification, to dissipate energy as efficiently as in the HIT case. Based on this study, it was possible to conclude that in stratified flows, due to the development of extreme drafts, 50% of

the total kinetic energy dissipation occurs in only the 10% of the domain volume, and potential energy is generally dissipated more efficiently than kinetic energy [139]. As a reference, in the Ocean 90% of the kinetic energy dissipation is accomplished within the 10% of the global oceanic volume [174].

2.2 Space-Filtering the Boussinesq equations

An assessment of the effect of the extreme vertical drafts on the energetics of stratified turbulent flows was possible in terms of their correlation with global spatial and temporal statistics, sometimes conditioned to select the region of space with extreme events. However, their intermittent occurrence makes it very difficult to assess how these extreme events affect the spectral energy density at the location where they occur. In other words, stratified flows characterized by powerful vertical drafts and temperature bursts end up being non-homogeneous. In contrast, classical Fourier techniques are based on global spectral decomposition that works better when applied to homogeneous systems. In other words, the straight implementation of a three-dimensional Fourier transform involves overall volume computations, thus averaging over regions that in the case of non-homogeneous flows have significantly variable features. To achieve a scale decomposition of kinetic and potential energy (as well as of other second-order quantities), which is also local in the physical space, to identify the regions where drafts develop, we adopted here the well-known space-filtering (SF) technique, analogously to what originally done in the frame of the Large-Eddy simulations (LES) approach. Here, we present our implementation of the SF approach for rotating stratified flows in the Boussinesq framework, while filtered plasma equations will be described in App. A. While in the case of LES simulations small scales are filtered, and modeled, to obtain more complex simulations at the cost of not having all the available scales of the system fully resolved, the SF technique is instead applied to the output of (DNSs), or to experimental and observational data, as we will see more in detail later in this chapter. Briefly, by knowing the fundamental equations that generate the analyzed data, it is indeed possible with the SF method to obtain quantities representing the cross-scale energy transfer rate (in the spectral space) which at the same time are defined point-wise in the physical

space. The latter is the real strength of this approach. In the following, we derive the evolution equations for the total energy, as well as for the kinetic and potential energies separately, by applying the space-filtering technique to the NSEs in the Boussinesq approximation (see Sec. 1.4) in the rotating stratified case. We will see in the next chapter how its implementation could be further improved by extending the definition to even more general filtering kernels accounting for the anisotropy characterizing many geophysical and astrophysical flows

2.2.1 Energy equations of the Boussinesq model

The governing equations in the dimensionless formulation for the incompressible fluid-velocity field, \mathbf{u} , and the (potential) temperature fluctuations, θ , in the Boussinesq approximation are

$$\nabla \cdot \mathbf{u} = 0 \quad (2.1)$$

$$\frac{\partial \mathbf{u}}{\partial t} + \boldsymbol{\omega} \times \mathbf{u} + 2\boldsymbol{\Omega} \times \mathbf{u} = -N\theta \mathbf{e}_z - \nabla \mathcal{P} + \nu \nabla^2 \mathbf{u}, \quad (2.2)$$

$$\frac{\partial \theta}{\partial t} + (\mathbf{u} \cdot \nabla) \theta = Nw + \kappa \nabla^2 \theta, \quad (2.3)$$

where $\boldsymbol{\omega} = \nabla \times \mathbf{u}$ is the flow vorticity, $\boldsymbol{\Omega}$ is the rotation rate of the system, $N \doteq \sqrt{-(g/\theta_0)\partial\bar{\theta}/\partial z}$ is the Brunt-Väisälä frequency, related to the background stratification of the fluid due to the gravity acceleration $\mathbf{g} = -g\mathbf{e}_z$, $\mathcal{P} = p/\rho_0 + |\mathbf{u}|^2/2 = \theta + |\mathbf{u}|^2/2$ is the total pressure¹ (per unit mass), and $w = \mathbf{u} \cdot \mathbf{e}_z$ is the vertical component of the flow (here taken along the stratification direction). The parameters ν and κ are the kinematic viscosity and the diffusivity, respectively. The Brunt-Väisälä frequency can also be seen as the inverse of the characteristic time of internal gravity waves which can develop into the fluid due to the density fluctuations, while the characteristic time of inertial waves is the inverse of the rotation rate $2\boldsymbol{\Omega} = f$, related to the Coriolis parameter f . From (2.2) and (2.3) it is straightforward to derive the equations for the evolution of kinetic (or flow) $\mathcal{E}_u = |\mathbf{u}|^2/2$ and potential (or thermal) $\mathcal{E}_\theta = \theta^2/2$ energy. Indeed, by taking the

¹This scalar includes the term $|\mathbf{u}|^2/2$ as a consequence of rewriting the non-linear term that would usually appear in the Navier-Stokes equation by using the vector identity $(\mathbf{u} \cdot \nabla)\mathbf{u} = \boldsymbol{\omega} \times \mathbf{u} + \nabla(|\mathbf{u}|^2/2)$

scalar product with \mathbf{u} of Eq. (2.2) and multiplying Eq. (2.3) by θ , one directly obtains,

$$\frac{\partial \mathcal{E}_u}{\partial t} + \nabla \cdot (\mathcal{P}\mathbf{u}) = -N\theta w + \nu \left[\nabla^2 \mathcal{E}_u - \|\boldsymbol{\Sigma}\|^2 \right], \quad (2.4)$$

$$\frac{\partial \mathcal{E}_\theta}{\partial t} + \nabla \cdot (\mathcal{E}_\theta \mathbf{u}) = N\theta w + \kappa \left[\nabla^2 \mathcal{E}_\theta - |\nabla \theta|^2 \right], \quad (2.5)$$

where we made use of the incompressibility condition $\nabla \cdot \mathbf{u} = 0$. If a volume average is considered with periodic or vanishing boundary conditions, the divergence terms right-hand side (RHS) in (2.4) and (2.5) easily read as,

$$\frac{\partial \langle \mathcal{E}_u \rangle}{\partial t} = -\langle N\theta w \rangle + \langle \mathcal{D}_\nu \rangle, \quad (2.6)$$

$$\frac{\partial \langle \mathcal{E}_\theta \rangle}{\partial t} = \langle N\theta w \rangle + \langle \mathcal{D}_\kappa \rangle. \quad (2.7)$$

From that the equation for the total conservative energy is,

$$\frac{\partial \langle \mathcal{E} \rangle}{\partial t} = \langle \mathcal{D}_\nu \rangle + \langle \mathcal{D}_\kappa \rangle, \quad (2.8)$$

If none injection term is present ϵ_{inj} , the energy is only dissipated in time as indicated by the terms $\mathcal{D}_{\nu,\kappa} < 0$.

2.2.2 Filtered Boussinesq equations

Following the approach described, for instance, in [46] (and references therein), here we apply the space-filtering (SF) technique to equations (2.2–2.3), deriving the evolution equations for the “filtered” kinetic and potential energies. The application of a filter implies specifying a particular scale ℓ_* , as reported in (1.7). The purpose of this procedure is to derive a set of equations for kinetic and potential energy that, for the particular case of a *low-pass filter*, describe the evolution of these energy channels for a given length scale $\ell < \ell_*$. As a consequence, the non-linear terms in the Boussinesq equation will give rise to the so-called “sub-grid terms”, which represent the energy transfer between (all) the scales $\ell \geq \ell_*$ and (all) the scales $\ell < \ell_*$ below the filter. The direction of this transfer is explicitly encoded in the sign of these terms: that is, positive if the energy is transferred to scales smaller than ℓ_* , in this case, the “sub-grid term” is seen by scales $\ell \geq \ell_*$ as a sink term, and vice versa if it is negative. We also remark that this procedure does not assume

locality (in Fourier space) of the interactions involved in the non-linear transfer through scale ℓ_* , so that any non-local and/or multiple coupling between any of the scales smaller than ℓ_* with any of the scales larger than ℓ_* are implicitly included in sub-grid terms. Moreover, the technique does not assume homogeneity (in the flow) which is what is implicitly assumed in classical spectral approaches, meaning that the “sub-grid” terms, since they are defined in the physical space, allow an analysis of the cross-scale energy transfer which is local (in the physical space) and can be directly related to structures and features within the fluid domain.

The space-filtered version of a generic field is denoted as (1.7), and it follows the commutation properties reported in (1.8). Since convolution is a linear operator, in general the following inequality should be considered $\widetilde{\mathbf{u}\mathbf{u}} \neq \widetilde{\mathbf{u}}\widetilde{\mathbf{u}}$ (see (1.13)). Following the definitions described in the previous section we can derive the filtered version of the Boussinesq equations by applying a general filter to (2.1)–(2.3)

$$\frac{\partial \widetilde{\mathbf{u}}}{\partial t} + \widetilde{\boldsymbol{\omega}} \times \widetilde{\mathbf{u}} + \mathcal{T}_{xu}^{(\omega)} + 2(\widetilde{\boldsymbol{\Omega}} \times \widetilde{\mathbf{u}} + \mathcal{T}_{xu}^{(\Omega)}) = -(\widetilde{N}\widetilde{\theta} + \mathcal{T}_N^{(\theta)})\mathbf{e}_z - \nabla \widetilde{\mathcal{P}} + \nu \nabla^2 \widetilde{\mathbf{u}}, \quad (2.9)$$

$$\frac{\partial \widetilde{\theta}}{\partial t} + \nabla(\widetilde{\theta}\widetilde{\mathbf{u}} + \mathcal{T}_{\theta u}) = \widetilde{N}\widetilde{w} + \mathcal{T}_N^{(w)} + \kappa \nabla^2 \widetilde{\theta}, \quad (2.10)$$

where we have introduced the following sub-grid terms:

$$\mathcal{T}_{xu}^{(\omega)} = \widetilde{\boldsymbol{\omega} \times \mathbf{u}} - \widetilde{\boldsymbol{\omega}} \times \widetilde{\mathbf{u}}, \quad (2.11)$$

$$\mathcal{T}_{\theta u} = \widetilde{\theta \mathbf{u}} - \widetilde{\theta} \widetilde{\mathbf{u}}, \quad (2.12)$$

and,

$$\mathcal{T}_N^{(\theta)} = \widetilde{N\theta} - \widetilde{N}\widetilde{\theta}, \quad (2.13)$$

$$\mathcal{T}_N^{(w)} = \widetilde{Nw} - \widetilde{N}\widetilde{w}, \quad (2.14)$$

$$\mathcal{T}_{xu}^{(\Omega)} = \widetilde{\boldsymbol{\Omega} \times \mathbf{u}} - \widetilde{\boldsymbol{\Omega}} \times \widetilde{\mathbf{u}}, \quad (2.15)$$

In geophysical flows, such as the atmosphere and the oceans, often constant and uniform stratification and a solid-body rotation can be assumed. In this case, it is worth noticing that, for $N = N_0 = \text{cst}$ and $\boldsymbol{\Omega} = \Omega_0 \mathbf{e}_z$ (with $\Omega_0 = \text{cst}$), the filtered equations simplify since $\mathcal{T}_N^{(\dots)} = 0$ and $\mathcal{T}_{xu}^{(\Omega)} = 0$, respectively. Therefore the filtered Boussinesq equations reduce to

$$\partial_t \widetilde{\mathbf{u}} + \widetilde{\boldsymbol{\omega}} \times \widetilde{\mathbf{u}} + \mathcal{T}_{xu}^{(\omega)} = -N\widetilde{\theta}\mathbf{e}_z - \nabla \widetilde{\mathcal{P}} + \nu \nabla^2 \widetilde{\mathbf{u}} + \widetilde{\mathbf{F}}_{\text{ext}} \quad (2.16)$$

$$\partial_t \tilde{\theta} + \nabla \cdot (\tilde{\theta} \tilde{\mathbf{u}} + \mathcal{T}_{\theta u}) = N \tilde{w} + \kappa \nabla^2 \tilde{\theta} \quad (2.17)$$

In deriving the filtered version of the energy equations, it is important to explicitly rewrite the filtered total pressure, $\tilde{\mathcal{P}}$, since it contains sub-grid terms. In fact, it is easy to see that

$$\tilde{\mathcal{P}} = \tilde{\theta} + \frac{|\tilde{\mathbf{u}}|^2}{2} = \tilde{\theta} + \frac{|\tilde{\mathbf{u}}|^2}{2} + \frac{1}{2} \mathcal{T}_{u^2}, \quad (2.18)$$

with

$$\mathcal{T}_{u^2} \doteq \widetilde{\mathbf{u} \cdot \mathbf{u}} - \tilde{\mathbf{u}} \cdot \tilde{\mathbf{u}} = \text{tr}[\mathcal{T}_{uu}], \quad (2.19)$$

where $\mathcal{T}_{uu} \doteq \widetilde{\mathbf{u} \mathbf{u}} - \tilde{\mathbf{u}} \tilde{\mathbf{u}}$ is the sub-grid (or ‘‘turbulent’’) Reynolds stress tensor of the flow (or, written by components, $\mathcal{T}_{uu;ij} = \widetilde{u_i u_j} - \tilde{u}_i \tilde{u}_j$). To obtain the equations for the filtered kinetic energy $\tilde{\mathcal{E}}_u \doteq |\tilde{\mathbf{u}}|^2/2$ we need to take the scalar product of (2.16),

$$\frac{\partial \tilde{\mathcal{E}}_u}{\partial t} + \nabla \cdot (\tilde{\mathcal{P}} \tilde{\mathbf{u}}) = -\tilde{N} \tilde{\theta} \tilde{w} + \nu [\nabla^2 \tilde{\mathcal{E}}_u - \|\tilde{\Sigma}\|^2] - \tilde{\mathbf{u}} \cdot (\mathcal{T}_{\times u}^{(\omega)} + 2\mathcal{T}_{\times u}^{(\Omega)}) - \tilde{w} \mathcal{T}_N^{(\theta)}, \quad (2.20)$$

where $\tilde{\Sigma}_{ij} = \partial_i \tilde{u}_j$ is the strain tensor associated to the flow velocity $\tilde{\mathbf{u}}$ at scales $\ell > \ell_*$. The RHS terms of (2.20), involving sub-grid quantities, are the terms that determine the transfer of flow energy through scale ℓ_* . Let us note that $\mathcal{T}_{\times u}^{(\omega)}$ can be rewritten in terms of the sub-grid Reynolds stress tensor \mathcal{T}_{uu} , as $\mathcal{T}_{\times u}^{(\omega)} = \nabla \cdot (\mathcal{T}_{uu} - \text{tr}[\mathcal{T}_{uu}]/2)$. Therefore, $\tilde{\mathbf{u}} \cdot \mathcal{T}_{\times u}^{(\omega)}$ is in effect related to the energy transfer through the scale ℓ^* that arises because of the interaction between the strain tensor at scales $> \ell$, $\tilde{\Sigma} = \nabla \tilde{\mathbf{u}}$, and the ‘‘turbulent’’ Reynolds stress tensor \mathcal{T}_{uu} ,

$$\tilde{\mathbf{u}} \cdot \mathcal{T}_{\times u}^{(\omega)} = \nabla \cdot \left[\left(\mathcal{T}_{uu} - \frac{\text{tr}[\mathcal{T}_{uu}]}{2} \mathbf{I} \right) \cdot \tilde{\mathbf{u}} \right] - \mathcal{T}_{uu} : \tilde{\Sigma}, \quad (2.21)$$

where in the last step we used the incompressibility condition, $\nabla \cdot \tilde{\mathbf{u}} = 0$. As a result, equation (2.20) can be rewritten as

$$\begin{aligned} \frac{\partial \tilde{\mathcal{E}}_u}{\partial t} + \nabla \cdot \left[(\tilde{\mathcal{E}}_u + \tilde{\theta}) \tilde{\mathbf{u}} + \mathcal{T}_{uu} \cdot \tilde{\mathbf{u}} \right] &= -\tilde{N} \tilde{\theta} \tilde{w} + \nu [\nabla^2 \tilde{\mathcal{E}}_u - \|\tilde{\Sigma}\|^2] \\ &+ \mathcal{T}_{uu} : \tilde{\Sigma} - 2 \tilde{\mathbf{u}} \cdot \mathcal{T}_{\times u}^{(\Omega)} - \tilde{w} \mathcal{T}_N^{(\theta)}, \end{aligned} \quad (2.22)$$

where the symbol ‘‘:’’ means tensor scalar product, i.e., $\mathcal{T}_{uu} : \tilde{\Sigma} = \mathcal{T}_{ij} \tilde{\Sigma}_{ji}$. In (2.22) we neglected the external forcing term, which was considered in the filtered momentum equation (2.16). This term represents a filtered energy injection rate $\tilde{\epsilon}_{inj}$ affecting the kinetic (and total) energy rate usually at a large scale.

Analogously, multiplying equation (2.10) by $\tilde{\theta}$, after rewriting some terms, it is possible to obtain the evolution equation for the filtered potential energy $\tilde{\mathcal{E}}_\theta \doteq |\tilde{\theta}|^2/2$:

$$\frac{\partial \tilde{\mathcal{E}}_\theta}{\partial t} + \nabla \cdot (\tilde{\mathcal{E}}_\theta \tilde{\mathbf{u}} + \mathcal{T}_{\theta u} \tilde{\theta}) = \tilde{N} \tilde{\theta} \tilde{w} + \kappa [\nabla^2 \tilde{\mathcal{E}}_\theta - |\nabla \tilde{\theta}|^2] + \mathcal{T}_{\theta u} \cdot \nabla \tilde{\theta} + \tilde{\theta} \mathcal{T}_N^{(w)}, \quad (2.23)$$

where now the sub-grid term $\mathcal{T}_{\theta u}$ plays the role of a sort of ‘‘turbulent’’ heat-flux vector for the temperature fluctuations $\tilde{\theta}$ at scales $> \ell$. It is worth noting that the divergence terms left-hand side (LHS) in (2.22) and (2.23) represent the energy transported through the domain because of the work of the mean flow, pressure and turbulence. In particular, these divergence terms vanish by taking a spatial average of the equations, which in this case reduces to the following expression

$$\frac{\partial \langle \tilde{\mathcal{E}}_u \rangle}{\partial t} = - \langle \tilde{N} \tilde{\theta} \tilde{w} \rangle + \langle \tilde{D}_\nu \rangle - \langle \mathcal{S}_u \rangle, \quad (2.24)$$

$$\frac{\partial \langle \tilde{\mathcal{E}}_\theta \rangle}{\partial t} = \langle \tilde{N} \tilde{\theta} \tilde{w} \rangle + \langle \tilde{D}_\kappa \rangle - \langle \mathcal{S}_\theta \rangle, \quad (2.25)$$

where

$$\tilde{D}_\nu = \nu [\nabla^2 \tilde{\mathcal{E}}_u - \|\tilde{\Sigma}\|^2], \quad (2.26)$$

$$\tilde{D}_\kappa = \kappa [\nabla^2 \tilde{\mathcal{E}}_\theta - |\nabla \tilde{\theta}|^2], \quad (2.27)$$

and the kinetic and potential sub-grid terms

$$\mathcal{S}_u = -\mathcal{T}_{uu} : \nabla \tilde{\mathbf{u}} + 2 \tilde{\mathbf{u}} \cdot \mathcal{T}_{xu}^{(\Omega)} + \tilde{w} \mathcal{T}_N^{(\theta)} \quad (2.28)$$

$$\mathcal{S}_\theta = -\mathcal{T}_{\theta u} \cdot \nabla \tilde{\theta} - \tilde{\theta} \mathcal{T}_N^{(w)} \quad (2.29)$$

The sub-grid terms in (2.28) and (2.29) indicate the energy crossing the filtering scale ℓ^* , and therefore they represent a local (in space) measure of the non-local (in Fourier) interactions between scale $\ell < \ell^*$ and $\ell \geq \ell^*$. According to the filtering type (e.g. high-pass, low-pass or band-pass), but also to the filtering function (e.g. Fourier, Gaussian, top-hat, Butterworth and so on) the meaning of the sub-grid terms can slightly change. However, the results do not, and indeed they are independent from the choice of the filtering kernel [67]. We developed the filtered Boussinesq equations using a notation which results in sub-grid terms having the same meaning of the classical spectral flux; therefore, as depicted in Fig. 2.4, the sign of \mathcal{S} indicates if the

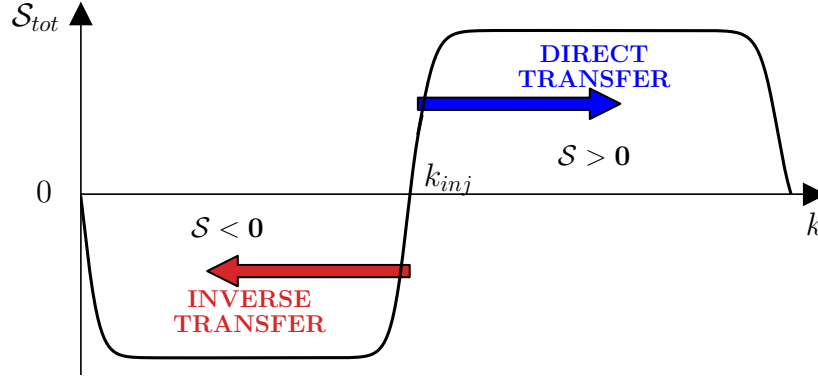


Figure 2.4. Schematic representation of the direction of the energy flux in the presence of a dual transfer, to large (red) and small (blue) scales. Analogously to what is the classical notation for the spectral energy transfer, if the sub-grid terms \mathcal{S}_α (with $\alpha = \{u, \theta, tot\}$) are positive the transfer is toward smaller scales, the opposite if negative.

net transfer is either direct (towards small scale) when $\mathcal{S} > 0$ or inverse (to large scale) when $\mathcal{S} < 0$. The first term on the RHS in (2.24) and (2.25) $N\tilde{\theta}\tilde{w}$ is present in both the equation for the filtered kinetic and potential energy with an opposite sign; this term, often referred as to buoyancy flux [73], represents the amount of energy converted from kinetic to potential (if positive) and vice versa (if negative) at the filtering scales. The buoyancy term indicates that stratification (due to gravity) is the key ingredient that couples the two energy channels which would be otherwise independent of each other. Gathering equations (2.22) and (2.23) together we obtain the expression for the filtered total energy

$$\begin{aligned} \frac{\partial \tilde{\mathcal{E}}}{\partial t} + \nabla \cdot [(\tilde{\mathcal{E}} + \tilde{\theta}) \tilde{\mathbf{u}} + \mathcal{T}_{uu} \cdot \tilde{\mathbf{u}} + \mathcal{T}_{\theta u} \tilde{\theta}] &= \tilde{D}_\nu + \tilde{D}_\kappa + \tilde{\theta} \mathcal{T}_N^{(w)} + \mathcal{T}_{\theta u} \cdot \nabla \tilde{\theta} \\ &+ \mathcal{T}_{uu} : \tilde{\Sigma} - 2 \tilde{\mathbf{u}} \cdot \mathcal{T}_{\times u}^{(\Omega)} - \tilde{w} \mathcal{T}_N^{(\theta)}, \end{aligned} \quad (2.30)$$

where the sub-grid \mathcal{S}_{tot} term for the total energy is the sum of the previously defined sub-grid terms for the kinetic and potential energy (2.29) and (2.29)

$$\mathcal{S}_{tot} = -\mathcal{T}_{uu} : \nabla \tilde{\mathbf{u}} - \mathcal{T}_{\theta u} \cdot \nabla \tilde{\theta} + 2 \tilde{\mathbf{u}} \cdot \mathcal{T}_{\times u}^{(\Omega)} + \tilde{w} \mathcal{T}_N^{(\theta)} - \tilde{\theta} \mathcal{T}_N^{(w)}, \quad (2.31)$$

By taking the spatial average, equation (2.30) reduces to

$$\frac{\partial \langle \tilde{\mathcal{E}} \rangle}{\partial t} = \langle \tilde{D}_\nu \rangle + \langle \tilde{D}_\kappa \rangle - \langle \mathcal{S}_{tot} \rangle \quad (2.32)$$

which tells us that, in the absence of an energy injection mechanism and in the unfiltered expression, the total energy rate is determined by dissipation due to kinematic viscosity and thermal diffusivity; however the rate of filtered total energy depends also on the amount of energy exchanged between spatial scales which here is represented by the sub-grid term.

We can summarize the equations for the filtered energy as

$$\frac{\partial \langle \tilde{\mathcal{E}}_u \rangle}{\partial t} = - \langle \tilde{N} \tilde{\theta} \tilde{w} \rangle + \langle \tilde{D}_\nu \rangle - \langle \mathcal{S}_u \rangle \quad (2.33)$$

$$\frac{\partial \langle \tilde{\mathcal{E}}_\theta \rangle}{\partial t} = \langle \tilde{N} \tilde{\theta} \tilde{w} \rangle + \langle \tilde{D}_\kappa \rangle - \langle \mathcal{S}_\theta \rangle \quad (2.34)$$

with

$$\mathcal{S}_u = -\mathcal{T}_{uu} : \nabla \tilde{\mathbf{u}} \quad (2.35)$$

$$\mathcal{S}_\theta = -\mathcal{T}_{\theta u} \cdot \nabla \tilde{\theta} \quad (2.36)$$

and

$$\mathcal{S}_{\text{tot}} = \mathcal{S}_u + \mathcal{S}_\theta = -\mathcal{T}_{uu} : \nabla \tilde{\mathbf{u}} - \mathcal{T}_{\theta u} \cdot \nabla \tilde{\theta} \quad (2.37)$$

The two remaining contributions of the sub-grid terms in (2.35) and (2.36) represent the energy transfer through scale for the standard hydrodynamic case.

The space-filtering (SF) approach can be easily applied to direct numerical simulations (DNSs), despite a large amount of data, since their application is based on three-dimensional gradients of either vector or scalar fields and on the knowledge of the governing equations of motion which determine the expression of the sub-grid terms. In a completely controlled scenario, as is the case for numerical simulations in general, the SF techniques have a straightforward application; indeed several works have been recently published combining the SF method with DNSs in a variety of contexts, ranging from magneto-hydrodynamics (MHD) [40, 6] to compressible fluid turbulence [94], and also in oceanic simulations [37, 9] or more in general DNSs in the Boussinesq framework [7]. In observational data, the SF technique is often applied to reduced models of the original equations since not all the components of the field gradient are available. This technique is indeed successfully applied to both observational and experimental data, as it has been for some very interesting

works (e.g., Aluie et al. [9], Buzzicotti et al. [37], De Leo and Stocchino [59], Manzini et al. [132]). Especially on observational data, the space-filtering approach gives information (in the spectral-temporal or spectral-spatial domain) that resemble what is usually obtained through wavelet analysis [71]; the latter has been widely adopted in the last decades for the analysis of turbulence in various physical systems [216]. However, the SF method, compared to the wavelet analysis, directly exploits the dynamical equations which can also be adopted to verify specific models in many physical frameworks; moreover, it allows the computation of third-order quantities $\propto U^3/L$ that gives a wider picture of how the energy is transferred in turbulent flows. In this work, we also implemented a novel definition of the filtering procedure which allows us the analysis of the anisotropic components of the energy flux, which is particularly important for the investigation of turbulent flows, such as the atmosphere and oceans where the Earth's rotation and gravity impose the anisotropy, or in the solar wind with a strong background magnetic field.

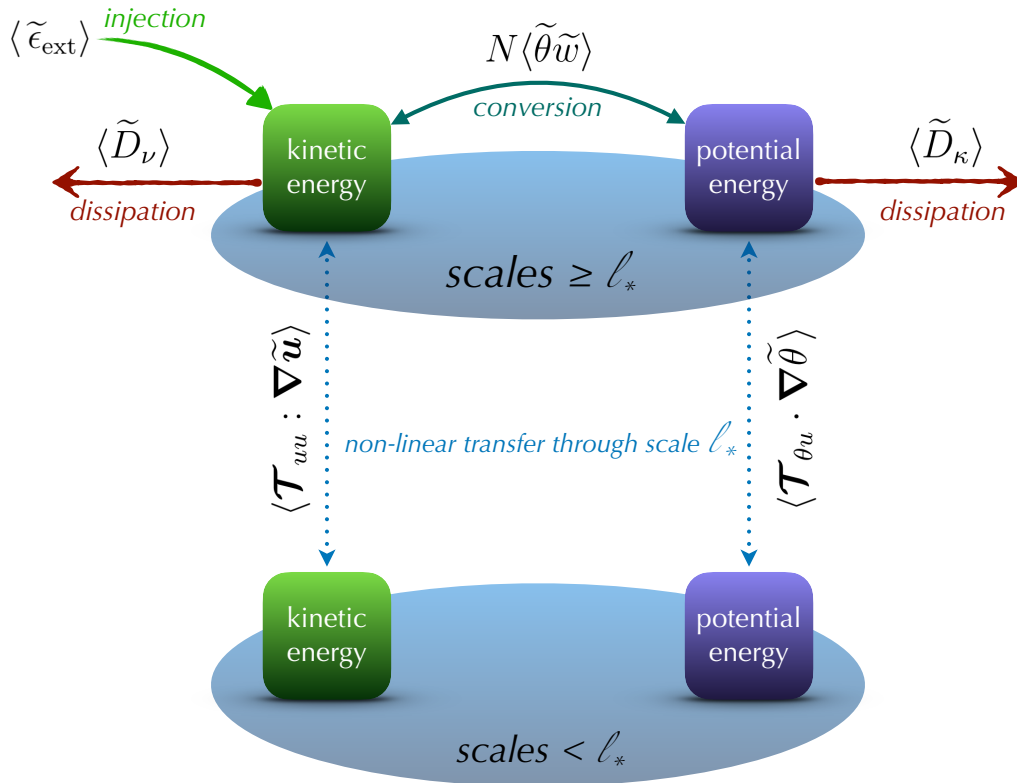


Figure 2.5. Scheme of the available energy routes after applying the space-filtering technique to the Boussinesq equations.

Chapter 3

Space-Filtering and spectral energy transfer rate

To understand how the energy is transferred in turbulent systems when multiple scales are involved, spectral analyses (in Fourier space) are commonly implemented since they provide information on the energy transfer through spatial (or temporal) scales. However, in order to know how the energy is distributed both spatially and through the scales, we can make use of the so-called space-filtering (SF) or coarse-graining (CG) approach. This is a common technique adopted in the analysis of PDEs, first introduced by Leonard [112] for modeling turbulent flows via Large-Eddy simulations (LES), then further developed by [86] as an investigation tool for turbulent systems. TheSF technique has been successfully applied in several turbulence domains. Eyink [67] and Aluie and Eyink [5] proved, without any assumptions of homogeneity or isotropy, the locality of turbulent cascades both with rigorous mathematical arguments and in direct numerical simulations DNSs. The same authors extended the application of the technique to geophysical flows described by the Navier-Stokes equations (NSEs) in the Boussinesq approximation [7], to compressible flows [8] and to astrophysical plasmas in the magneto-hydrodynamics (MHD) regime [6]. Several authors employed the SF technique to study how the presence of coherent structures affects the transfer of energy across scales both in neutral and electrically conductive fluids; in particular, Motoori and Goto [157] revealed the hierarchy and the sustaining mechanism of vortex structures in turbulent

channel flow simulations at high friction Reynolds number, Camporeale et al. [40] combined the SF approach with wavelet analysis to prove that coherent structures in plasmas, described by 2.5D Hall-MHD simulations, represent locations of enhanced energy transfer in a particular range of scales, and Manzini et al. [133] observed, in fully 3D Hall-MHD simulations, how magnetic reconnection sites affect the energy dissipation. In addition, the SF technique has been successfully applied to experimental data of water channel flow [14], quasi-2D laboratory flow [114, 70] and tidal flows [59], and also to observational data, as in Buzzicotti et al. [37] where they analyze the scale dependence of the geostrophic kinetic energy using satellite images of the oceanic flow at high latitude, or Rai et al. [184] which studied the scale interaction between wind and the geostrophic ocean flow showing that wind releases kinetic energy into the ocean only at a scale larger than $\sim 200\text{km}$. The direct application of the technique to observational and experimental data remains however much more complicated in many situations because of limited data sets, strong approximations and assumptions. As it is possible to understand from the various applications described above, the main strength of the SF technique, which complements the classical Fourier approach, is that this method allows probing the dynamics of a turbulent system simultaneously in scale and in the physical space, resulting particularly suited for non-homogeneous systems. Indeed, this approach provides a direct quantification of the direction (upscale or downscale) and intensity of the energy flux across scales, maintaining, at the same time, local (in physical space) information on how energy is transferred in the domain. The space locality is a key point of this method not implying the assumptions of homogeneity or isotropy. Recently, Hellinger et al. [94] compared this approach with the Karman-Howarth-Monin (KHM) equation for compressible 3D hydrodynamics simulations. The authors found agreement between the two approaches even though a few discrepancies were observed, especially in the localization of different turbulence processes (e.g., inertial range, dissipative effects and others), this is not surprising, as the authors claim the structure functions and space-filtering approaches are very different procedures. Indeed, also Kuzzay et al. [110] pointed out that the SF technique adopted by Aluie and Eyink [5], Camporeale et al. [40] and many other authors, derived from the

LES approach, does not provide an easy and direct comparison with the classical third-order structure functions. The main difficulty relies on the definition of the filtered energy, defined as the square of the filtered fields $\tilde{\mathcal{E}}_\phi = \tilde{\phi}^2/2$, which determines the type of structure functions one chooses to study. Therefore, the authors [110] proposed an alternative definition of the large-scale energy based on the filtering approach which is directly related to the energy flux, leading to a local version of the 3/4-law of MHD which does not rely on any assumption of isotropy and homogeneity. It has been also pointed out by Sadek and Aluie [190] that there exist a direct connection between SF and wavelet analysis, the latter widely used in many studies to overcome Fourier analysis' limitations. The wavelet analysis, indeed, is essentially a band-pass filtering with a kernel function with varying amplitude, corresponding to the different filtering scales. Wavelets have been used extensively since Farge [71] to investigate local properties of turbulence such as energy density, spectrum, and intermittency [35, 227].

Here, we try to make another step in understanding the relation between classical spectra (Fourier) approaches and the space-filtering technique by comparing the two approaches in several DNS where the behaviour of the energy flux is well known and therefore they can represent benchmark cases to further validate this technique.

3.1 Total Energy Flux

A considerable effort has been made within the scientific community in characterizing turbulence by analyzing the transfer of energy among scales in Fourier space (*e.g.*, Mininni et al. [151], Verma [217], Debliquy et al. [60], Mininni et al. [152]), as already mentioned, this approach is particularly useful when we are interested in quantifying globally the scale-by-scale energy budget. However, its limits arise when we try to link the energy transfer with local properties or structures of the flow which is often the case when dealing with non-homogeneous and/or anisotropic systems. In the classical spectral framework, we make use of the Fourier transforms ($\hat{\mathbf{u}}$) of the physical fields (\mathbf{u}),

$$\mathbf{u} = \sum_{\mathbf{k}} \hat{\mathbf{u}}(\mathbf{k}) e^{i\mathbf{k}\cdot\mathbf{x}}, \quad \hat{\mathbf{u}}(\mathbf{k}) = \frac{1}{V} \int \mathbf{u}(\mathbf{x}) e^{-i\mathbf{k}\cdot\mathbf{x}} d\mathbf{x}^3 \quad (3.1)$$

which is computed over the entire domain, globally, and therefore it does not provide information about the spatial locality. By doing the Fourier transforms of the Navier-Stokes equations (NSEs) and taking the dot product with the spectral representation of the field, we end up obtaining the evolution of the kinetic energy passing through a given scale, identified by its wave number k . If we consider, for the sake of simplicity, the ideal (non-viscous) HD framework,

$$\partial_t E_u(k) = - \int \sum_q \mathbf{u}_k (\mathbf{u} \cdot \nabla) \mathbf{u}_q = \sum_q \mathcal{T}_{uu}(q, k) \quad (3.2)$$

$\mathcal{T}_{uu}(q, k)$ is the *transfer function* indicating the rate of energy exchanged between the shells (or modes) k and q . Indeed, (3.2) involves that $\mathcal{T}_{uu}(q, k) = -\mathcal{T}_{uu}(k, q)$, highlighting how the rate of energy passing from the shell q to k must be equal to the rate at which the shell k is receiving energy from q [1, 64, 217]. The transfer function allows evaluating the energy exchange taking place between various Fourier modes because of nonlinear triadic interactions between wavenumbers, satisfying the relation $\mathbf{k} + \mathbf{p} + \mathbf{q} = 0$, which are at the basis of the energy transfer in turbulence [107]. The previous expression for the transfer function (3.2) is indeed equivalent to summing over all the wavenumbers p of the advecting field satisfying the triadic relation with k and p which represent the exchanging energy modes. The definition of transfer function accounts thus for both local and non-local interactions, but whether the former or the latter are dominant cannot be evaluated. However, in a comparison with the SF approach, we are mainly interested in the *energy flux* (e.g. kinetic, potential and magnetic), which can be defined as,

$$\Pi_u(k) = - \sum_{k' < k} \sum_q \mathcal{T}_{uu}(k', q) \quad (3.3)$$

this quantity further highlights the net contribution of local and non-local interaction with the selected mode k (see panel (a) of Fig. 3.1). However, in the total energy flux, the non-local contributions often cancel out leaving the total flux dominated by local interactions [220, 67]. The energy flux $\Pi_u(k)$ can be seen as the rate of energy exchanged by the modes inside a shell in the interval $[k, k + 1]$; if the flux is positive (negative) the energy is transferred to scale smaller (larger) than k . The concept can be extended to the classical definition of direct (downscale) and inverse (upscale)

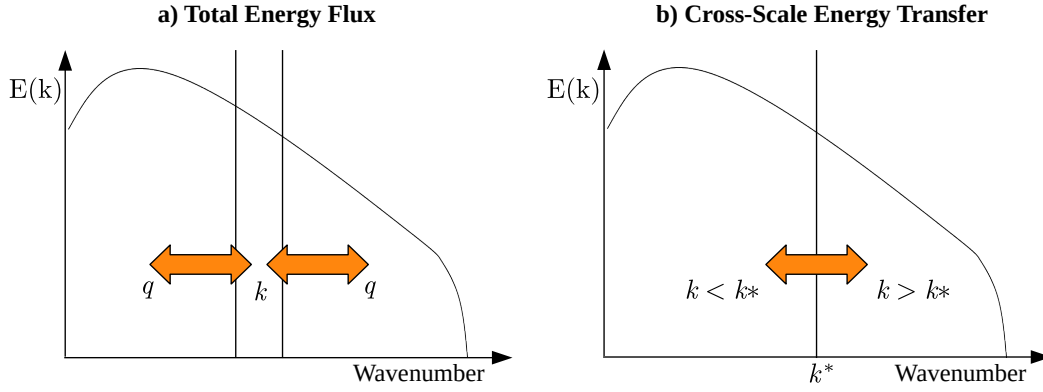


Figure 3.1. Schematic representation of the comparison between the total energy flux provided by the Fourier analysis (a) and the cross-scale energy transfer (b) provided by the sub-grid terms after the application of a low-pass (or high-pass) filter.

turbulent cascade whether a clear range with constant energy flux is observed. In the Boussinesq model (Sec. 2.2.2) an equation for the evolution of a scalar is coupled with the momentum equation through the buoyancy term Nw , with N Brunt-Väisälä frequency and w the vertical velocity. However, even if the scalar field only represents a passive quantity the equations for the energy conservation should be completed considering the evolution of the potential energy as well (see (2.5)), being the total energy $\mathcal{E}_T = \mathcal{E}_u + \mathcal{E}_\theta$. Since the scalar field is non-linearly advected by the velocity field, we can define the spectral flux of the potential energy, indicating the energy transfer across scales, in an analogous way to what we did for the kinetic energy. Therefore, the potential energy flux can be defined as,

$$\Pi_\theta(k) = - \sum_{k' < k} \sum_q \mathcal{T}_{\theta\theta}(k', q) \quad (3.4)$$

with

$$\mathcal{T}_{\theta\theta}(q, k) = - \int \theta_k (\mathbf{u} \cdot \nabla) \theta_q \quad (3.5)$$

Nevertheless, as we will see in the following, both the kinetic and potential energy transfer, across wave numbers in the Boussinesq model, are strongly affected by the energy exchange between the two channels (which is not the case if $N = 0$). In particular, in our simulations, only the velocity field is forced and the temperature fluctuations would be zero if θ was not coupled with the velocity field.

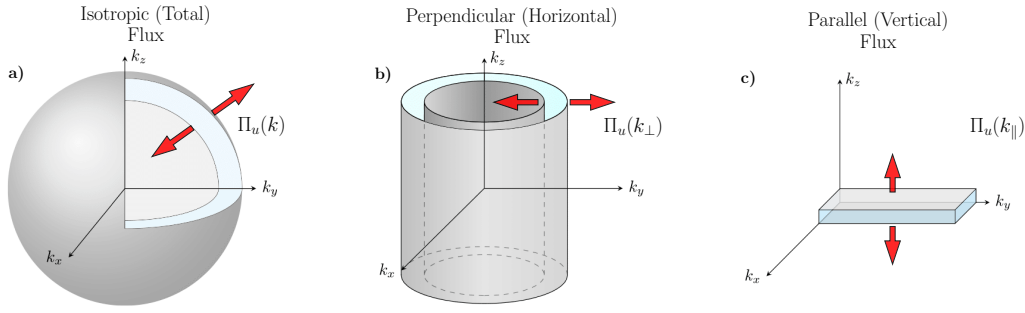


Figure 3.2. Isotropic (or spherical) total energy flux, panel a), and the anisotropic flux representations in the form of cylindrical (or axisymmetric) shells for the perpendicular (or horizontal) flux, panel b), and of planar shells for the parallel (or vertical) flux, panel c). Here, gravity is assumed to be in the z direction.

3.1.1 Anisotropic energy fluxes

It is well-known that in geophysical flows, that are strongly stratified, gravity inhibits the vertical motions, creating typical features, such as pancake structures, which make the fluid both anisotropic and non-homogeneous. The classical turbulence theory by Kolmogorov (K41) and the statistical tools derived, such as the energy fluxes, is strongly based on the assumption of homogeneity and isotropy, therefore the standard interpretation of energy cascade may not be valid anymore in this framework. This is also the case for MHD turbulence, especially in the astrophysical context when often an ambient magnetic field imposes a direction of anisotropy. For this reason, it is often useful distinguish between the perpendicular (or horizontal) and a parallel (or vertical) component of the energy flux. Billant and Chomaz [19] pointed out that, even in strongly stratified fluids, the vertical Froude number $Fr_v = U/L_v N$ is $O(1)$ meaning that when length scales of the order of the buoyancy scale $L_B = U/N$ are considered the idea of energy cascade proposed by Kolmogorov, characterized by a direct energy transfer, may be still valid. The axisymmetric energy transfer function is obtained from,

$$\mathcal{T}_{uu}(k_{\perp}, k_{\parallel}) = - \int \mathbf{u}_k (\mathbf{u} \cdot \nabla) \mathbf{u}_q \times k \sin \Theta d\phi \quad (3.6)$$

which can be integrated over cylinders (perpendicular), planes (parallel) or spheres (isotropic) to obtain the perpendicular (to the direction of anisotropy imposed by

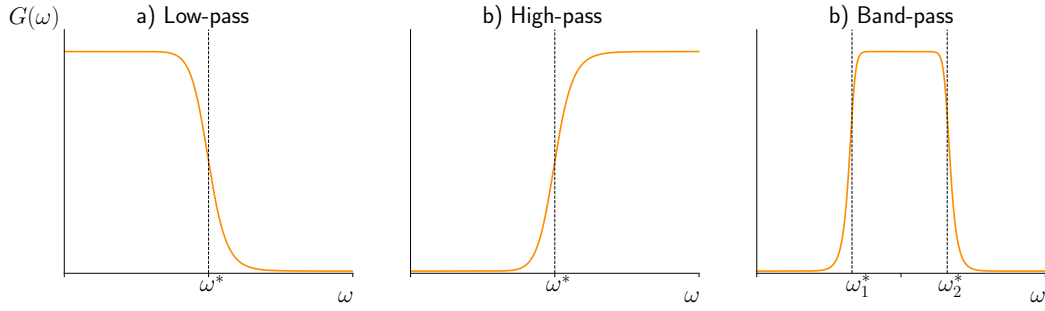


Figure 3.3. Cartoon of the three principal kinds of filters represented in the 1D version in the Fourier space. The three panels show the filter kernel $G(\omega)$ as a function of the frequency ω for: (a) low-pass, (b) high-pass and (c) band-pass filter.

gravity, see Fig. 3.2),

$$\Pi_u(k_\perp) = - \sum_{k'_\perp < k_\perp} \sum_{k_\parallel} \mathcal{T}_{uu}(k_\perp, k_\parallel) \quad (3.7)$$

and the parallel energy flux,

$$\Pi_u(k_\parallel) = - \sum_{k'_\parallel < k_\parallel} \sum_{k_\perp} \mathcal{T}_{uu}(k_\perp, k_\parallel) \quad (3.8)$$

these quantities represent the anisotropic energy flux passing either through a cylinder or a plane in the Fourier space, and do not vanish when integrated over all the wave numbers [137, 148], unlike (3.3).

3.2 Space-Filtering to investigate the anisotropic flux

In the previous chapter, we presented the filtered Boussinesq equations and their sub-grid terms which are the focus of this analysis. We explained how they provide a local (in space) representation of the cross-scale energy transfer rate and introduced the Fourier fluxes. In the following, we make quantitative and qualitative analyses of the comparison between the space-filtering (SF) technique and the classical Fourier approach. Indeed SF represent a valuable tool to (locally) analyze the scale interactions in turbulent systems, and several authors have already shown its reliability in reproducing all the expected spectral features of turbulence [94, 172, 110]. Several kinds of filters have been used (the most common are the Gaussian filter, the

Fourier filter, the top-hat filter and the Butterworth filter). They can be grouped into three main categories (see Fig. 3.3): low-pass and high-pass filters essentially give the same kind of information, that is the sub-grids terms indicate the rate of energy passing from wave numbers $k < k^*$ (larger scales) to wave numbers $k > k^*$ (smaller scales) in case of a low-pass filter (or vice versa in case of a high-pass filter). The former is exactly the approach derived from LES for filtering out the small scales which sub-grid models indeed represent. Another category of filters commonly used is the band-pass filters (e.g. Gaussian, top-hat and Fourier), which provide sub-grid terms quantifying the energy transfer rate between modes inside and outside the filtering band. This kind of filter is particularly useful since its filtering operation more closely resembles what is commonly done in the classical Fourier approach, nevertheless, band-pass filters are strongly dependent on the filter width which can affect the results obtained [1]. For all these reasons, in this analysis we applied a Butterworth (low-pass) filter $G^{(n)}(k) = 1/[1 + (k/k^*)^{2n}]$, with $n = 4$ and k^* the characteristic wave number above which fluctuations are filtered out. As it is evident this filter does not depend on any additional parameter, the only choice resides in the filtering degree n indicating how sharp will be the transition around the filtering scale, higher values of n mean sharper low-pass filtering. In contrast, whether a small value of n is picked the energy transfer rate will be overestimated accounting for effects coming from wave numbers around the filtering scale k^* . Despite the wide application of the isotropic version of the space filtering technique in 1D [132], 2D/2.5D [40, 37] and 3D [9, 133] turbulent systems, there are no (or few) works in literature implementing the anisotropic SF [133, 132], which would be particularly worth in many geophysical and astrophysical frameworks, such as the atmosphere, the oceans and the solar wind, where gravity, the Earth's rotation and a background magnetic field impose a clear direction of anisotropy. To tackle this issue and to analyze stratified turbulent DNSs, we implement a more general Butterworth filter $G^{(n)}(k)$ which can have different support geometries, instead of simply a spherically symmetric filter. In particular, we are mainly interested in the axisymmetric and parallel (see Fig. 3.2) geometry, also for a direct comparison with the anisotropic representation of the energy transfer rate, Eqs. (3.7) and (3.8). In

this new framework, we can define the filtering operation of a generic physical field, such as the velocity $\mathbf{u}(\mathbf{x})$, as the convolution with a filtering kernel with a support depending either on $k_{\perp} = (k_x^2 + k_y^2)^{1/2}$ or $k_{\parallel} = |k_z|$,

$$\begin{aligned}\tilde{\mathbf{u}}(\mathbf{x}) &= \int_V \mathbf{G}_{\ell_{\perp}}(\mathbf{x} - \boldsymbol{\xi}) \mathbf{u}(\boldsymbol{\xi}, t) d^3 \boldsymbol{\xi} \\ \tilde{\mathbf{u}}(\mathbf{x}) &= \int_V \mathbf{G}_{\ell_{\parallel}}(\mathbf{x} - \boldsymbol{\xi}) \mathbf{u}(\boldsymbol{\xi}, t) d^3 \boldsymbol{\xi}\end{aligned}\tag{3.9}$$

these operations allow us to define the anisotropic version of the sub-grid terms, $\mathcal{S}_u(k_{\perp})$ and $\mathcal{S}_u(k_{\parallel})$, as well as the spherical version to make a thorough analysis of both the isotropic and axisymmetric energy transfer rates. Indeed, in the next pages we will show how, in several DNSs of turbulent flows, this novel implementation of the SF technique can capture the main features of the Fourier fluxes, representing a valuable proxy for the cross-scale energy rate with the addition of the locality in the physical space. We expect to observe quantitative differences between the two quantities since the intrinsically different approaches of the two methods. At the same time, the standard spectral flux represents a local-in-Fourier-space representation of the energy transfer rate, the SF technique can be considered as a cross-scale energy transfer between scales above and below the filtering one, therefore not strictly local in the spectral space. However, in the latter, the fluxes are defined point-wise in the physical space of quantities which allows us to evaluate the rate of energy passing through a given scale. This is a crucial difference between the two methods, and it may be more relevant when strong non-local (in Fourier) interactions due to the non-linear term in the NSEs are present, and deeply resides in the different filtering operation performed by the two methods. Indeed, the standard approach to obtain the energy flux is based on filtering the physical fields with a Fourier filter, which has the advantage of selecting specific modes and studying the interactions with the selected scale but losing the spatial information of these structures. On the contrary, the SF approach manifests an issue of locality in the Fourier space, allowing only an evaluation of the rate of energy crossing the filtering scale. After an extensive validation of the method, the axisymmetric sub-grid terms will be used to highlight how stratified turbulent flows, presenting non-homogeneities, extreme events and coherent structures, locally inject, transfer and dissipate energy in various regimes

defined by the controlling parameters (i.e., Reynolds, Froude and buoyancy Reynolds numbers).

3.2.1 Direct numerical simulations

In this section, we briefly introduce the numerical framework adopted for all the DNSs analyzed through the manuscript. Contrary to the LES (see Introduction) approach, DNSs integrate the governing equations of a turbulent system without resorting to any modelling for the small scales. Among the various numerical schemes to solve PDEs, the GHOST [153] uses pseudo-spectral methods which have the main advantage of simulating the dynamics at all the scales with almost zero numerical dissipation, which is not the case for other approaches, such as finite-volume or finite-difference, kinetic codes and Lattice Boltzmann methods [75]. GHOST is written mainly in Fortran 90/95 with a hybrid MPI/OpenMP parallelization, and with the option to run also on GPUs [189]. Despite the huge computational cost, DNSs represent the optimal solution for studying the smallest scales in turbulent flows and the effects arising from non-linear interactions, which would not be possible with other numerical approaches (e.g. LES, RANS and URANS), and it provides information about all the physical quantities in any position of the domain. GHOST has been adopted in several works ranging from astrophysical [149, 150, 151] to geophysical turbulence [180, 138] for its versatility, high computing performance and the reliability. The hybrid parallelization of this numerical scheme achieves optimal scaling performance up to $\sim 20,000$ computing core, resulting in an average efficiency of $\sim 80\%$. The simulation domain is optimally decomposed on the various processes, allowing for an efficient implementation of the Fast-Fourier transform (FFT) at the core of pseudo-spectral methods. Time integration of the equations is performed using a second-order Runge-Kutta scheme (RK2); most of the simulations are given in single precision (round-off error $\sim 6 \cdot 10^{-8}$), which does not affect the quality of the results at the resolution considered here, to reduce the computational impact in terms of memory; however also the possibility of running simulations in double precision is provided. The set of simulations analyzed in this work has been obtained by numerically integrating the Boussinesq equations in the purely

stratified framework (see Sec. 2.2.2) with the GHOST code. It is composed by seven DNSs of fully developed stably stratified turbulence performed mainly for hundreds of turnover time, in which a random mechanical forcing guarantees the turbulent state generally imposed on a large-scale isotropic shell k_f (only 1 run with k_f at intermediate scale S20, see Tab. 3.1). The initial conditions for all the runs consist of null potential temperature ($\theta = 0$) and all the initial energy randomly distributed in terms of kinetic energy on spherical shells at $k_0 = 2.5$ in Fourier space, resulting in an initial kinetic spectrum with a Dirac's delta shape which peaks at k_0 where all the energy is at $t_0 = 0$. We applied the SF technique to such DNSs, with 512^3 grid-point resolution, which is an acceptable trade-off in terms of computational cost, scale separation and the possibility of performing very long simulations with a high temporal frequency of the output. Moreover, the SF method is a very memory-consuming algorithm, since for each time step the analysis produces for each sub-grid term (i.e., 3 sub-grid terms for Boussinesq equations of purely stratified flows) a cube with the same dimension of the simulation domain for all the resolved spectral scales ($k_{max} = n_P/3$). In other words, for a 512^3 simulation, the SF technique can produce between $\sim 100\text{GB}$ and $\sim 800\text{GB}$ of data, which require a significant amount of memory and computing hours. However, one single run at higher resolution 1024^3 (H1, see Tab 3.1) was analyzed, partially allowing a convergence analysis of the space-filtering approach and further exploration of the parameter space (e.g. higher Reynolds). From the values of the simulations parameter reported in Tab. 3.1, which are widely described in the next section (Sec. 3.2.2), it is possible to appreciate the accuracy of each computation, as expressed through the ratio between the smallest resolved scale (corresponding to the wave vector k_{max}) and the Kolmogorov dissipation wave number k_{max}/k_η (see Tab. 3.1) which varies between 1.5 and 2. For the stably stratified runs this evaluation is made considering values of the large-scale buoyancy Reynolds R_B , always greater than 1, meaning that globally the small scales in our simulations have recovered isotropy. However, sometimes the Ozmidov scale is not well resolved, i.e. $k_{Oz} > k_\eta$, as is the case for most of the interval analyzed described in Tab. 3.1. Most of the runs have been performed in a range of parameters which is relevant for geophysical studies and also significant for the

analysis of large-scale extreme events developing in stratified turbulent flows. Our analysis is conducted by varying the Froude number, with values of the Reynolds number smaller than those measured in the atmosphere or the oceans ($\text{Re } 10^8$). However Re -up to 10^6 have been recently reached with the largest simulation of rotating stratified turbulence ever made (i.e., $12,288^2 \times 384$ [2]), with a non-unitary aspect ratio. In our simulation of stratified turbulence, the Reynolds number does not vary much (Re between 3,500 and 4,000), although the buoyancy Reynolds number is the real governing parameter in atmospheric and oceanic flows. We recently started exploring regimes of higher R_B ($R_B \geq 100$) which are more realistic in geophysical systems with higher resolution DNSs (e.g. 1024^3) but even larger simulations would be worth. Three of the runs included in the analysis have been performed as a benchmark for evaluating the space-filtering technique in a well-controlled environment where the behaviour of the scale-to-scale energy transfer is known like in the case of homogeneous and isotropic turbulence (run H1), or it has been already studied as in the case of previously performed stratified simulations, with a large-scale forcing [137].

3.2.2 Operative definitions of the governing parameters

The purpose of this section is to summarize the main characteristic length scales and the relative controlling parameters involved in the turbulent flows analyzed through this manuscript as they are examined starting from the DNSs. All the values of the quantities described are reported in Tab. 3.1. We start introducing the integral scale defined as,

$$L_{int} = 2\pi \frac{\int E_V(k) k^{-1} dk}{\int E_V(k) dk} \quad (3.10)$$

where $E_V(k)$ is the kinetic power spectral density. Generally, the integral scale is well defined by the large-scale forcing injecting energy into the flow, however in simulations it slightly varies, therefore we use as integral scale the isotropic shell in Fourier space where the forcing is applied in simulations to define all the controlling parameters, therefore,

$$L \equiv L_f = 2\pi/k_f \quad (3.11)$$

The parameter controlling the strength of stratification in our runs is the Brunt-Väisälä frequency, which can be written in physical dimensionless units as,

$$N = \sqrt{\frac{-g\partial_z\theta}{\theta_0}} \quad (3.12)$$

being proportional to the vertical fluctuations of the potential temperature along the z direction $\partial_z\theta$ with respect to a background reference temperature θ_0 . In our simulations, the integral Reynolds number is defined as,

$$\text{Re} = \frac{UL}{\nu} \quad (3.13)$$

with

$$U \equiv U_{rms} = \sqrt{\langle |\mathbf{u}|^2 \rangle} \quad (3.14)$$

However it is possible to define also a "small-scale" Reynolds number,

$$\text{Re}_\epsilon = \frac{(\epsilon_V L)^{1/3}}{\nu} \quad (3.15)$$

obtained using the relation $\epsilon_V \sim U^3/L$, being ϵ_V the kinetic energy dissipation rate,

$$\begin{aligned} \epsilon_V &= \nu \langle (\nabla \mathbf{u})^2 \rangle = 2\nu E_\omega \\ \text{with } E_\omega &= \frac{1}{2} \langle |\boldsymbol{\omega}|^2 \rangle = \frac{1}{2} \langle |\nabla \times \mathbf{u}|^2 \rangle \end{aligned} \quad (3.16)$$

In stratified turbulence, the parameter governing the relative strength of gravity waves versus turbulent motions is the Froude number,

$$\text{Fr} = \frac{U}{LN} \quad (3.17)$$

which can be as well defined in terms of kinetic energy dissipation rate as,

$$\text{Fr}_\epsilon = \frac{1}{N} \left(\frac{\epsilon_V}{L^2} \right)^{1/3} \quad (3.18)$$

Run	H1	S20	S89	S3	S5	S8	S12	S14	S16
n	1024	512	512	512	512	512	512	512	512
U_{rms}	0.563	0.317	0.612	1.182	1.438	1.527	1.528	1.668	1.310
Re	6700	99.6	452.7	2970	3614	3837	3849	4192	3827
Re_ϵ	4564	79	262	1581	1380	1325	1314	1326	1342
N	0	8.0	8.0	2.948	5.0	8.0	11.8	14.0	16.0
Fr	∞	0.126	0.104	0.160	0.114	0.076	0.052	0.045	0.038
Fr_ϵ	∞	0.100	0.060	0.085	0.044	0.026	0.018	0.015	0.013
R_B	∞	1.58	4.86	76.0	47.0	22.2	10.4	8.5	5.6
R_β	∞	0.805	0.942	11.51	2.677	0.908	0.423	0.297	0.237
k_f	2.5	20	8.5	2.5	2.5	2.5	2.5	2.5	2.5
k_{max}	342	171	171	171	171	171	171	171	171
k_η	222	85	88	100	90	87	87	87	88
k_B	∞	25	13	2.5	3.5	5	8	8.5	12
k_{Oz}	∞	100	92	16	43	93.5	169	216	259

Table 3.1. The table summarizes the main parameters of all the simulations performed for this analysis. The number of grid points per dimension n , the forcing wave number k_F , the root mean square velocity $U_{rms} \equiv U$, the Reynolds number Re, the buoyancy frequency $N = (-g\partial_z\bar{\theta}/\theta_0)^{1/2}$, the Froude number $Fr = U/LN$ and the buoyancy Reynolds $R_B = ReFr^2$, being L the integral scale, taken as the scale of the forcing $L \equiv L_F = 2\pi/k_F$ and ν the kinematic viscosity.

The combination of Froude and Reynolds numbers combines in the buoyancy Reynolds number

$$R_B = ReFr^2 \quad \text{or} \quad R_{IB} = \left(\frac{\ell_{Oz}}{\eta}\right)^{4/3} \quad (3.19)$$

which is a measure of the relative interplay between buoyancy and dissipation, as clearly expressed in the ratio between the Kolmogorov length scale η and the Ozmidov scale ℓ_{Oz} , which read as,

$$\eta = 2\pi \left(\frac{\epsilon_V}{\nu^3}\right)^{-1/4} \quad (3.20)$$

and

$$\ell_{Oz} = 2\pi \left(\frac{\epsilon_V}{N^3}\right)^{1/2} \quad (3.21)$$

when the buoyancy Reynolds is close to unity, the balance between buoyancy and dissipative effects happens at the Kolmogorov scale. Another characteristic length scale which is important in stratified turbulence is the buoyancy scale,

$$\ell_B = 2\pi \frac{U}{N} \quad (3.22)$$

which represents the typical scale of the vertical motions, indeed it has also been often referred to as a vertical integral scale and, therefore adopted to derive the vertical expression of the governing parameters; for instance, it would be possible to define a vertical $Fr_h = U/L_B N$, observing that within the strata Fr is always close to unity being of the same order or even negligible with respect to turbulent eddies [19].

3.2.3 Validation of the Space-Filtering technique in DNS

To give a more quantitative comparison between the space-filtering technique implemented in this work and the classical Fourier energy flux, both in the isotropic and anisotropic setup, we test the two approaches using two different DNSs (runs H1 and S20). Run H1 is a high spatial resolution homogeneous isotropic turbulence (HIT) simulation where we expect to observe no difference between the isotropic and anisotropic energy transfer rate, and we expect to observe minor discrepancies between the two approaches. Run S20 on the contrary is a DNS of stably stratified with a mechanical forcing applied at intermediate scales since it has been observed that the perpendicular component of the energy flux rate shows a dual (upscale and downscale) transfer when forcing is applied at sufficiently small wave numbers still having both scales above and below the forcing scale well resolved [137]. The comparison between the two different approaches needs to be taken carefully into consideration for the obvious differences explained in the previous section. However, discrepancies and differences between the sub-grid terms and the spectra flux may evidence interesting features of the energy transfer in these flows. For instance, larger differences between the two may be interpreted as an enhancement of *non-local* cross-scale interactions mediating the energy transfer.

HIT run at high spatial resolution

In Fig. 3.4 it is reported the one-dimensional version of the Butterworth filter employed for the space-filtering technique used in the manuscript, together with the isotropic (first line) and anisotropic kinetic energy sub-grid term \mathcal{S}_u , in the parallel (second line) and perpendicular (third line) frameworks, at three different filtering scales ℓ^* , i.e. $\ell_1^* = 1.257$, $\ell_2^* = 0.314$ and $\ell_3^* = 0.062$, with $\ell^* = 2\pi/k^*$. The three snapshots are taken from homogeneous isotropic turbulence (HIT) DNS performed at a resolution 1024^3 , which allows reaching a Reynolds number ($Re = 6,700$) double with respect to the other simulations (512^3); all the parameters of this run are summarized in Tab. 3.1, where the Reynolds number is defined as $Re = UL_f/\nu$ (3.13) with U the root mean square flow velocity, $L_f = 2\pi/k_f$ (3.11) the integral scale taken as the scale of forcing and ν the kinematic viscosity. The ratio between the maximum and the Kolmogorov wave numbers is $k_{max}/k_\eta \approx 1.54$, therefore we fully resolve the small scales. The sub-grid term is computed over five time steps covering almost one turnover time $\tau_{NL} = U/L_f$ after the peak of dissipation or the peak of enstrophy (see (3.16)), and then averaged to obtain smoother curves and more points to have a convergent statistics; indeed, in homogeneous isotropic turbulence when a stationary turbulent state is reached, statistics computed either over temporal or spatial ensembles are equivalent. The three-dimensional renderings of Fig. 3.4 show interesting features of the space-filtering technique. Although the run is characterized by isotropic structures (top left cube), the filters highlight structures of energy transfer rate which resemble the geometry of the filter itself, i.e. isotropic for the spherical filter, tube-like for the parallel filter and pancake-like for the perpendicular version. These particular geometries are exactly what is observed in structures in HIT, rotating turbulence (see Godeferd and Moisy [88] and reference therein) and stratified turbulence [239, 116].

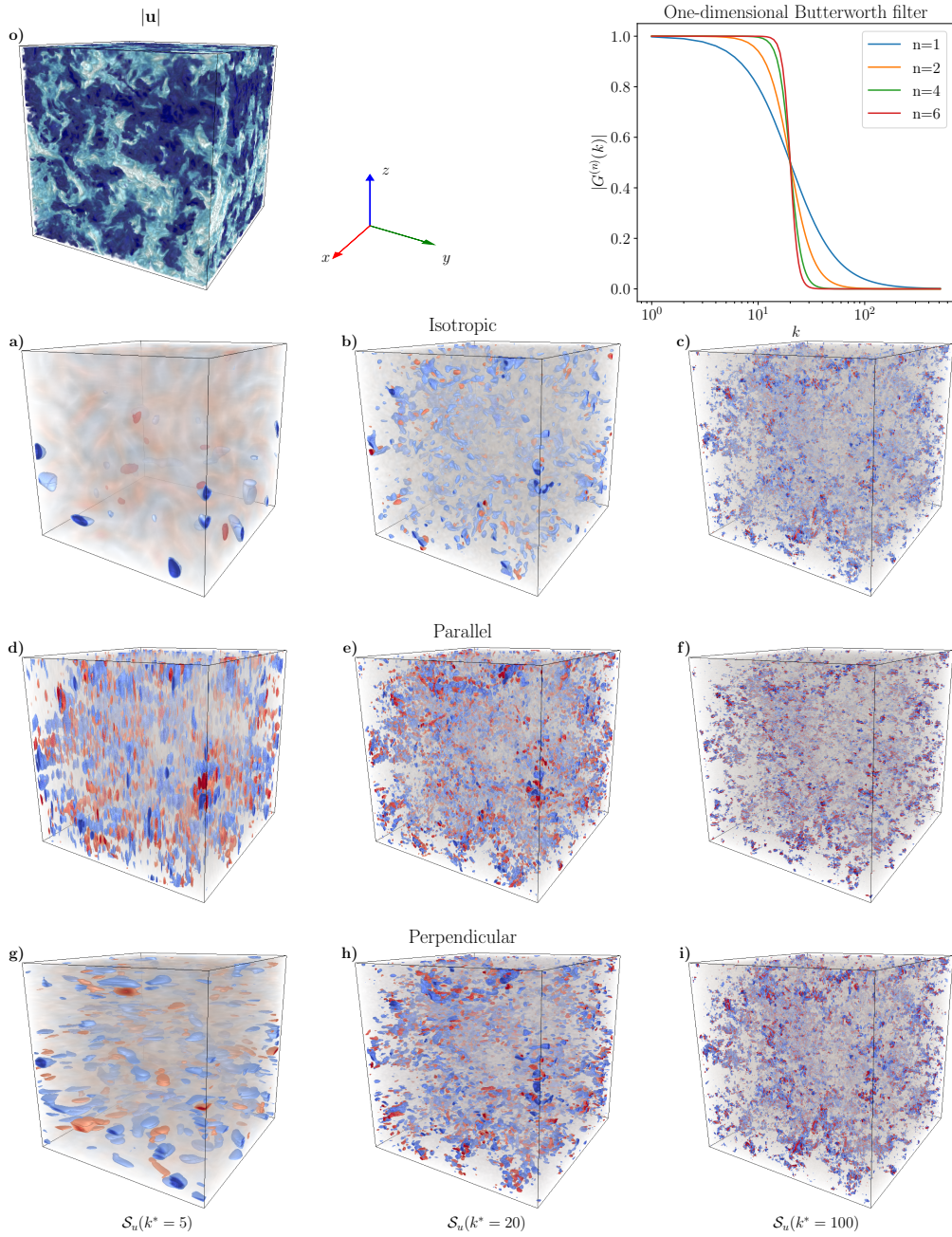


Figure 3.4. Top panel: 1D Butterworth filter for different values of n . The 3D renderings represent the kinetic energy sub-grid term \mathcal{S}_u in the isotropic, panels a)–c), parallel, panels d)–f), and perpendicular version, g)–i), for three decreasing scales identified by the wave numbers $k = 5, 20$ and 100 .

As already mentioned, we expect for this run essentially the same behavior of the three components (isotropic, parallel and perpendicular) of energy flux, with an

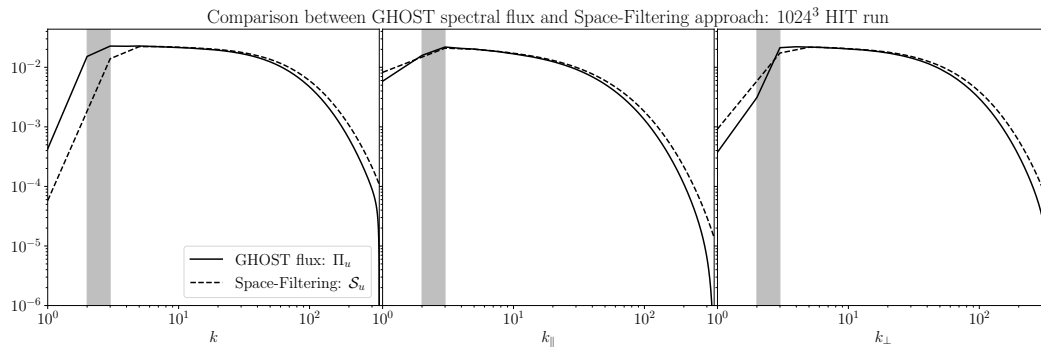


Figure 3.5. Comparison between the spectral Fourier flux (black solid) and the kinetic sub-grid term obtained from the SF technique (black dashed) for the isotropic (left), parallel (center) and perpendicular (right) filtering kernel. Quantities are averaged over five snapshots resulting in almost one turnover time τ_{NL} for a HIT simulation with 1024^3 grid points (H1, Tab. 3.1). The gray shaded area represents the spherical shell where a random mechanical forcing is applied.

evident constant inertial range in the total (isotropic) flux where the energy cascades from scale to scale.

The results of the comparison are represented in Fig. 3.5 where the three components of the flux Eqs. (3.3), (3.8) and (3.7), obtained from the GHOST code, are represented with a black solid line in the left, middle and right panel for the isotropic, parallel and perpendicular flux, respectively. The kinetic energy sub-grid term \mathcal{S}_u is depicted with a dashed black line. The total energy flux (left panel), as well as the isotropic sub-grid term, show a clear energy direct (to small scale) cascade of energy between nearly $k \geq 3$ and $k \sim 40$ where local non-linear interactions between eddies of similar size (in Fourier) interacting distributing energy to always smaller scales, in the classical Kolmogorov picture of HIT. In the inertial range, the two methods are equivalent and essentially proportional to the kinetic energy cascade rate of the turbulent flow. At large scale, around $k_f = 2.5$ where the forcing is applied and a non-local component transfer can be relevant the space-filtering technique gives opposite results, underestimating the flux at a large scale while the same is always overestimated for the anisotropic components in the same range of wave numbers (up to k_f). Beyond the inertial range, there is little discrepancy between the two approaches at the dissipative scale (large wave numbers). Here, the SSF always shows

higher values to the Fourier flux which are probably related to an underestimation of dissipative effects and therefore discrepancies could be reduced by computing the filtered term \tilde{D}_ν (2.26) which should be subtracted to \mathcal{S}_u with a significant effect only at the very small scales. The parallel and perpendicular sub-grid terms show results consistent with what was previously concluded for the isotropic component, with a more evident inertial range for the perpendicular component (right panel). By looking at both the panels in Fig. 3.5 and the 3D renderings of Fig. 3.4 it seems that the anisotropic version of the energy transfer rate, both in the classical and SF approach, tend to overestimate the total flux (isotropic) at large scale. More than the high average values of Fig. 3.5, by comparing the structures in the different rows of Fig. 3.4, the first two columns representing relative large scales show a significantly higher difference in the amount of structures between the isotropic (being more realistic) and anisotropic flux, while the same differences are less evident or almost vanishing at small scales (third column). The HIT run has helped assess the method's reliability and convergence with enhanced and better-resolved statistics. Also for this reason in the next sections, we validate the SF with a DNS of stably stratified turbulence, at lower resolution 512^3 , forced at an intermediate scale, to have enough resolution above and below the forcing wave number to observe both a direct and inverse energy transfer if present.

Stably stratified run with forcing at intermediate scale

The main results in this manuscript (see Chap. 4) are obtained for the anisotropic versions of the SF technique, since in stably stratified flow gravity imposes a strong direction of anisotropy along z , and therefore the two components $k_\perp = (k_x^2 + k_y^2)^{1/2}$ and $k_\parallel = k_z$ behave differently; however for the validation of the technique we still analyze also the isotropic component in order to have a complete assessment of the computed sub-grid terms. The stratified run performed for this step has a Froude number very close to those observed in the atmosphere $Fr \sim 0.1$ [29], however the Reynolds number is smaller $Re \simeq 100$, leading to relatively small buoyancy Reynolds numbers. This is the consequence of the choice of applying a random forcing at relatively large scale to give to the system the opportunity of developing a dual,

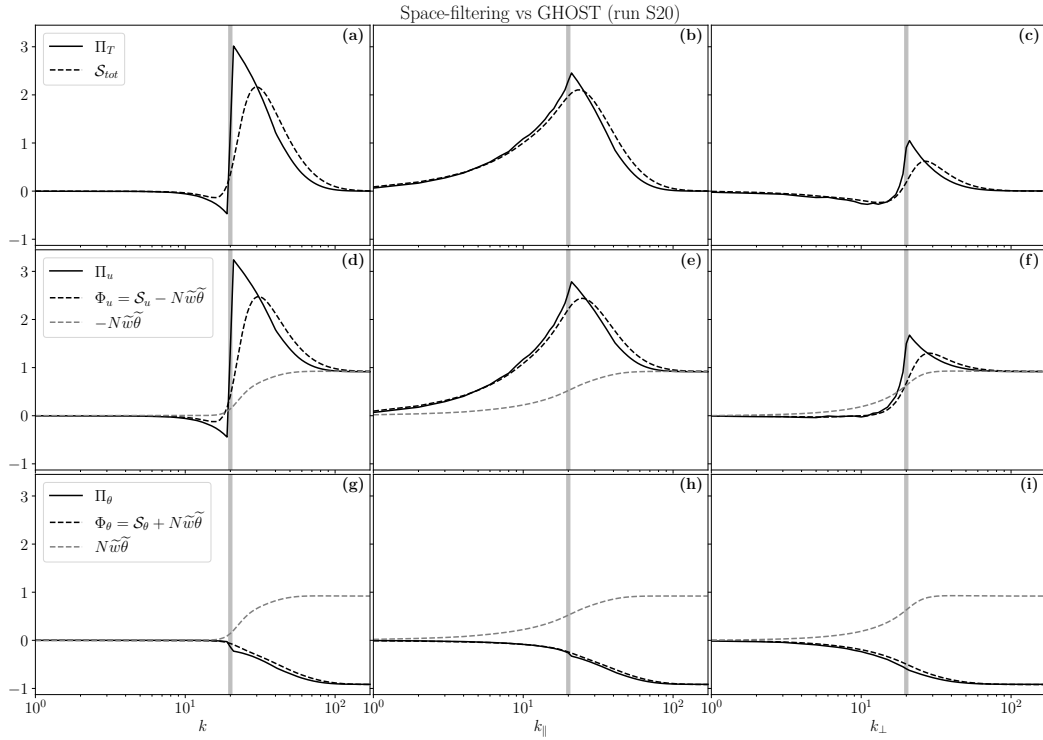


Figure 3.6. Panels (a)–(c): comparison between the isotropic (left), parallel (center) and perpendicular (right) scale-to-scale Fourier total flux Π_{tot} (black solid lines) and the sub-grid terms (black dashed lines) for run S20. In panels (d)–(f) and (g)–(i) the same comparison for the kinetic and potential energy fluxes, respectively. Within the single energy channels, $\tilde{\Phi}$ is the sum of the conservative terms on the right-hand side of Eqs. (2.33)–(2.34). The channel-conversion terms alone $\mp N\langle\tilde{\theta}\tilde{w}\rangle$ are also shown (gray dashed lines). A vertical dashed area denoting $k_f = 20$ is provided.

direct and inverse, transfer of energy in the perpendicular direction (in Fourier space), as observed in Marino et al. [137]. All the parameters of run S20 are listed in Tab. 3.1. These parameters have also been chosen to have the same buoyancy frequency $N = 8.0$ of the run, at the peak of the probability of developing large-scale extreme events [72], leading to a Froude number which is close to one of the most interesting run in terms of vertical drafts (S8, $Fr = 0.076$), even though in S20 no extreme events can be observed. A simulation with similar parameters to S20, and in particular with a forcing in the same range, has been widely analyzed in terms of spectral energy transfer in Marino et al. [137] which highlighted how the different components of the energy transfer (isotropic, perpendicular and parallel)

behave differently in presence of a direction of anisotropy, such as when gravity or rotation are present. In this analysis it has been pointed out that the isotropic flux $\Pi_T(k)$ is almost zero for $k < k_f$, indicating that almost no energy goes across spheres (in Fourier space) towards small wave numbers. On the other hand the parallel flux $\Pi_T(k_{\parallel})$ is positive and dominant for all wave numbers, indicating a strong transfer towards smaller vertical scales. Completely different is the behavior of the perpendicular component of the flux $\Pi_T(k_{\perp})$ showing a range with negative values for $k < k_f$, indicating an inverse energy transfer (to large scale), and a positive flux for $k > k_f$. Since such particular behavior has been highlighted by the Fourier analysis of the scale-to-scale energy transfer in previous works [137], here we want to show that this feature is recovered also within our implementation of the space-filter approach. This comparison is reported in Fig. 3.6(a)–(i), where we show the *total* (a)–(c), *kinetic* (d)–(f) and *potential energy flux* (e)–(i) computed both with the Fourier method $\Pi_T(k_{\perp})$ (3.7) (solid black line) and with the sub-grid terms $\langle \mathcal{S}_{\text{tot}} \rangle = \langle \mathcal{S}_u + \mathcal{S}_{\theta} \rangle$ (dashed black line), as well as the energy flux associated with the single energy channels, i.e., *kinetic* (b) and *potential* (c) energy separately. For the latter cases, the Fourier flux (black lines) is compared with the sum of the conservative terms on the right-hand side of Eqs. (2.33)–(2.34), i.e., $\tilde{\Phi}_u = \mathcal{S}_u - N\tilde{\theta}\tilde{w}$ and $\tilde{\Phi}_{\theta} = \mathcal{S}_{\theta} + N\tilde{\theta}\tilde{w}$, respectively (red lines). From all the panels in Fig. 3.6 is evident the excellent agreement between the two approaches, both at large and small scales and for any component of the sub-grid terms. For $k > k_f$ the energy fluxes always indicate a downscale energy transfer of total energy, panels (a)–(c), with a modulation of the intensity of the transfer rate going from the isotropic to the perpendicular component of the total energy flux. It is worth reminding that since we do not have enough scale separation to observe a constant flux, both above and below the forcing wave number, also for the spherical total energy flux we cannot refer to a direct/inverse energy cascade. Still, we always present the result in terms of net transfer looking at the sign of the flux to get an indication of the direction. By looking at the axisymmetric version, panel (c), the behavior previously described in terms of total Fourier energy flux is correctly recovered with the SF technique, showing an inverse energy transfer at scale $k_{\perp} < k_f$ and a direct energy

transfer in the range $k_{\perp} > k_f$, with an inversion point with almost zero net rates of total energy at $k_{\perp} \sim k_f$. Such a good agreement is also obtained for the single channels of the energy transfer, in panels (f) and (i). In this case, some interesting features emerge from the analysis with the SF approach, in particular the role of the conversion term $N\langle\tilde{\theta}\tilde{w}\rangle$, also known as buoyancy flux (dashed gray line in panels (d)–(i)), indicating the conversion from kinetic to potential energy if positive and vice-versa if negative, at scales $k_{\perp} > k_f$. Indeed, we can see from panel (f) how this term becomes the dominant contribution to the perpendicular flux at $k_{\perp} \gtrsim 90$, where $\langle\Phi_u\rangle \approx -N\langle\tilde{\theta}\tilde{w}\rangle$: this means that kinetic energy is almost totally converted into potential energy at small scales. (let us remind that when $N\langle\tilde{\theta}\tilde{w}\rangle$ is positive, it represents a sink term for $\langle\tilde{\mathcal{E}}_u\rangle$ and a source term for $\langle\tilde{\mathcal{E}}_{\theta}\rangle$; cf. Eqs. (2.33)–(2.34).) This is consistent with the fact that the flux of total energy, both computed as $\langle S_{tot}\rangle$ or as Π_T , goes to zero at small scales, *i.e.* there is no net cascade towards smaller scales in that range, but just a *small-scale kinetic-to-potential energy conversion* (plus dissipation—not shown here). By looking at the potential energy rate, panel (i), with the space-filtering analysis we can see that the negative values, in this case, do not indicate an inverse cascade of potential energy in the whole range of wave numbers but, since for the potential energy channel there is no external forcing, then this channel is only fed by the conversion of kinetic energy $\langle\Phi_{\theta}\rangle \approx N\langle\tilde{\theta}\tilde{w}\rangle$ at every scale. In fact, the transfer of potential energy mediated by the non-linear term $\langle S_{\theta}\rangle$ still exhibits simultaneously positive (direct transfer) and negative (inverse transfer) values, although in this case the inversion scale – *i.e.*, the scale at which $\langle S_{\theta}\rangle$ changes sign – is not exactly at k_f , but at slightly larger scales (around $k_{\perp}/k_0 \approx 10$). The behavior of the potential energy transfer for the three components, panels (g)–(i), is pretty much the same, with an almost zero flux at $k < k_f$ and a negative transfer dominated by the conversion term at scale $k > k^*$, probably because we analyzed a simulation forced only in the velocity field and with zero temperature fluctuations at $t = 0$, therefore its evolution in our case is triggered by the coupling between the velocity and (potential) temperature embedded in the equation of motions (see Eqs. 1.34 and 1.35). The isotropic flux is almost zero for $k < k_f$ and all the energy channels (kinetic and potential), therefore no energy is crossing spherical shells in

Fourier space for small wave numbers, however, this is not the case for the parallel component of the kinetic and total energy transfer (panels (b) and (e)) where we observe a flux to small scale which is dominant over the other component for all the wave numbers, contrary to what happens for the perpendicular component showing a dual behavior.

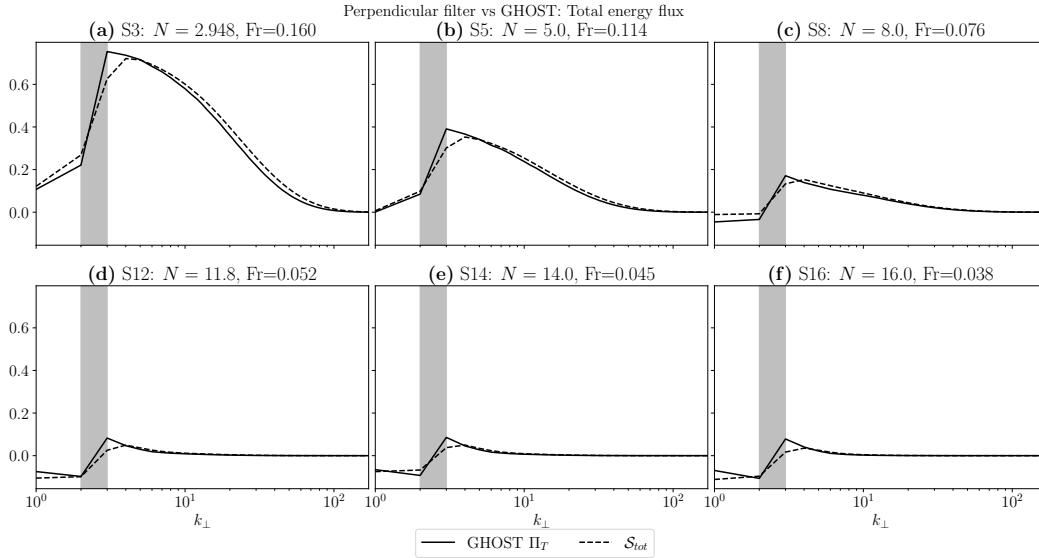


Figure 3.7. Comparison of the total energy transfer as depicted by the Fourier flux (continuous lines) and the total sub-grid term (dashed lines), as written in (2.30) for the six runs only stratified. From panel (a) to panel (f) are represented simulations from S1 to S6 (see Tab 3.1). The gray shaded area represents the shell $k \in [2, 3]$ where the mechanical forcing is applied.

3.2.4 Stably stratified runs varying the Froude number

The next step of the space-filtering (SF) validation consists in comparing the sub-grid terms with the classical spectral fluxes for a set of DNSs of stratified turbulent flows with different values of the stratification (N), therefore varying the Froude number Fr . The main parameters describing these simulations are summarized in Tab. 3.1, and they will be widely described in the next chapter; however the six runs analyzed here represent a subset of a wider parametric study which has been performed using 17 DNSs in Feraco et al. [72], as well as for the results in Chap. 5 of this manuscript. The first aspect, clearly highlighted by both the sub-grid

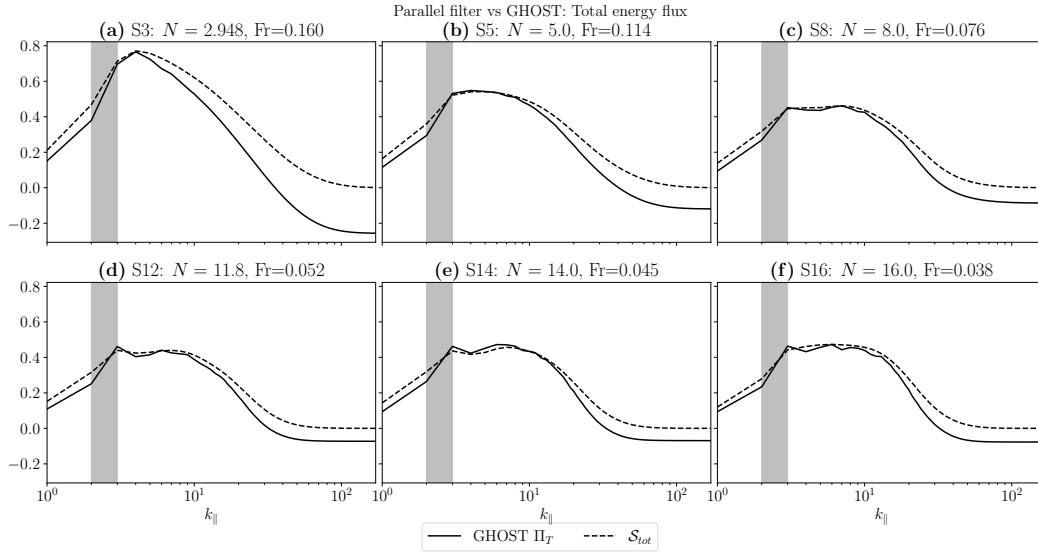


Figure 3.8. Same as Fig. 3.7 for the parallel total energy transfer $\mathcal{S}_{tot}(k_{\parallel})$.

terms (black dashed lines) and the energy fluxes (black solid lines) in Fig. 3.7, is the decreasing of the energy transfer rate for increasing stratification, as expected from other results obtained with different analyses [139]. It is worth remarking that all these simulations have the same random forcing at large scale $k \in [2, 3]$ (gray shaded area). The six runs are selected to have significantly different levels of large-scale intermittency (i.e., vertical drafts), as highlighted by the kurtosis of w in Fig. 5.1. Nevertheless, the presence of extreme events cannot be appreciated by the energy transfer averaged on the entire volume, which further evidence the “locality” (in space) of the SF approach. The comparison between the axisymmetric expression of the total sub-grid term \mathcal{S}_{tot} and the total energy flux Π_T shows a great agreement for all the runs, with slightly higher discrepancies around the energy injection scale $k \approx 2.5$. As the stratification intensifies (for $N \gtrsim 8.0$), the total energy flux starts developing an inverse (upscale) transfer for $k_{\perp} < k_f$, as already observed in Marino et al. [137], however, we do not have enough resolution in this range to draw conclusions concerning the role of stratification in driving the dual transfer. Instead, since for smaller Fr number stronger vertically sheared horizontal winds (VSHWs) develop into the flow, the latter may be the main reason for such energy going towards large scales. In Fig. 3.8 the same comparison for the parallel filter

always shows a good agreement between the two methods in terms of average spectral features recovered, even though larger differences are observed. In particular, the total energy fluxes $\Pi_T(k_{\parallel})$ become negative at large wave numbers $k_{\parallel} \gtrsim 35$, especially for weak stratification $N \lesssim 5.0$, while this is not the case for the corresponding total sub-grid terms \mathcal{S}_{tot} which instead vanish at small scales for all the simulations. The space-filtering technique in many cases seems to overestimate the energy transfer at small scales, and this effect is more pronounced at large Froude, which might be related to dissipative effects that could be included by computing the terms \tilde{D}_ν and \tilde{D}_κ in Eqs. 2.33. Contrary to what is observed for the perpendicular fluxes, here the stratification does not seem to inhibit the energy transfer that is almost constant at the intermediate scale in every panel (Fig. 3.8(a)–(f)). The same simulations will be further analyzed in the next chapters, focusing on the effect of large-scale vertical drafts on the energetics of these flows.

Chapter 4

Local energy injection by vertical velocity drafts in stratified geophysical flows

4.1 Characterization of local energy injections by vertical drafts

After having been observed both in the atmosphere and oceans, extreme vertical drafts were carefully characterized, including in their connection to small scale phenomena, such as dissipation. In particular, correlation and causation between these extreme events and enhanced values of dissipation have been pointed out in Marino et al. [139], as already introduced in Sec. 2.1. The authors concluded that vertical drafts are, as a matter of fact, dissipative structures, necessary in stably stratified fluids to dissipate energy as efficient as in homogeneous isotropic turbulent flows. However, such results do not allow to draw definitive conclusions on how the emergence of these events represents a local (in the physical space) injection of energy enhancing the turbulent cascade rate at an intermediate scale (inertial range) and ultimately increasing the small-scale dissipation. Here, our main purpose is to characterize vertical drafts in terms of the typical length scales at which they affect the dynamics of the fluid and the energy transfer at different wave

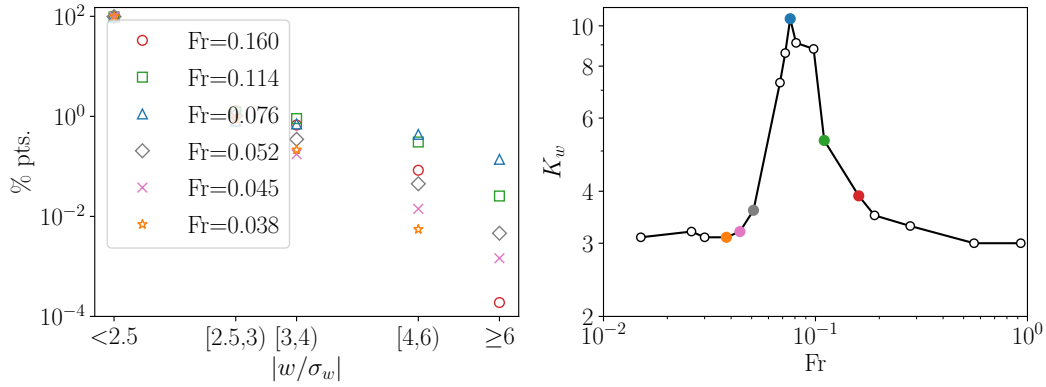


Figure 4.1. (Left) Percentage of points having the vertical velocity w in a specific range of values, computed over bins at increasing w for all the runs in Tab. 3.1. (Right) The trend of the vertical velocity kurtosis K_w as a function of the Froude number (reprinted from Feraco et al. [72]).

numbers. For this reason, the space-filtering (SF) approach represents the optimal technique, since it allows the analysis of the spectral energy transfer with quantities defined point-wise in the physical domain. In particular, we applied the SF to a set of six direct numerical simulations (DNSs) of stably stratified flows, obtained by integrating the Boussinesq equations (Sec. 2.2.2), presenting a different intensity of large-scale intermittency modulated by the Froude number, as pointed out in Feraco et al. [72] and also reported in Fig. 4.1. We will pay particular attention to run S8 (see parameter Tab. 3.1), in which extreme events are significantly more numerous, i.e. the peak in the right panel of Fig. 4.1 shows a global kurtosis $K_w \simeq 11$ indeed. The right panel in Fig. 4.1 also highlight how the vertical drafts occupy a very small portion of the simulation domain; indeed, values with $|w/\sigma_w| > 4$ represent only 0.4% of the volume for the run with the strongest large-scale intermittency (run S8, blue triangles in Fig. 4.1). For the other runs, this percentage is even smaller, whereas for smaller values of vertical velocity ($|w/\sigma_w| < 3$) the percentage of points is almost the same for all the simulations, independently from the Froude number. In Fig. 4.2 an example of the application of the SF technique is represented by the two three-dimensional renderings taken from a snapshot with many vertical drafts for run S8: (b) vertical velocity field w , where values $|w/\sigma_w| > 4$ are highlighted in red if positive and blue if negative, while lower values are depicted in transparency; in

Bin	% volume					
	S3	S5	S8	S12	S14	S16
$ w/\sigma_w < 2.5$	97.94	97.53	97.92	98.56	98.97	98.88
$2.5 \leq w/\sigma_w < 3$	1.300	1.233	0.802	1.042	0.838	0.902
$3 \leq w/\sigma_w < 4$	0.670	0.903	0.704	0.348	0.175	0.213
$4 \leq w/\sigma_w < 6$	0.084	0.307	0.436	0.045	0.015	0.005
$ w/\sigma_w \geq 6$	0.002	0.026	0.138	0.005	0.002	0.000
global K_w	3.9	5.3	10.4	3.6	3.2	3.1

Table 4.1. Percentage of volume filling per bin of vertical velocity w for all the six stratified turbulence simulations.

panel (c) the same as for the total sub-grid energy transfer $-\mathcal{S}_{tot}$, computed at scale $k_{\perp} = 10$. Positive values (red), being significantly more numerous and intense within the domain, indicate a transfer to a small scale, the opposite happens for negative values (blue), which are indeed sporadic patches into the fluid. The left panel (a) shows the by-plane kurtosis K_w of w (in black) and the average of the absolute sub-grid energy transfer $\langle |\mathcal{S}_{tot}(k_{\perp} = 10)| \rangle$ (in gray). There is a clear correlation between vertical slices with a high number of extreme events and enhanced energy transfer, both in the same locations and in the near surroundings. In some regions of the simulation domain, the sub-grid term almost perfectly maps the extreme vertical velocity structures in terms of shape and extension, highlighting the reliability of this approach for studying non-homogeneous systems. In the following we applied only the anisotropic (parallel and perpendicular) version of the filtering, even though particular attention is paid to the axisymmetric filter since it allows to decouple vertical layers. Indeed, even considering that horizontal motions dominate in a stably stratified environment, the flow develops a strong vertical variability and reorganizes itself into horizontal layers [159, 95], therefore geophysical fluid motions along the vertical direction are particularly interesting at these scales.

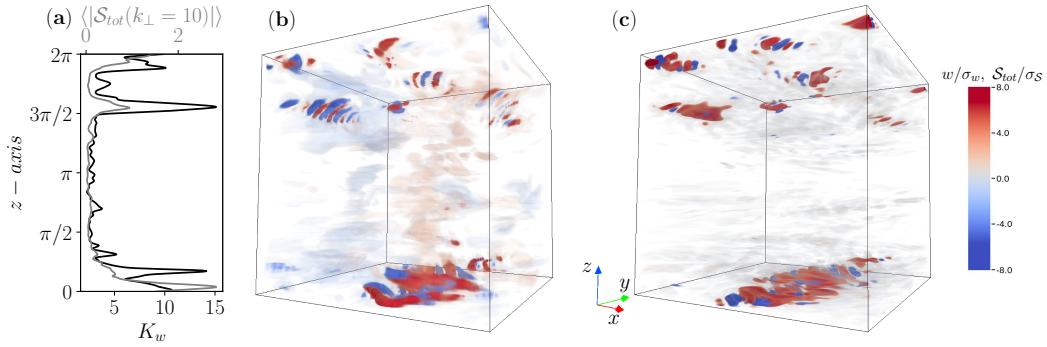


Figure 4.2. (a) Vertical profile of the kurtosis $K_w(z)$ of w (black) and the average of the absolute value of the total sub-grid energy transfer $\langle |S(k_{\perp} = 10, z)| \rangle$, (gray), both computed over horizontal planes. (b) Three-dimensional rendering of the vertical velocity w , where values $|w/\sigma_w| > 4$ are represented in solid red (positive) or blue (negative), while smaller values are depicted in transparency. (c) The same range of extreme values is selected for $S(k_{\perp} = 10)/\sigma_S$, where positive (negative) values indicate downscale (upscale) energy transfer.

4.1.1 Anisotropic energy transfer in the presence of vertical drafts (run S8)

Leveraging the space-filtering technique it is also possible to analyze the energy transfer by computing the sub-grid terms on sub-domains identified either by spatial coordinates or characteristic features of the flow. The presence of vertical drafts can be quantified by the forth-order moment (i.e., kurtosis) of the vertical velocity w probability distribution function (PDF), which highlights PDFs with non-Gaussian tails at values of w larger than several standard deviations σ_w . probability distribution functions of the vertical velocity and temperature have been shown in Feraco et al. [72], Feraco et al. [73], Rorai et al. [188], Capet et al. [42] and others, and we qualitatively observed in Fig. 4.2 how extreme values of w approximately correspond to extreme values of energy transfer, identified by the total sub-grid term S_{tot} . In Fig. 4.3 we also show that the presence of large values of S_{tot} depend on the considered scale k ; the three distributions (panels a–c) clearly show a leptokurtic behavior at all the scale with evident non-Gaussian tails, here highlighted as values $|S_{tot}/\sigma_{S_{tot}}| > 4$ in blue or red, negative or positive, respectively. The extreme values seem to increase for increasing wave numbers suggesting that the energy

transfer has intermittent fluctuations resembling those of the scale-dependent field increments $\Delta_\ell \mathbf{u}$, even though the PDF of \mathcal{S}_{tot} show a strong non-Gaussian shape also at large scale $k_\perp = 5$. The same behavior is observed for k_\parallel (not shown). However there is also an interesting difference in observing the cross-scale transfer at various scales; in particular, at large scale $k_\perp = 5$, panel (a), the PDF is highly asymmetric, with a tail of positive values being far more populated than the negative one. This is not the case for the PDFs at $k_\perp = 17$ (panel b) and $k_\perp = 33$ (panel c). An asymmetric distribution indicates a mean energy flux \mathcal{S}_{tot} which is strongly positive and therefore directed toward small scales, whereas when the distribution is more symmetric positive and negative extreme values approximately cancel out producing a low (almost null) net flux. The presence of numerous positive extreme values of total energy transfer may be likely associated with the presence of vertical drafts being particularly active at this length scale. Notably, $k = 5$ for this run is also the buoyancy scale $k_B = 2\pi/\ell_B = 2\pi U/N$, with U r.m.s. speed and N the Brunt-Väisälä frequency (see Tab. 3.1, indicating the characteristic length scale of strata created by the imposed background stratification and being known as the typical scale dominating vertical motions in stably stratified flows [19]). However, to further corroborate this hypothesis we computed averages of all the sub-grid terms (i.e. kinetic, potential and buoyancy flux) over different sub-domains created starting from the whole simulation box $N = 512^3$. Since the extreme events are easily identified as points with vertical velocity several standard deviations far from the mean value (usually $|w/\sigma_w| > 4$), we divided the spatial domain in bins according to values of w . The largest bin is for $|w/\sigma_w| < 2.5$, representing those points having vertical velocity within the Gaussian core of the distribution and, as also reported in Tab. 4.1, filling the majority $\gtrsim 97\%$ of the volume even at the peak of kurtosis (i.e., run S8). Second and third bin, $|w/\sigma_w| \in [2.5, 3)$ and $|w/\sigma_w| \in [3, 4)$ respectively, are somewhat transitional intervals creating a distinct separation between points with a Gaussian behavior and extreme events. Indeed the last two bins are only those containing values of vertical velocity several standard deviations far from the average value; for instance, values with $|w/\sigma_w| \geq 4$ already represent intermittent events filling only a tiny portion of the entire volume, i.e. $\sim 0.6\%$ for the run with

the highest number of events (S8, see Tab. 4.1). The number and range of vertical velocity bins are arbitrary and principally depend on the constraint of having enough points to obtain convergent low-order statistics in every bin. Therefore, the division reported in Tab. 4.1 is a conservative choice that allows making a comparison also with runs without vertical drafts (e.g. runs outside the peak of K_w , see Fig. 4.1), as we will show in Sec 4.2. However, to deeply analyze the most intermittent run (S8) we divided the last interval into two separate bins $|w/\sigma_w| \in [6, 8)$ and $|w\sigma_w| \geq 8$ still having enough samples to produce significant statistics. It is worth stressing again that this type of analysis is only possible thanks to the characteristic of a space-filter approach, which retains the real-space information of the transfer through scale. In Fig. 4.4 we report panels showing the non-linear transfer through scales of total energy $\langle \mathcal{S}_{\text{tot}} \rangle$ (a), of the kinetic-to-potential conversion term (or buoyancy flux) $N\langle \tilde{\theta}\tilde{w} \rangle$ (b), and of the non-linear energy transfer through scales of kinetic (c) and potential (d) energies, $\langle \mathcal{S}_u \rangle$ and $\langle \mathcal{S}_\theta \rangle$, respectively, versus k_\perp when the average of these quantities is conditioned over different values of $|w/\sigma_w|$ (see legend). There are a few important features that are highlighted by these plots. Generally, for all the quantities, larger values of $|w|$ correspond to higher energy transfer at every scale. The transfer rate for extreme events $|w/\sigma_w| > 4$ is several orders of magnitude more intense than the average rate produced by the bulk of points (black lines, $|w/\sigma_w| < 2.5$) which, on the contrary, is pretty low as a result of several regions with opposite values of the “local” energy transfer that cancel out. By looking at the four energy channels separately in Fig. 4.4, various interesting behaviors can be noticed. First, the direct transfer (i.e., towards smaller scales) of total energy is strongly enhanced over a broad range of intermediate perpendicular scales, namely $2 \lesssim k_\perp / \lesssim 20$, when increasingly extreme values of the vertical flow are encountered (Fig. 4.4(a)). This range partially overlaps with the forcing scale $k_f = 2.5$. Second, there is a significant conversion from kinetic to potential energy approximately over the same range of scales, and it is larger for larger values of w (Fig. 4.4, panel b). At large scale $k_\perp \lesssim 10$ the energy conversion is almost null, then at an intermediate scale, $10 \lesssim k_\perp \lesssim 30$, the filtered buoyancy flux $N\langle \tilde{\theta}\tilde{w} \rangle$ increases the more rapidly the larger are values of the vertical velocity $|w|$. Indeed, nearly all the kinetic-to-potential

energy transfer in the system occurs in the range $10 \lesssim k_{\perp} \lesssim 30$ (after $k_{\perp}/\approx 30$, the conversion is almost saturated, meaning that there is no significant additional contribution as smaller scales are included). Also, note that the fact that the curve of $N\langle\tilde{\theta}\tilde{w}\rangle$ decreases at $k_{\perp}/\gtrsim 40$ means that part of the potential energy is converted back into kinetic energy at the smallest scales, especially for high values of $|w|$ (this may explain the small amount of inverse transfer of kinetic energy that can be seen in Fig. 4.4(c) at small scales). Third, vertical drafts seem to play a different role for the two energy channels (Fig. 4.4(c)–(d)). In fact, while extreme values of w result in an enhancement of the direct cascade in kinetic energy at intermediate scales (the same effect is also seen in the total energy), with a peak around $k_{\perp} \simeq 5$, these drafts are instead triggering a simultaneous direct and inverse flux in potential energy (emerging at $k_{\perp} \gtrsim 20$ and at $k_{\perp} \lesssim 10$, respectively). This means that, from the perspective of kinetic energy, drafts boost the intermediate-scale direct cascade that is already present due to the external forcing at large scales, while, through the coupling term $N\tilde{\theta}\tilde{w}$, the potential-energy channel perceives these events as an external injection of energy in the range $10 \lesssim k_{\perp} \lesssim 20$. It is also important to notice that vertical drafts seem necessary to trigger a dual potential energy transfer since it can be observed only for $|w/\sigma_w| > 4$. Finally, the above analysis highlights the role of extreme events in locally driving the energy transfer in stratified flows at a particular Froude numbers around $\text{Fr} \approx 0.08$. Interestingly, as previously mentioned, the stable stratification imposed in this simulation is associated with a buoyancy scale (see Sec. 3.2.2) $k_B \approx 5$, being also approximately the scale at which the total perpendicular energy transfer peak (Fig. 4.4(a)–(d)). The buoyancy scale indicates the width of (potential) temperature layers and seems to represent a sort of bound for the vertical extension of the most extreme events, even though the peak in the figure is broad, including numerous smaller and larger drafts. However, the maximum extension of these phenomena cannot be completely appreciated because of the effect of the large-scale forcing at $k_f = 2.5$ and the finite size of the box. In addition, we will see in the following that the position of such peak does not move significantly varying the Froude number, and therefore varying the layer thickness. The same analysis has been performed for the parallel component $k_{\parallel} \equiv k_z$ of the

space-filtering quantities, and the results are reported in Fig. 4.5(a)–(d). There are a couple of features resembling what is already observed for the axisymmetric flux: first, the direct proportionality between $|w|$ and the energy transfer is conserved for all the energy channels (panels (a)–(d)). Second, the effect of the draft seems to maximize always at intermediate scale $3 \lesssim k_{\parallel} \lesssim 20$; also along the vertical direction, there is a net conversion of kinetic-to-potential energy $N\tilde{\theta}\tilde{w}$ feeding the potential energy channel (panel b). However, in general, the picture emerging from the parallel component of the cross-scale energy transfer is pretty different, as was expected since the intrinsic anisotropy of stratified flows. At first, it is simply noting that the characteristic length scale at which vertical drafts maximize their effect seems to move to a smaller scale $k_{\parallel} \approx 10$; this means that, despite the typical vertical length scale is represented by the buoyancy scale $k_B = 5$, extreme events tend to be on average smaller along the direction of gravity and therefore their geometry resembles the characteristic pancake-like shape observed many times in stratified systems [88]. Such a picture is also consistent with what was qualitatively appreciated from the three-dimensional rendering at the beginning of this chapter (see Fig. 4.2). Second, the filtered buoyancy flux (panel b) exhibits a smoother increase up to $k_{\parallel} \approx 15$, but then at smaller scales more than a half of the energy is converted back from potential to kinetic probably inducing an inverse kinetic energy transfer in that range (see panel c) only for the values of $|w/\sigma_w| > 4$; which is what we have already observed partially for the perpendicular filter (see Fig. 4.4 panel c). Finally, even though the above analysis highlights the average value of the energy transfer through scale within each range of $|w/\sigma_w|$, this only partially provides insights on the overall impact of extreme events on such transfer at a global level. To further confirm this idea in Fig. 4.7 we report the cumulative distribution of the non-linear transfer through scales of total (panel a), kinetic-to-potential (b), kinetic (c) and potential (d) energy as a function of the percentage of the volume occupied. The trend in these curves clearly shows that the smaller the scale k_{\perp} , the more intermittent the energy transfer, since all of them increase more rapidly as large wave numbers (warmer colors) are considered. At large scale (shades of blue) kinetic and potential energy fluxes exhibit an almost exact equipartition, whereas the filtered buoyancy

flux (panel b) is pretty much localized in structure at small k_{\perp} . In Pearson and Fox-Kemper [174], using data from a global oceanic model, it was observed that about 90% of the total dissipation in the ocean is achieved in only the 10% of the volume; a similar result has been obtained by Marino et al. [139] in direct numerical simulations of stably stratified flows, where the presence of vertical drafts allows reaching the 50% of kinetic dissipation by considering again only the 10% of the total volume. Here, the space-filtering technique provides similar information but is scale-dependent. In Fig. 4.8, we can see a clearer plot obtained from the cumulative distribution function (CDF) in Fig. 4.7 representing the volume that is necessary to obtain a determined percentage of cross-scale energy transfer. In other words, points for a given colored curve in Fig. 4.8 are obtained as intersections between the various curves in Fig. 4.7 and a vertical line at a fixed percentage of volume filling (i.e. 50%, 60%, 70%, 80% and 90%). The results for all the energy channels are pretty consistent with what was previously observed for the dissipation [174, 139]. In addition, we can appreciate that the 50% of total energy transfer is given by approximately the 10% of the volume already at intermediate scale $k_{\perp} \gtrsim 20$, while in the range $3 \lesssim k_{\perp} \lesssim 20$, where we saw the effect of vertical drafts maximizes, all the curves in Fig. 4.8 show an exponential decrease, indicating that the energy flux is more and more concentrated in small structures identified by the vertical velocity. The kinetic and potential non-linear transfer (panels c and d) show essentially the same behavior which is also reflected in the total energy (panel a), slightly different is the trend of the filtered buoyancy flux (panel b) which is almost constant for $k_{\perp} \gtrsim 4$. This analysis highlights the role of vertical drafts in locally injecting a significant amount of energy having an impact on both the kinetic and potential energy transfer and distribution in stratified flows, through the kinetic-to-potential conversion term.

4.1.2 Time variation of the cross-scale energy transfer with vertical drafts

In the previous section, we analyzed a few time steps corresponding to almost one turn-over time with many vertical drafts, therefore characterized by a very high

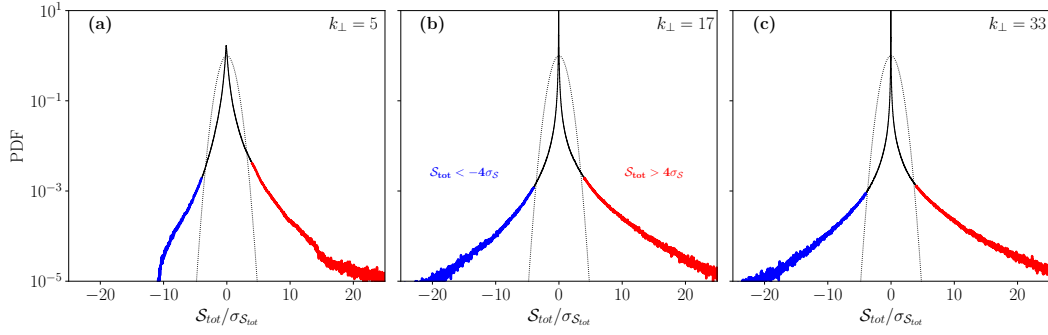


Figure 4.3. probability distribution function (PDF) of the total energy sub-grid term \mathcal{S}_{tot} computed at three different filtering scale $k_{\perp} = 5, 17, 33$ for run S8. Black dotted line is a Gaussian distribution drawn as a reference. In red (blue) we highlighted $\mathcal{S}_{tot}/\sigma_{\mathcal{S}_{tot}} > 4$ ($\mathcal{S}_{tot}/\sigma_{\mathcal{S}_{tot}} < -4$).

value of the vertical velocity kurtosis K_w . However, this simulation (run S8) has been integrated for hundreds of turn-over times exhibiting a very peculiar pattern of K_w with alternating peaks having values of the kurtosis as high as $K_w \approx 10$ and troughs close to the Gaussian reference. Such behavior has been thoroughly analyzed in Marino et al. [139], and we reported a detail in Fig. 2.2 showing this particular oscillating trend for the entire simulation time. This kind of intermittency with slow but strong quasi-periodic variations differs from the classical small-scale intermittency; Marino et al. [139] proposed, to reproduce such behavior, a simple model which is a modified version of the reduced model for field gradients in stratified turbulent flows presented in Sujovolsky et al. [203], Sujovolsky and Mininni [201] (see equations in Marino et al. [139]). The model provides a viscous damping and a forcing term added phenomenologically; in particular, they tested a forcing given by a superposition of harmonic oscillations with frequencies centered around the buoyancy frequency N and small amplitude. The other characteristic length scale adopted in the simplified model is the Ozmidov length ℓ_{Oz} (see Sec. 3.2.2) controlling the dissipative effects, whose choice can be viewed as partitioning the flow between larger scales governed by quasi-geostrophic dynamics and strongly stratified turbulence at small scale. The equations have been integrated using parameters, such as N and ℓ_{Oz} , compatible with run S8 and the results of the systems' time variability are shown in Fig. 6 of Marino et al. [139]. Such a simple model shows a bursty behavior

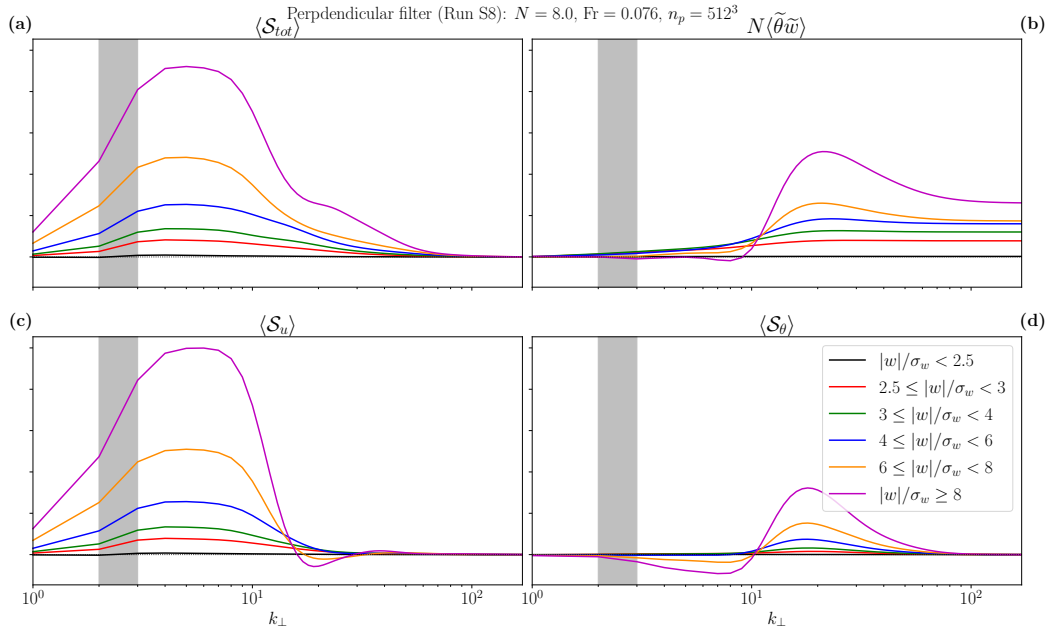


Figure 4.4. Results of the filtered total energy (a), buoyancy flux (b), kinetic (c) and potential (d) energies as a function of the filtering wave number $k_\perp = \sqrt{k_x^2 + k_y^2}$ for the axisymmetric version of the filtering kernel applied to runs S8. The gray shaded area indicates the shell where kinetic energy is injected.

reminiscent of the so-called on-off intermittency [179, 167, 191], that is long periods of very small fluctuations, followed by irregular (but sometimes repetitive) bursts reminding what is observed for K_w in Fig. 2.2, typically separated by times much larger than the characteristic timescale in the system. In terms of out-of-equilibrium statistical mechanics, the authors adopted the simplified model to partially explain the origin of vertical events involving a nonlinear resonant-like amplification of waves by eddies, as processes occurring in self-organized criticality (SOC) systems in which the strong events trigger a cascade of smaller extreme events. A different way to explain such behavior, also proposed in Marino et al. [139], is by postulating a fast evolution of the system between two slow manifolds (one associated with waves, the other with the overturning eddy instabilities); this provides even evidence for the dynamical coupling between large-scale extreme events and small-scale intermittent dissipation, which ultimately demonstrates the causation between these phenomena. For all these reasons it is particularly worth observing the impact of vertical drafts

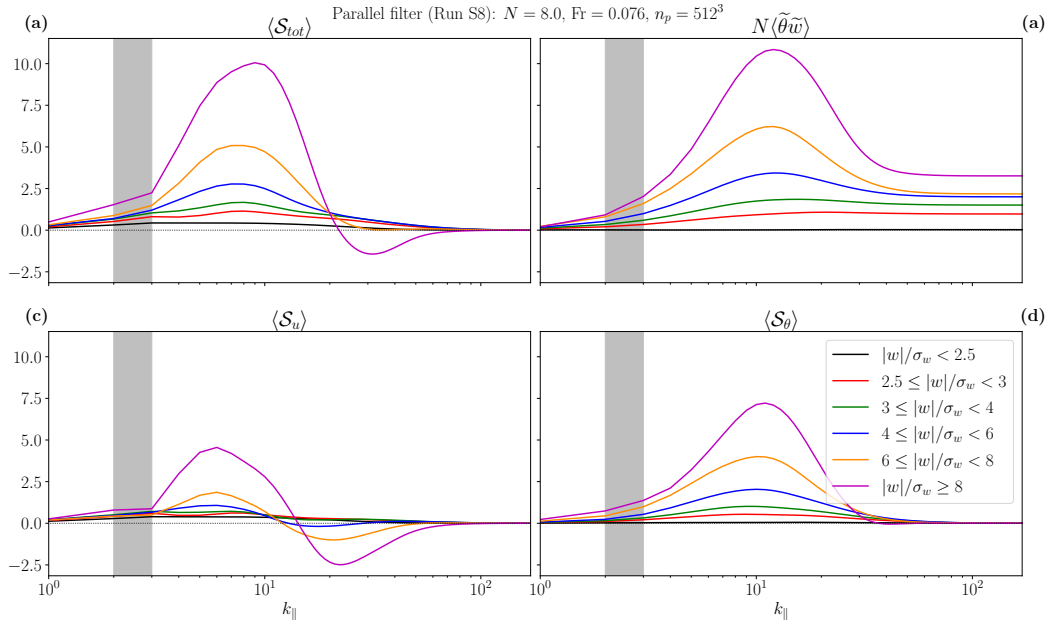


Figure 4.5. Same as Fig. 4.4 for the parallel filter $k_{||} = |k_z|$

on the non-linear energy transfer as a function of time, since their presence and the associated steepening of gravity waves may lead to enhanced (local-in-time) transfer, as was already the case for the local-in-space contribution analyzed in the previous section. In this section we analyzed more than $100\tau_{NL}$, between $t \approx 170\tau_{NL}$ and $t \approx 270\tau_{NL}$ (the red portion in Fig. 4.9), corresponding to an interval with very intense peaks of vertical velocity kurtosis $K_w \sim 10$ alternating with troughs close to the Gaussian reference value $K_w \simeq 3$. The temporal profile of K_w for the entire integration time is reported in Fig. 4.9. We observe that in this range of parameters, the kurtosis exhibits the oscillating behavior that we previously described, however even at times corresponding to plateau the value of K_w is always higher than the reference for a normal distribution indicating the presence of vertical drafts at any time, with a significant temporal variability.

In Fig. 4.10 we report the scale-time variation of the volume-averaged non-linear transfer of total $\langle \mathcal{S}_{tot} \rangle$, kinetic $\langle \mathcal{S}_u \rangle$, potential $\langle \mathcal{S}_\theta \rangle$ and kinetic-to-potential $N\langle \tilde{\theta}\tilde{w} \rangle$ energy for the entire interval previously shown in red in Fig. 4.9. The volume average is performed on different domains identified by vertical velocity values w either below $3\sigma_w$ or above $5\sigma_w$. All the quantities are normalized by the average kinetic energy

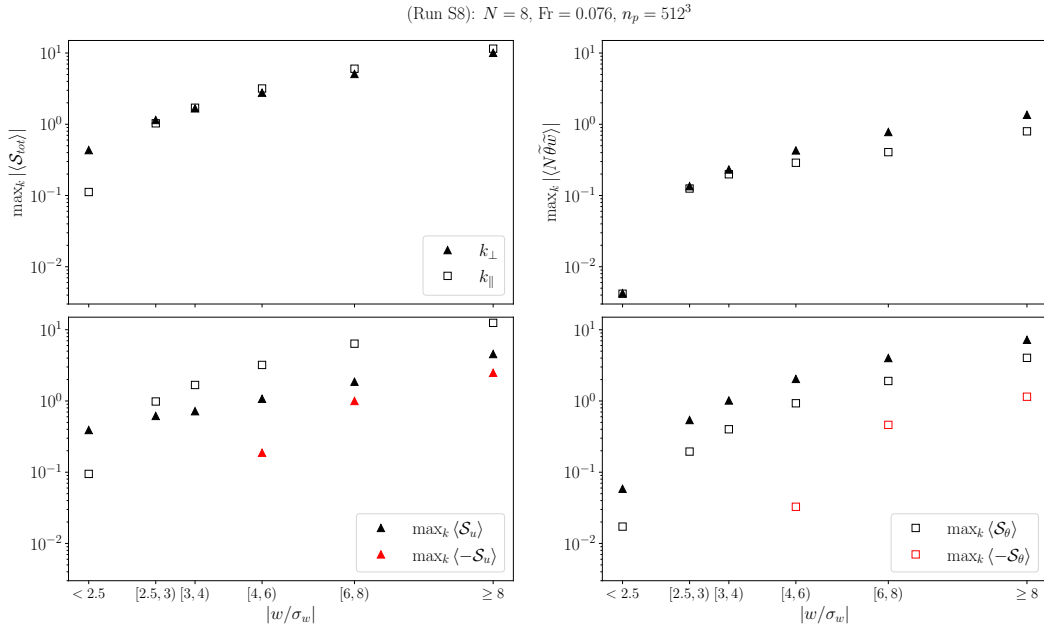


Figure 4.6. Maximum non-linear energy transfer, represented by the four sub-grid terms, computed as a function of the perpendicular (triangles) or parallel (squares) wave number for the six different curves in Fig. 4.4 and 4.5 identified by different ranges of the vertical velocity w (x-axis). For kinetic and potential energy transfer the maximum is computed with sign since they show both a direct and inverse transfer (see Figs.4.4–4.5).

injection rate $\langle \mathbf{F}(t) \cdot \mathbf{u}(t) \rangle$. The black dashed line in panel (b) is the temporal profile of the vertical velocity kurtosis K_w which is strongly correlated with the intensity of transfer for all the energy channels, as was expected by the previous results. The total and kinetic transfer related to vertical drafts (panels a and c) show the typical behavior of a direct cascade in fully developed turbulent flows concentrated in smaller but more numerous structures, and therefore smaller on average for increasing wave number. On the other hand, the trend of S_θ and $N\tilde{\theta}\tilde{w}$ (panels b and d) which, as we also observed in the previous section, is significantly different at large and small scales, with a transition around $k_\perp \sim 10 - 20$ probably associated to the peak of the effect of vertical drafts on the flow. Such difference between kinetic and potential transfer might be due to the fact that in this simulation there is a random forcing continuously injecting kinetic energy, whereas the (potential) temperature field is driven by the coupling with the velocity $N\theta w$. In Fig. 4.10 we also observe the same effect, highlighted by the evidence that the kinetic flux

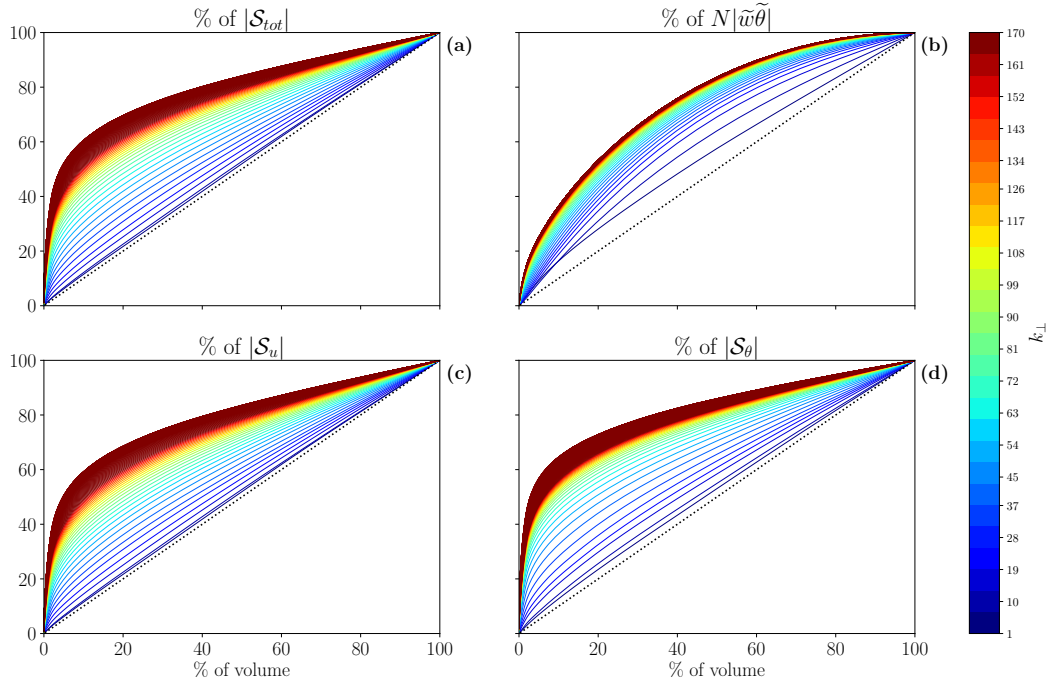


Figure 4.7. The four panels show the percentage of volume (x -axis), identified in terms of increasing values of vertical velocity w , necessary to reach a given percentage of energy transfer (y -axis). In other words, each panel represents the scatter plot between the cumulative distribution of the vertical velocity field w and of the non-linear energy transfer at any wave number k_\perp : (a) total, (b) kinetic-to-potential, (c) kinetic and (d) potential.

is higher at very large scale $k_\perp \simeq 3$ and probably modulated by the intensity of the random forcing being δ -correlated in time. Also in this figure, we report the variation of K_w as a black dashed line in panel (b), while in panel (c) the time curve of the kinetic energy injection is reported as the black dashed line as well. Indeed, in Fig. 4.10 sub-domains with low or high vertical velocity, left or right panels respectively, are represented with different palettes to highlight more temporal and spectral features of the energy transfer. For $|w\sigma_w| > 5$ the peak of total and kinetic energy transfer is always at scales smaller than the forcing ($k_f \approx 2.5$), and it shows approximately the same temporal modulation with peaks and troughs, which is also followed by K_w . At the same time, the kinetic-to-potential coupling (panel b), peaks as well, further highlighting the role of the velocity in driving the temperature field. The filtered buoyancy flux $N\tilde{w}\tilde{\theta}$ for $|w/\sigma_w| > 5$ (panel h) shows almost the

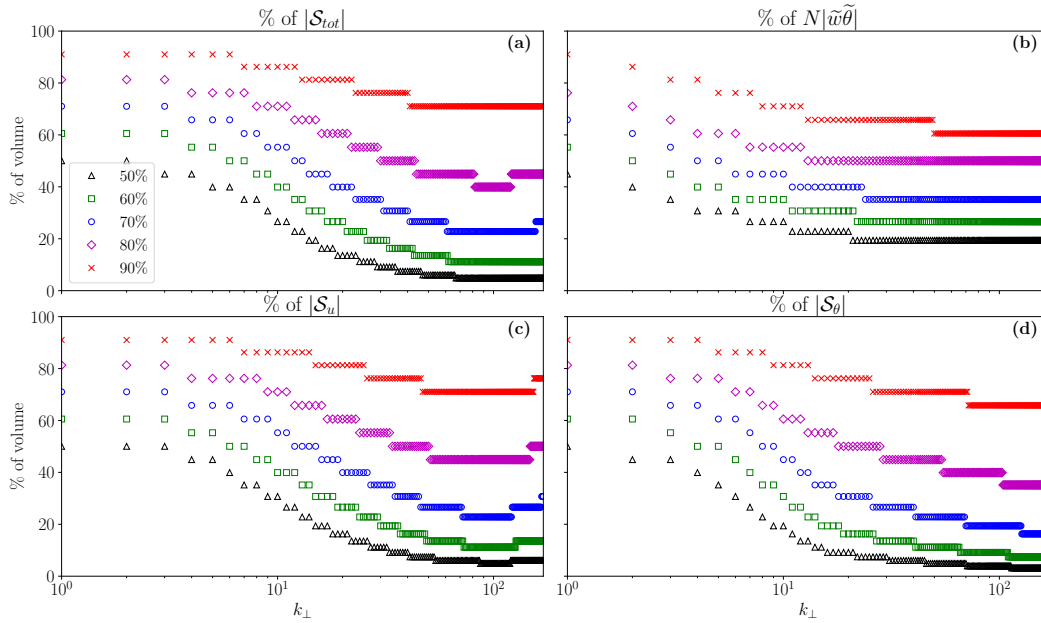


Figure 4.8. Percentage of the volume necessary to reach a fixed percentage of cross-scale energy transfer (see legend) as a function of the perpendicular wave number k_{\perp} .

same behavior, with peaks at slightly smaller scale $k \sim 20$, suggesting that smaller but more energetic structures are responsible for the energy conversion. In most of the flow regions ($|w/\sigma_w| < 3$), the net transfer is from potential to kinetic energy ($N\tilde{\theta}\tilde{w} < 0$ as it is often observed in the atmosphere and oceans (available potential energy, [122, 187, 20]), but when K_w peaks the energy conversion invert passing from kinetic to potential (yellow vertical traces, panel (b)). The time-scale variation of the potential energy transfer for $|w/\sigma_w| > 5$ is completely different with a dual axisymmetric flux around $k \approx 10 - 20$ persistent in time. Interestingly the inverse transfer of potential energy (to large scale) seems to temporarily disappear at late times $t \sim 260\tau_{NL}$ when the kurtosis is at its minimum. The same range of length scales $k \approx 10 - 20$ exhibits the maximum kinetic energy (and total) energy transfer associated with vertical drafts

Since the clear correlation between the volume-averaged non-linear energy transfer and the time profile of the kurtosis revealed in the previous figures, we computed the linear correlation between $K_w(t)$ and the various flux terms computed for both $|w/\sigma_w| < 3$ and $|w/\sigma_w| > 5$. We remark that $K_w(t)$ is computed on the entire

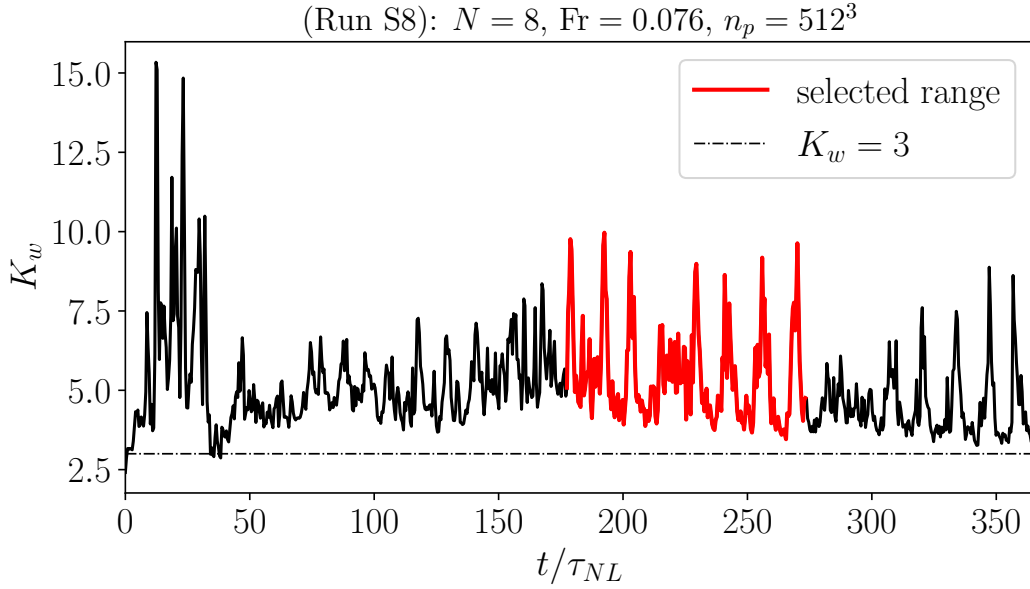


Figure 4.9. Kurtosis K_w of the vertical velocity for the entire integration time of run S8. In red, the interval analyzed in this section, and the black dash-dotted line represents the Gaussian reference value for the kurtosis $K_w = 3$.

domain. The results are reported in Fig. 4.11. The correlation is evaluated by using the Pearson's correlation coefficient ρ , defined as

$$\rho = \frac{\langle (X - \bar{X})(Y - \bar{Y}) \rangle}{\sigma_X \sigma_Y}$$

with X and Y two arbitrary time- (or space-) varying quantities. ρ varies from -1 for inversely proportional to 1 for directly correlated variables, while if $|\rho| \leq 0.5$ the two are almost randomly correlated. As expected from what was previously observed, the correlation of the total (black crosses) and kinetic flux (red circles) with $K_w(t)$ is particularly high at every scale for vertical drafts (Fig. 4.11(b)). A small decrease is observed at $k_\perp > 60$ whereas this does not happen for $w < 3$ (panel a) for which the correlation stays above 0.9. Such behavior is likely due to the effect of extreme events on the entire fluid; large-scale drafts enhance turbulence at an intermediate scale, as highlighted in the previous section, where their effect is maximized. The energy locally injected by the drafts ultimately boosts dissipation and allows stratified flows to dissipate as efficiently as homogeneous isotropic turbulent fluids [139]. The behavior shown by the kinetic-to-potential transfer (green triangles) suggests that the

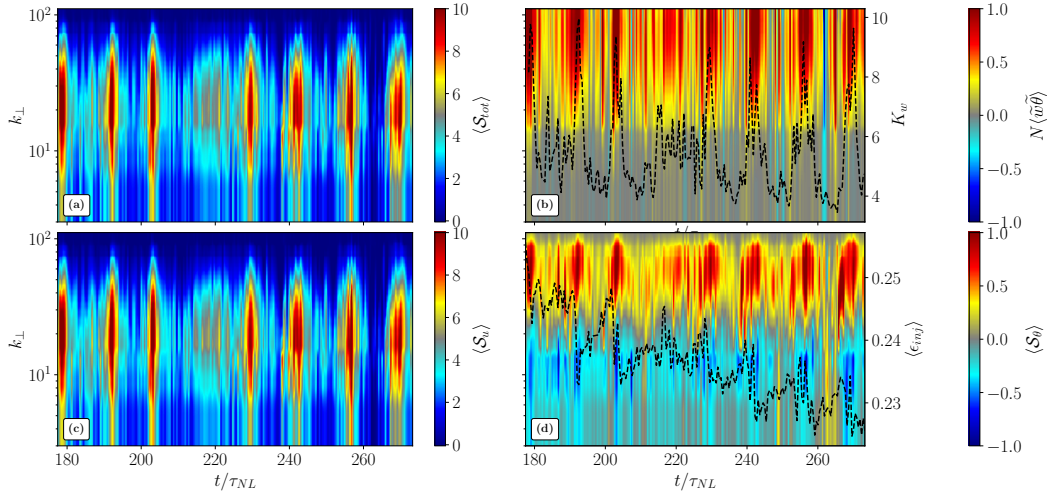


Figure 4.10. 2D visualization of the: (a) total, (b) kinetic-to-potential, (c) kinetic and (d) potential energy transfer given by points with $|w/\sigma_w| > 5$. On the x -axis time is expressed in units of turnover time, while the y -axis indicate the spatial scale. The black dashed line in panel (b) is the kurtosis K_w , and the dashed line in panel (s) represents the amount of kinetic energy injected at any given time.

vertical velocity kurtosis, and therefore the vertical drafts, only partially temporal correlate with this term, with almost zero correlation at very large scale and moderate at small $\rho \simeq 0.5$ (panel b). On the contrary, when the majority of the domain is taken into account (panel a) ρ is slightly higher for the whole range of scales, again likely indicating a more spread buoyancy flux. The linear correlation between K_w and the potential cross-scale transfer is significant at every k_{\perp} for $|w/\sigma_w| > 5$; indeed, for $k_{\perp} \lesssim 10$ the two quantities are strongly inversely proportional since, as we observed in Sec. 4.1, the potential flux is negative at such scales. Thus negative values of ρ mean that higher values of K_w are statistically associated with an enhanced negative (to larger scale) transfer of potential energy. Around $k_{\perp} \simeq 10 - 20$ the correlation is almost null because of the flux which is very low and therefore independent of the variation of kurtosis. Then, moving to $k_{\perp} \gtrsim 20$, the correlation is again elevated but now directly proportional since the potential flux is positive (to a smaller scale) in this range. In general, this kind of analysis further highlights relationships between the emergence of vertical drafts and the local energy transfer, nevertheless the Pearson's' correlation coefficient only measures linear monotonic relations. Thus it

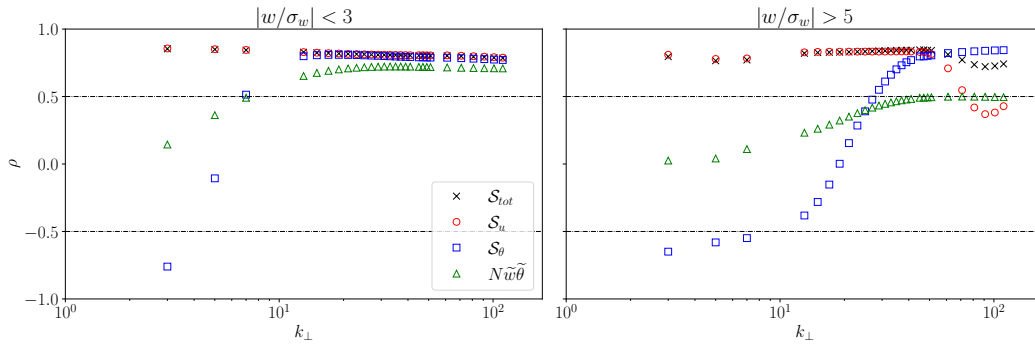


Figure 4.11. Pearson's correlation coefficient ρ between $K_w(t)$ and the volume-averaged cross-scale energy transfer as a function of the filtering scale k_{\perp} . Horizontal black dashed lines separate regions of low correlation $|\rho| < 0.5$ from the others.

is not able to correctly capture non-linear and non-monotonic dependencies as it may happen for the quantities here considered, since they involve spatial gradients for instance. Moreover, the correlation highlighted in these results does not imply causation between the presence of drafts, evaluated through the kurtosis of w , and the cross-scale energy flux. As already shown in Marino et al. [139], to prove causation, the same analysis should be performed by applying a time shift to one of the two time series involved in the correlation; however, this is beyond the purpose of this manuscript, and it may be an interesting point to further study in the next future. Also, the choice about the correlation coefficient can be improved by accounting for different correlation metrics being able to also capture non-linear and non-monotonic dependence, such as the mutual information [56]. In addition, it is worth reminding that points with $|w/\sigma_w| > 5$ are a tiny percentage with respect to points with $|w/\sigma_w| < 3$, filling almost the 99% of the volume, therefore statistical results on the former are inevitably affected by larger errors, especially when high-order statistics are computed.

Finally, we analyzed the temporal variation of the length scales, identified in terms of perpendicular wave number k_{\perp} , at which the volume-averaged energy transfer has its maximum. Also in this case we computed the non-linear flux on the same two sub-domains having $|w/\sigma_w| < 3$ and $|w/\sigma_w| > 5$ respectively, and the results are summarized in Fig. 4.12. Red circles refer to regions with enhanced large-scale intermittency ($|w/\sigma_w| > 5$), while regions with vertical velocity within three standard

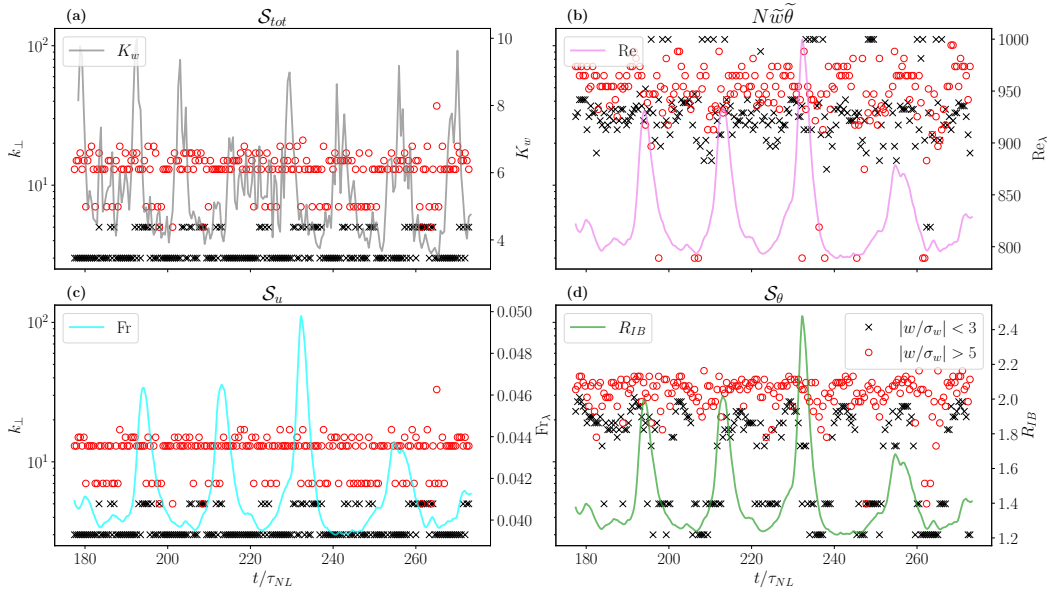


Figure 4.12. Temporal variation of the scale k_{\perp} at which the maximum of energy transfer occurs, computed both for points with vertical velocity $|w/\sigma_w| < 3$ (black crosses) and $|w/\sigma_w| > 5$ (red circles). Along with the optimal scale, we report the time variation of the kurtosis K_w (gray), Reynolds (pink), Froude (cyan) and buoyancy Reynolds (green) numbers, computed as in Sec. 3.2.2.

deviations are represented with black crosses. Along with the wave number of peak k_{peak} we reported again the vertical velocity kurtosis K_w (panel a), but also the small-scale Reynolds $\text{Re}_{\epsilon} = (\epsilon_V L)^{1/3}/\nu$ (3.15) (panel b), Froude $\text{Fr}_{\epsilon} = (\epsilon_V L^{-1})^{1/3}/N$ (3.18) (panel c) and buoyancy Reynolds numbers $R_{IB} = (\ell_{Oz}/\eta)^{4/3} = \text{Re}_{\epsilon} \text{Fr}_{\epsilon}^2$ (3.19) (panel d). The temporal variation of such parameters has been computed taking the Brunt-Väisälä frequency $N = 8.0$, the integral scale $L = 2\pi/k_f \simeq 2.51$ and the kinematic viscosity $\nu = 10^{-3}$ as fixed for this simulation and considering the time variation of the volume-averaged kinetic dissipation $\epsilon_V(t) = \nu \langle (\nabla \mathbf{u}(t))^2 \rangle$. If we focus on the changes of k_{peak} related to the vertical velocity kurtosis, it is straightforward the different behavior of regions with $|w/\sigma_w| < 3$ and regions with $|w/\sigma_w| > 5$ almost in every panel. Concerning the total and kinetic energy transfer (Fig. 4.12, panels a and c), the characteristic length scale is always smaller $k_{\perp} \simeq 7 - 20$ for extreme events. In addition, red circles and black crosses seem to behave the opposite according to K_w , indeed. At the same time, the length scale of vertical drafts decreases for

increasing values of kurtosis, for points with w within three σ_w the opposite seems to happen with a typical scale moving to larger wave numbers concurrently with troughs of K_w . The same modulation is less evident for the potential and filtered buoyancy flux (panels b and d), having probably the same behavior because the temperature field is strongly driven by $N\theta w$ in our simulations as we widely saw in the previous results. For these quantities, the length scale associated with the peak of volume-average energy transfer seems to be in counter-phase with the kurtosis and even all the other parameters, but shows globally a smaller variation of the scale than what was observed for the other energy channels. In general, the characteristic scale associated with $|w/\sigma_w| > 5$ appears in the entire time range smaller than what is observed in Sec. 4.1 ($k_{peak} \simeq 5$); however, two major factors certainly affect such discrepancy; at first, in the two analyses the division of the flow in sub-domains is different, finer in the previous section and binary in this one, and this leads to a large bin including regions having high vertical velocity but probably very different features. Second, and more important, the two results refer to different times of the simulation concerning significantly different phenomena, early for the results of Sec. 4.1 ($t \simeq 13\tau_{NL}$) and late times for the last analysis ($170 \lesssim t \lesssim 270$). Indeed, as previously mentioned, our stratified flow DNSs, where kinetic energy is injected to sustain a fully developed turbulent state for hundreds of turnover times, tends to develop vertically sheared horizontal winds (VSHWs) with energy piling-up at large scales and dominating the horizontal motions. This may also influence some features of vertical drafts or of the fluid itself, such as the characteristic length scales (i.e. integral scale L , buoyancy L_B and Ozmidov scales ℓ_{Oz}), leading the flow to explore other parameter configurations and thus modulating the emergence of large-scale extreme events as we further see in the next section.

4.2 Local energy transfer variation with Froude number

We have seen that the Froude number strongly modulates the presence of vertical drafts (see Fig. 4.1) and therefore the level of stratification. Globally, the intensity of large-scale intermittency can be characterized through the kurtosis of the vertical velocity, (the same for temperature θ , not shown here) and its variation as a function

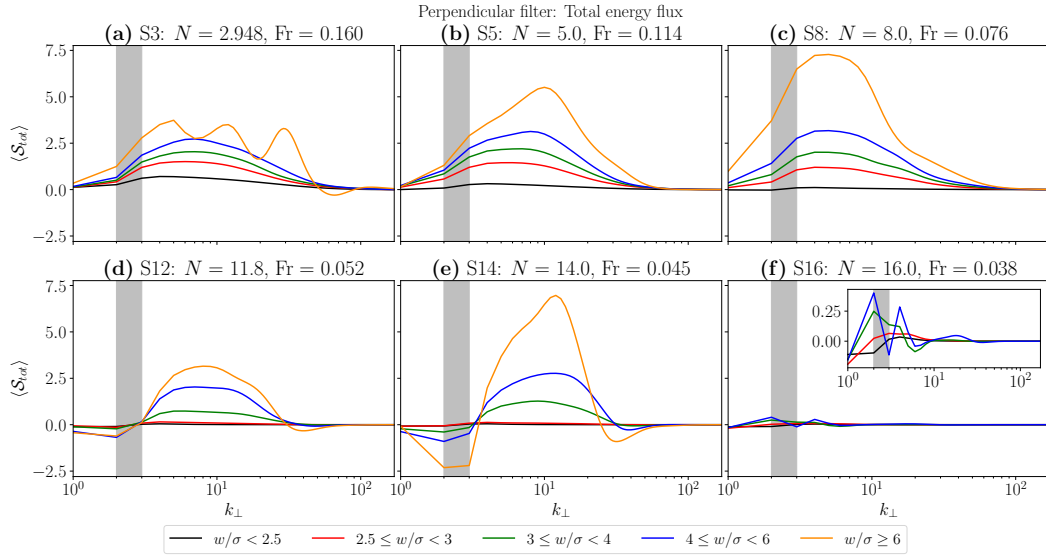


Figure 4.13. Total cross-scale energy transfer, obtained from the axisymmetric filtering, for runs from S3 to S16 in Tab. 3.1 (panels (a)–(f), respectively). Curves of different color are obtained by computing the transfer term over regions with values of vertical velocity. The gray shaded area indicates the forcing scale $k_f \in [2, 3]$.

of Fr shows a peculiar non-monotonic behavior with a peak at $0.06 \lesssim \text{Fr} \lesssim 0.1$. This is shown in Fig. 4.1 (left panel) for 17 DNSs analyzed in this thesis work (see Tab. 5.1), however in this section only six runs, represented by colored points, will be used for the aim of studying the variability of the cross-scale energy flux with the stratification regime, identified by the Froude. Indeed, various works have already shown that the presence and behavior of vertical drafts are strongly modulated by the intensity of stratification [72, 73]; for instance, in Feraco et al. [72] a simple 1D model has been employed to explain the rise of K_w and the asymmetry between the rising and falling part of the curve (see Fig. 4.9); at large Fr (weak stratification) the non-linear term dominates the dynamics and turbulence is very close to the homogeneous isotropic turbulence (HIT) case. On the other side, for small Fr, the linear term related to gravity waves $N\theta w$ is the dominant contribution leading, for very small Froude numbers, to a quasi-2D turbulence. At intermediate Froude (i.e., $0.06 \lesssim \text{Fr} \lesssim 0.1$) which are particularly interesting for geophysical studies, resonant effects between waves and turbulent eddies arise resulting in peculiar dynamics intermittently characterized by the emergence of large-scale extreme events in the

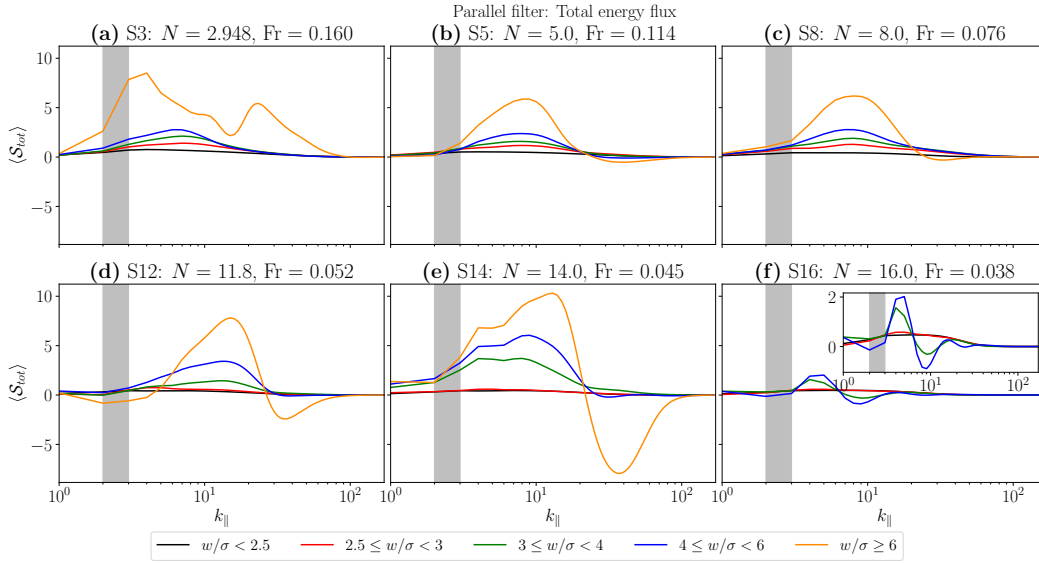


Figure 4.14. Same as Fig. 4.13 for the parallel $k = |k_z|$ filter.

vertical velocity and (potential) temperature as well. Of course, the presence and intensity of vertical drafts are not the only features affecting the energy transfer, indeed, as discussed before, the regime of stratification strongly determines the dynamics and therefore how the energy is transferred through structures. We already introduced in Chap. 1 that different kinds of turbulence (e.g HIT, 2D and others) lead to different behaviors of the energy flux based on theoretical arguments related to system invariants. The same analysis performed in Sec. 4.1 has been implemented to five other runs with different Fr and the non-linear energy terms, obtained by the space-filtering (SF) technique, computed on sub-domains identified by values of vertical velocity w reported in Tab. 4.1. It is clear, also observing Fig. 4.9, that the bulk of the flow, $|w/\sigma_w| < 4$, is mostly independent on the Froude number, filling almost the same percentage of the volume for all the runs; but, as soon as we take into account higher values of w , a significant discrepancy arises between the simulations which is in accordance to what measured by $K_w(\text{Fr})$ and noticed in previous works [72, 73, 139]. Figs. 4.13– 4.19 summarize the total (Fig. 4.13), kinetic (Fig. 4.15), potential (Fig. 4.17) and kinetic-to-potential (Fig. 4.19) non-linear energy transfer obtained by the axisymmetric filtering approach, i.e. $k_{\perp} = (k_x^2 + k_y^2)^{1/2}$; the same for the parallel filter is shown in Figs. 4.14– 4.20. The effect of vertical

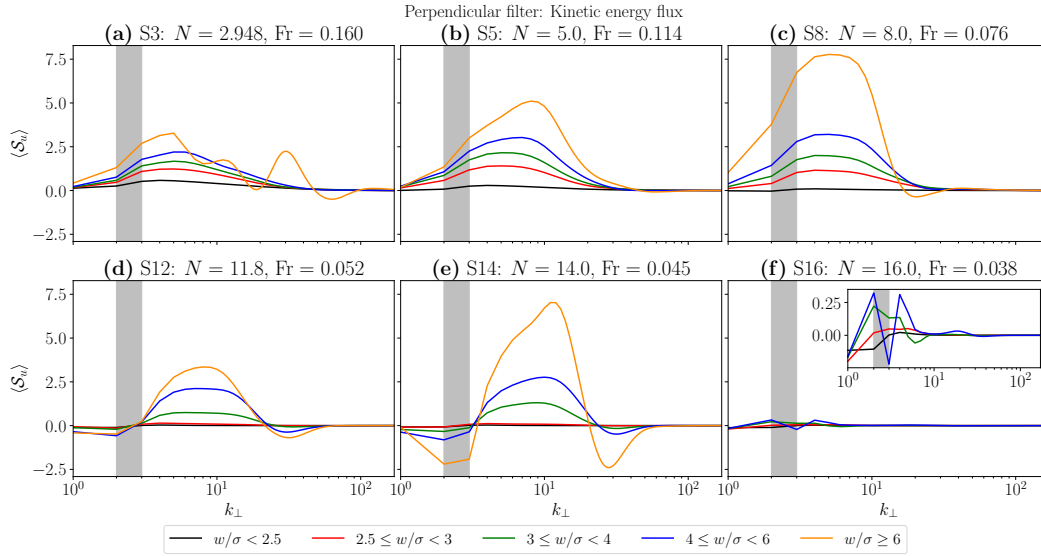


Figure 4.15. Perpendicular kinetic cross-scale energy transfer for runs from S3 to S16 in Tab. 3.1 (panels (a)–(f), respectively). Curves of different color are obtained by computing the transfer term over regions with values of vertical velocity.

velocity drafts respectively on the perpendicular and parallel components of the flux is significantly different, showing that they locally release a larger amount of energy preferentially in modes with $k_{\perp} \neq 0$. Despite we tried to create intervals of w to have a convergent statistics, it is clear both by Tab. 4.1 and Fig. 4.13 that for runs S3 and S16 we do not have enough points for $|w/\sigma_w| > 6$; this will affect all the following results for those two simulations which therefore have to be taken carefully.

Cross-scale total energy transfer:

By looking at the total energy transfer in Fig. 4.13, it appears that the intensity of stratification does not affect the average energy rate of the most extreme values of w . Indeed, contrary to what previously observed for the volume-averaged flux (see Fig. 3.7) where the increasing of stratification inhibits the energy transfer, in this case the total transfer rate, given by points with $|w/\sigma_w| > 4$, has its maximum at the peak of kurtosis K_w (run S8, i.e. most number of extreme events), corresponding to panel (c) in Fig. 4.13. The picture is different for the parallel filter in Fig. 4.14, for which the total transfer given by regions with $|w/\sigma_w| > 4$ looks pretty constant for runs S5, S8 and S12, while the same shows high fluctuations for $Fr = 0.045$

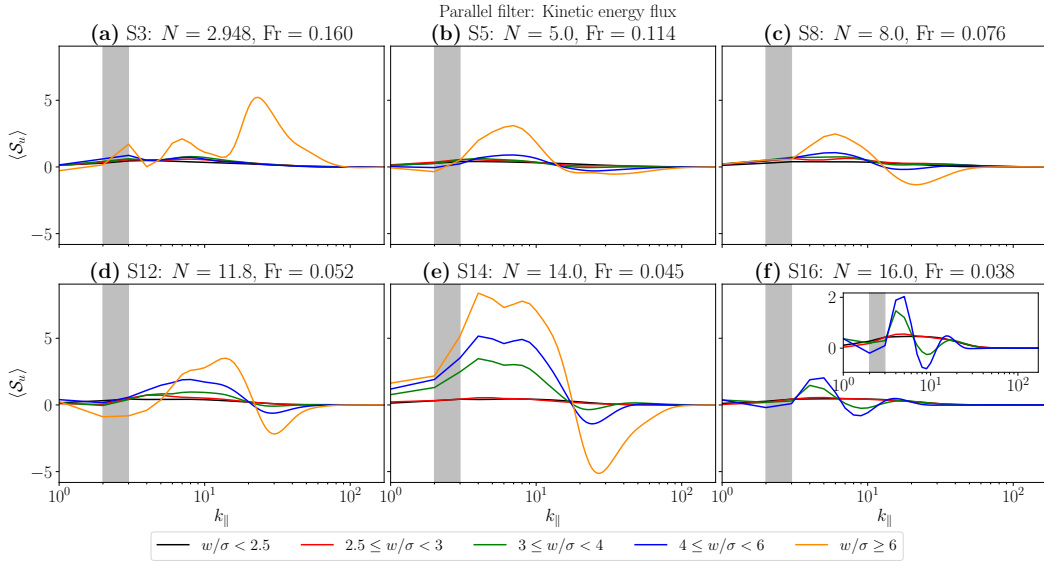


Figure 4.16. Same as Fig. 4.15 integrated in parallel shells $k = |k_z|$.

(run S14). Probably, the parallel component of the flux is more affected by the contribution of gravity waves being more and more intense for decreasing Froude. In general, we observe that vertical drafts, identified by intense values of the vertical velocity w , tend to inject amount of energy several times larger than the flow average (black curves) in the inertial range, with a peak which is partially modulated by the buoyancy scale $\ell_B = 2\pi U/N$. Such energy injection produces an enhanced transfer towards smaller scales at any Froude, being obviously proportional to the amount of the extreme events. We will see in the following that this boosted turbulent transfer is mainly due to kinetic energy transfer for the perpendicular component $\mathcal{S}_{tot}(k_{\perp})$, while the potential energy is the principal contribution of the total parallel flux $\mathcal{S}_{tot}(k_{\parallel})$.

Cross-scale kinetic energy transfer:

As mentioned earlier, the main contribution to the perpendicular cross-scale transfer comes from the kinetic energy $\mathcal{S}_u(k_{\perp})$, shown in Fig. 4.15. Indeed, this appears particularly sensitive to values of w , showing a peak many times larger than the others for $|w/\sigma_w| > 6$ at run S8 (i.e., Fig. 4.15(c)). On the contrary, the kinetic flux for $|w/\sigma_w| < 6$ varies less among the six simulations. For runs with a significant

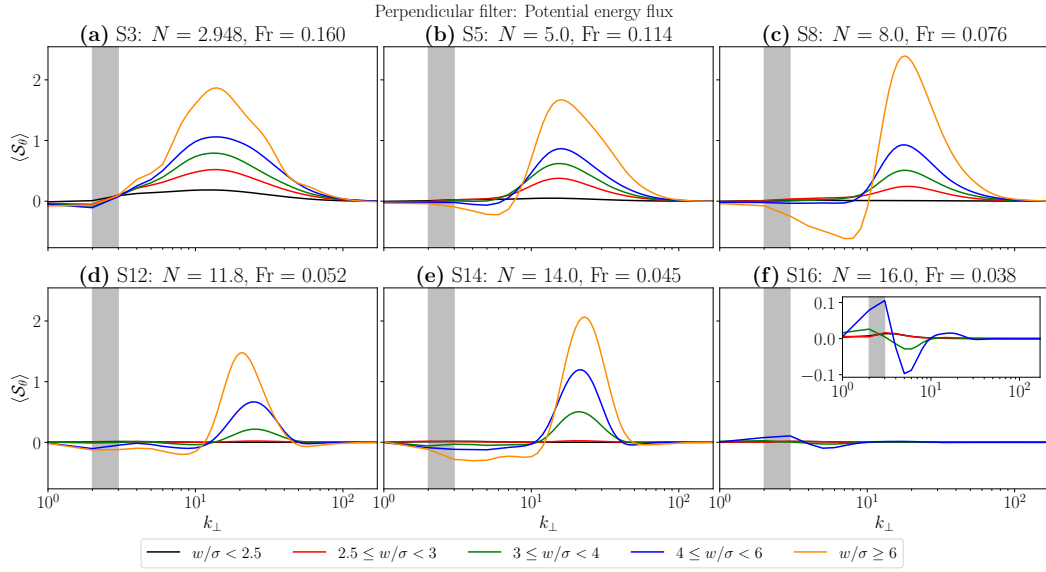


Figure 4.17. Potential cross-scale energy transfer for the perpendicular filter $k = \sqrt{k_x^2 + k_y^2}$ and the same runs (S3 to S16).

level of large-scale intermittency, such as S8, S12 and S14, the axisymmetric kinetic energy transfer manifests a weak inverse transfer ($\mathcal{S}_u < 0$) for $k_\perp \gtrsim 20$ and intense values of w ; we will see later that this is probably because of the coupling with the temperature field. The same upscale transfer is observed for the same runs also in the parallel component of the kinetic energy flux $\mathcal{S}_u(k_\parallel)$ in Fig. 4.16. However, the scenario in this case is a bit more complicated and the effect of drafts on the local transfer is not so evident, as highlighted by the small values in panel (c) of the same figure. It is also worth noticing that, for all the simulations and the components of the flux, the amount of kinetic energy locally injected by values with intense vertical velocity is in general significantly higher than the energy injected by the random forcing.

Cross-scale potential energy transfer:

The behavior of the non-linear potential energy transfer is fairly different by looking either at its axisymmetric (Fig. 4.17) or parallel (Fig. 4.17) component. We interpret this in terms of the differences we already highlighted for the kinetic energy in the previous paragraph; in particular, the different effect of drafts on the local injection of energy determines a stronger or weaker coupling between the velocity and

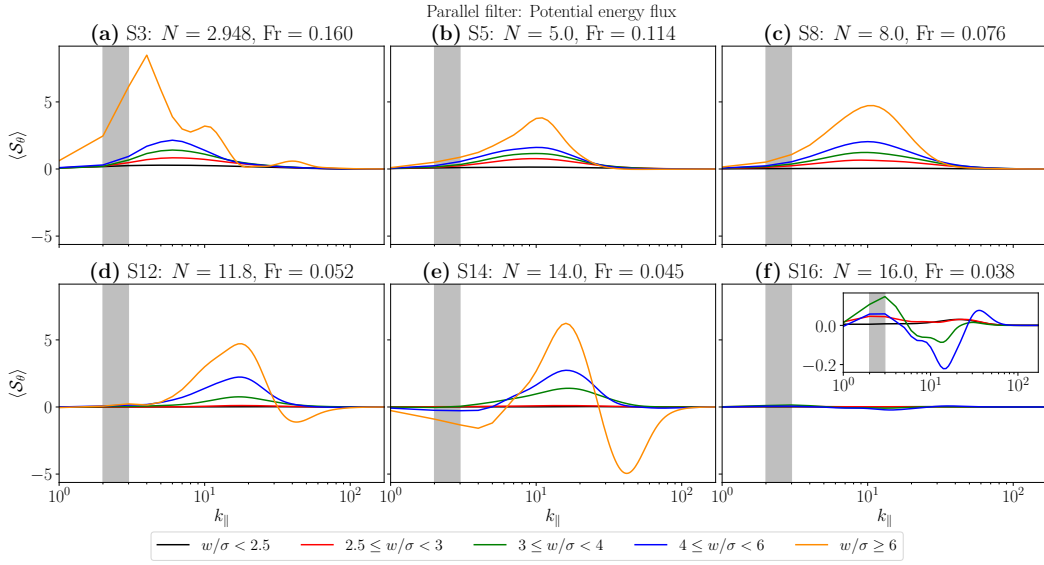


Figure 4.18. Same as Fig. 4.17 for the parallel filter.

temperature field, intrinsically given by the buoyancy term $N\theta w$ in the governing equations. The perpendicular flux $\mathcal{S}_\theta(k_\perp)$ shows a dual transfer around $k_\perp \approx 12$ for runs S8, S12 and S14 (smaller for S5, $k_\perp \approx 8$), which is approximately in the range where we observed previously that the effect of vertical drafts on the kinetic energy transfer is maximized. Therefore, since our simulations present zero temperature fluctuations at $t = 0$, the emergence of extreme events do couple the velocity and (potential) temperature field, which locally injects energy into this latter producing simultaneously a direct and inverse transfer of potential energy. In other words, extreme vertical drafts are strictly connected with both large-scale buoyancy-driven instabilities and small-scale turbulence in terms of production of vorticity, as we will see more in detail by means of a simple 1D model in the next chapter. The perpendicular component of the potential energy flux $\mathcal{S}_\theta(k_\parallel)$, in Fig. 4.18, represents instead the major contribution to the direct (towards small scale) transfer of total energy $\mathcal{S}_{tot}(k_\parallel)$ observed in Fig. 4.14. However, in this case we do not observe any particular variation with respect to the stratification (Fr number), likely reflecting what already appreciated for the kinetic energy.

Cross-scale kinetic-to-potential conversion:

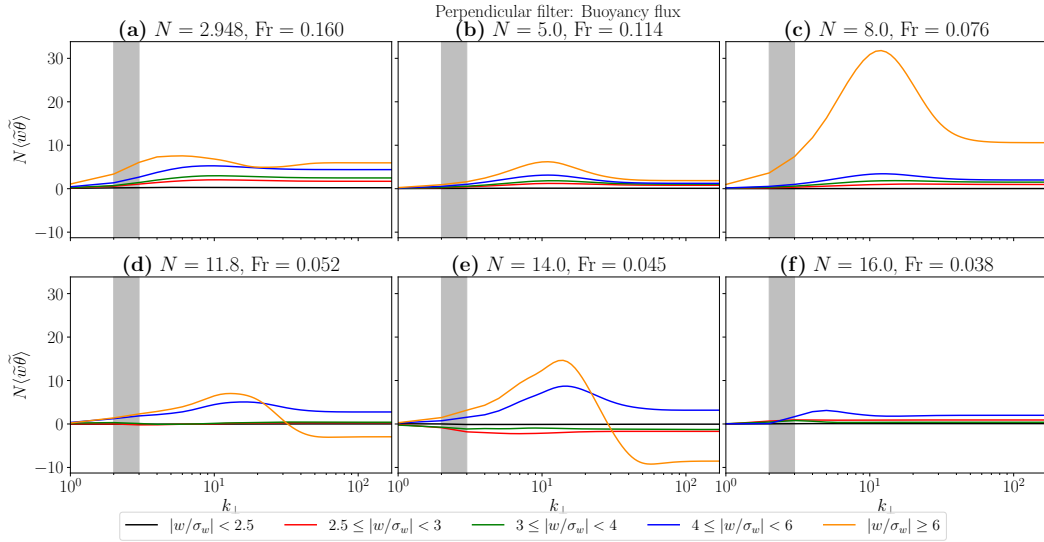


Figure 4.19. Perpendicular filtered buoyancy flux for runs from S3 to S16 (panels (a)–(f)).

It is worth reminding that the filtered buoyancy flux $N\tilde{\theta}\tilde{w}$ represents the kinetic-to-potential energy conversion whether negative ($N\tilde{\theta}\tilde{w} < 0$) at $\ell > \ell^*$, and the opposite when it is positive ($N\tilde{\theta}\tilde{w} > 0$). Therefore, in all the simulations we always observe a net conversion of energy from kinetic to potential probably due to the forcing acting on the velocity field only. Indeed, here both the perpendicular and parallel components of the buoyancy flux, in Figs. 4.19 and 4.19, show mostly the same qualitative behavior and pretty similar variation with the Froude number. Surprisingly, we observe an intense kinetic-to-potential transfer for run S3, panels (a) of Figs. 4.19–4.19, which is probably largely driven by the large scale forcing, but at the same time is showing that the coupling between velocity and temperature mostly occurs at intermediate scale for the perpendicular component $k_{\perp} \approx 15$, while for the parallel buoyancy flux this happens very close to the forcing scale $k_f \simeq 2.5$. In the range of scale where we observed that the effect of vertical drafts is maximal (i.e. $7 \lesssim k \lesssim 30$), principally for the axisymmetric fluxes both partially also for the other filter, also the conversion from kinetic to potential energy has its maximum, confirming the hypothesis of vertical drafts driving temperature instabilities. For scale $k \gtrsim 30$ a large amount of energy is converted back from potential to kinetic, as evidenced by the decreasing of the term $N\tilde{\theta}\tilde{w}$ at small scales, probably driving the inverse transfer of kinetic energy previously observed. This happens in general for

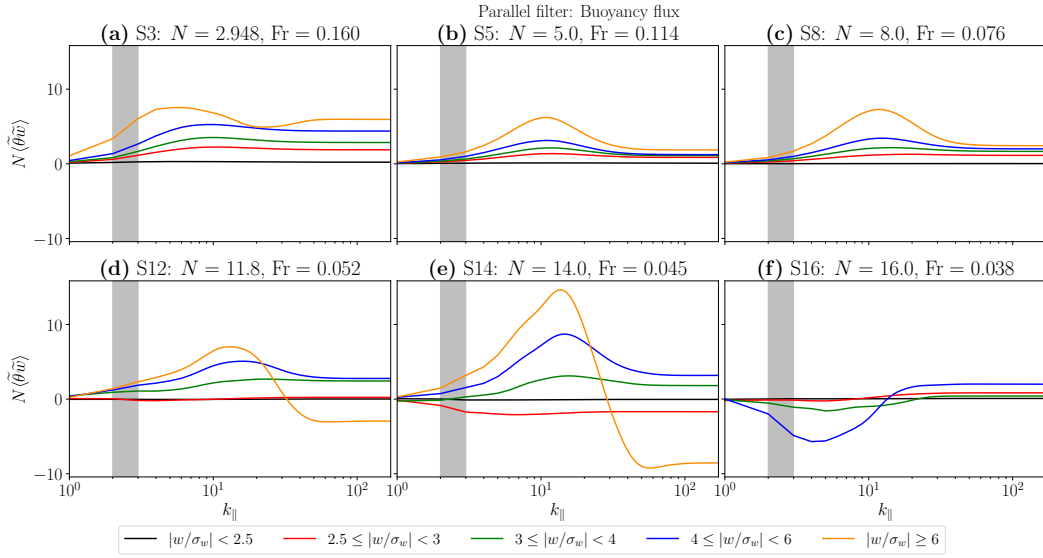


Figure 4.20. Same as Fig. 4.19 for the parallel filter.

all the simulations with a minimal amount of large-scale intermittency (i.e., runs from S5 to S14) without any significant trend with the stratification intensity. For runs with strong background stratification (S12 and S14), the most extreme events $|w\sigma_w| > 6$ produce a negative (from potential to kinetic) net energy conversion almost at any k (both k_{\perp} and k_{\parallel}). However, we cannot conclude exactly whether this is either the effect of the interaction between drafts and strong gravity waves or simply fluctuations due to unresolved statistics, especially for run S14. The unfiltered version of the buoyancy flux and its statistics will be further analyzed in relation to large-scale intermittency of both the vertical velocity and temperature fields in the next chapter, where we will see more in detail the link between vertical drafts and local instabilities within the flow.

Chapter 5

Link to small-scale intermittency and the buoyancy flux

5.1 Comparison of the kurtosis of large- and small-field components

We have seen in the introduction how small-scale (or internal) intermittency is a peculiar feature of turbulence, from laboratory experiments and direct numerical simulations to geophysical flows, as it has been observed in many instances in the atmosphere and oceans. Internal intermittency produces intense localized variations of the energy dissipation, and therefore the small-scale gradients. As we observed in the previous chapters for the case of large-scale intermittency, the presence of burst in the field gradients produces a departure from the Gaussian behavior of the probability distribution function (PDF) of the field one-point derivatives. Numerous are attempts of accurately model intermittency in turbulence, for instance with log-normal or log-Lévy models [174, 195]; however, it remains a challenging question which is nowadays fundamental to improve weather and climate models to simulate the unresolved small scales. Therefore, unraveling the link between internal intermittency and large-scale vertical velocity and temperature burst might be an

Run	S40	S24	S20b	S16	S14	S12	S9	S85	S8	S7	S6	S5	S3	S2	S1	S08	S05
N	40	23.5	20	160	14	11.8	9.0	8.5	8.0	7.372	6.0	5.0	2.948	2.2	1.5	0.8	0.5
$Re/10^3$	3.9	3.8	3.8	3.8	3.8	3.8	3.9	3.8	3.8	3.8	3.7	3.6	3.0	2.6	2.6	2.8	2.9
Fr	0.015	0.026	0.030	0.038	0.044	0.051	0.068	0.072	0.076	0.081	0.098	0.11	0.16	0.19	0.28	0.56	0.93
R_B	0.87	2.5	3.4	5.6	7.3	10.2	17.7	19.7	22.1	25.2	35.9	47.5	75.2	90.9	201	895	2560
K_u	2.3	2.4	2.3	2.1	2.3	2.3	2.3	2.3	2.3	2.3	2.3	2.3	2.5	2.6	2.9	2.8	2.8
K_v	2.2	2.3	2.2	2.3	2.1	2.0	2.1	2.1	2.1	2.1	2.1	2.1	2.6	2.8	2.7	2.8	2.8
K_w	3.1	3.2	3.1	3.1	3.2	3.6	7.3	8.6	10.4	9.1	8.8	5.3	3.9	3.5	3.3	3.0	3.0
K_θ	3.3	3.4	3.4	3.5	3.5	3.6	4.0	4.3	4.3	4.1	4.1	3.6	3.1	2.9	2.8	2.7	2.7
$K_{\partial_x \theta}$	4.7	4.9	6.5	11.7	16.0	45.6	118.0	101.5	112.2	71.7	53.0	28.6	17.5	15.9	15.6	13.6	13.5
$K_{\partial_y \theta}$	5.0	5.2	6.1	14.9	58.7	157.0	165.0	140.0	150.1	88.1	84.2	34.5	18.5	15.3	16.0	13.5	13.1
$K_{\partial_z \theta}$	9.8	6.3	6.5	6.4	6.1	6.5	8.7	8.8	10.3	8.7	11.1	8.7	10.2	11.8	16.9	15.3	15.3
$K_{\partial_x u}$	4.0	4.5	4.0	4.0	7.4	9.9	49.6	37.3	38.6	33.9	26.0	16.3	7.3	6.03	5.5	5.7	5.8
$K_{\partial_y v}$	3.9	4.6	4.6	6.1	22.7	59.5	83.5	71.2	57.4	41.2	35.9	19.2	7.5	6.0	5.5	5.7	5.8
$K_{\partial_z w}$	3.4	3.7	5.3	27.5	67.4	90.1	88.4	73.7	56.7	38.3	25.6	13.0	6.0	5.4	5.2	5.6	5.8
$K_{\partial_x u}$	5.2	5.9	5.8	5.2	22.7	59.5	60.7	55.7	8.5	51.0	44.6	25.1	10.1	8.6	8.1	8.6	8.8
$K_{\partial_z u}$	4.4	3.9	4.0	4.0	4.01	3.9	3.8	3.9	3.9	3.8	4.2	4.3	6.0	6.9	7.5	8.3	8.7
$K_{\partial_x v}$	4.3	5.0	4.3	6.0	7.7	8.8	58.5	39.4	8.6	41.4	36.5	23.0	10.0	8.2	7.9	8.5	8.7
$K_{\partial_z v}$	3.8	4.2	3.7	3.9	3.8	3.7	3.9	3.8	3.9	3.8	4.0	4.1	5.9	6.9	7.5	8.4	8.6
$K_{\partial_x w}$	5.0	5.6	8.4	25.1	61.9	176.1	361.6	225.0	258.4	133.8	78.4	35.8	11.3	8.7	7.7	8.3	8.7
$K_{\partial_y w}$	5.4	6.1	10.8	41.4	222.1	354.0	236.0	191.1	199.1	112.1	89.5	36.6	11.6	8.8	7.7	8.5	8.6

Table 5.1. Main parameters for the entire set of runs, namely the buoyancy frequency N , the Reynolds number Re , the Froude number Fr , and the buoyancy Reynolds number R_B (first four rows). The other rows report the kurtosis of the three components of the velocity and the temperature K_α , with $\alpha = [u, v, w, \theta]$, all the velocity and temperature gradient components. Values are averaged for ≈ 8 turnover times after the peak of dissipation in each run. The runs with bold names are those analyzed in the previous chapter as well.

important element to include in models for geophysical flows.

Considering the deep connection between large-scale intermittent events and dissipation highlighted in Marino et al. [139], and ultimately the clear evidence that vertical drafts locally inject energy at intermediate scales, in the following analysis the purpose is to further study the connection between small- and large-scale intermittency using a large set of DNSs of stably stratified flows [72, 73, see], employing the kurtosis K computed both for the physical fields and their gradients. In Tab. 5.1 the main parameters and the kurtosis results are reported for every run. K_α , where α is either a field or a gradient component, has been computed collecting points for ≈ 8 turnover times; it is worth to remember that $K_\alpha \simeq 3$ means a Gaussian-like

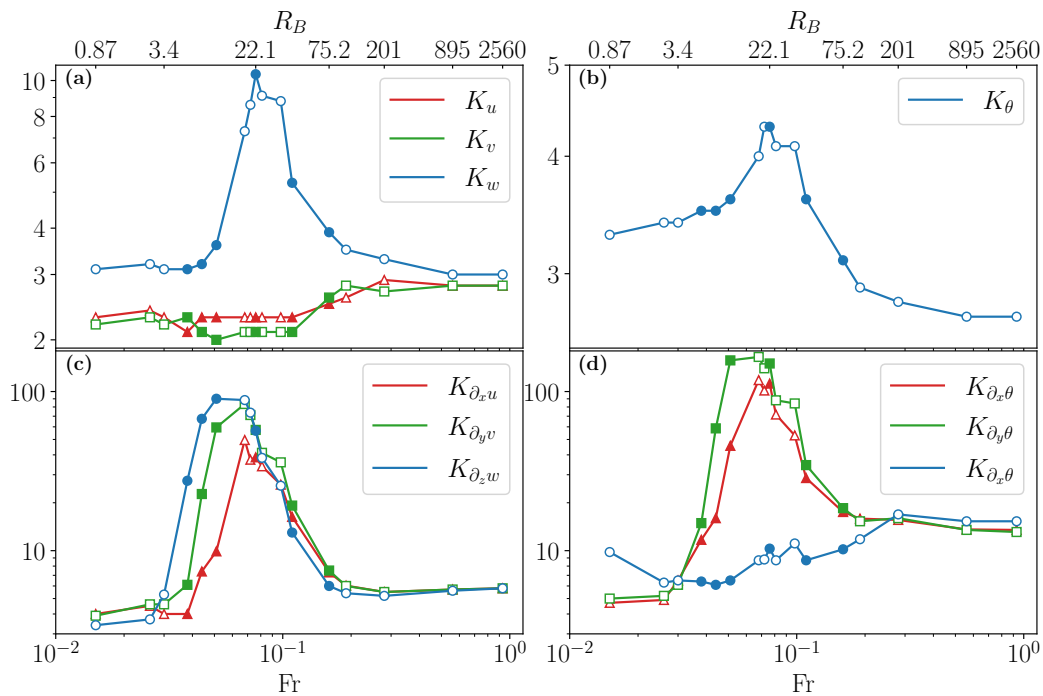


Figure 5.1. (Top left) Kurtosis of the three component of the velocity field K_u (red), K_v (green) and K_w (blue). (Top right) Kurtosis of the (potential) temperature K_θ and (bottom right) their gradient components $K_{\partial_\alpha \theta}$, with $\alpha = [x, y, z]$. (Bottom left) Kurtosis of the diagonal component of the velocity gradient $K_{\partial_x u}$, $K_{\partial_y v}$ and $K_{\partial_z w}$. Coloured points represent those runs also analyzed in the previous chapter; the top axis shows the range of buoyancy Reynolds, as reported for each run in Tab. 5.2.

shape of the PDF.

In Fig. 5.1 are presented the main results summarized in Tab. 5.1. The non-monotonic behavior of the fourth-order moment is evident for almost all the gradient components (panels (c) and (d)). Whereas the behavior of the vertical component of the velocity and temperature was already known from Feraco et al. [72]. However, it is always worth noting how the horizontal components of the velocity field (u and v) do not show any trend, staying Gaussian ($K_{u,v} \simeq 3$) or slightly sub-Gaussian ($K_{u,v} \lesssim 3$) in all the simulations, pointing to the fact that the large-scale intermittent behavior of the sole vertical velocity w (and/or of the buoyancy) can enhance small-scale intermittency, as seen from the spatial derivatives both of the velocity and of the buoyancy (see panels (c) and (d) Fig. 5.1). Even though the kurtosis of

the temperature (or buoyancy) θ exhibits the same behavior as w , their values are significantly smaller indicating extreme events which deviate less from 3σ ; such a difference could be probably due to the fact that in our simulations we inject only kinetic energy, therefore the temperature field is forced only by the coupling with the velocity field which is modulated in particular by the buoyancy Reynolds.

The diagonal components of the velocity field $\partial_i u_i$ are reported in Fig. 5.1, panel (c), showing the same trend as the one observed for K_w , with values almost one order of magnitude higher, indicating high levels of small-scale intermittency in terms of extreme values of field gradients. The other components of the velocity gradient $\partial_i u_j$ are only reported in Tab. 5.1; most of them exhibit however the same variation, except for $\partial_z u$, $\partial_z v$ and $\partial_z \theta$ (also represented in panel (d) Fig. 5.1). On the top axis of the same figure it is reported the range of variation of the buoyancy Reynolds number for the set of simulations; it is worth reminding that in our case the R_B variations are mainly due to the Froude number since the Reynolds varies only by $\approx 30\%$. We observe that runs with high values of kurtosis lie in a range $10 \leq R_B \leq 200$, indeed the intermittent dynamics at large scale have already been interpreted in terms of the interplay between waves and turbulence with a simple 1D model in Feraco et al. [72], in which the flow is considered to be able to explore different regimes, well-highlighted by the buoyancy Reynolds, where the relative strength of waves and turbulent eddies plays the central role in the dynamics. Such relation between large- and small-scale (or internal) intermittency can also be understood in terms of a simplified model for stably stratified flows involving only the field gradients, which is also helpful to give a possible interpretation of the mechanism feeding extreme vertical drafts.

5.2 A mechanism for the generation of large-scale vertical drafts

At the end of the previous section, we observed how the gradient components of the horizontal velocity u , v and the temperature θ along the vertical direction z do not show any trend with the Froude number. The small kurtosis values of $\partial_z \theta$, in

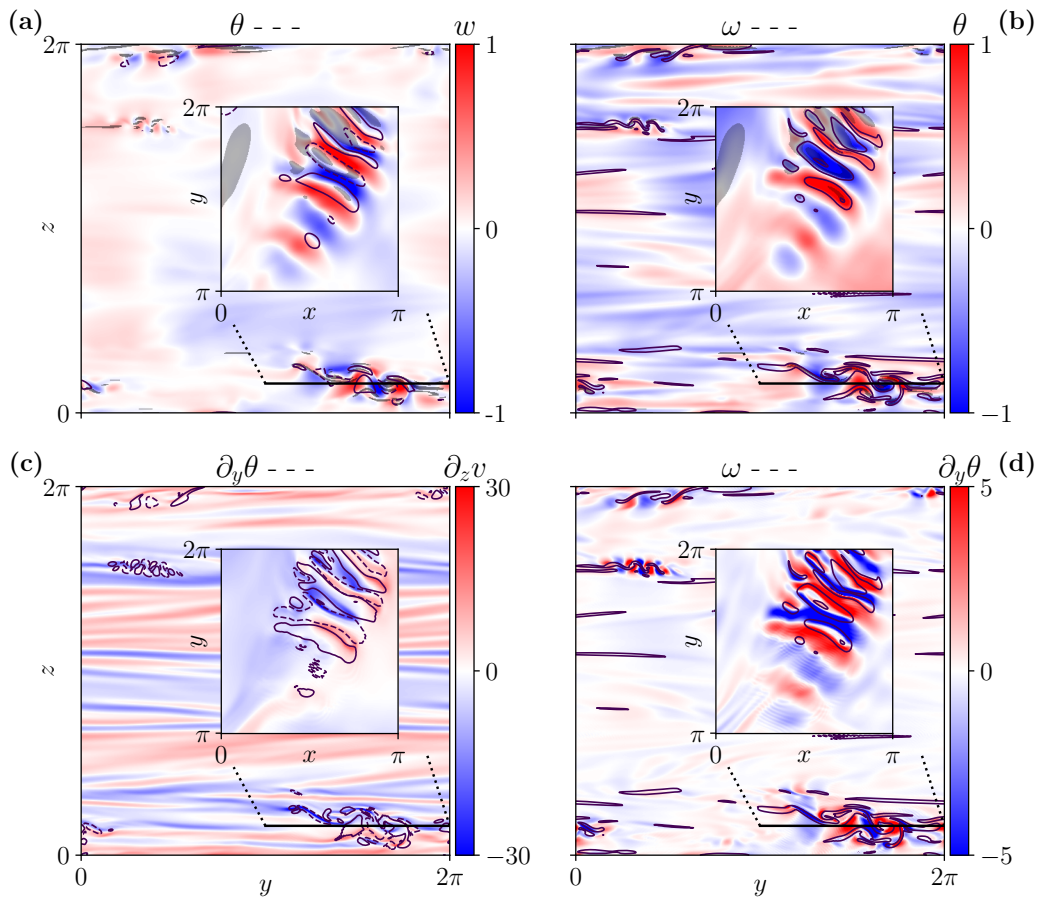


Figure 5.2. Vertical 2D slices (with the insets showing a horizontal slice of $1/4$ of the domain at the region of the extreme event) for run S8. Correlations of θ and w , $\omega = |\boldsymbol{\omega}|$ and θ , $\partial_y \theta$ and $\partial_z v$, and ω and $\partial_y \theta$ are shown (the first quantity in colors, the second with contours). Contours are at $\pm 3\sigma_\theta$ for θ , and $\pm 4\sigma$ for all other fields. Gray shaded areas indicate regions with $\partial_z \theta > N$.

particular, can be understood since the level of stratification N dynamically bounds this gradient component, $\partial_z \theta < N$. When $\partial_z \theta \geq N$, heavier fluid parcels move on top of lighter ones reversing the background stratification and triggering instabilities; this mechanism creates local convection within the fluid. Thus, such buoyancy-driven instabilities are strictly related to the emergence of large-scale vertical drafts, and this can be seen considering a simplified version of the Navier-Stokes equations (NSEs) for the component $\partial_z \theta$, where viscous effect is neglected,

$$D_t(\partial_z\theta) = (N - \partial_z\theta)(\partial_z w) - (\partial_x\theta)(\partial_z u) - (\partial_y\theta)(\partial_z v) \quad (5.1)$$

the equation describes how variations of $\partial_z\theta$ can be introduced either by strain in the horizontal winds ($\partial_z u$ and $\partial_z v$), being bounded to Gaussian values of kurtosis and slightly inversely proportional to the intensity of stratification (see Tab. 5.1), or by the saturation of the first term RHS in Eq. (5.2) when $\partial_z\theta \approx N$. For these values, triggered instabilities make the other gradient grow explosively. Indeed, even though high values of kurtosis of the velocity and temperature gradients are a universal feature of turbulence, in this case there is an additional enhancement of small-scale intermittency due to the emergence of vertical velocity and temperature drafts. This results eventually, with enhanced energy dissipation in stratified flows characterized by large-scale intermittency, whereas this is usually smaller than the homogeneous isotropic turbulence (HIT) case, as shown in Marino et al. [139]. Thus, we can say that large-scale extreme events are generated via buoyancy-driven instabilities, also feeding the interaction mechanisms between small- and large-scale intermittency, and this is well depicted by the four panels in Fig. 5.2, representing vertical cuts (y, z) and horizontal cuts (insets) of the original 3D domain. In panel (a) temperature iso-contours, black solid if positive and dashed if negative, are superimposed to the vertical velocity field showing how localized burst of w essentially mapped also from the extreme values of θ , with a phase shift between $\approx 2\pi$. This difference can be further appreciated by the inset, zooming on a horizontal cut over the structure visible in the bottom right part of the domain. Here we see a quasi-periodic structure alternating positive and negative extreme values, both in w and θ . Panel (b) highlights the same relationship but between the temperature θ and the modulus of the vorticity $\omega = |\boldsymbol{\omega}|$; these small-scale structures, evidenced by the vorticity, are the results of instabilities produced by vertically sheared horizontal winds VSHW(s) which are characteristic features of stably stratified flows, and which we show here in panel (c) through the gradient component $\partial_z v$ (the same results for $\partial_z u$). Indeed, such horizontal shears are particularly prone to Kelvin-Helmholtz instabilities KHIs, modulating the shape of layers at small scales and thus creating horizontal gradients of (potential) temperature θ and high values of vorticity $D_t\boldsymbol{\omega} \approx -N(\partial_y\theta\hat{e}_x - \partial_x\theta\hat{e}_y)$

(where viscous effect, forcing and vortex stretching were neglected). This results in a correlation between ω and the horizontal gradients of θ which is shown in panel (d). Therefore, the generation of vorticity is the mechanism supplying the small-scale intermittency, allowing a direct link between large- and small-scale extreme values. On the other hand, from (5.2) it is clear that fluctuations of the horizontal gradients of θ may eventually produce a nonlinear amplification of the vertical gradients of the horizontal velocity ($\partial_z u$ and $\partial_z v$), as it is highlighted in panel (c) for $\partial_y \theta$ and $\partial_z v$ (last term RHS in (5.2)). This mechanism of coupling between small-scale instabilities produced by large-scale structures (i.e. VSHWs) may proceed with the generation of extreme up- and down-drafts, and with very strong velocity fluctuations due to values of $\partial_z \theta \geq N$, creating buoyancy instabilities of the stable background stratification. Indeed, such regions with $\partial_z \theta \geq N$ coincide mostly with the regions presenting the most extreme values, as shown by the gray-shaded areas in panels (a) and (b). In summary, large-scale extreme events increase small-scale intermittency through the generation of vortical motions. However, the main mechanism of vorticity production is through buoyancy-driven instabilities, resembling in some way a large-scale baroclinic instability, and not through vortex stretching. These results also explain the enhanced dissipation, as observed in Marino et al. [139], since it is roughly proportional to the enstrophy $\propto \omega^2$, and the general lack of filament structures in stratified flows, contrary to what is observed in HIT. Moreover, the increase of the background stratification N (smaller Fr numbers) makes more difficult to have the condition $\partial_z \theta \geq N$; therefore this gives an explanation of the absence of extreme events at low Froude. The behaviour of the gradient components of u and θ , and in particular their kurtosis, suggest that small-scale related to large-scale extreme events are in a more mixed state compared to other regions of the fluid reinforcing the idea of a non-homogeneous medium. The same enhanced turbulent patches present a higher degree of isotropy, even though this should not be confused with the classical HIT concept of isotropy recovery, which usually happens at scale $\approx \ell_{Oz}$ in stratified flows; but, since in these flows the dynamics is dominated by horizontal motions $u_{\perp} \gg w$, whereas the imposed stratification and gravity suppress vertical displacement, the presence of extreme vertical drafts locally reduces the

Run	S40	S24	S20b	S16	S14	S12	S9	S85	S8	S7	S6	S5	S3	S2	S1	S08	S05
N	40	23.5	20	16.0	14.0	11.8	9.0	8.5	8.0	7.372	6.0	5.0	2.948	2.2	1.5	0.8	0.5
$Re/10^3$	3.9	3.8	3.8	3.8	3.8	3.8	3.9	3.8	3.8	3.8	3.7	3.6	3.0	2.6	2.6	2.8	2.9
Fr	0.015	0.026	0.030	0.038	0.044	0.051	0.068	0.072	0.076	0.081	0.098	0.11	0.16	0.19	0.28	0.56	0.93
R_B	0.87	2.5	3.4	5.6	7.3	10.2	17.7	19.7	22.1	25.2	35.9	47.5	75.2	90.9	201	895	2560
K_w	3.1	3.2	3.1	3.1	3.2	3.6	7.3	8.6	10.4	9.1	8.8	5.3	3.9	3.5	3.3	3.0	3.0
K_θ	3.3	3.4	3.4	3.5	3.5	3.6	4.0	4.3	4.3	4.1	4.1	3.6	3.1	2.9	2.8	2.7	2.7
K_{B_f}	10.25	11.34	12.31	13.57	13.28	29.24	118.6	146.8	156.8	82.51	80.02	30.75	13.02	10.26	8.29	7.36	7.43
$Sk_w/10^{-2}$	-5.3	-2.7	-3.4	-4.1	-4.2	-1.3	-8.0	-1.8	-2.5	-0.01	-0.5	-1.4	-1.3	-1.3	-2.4	-0.07	-1.4
$Sk_\theta/10^{-2}$	-17	-0.83	-1.6	0.5	-1.5	-2.1	-4.2	-4.8	-9.5	-7.0	-8.1	-5.2	-1.5	-9.8	-2.0	-2.6	-4.2
$Sk_{B_f}/10^{-2}$	2.4	-3.7	17	25	-3.2	56	87	94	149	93	107	84	76	82	89	119	140
β	0.11	0.10	0.098	0.090	0.085	0.085	0.088	0.088	0.088	0.090	0.10	0.12	0.32	0.52	0.59	0.61	0.63
R_{IB}	0.01	0.25	0.33	0.50	0.62	0.87	1.56	1.73	1.94	2.28	3.61	5.60	23.1	47.1	119	544	1601
$B_f/10^{-2}$	0.38	-0.14	0.69	0.78	-0.44	0.84	0.15	0.65	0.42	0.63	0.82	1.3	4.1	5.7	8.2	8.8	5.6
$\hat{\Gamma}$	0.081	0.10	0.10	0.11	0.12	0.11	0.12	0.13	0.13	0.14	0.17	0.20	0.38	0.48	0.59	0.50	0.28
S_α	0.97	0.97	0.97	0.97	0.97	0.97	0.95	0.94	0.94	0.93	0.87	0.80	0.48	0.36	0.29	0.28	0.27

Table 5.2. For the same runs listed in Tab. 5.1 here we report again the main parameters, the kurtosis of the vertical velocity K_w , temperature K_θ and buoyancy flux K_{B_f} , and their skewness Sk_α . Finally, we summarize the average value of some mixing proxies.

anisotropy level. As we will see in the following, since where extreme vertical burst occur the horizontal component of the velocity remain significantly lower, this results in patches of small kinetic helicity.

5.3 Effect of large-scale intermittency on the mixing properties of stratified flows

One way of measuring the mixing properties of stratified flows is by using the point-wise vertical flux of (potential) temperature, or buoyancy flux, $B_f = Nw\theta$. It represents the exchange between kinetic and potential energy, since it directly arises in the primitive equations for the energy conservation of the Boussinesq model (Sec. 2.2.2). We already analyzed the buoyancy flux in the framework of the space-filtering technique in the previous chapter; here, we focus on the intermittency of the buoyancy flux by analyzing both the skewness $Sk_x = \langle x \rangle^3 / \langle x^2 \rangle^{3/2}$ and the kurtosis, as we already did for the velocity and temperature fields, as well as for their gradients. The results, summarized for the same set of simulations analyzed before in Tab. 5.2, are reported in Fig. 5.3.

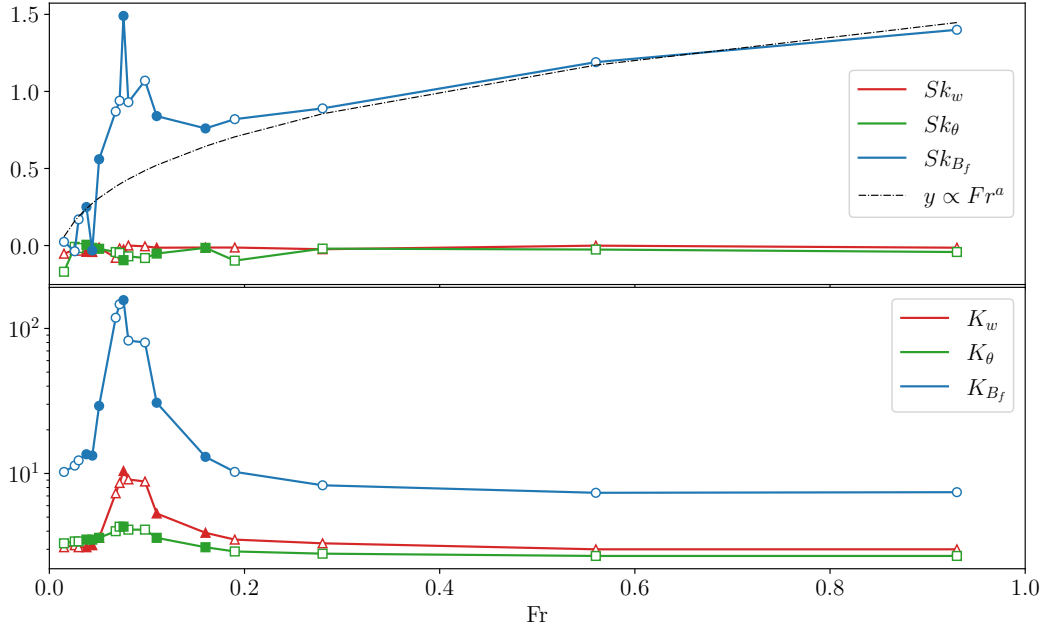


Figure 5.3. Top: skewness of the vertical velocity w (red), of the temperature fluctuations θ (green) and of the buoyancy flux B_f (blue) as a function of Froude number for the 17 runs of this study (see 5.2). A power-law fit $Sk_{B_f} \sim Fr^a$, with $a = 0.013$, is added (black dashed line). Bottom: kurtosis of w (red), θ (green) and of the buoyancy flux B_f (blue) for the same runs. Note the difference of scale compared to the plot for skewness.

All the statistical moments depicted in Fig. 5.3 show a clear variation around the critical value of $Fr \approx 0.076$, corresponding to run S8; the only curves that are almost constant, and close to zero, are the skewness of the vertical velocity w and the temperature field θ (top panel), meaning that positive/negative fluctuations have equal probability to occur. This is not the case for SK_{B_f} which slightly increases as a function of Froude, with a behaviour that can be approximately recovered by a power-law $Sk_{B_f} \sim Fr^a$, with $a \simeq 0.013$. The increase in the buoyancy flux skewness can be explained as a preferential coupling between extreme events in w and θ , indeed $Sk > 0$ indicates the longest positive tail of the PDF, which in the case of B_f is the result of the coupling between either updrafts (positive) or downdrafts (negative) in both the vertical velocity and temperature fluctuations. Such increase in the skewness however needs to saturate going to higher Fr , since we are moving to regimes where the stratification is weakening, and the scalar field is always more

decorrelated from the velocity field, resulting ultimately in a passive scalar when the HIT case is recovered. In the bottom panel the forth-order moment of w , θ and B_f are represented, showing the known behavior for the vertical velocity and temperature field (e.g., Feraco et al. [72], Feraco et al. [73]), and coherently the same trend is observed for the kurtosis of the buoyancy flux. The variation of K_{B_f} can be due to two main reasons: first that the buoyancy flux is quadratic in w and θ , whereas the second can be readily appreciated by recovering the 1D modified Vieillefosse model [218, 219] in which a wave term and the coupling between vertical velocity and temperature are added. We already mentioned in Ch.r 2 that this simple turbulence model is helpful to reproduce the high level of large-scale intermittency for $Fr \simeq 0.05 - 0.3$. Its dynamics clearly show how the interplay between waves and turbulence in an intermediate regime where it may generate resonant effects is crucial to the emergence of large-scale intermittency. By rewriting the model derived in Feraco et al. [72] without the term due to dissipation and forcing:

$$D_t \delta w = -\delta w^2 / \ell_z - N \delta \theta, \quad (5.2)$$

$$D_t \delta \theta = -\delta w \delta \theta / \ell_z + N \delta w, \quad (5.3)$$

where we recall that δw and $\delta \theta$ are the vertical velocity and temperature variations on a fixed scale ℓ_z ; the characteristic length scale has been chosen $\ell_z = \ell_{O_z}$ in Feraco et al. [72], implying vertical motions and gradients which dominate the dynamics over the horizontal components. From Eqs. (5.2) and (5.3) it is straightforward to derive equations for the total energy $\delta e_T = (\delta w^2 + \delta \theta^2)/2$ and buoyancy flux $\delta b_f = N \delta w \delta \theta$ of the fluctuations, which read as,

$$D_t \delta e_T = -[2\delta w / \ell_z] \delta e_T, \quad (5.4)$$

$$D_t \delta b_f = -[2\delta w / \ell_z] \delta b_f - N^2 (\delta \theta^2 - \delta w^2). \quad (5.5)$$

The buoyancy flux does not give any contribution to the total energy, as we have already seen in the primitive equations. In contrast, the evolution of δb_f depends on the difference between the potential and kinetic energy of the variations at scale ℓ_z . The evolution of δe_T and δb_f is the same if the equipartition of energy is satisfied; however, this is not the case in stratified flows, where the dynamics of the buoyancy

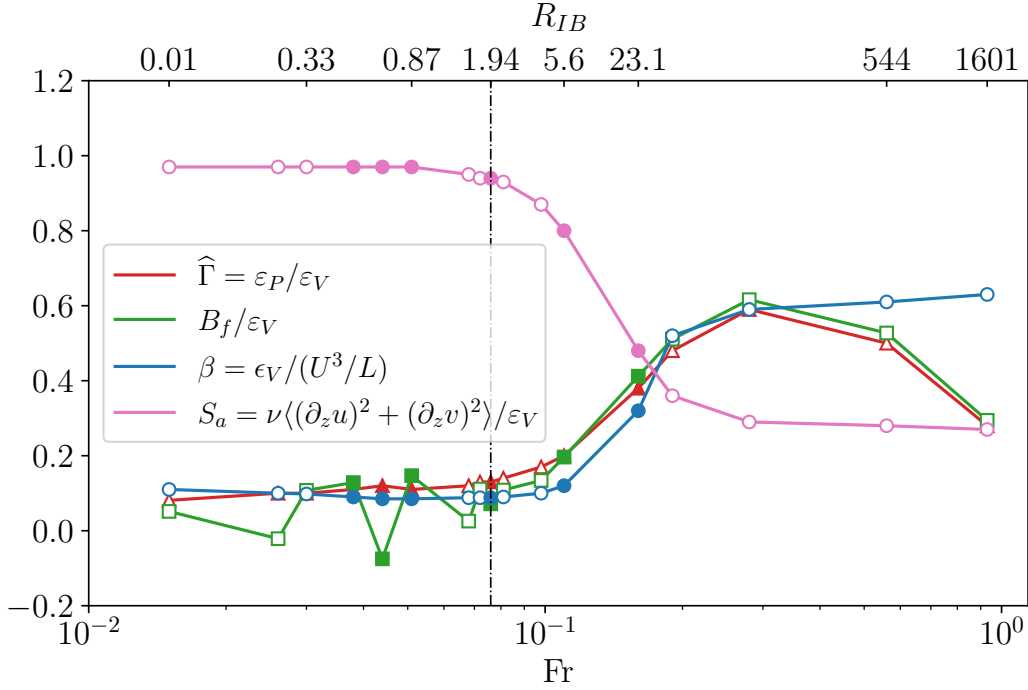


Figure 5.4. Mixing efficiency $\hat{\Gamma}$ (red), buoyancy flux normalized by kinetic energy dissipation (green), efficiency of kinetic energy dissipation β (blue) and finally S_a , i.e. the VSHWs, normalized by kinetic energy dissipation (pink), all as a function of Froude number Fr . The peak of kurtosis of the vertical velocity is marked by a vertical dashed red line.

flux is significantly affected by the wave dynamics and the exchange of energy between the two channels. This kinetic-potential differential is the additional source of the high variation of the buoyancy flux, as shown in Fig. 5.5. The left panel show the skewness of the perpendicular $E_P - E_{v_\perp}$ (red) and vertical energy defect $E_P - E_w$ (blue), normalized by the total energy; the right panel their respective kurtosis. The high values of kurtosis and skewness of the vertical component of the energy defect (blue curves) in the range $Fr \simeq 0.05 - 0.3$ completely resembles the behavior observed for the other quantities so far, further confirming that the difference between vertical kinetic and potential energy represents an important source for large-scale intermittency.

Other ways to evaluate the mixing properties of stratified flows are analyzed and compared to the point-wise buoyancy flux. The values, obtained for all the simulations, are reported in Tab. 5.2; we adopted three additional metrics of mixing,

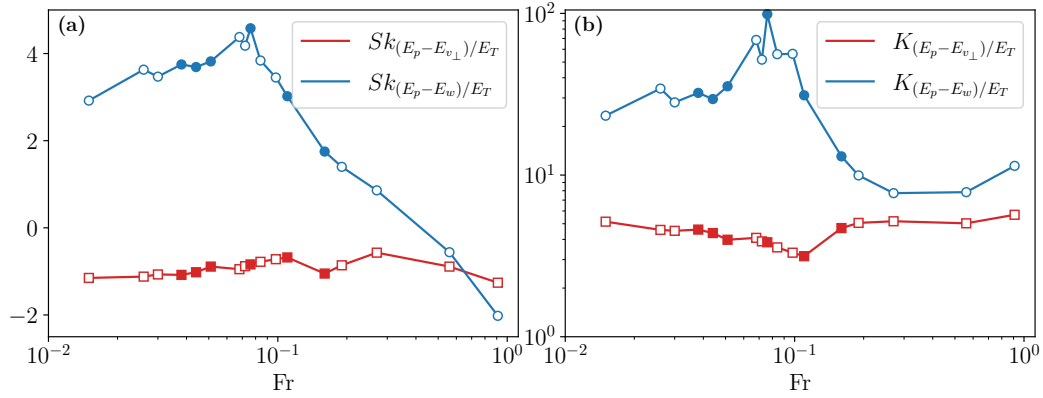


Figure 5.5. Skewness (left) and kurtosis (right) of the energy defects, normalized by the total energy, as a function of Froude number (see legends for definitions). There is a clear correlation between the lack of equipartition of vertical and potential energy (blue plots) and the strong intermittency close to $Fr \approx 0.076$. On the other hand, the statistics of the energy difference between the horizontal and potential modes do not vary substantially across Fr .

together with the buoyancy flux largely discussed yet.

The *efficiency of kinetic energy dissipation* is the total volume energy dissipation $\varepsilon_V = \nu |\nabla \mathbf{u}|^2$ normalized by the characteristic scales of the system $\beta = \varepsilon_V / (U_{rms}^3 / L)$, namely the rms velocity U_{rms} and the integral scale L .

The *irreversible mixing efficiency* has been already assessed in Feraco et al. [72] where it was found that the normalized rate of the potential energy dissipation $\hat{\Gamma} = \varepsilon_P / \varepsilon_V$ scales linearly in the range where extreme events develop, whereas it is almost constant on different levels for high values of the stratification, consistently with other studies and with observations.

Finally, the normalized *shear dissipation* $S_a = \nu \langle (\partial_z u)^2 + (\partial_z v)^2 \rangle / \varepsilon_V$ measures the small-scale anisotropy by comparing the amount of dissipation given by vertical shears of the horizontal velocity to the kinetic energy dissipation ε_V .

In Fig. 5.5 we can see, as a function of the Froude number, the irreversible mixing efficiency $\hat{\Gamma}$ (red), the buoyancy flux normalized by the total kinetic energy dissipation B_f / ε_V (green), the efficiency of kinetic dissipation β (blue) and the shear dissipation S_a (pink); top axis shows the corresponding values of the interaction parameter $R_{IB} = \varepsilon_V / (\nu N^2) = \beta R_B$, also defined in (3.19) as a ratio between the Ozmidov and

Kolmogorov length scales. The first relevant aspect emerging from the behavior of these curves is that, contrary to what is observed for higher-order moments, the average value does not seem to be affected by the presence of large-scale intermittency; however this is expected since extreme events are rare and therefore their emergence may not be evaluated on averaged quantities. On the other hand, three evident regimes can be distinguished, with the intermediate one, in particular, occurring around $Fr = 0.076$ (run S8), where a rapid increase of all the curves is observed. The region at low Fr number (high stratification) is characterized by a plateau whose value is likely to depend on the Reynolds number [181] for all the quantities, except the vertical shear S_a which is maximal when the flow is strongly stratified and dominated by vertical sheared winds. One could state that, at low Fr, vertically sheared horizontal winds are the main structure dissipating energy, allowing the flow to return in a state where inertial waves dominate it. The constant and then increasing regimes for S_a have already been observed in Brethouwer et al. [30] for values of the interaction parameter up to $R_{IB} \approx 15$; we found a very good agreement with their result for the entire range of R_{IB} . There is a small difference at the point where a clear transition is observed, which is $R_{IB} \approx 3$ in Brethouwer et al. [30], while in our work the transition seems to occur at around $R_{IB} \approx 5$ and 10; there is however a major difference between their and our investigation since they adopt a two-dimensional forcing, thus allowing vertical velocity fluctuations only by the coupling with gravity waves. Also, the normalized buoyancy flux at low Fr slightly differs from the other curves since we observe a few changes of sign in that range, and in particular it assumes negative values for two runs (S24 and S14). By moving towards a region where vertical drafts dominate, we see in Fig. 5.4 how large-scale extreme events generate more turbulence, increasing the dissipation efficiency [139], e.g. β and $\hat{\Gamma}$. While, for the runs with higher Froude the behavior of the various quantities is different according to their definition; indeed, we observe a consistent increase of the dissipation efficiency β that should attain unitary values approaching the HIT case. On the contrary, considering metrics involving (potential) temperature fluctuations means that they have to inevitably decrease when turbulent motions dominate over waves (low stratification) and thus regimes where temperature

fluctuations are decoupled from the velocity field.

Chapter 6

Low-dimensional representation of large-scale intermittency in stratified flows

Nowadays the majority of the most important results in science are obtained after the analysis of huge amounts of data either coming from high-resolution direct numerical simulations (DNSs) or observational measurements. The ever increasing computing capabilities allows the storage of hexa- or peta-bytes of data, being fundamental not only for scientific but especially for technological purposes. Hence, there is an inherent need for devising methodologies for data reduction and creation of reduced order models which could help with the storage and analysis of high-dimensional data sets. In computational fluid dynamics, the introduction of data compression may be worth not only for reducing the disk space occupied by numerical simulations but also for post-processing purposes [154], to study the system dynamics in a lower-dimensional space [52, 169] and even to create a model being able to reproduce the flow dynamics with high spatial and temporal resolution [82, 200]. One major challenge in this area is the ability to sufficiently estimate the (reduced) flow fields with realistic features allowing (i) simulation restarts using the compressed data without a significant impact on the long-term behavior of the simulated flow (ii) the compressed data to still preserve the essential statistical properties of the turbulent

flow with reasonable accuracy [154]. The first point is particularly important worth for the intrinsic chaotic behavior of the Navier-Stokes equations (NSEs), for which minor variations in the initial conditions can determine completely different behaviors after some time, while the second point becomes more difficult for stratified flows in the intermittent regime. In the last year, interest has grown for the application of Machine Learning (ML) methods to computational fluid dynamics (CFD). In fact, because of their intrinsic non-linear formulation, artificial neural networks (ANNs) are highly proficient in capturing non-linear and complex interactions. In addition, the introduction of physics-informed ML techniques [see 57, for a review], where physical knowledge about the systems are considered to add either information or constraints on the created model, has exponentially increased the interest on neural networks for scientific research [74, 41, 10]. For dimensionality reduction or data compression autoencoders are widely used since they can easily perform non-linear projections thanks to non-linear activation functions, allowing the creation of well-performing reduced order models. [154, 87, 165, 230, 161]. Most of the reduction methods for turbulent flow analyze homogeneous isotropic turbulence (HIT) which is a simpler case than the simulations of stratified flows considered in this thesis. Indeed, despite the universal non-linear dynamics of turbulence, HIT presents statistical features which are stationary both at large and small scales when a fully-developed turbulent state is reached. On the contrary, we have already seen in this manuscript how the statistics of stratified flows can drastically change if computed in different regions of the domain or at different times, as well as with varying the controlling parameters such as the Froude number. The presence of large-scale intermittency represents in fact an additional challenge for a reliable low-dimensional representation since regions with extreme events are in general those of the phase space with sparse data, and they present very large dimensional attractors which in combination with the occurrence of transient and rare events make the application of classical technique significantly cumbersome [222]. Therefore, in this analysis we implemented a reduction technique for 3D DNSs of stratified flows using Convolutional Autoencoders (CAEs) where we add statistical constraints based on our knowledge of these flows. Such information are introduced to tackle

Id	Compression factor	No. Layers	No. params.	Latent space
CF2	2	7	321,156	$64 \times 64 \times 128$
CF4	4	8	339,892	$32 \times 32 \times 256$
CF8	8	9	324,772	$32 \times 32 \times 128$
CF16	16	11	349,804	$16 \times 16 \times 256$

Table 6.1. Description the four Convolutional Autoencoders architecture: the compression factor (CF), the number of layers referring to both the encoding and decoding part of the network. The number of parameters account for all the weights and biases which have to be optimized during the training phase, and the latent space is the reduced space after the encoding network is applied.

the highly variability of the statistics, and in particular of the forth-order moment of vertical velocity w PDF, due to the presence of large-scale vertical drafts. We introduce additional terms to the loss function, that being the objective function which the CAEs minimizes during the training phase, accounting for the error on the reconstruction of the statistical moments of the distribution of w up to the forth-order, so that the statistical properties of the reconstructed field are preserved.

6.1 Statistical-Informed Convolutional Autoencoders

In general, an autoencoder [62] is an unsupervised feed forward artificial neural network (ANN) that aims to reconstructing the original data through a process involving data compression and recovery. Indeed, its main objective is to create a reliable and reduced representation of the input data set, being particularly helpful for either creating reduced model or simpler but still informative representation of high-dimensional data. The network consists of an encoder part $P : \mathbb{R}^D \rightarrow \mathbb{R}^d$, being an operator which compressed the data (input) into a smaller space representation (or latent space), and a decoder part $Q : \mathbb{R}^d \rightarrow \mathbb{R}^D$, which reconstructs the encoded data back to the original input dimension. When the mapping kernel is linear, the autoencoder can be considered as a singular value decomposition analysis. Instead if they employ convolutional layers to perform the encoding and decoding operations on

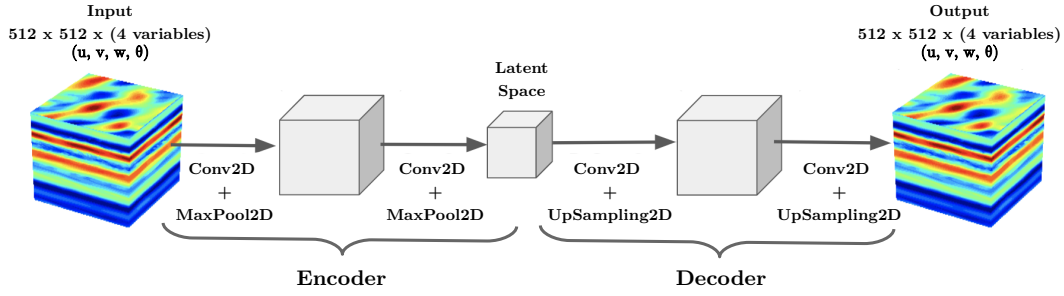


Figure 6.1. Schematic representation of a symmetric Convolutional Autoencoder (CAE) as it is implemented in general in this work.

images, or more in general on 2D (or higher) data, they are named as Convolutional Autoencoder (CAE). During the convolution operation, the kernel swipes the data domain to extract features and learn spatial and/or temporal dependencies. The process is then carried out across multiple layers, obtaining representative features in a hierarchical sense [141]; CAEs with many hidden layers can be considered as deep neural networks (DNN). The initial layers learn low-level or particular details about the data, while subsequent layers focus on larger and larger-scale information. In our work we developed four CAEs with different compression factors (CFs), defined as the ratio between the input and the latent dimensions, from 2 to 16; an example of a general CAE architecture used in our implementations is shown in Fig. 6.1. In Tab. 6.1 we report the main characteristics of the four CAEs implemented here; starting from CF2, we obtained higher CFs by adding more hidden layer to the initial architecture, but trying to keep the number of parameters as fixed as possible in order to make a more fair comparison of the four networks performance. Indeed, the number of weights and biases, as highlighted by the values in Tab. 6.1, varies only by $\approx 10\%$. On the other hand, more hidden layers allow networks with higher CF to learn more features of the original fields during the compression step. The number of hidden layers is intended for the entire CAE architecture, comprising both the layers of the encoding n_e and decoding n_d part; they usually have an amount of layers which follow the relation $n_d = n_e + 1$, while the CAE is symmetric if the total number of layers is even.

	Original	CF2	CF4	CF8	CF16
$ \langle \nabla \cdot \mathbf{u} \rangle \quad [\times 10^{-11}]$	0.42	1.83	3.26	2.37	2.06
$\max \{ \nabla \cdot \mathbf{u} \}$	$5.9 \cdot 10^{-4}$	538	410	573	530

Table 6.2. Order of magnitude and maximum value of the divergence of the velocity field after the reconstruction with the different CAEs.

6.1.1 By-plane approach to fluid anisotropy

We already mentioned in the introduction of this chapter that the final objective is to obtain a tool which is able to reproduce most of the features of the velocity \mathbf{u} and temperature θ fields of a fluid which is anisotropic but moreover non-homogeneous due to the presence of large-scale events intermittent in space and time. Therefore, our approach consists in applying various changes to the classical CAE algorithm to make it the more suitable and better perform for this challenging task. There are four main key ingredients in our application of CAE to highly intermittent stratified flows. At first, since stratification creates a direction of anisotropy, even though we deal with fully three-dimensional simulations the original cubic data are divided into horizontal planes along the vertical direction. Then, for each time and height value z , planes for every velocity component (u , v and w) and for θ are stacked together creating three-dimensional input data with dimensions $512 \times 512 \times 4$, as indicated in Fig. 6.1. Before being divided, the data are normalized $\hat{x} = (x - \mu)/\sigma$ using the average μ and standard deviation σ computed on each simulation cube. In this approach, we believe that passing the information from the three components of the velocity, together with the temperature, is essential for the CAE to better reconstruct the flow dynamics at a given time t and altitude z , since their variation is strictly correlated within the primitive equations. This approach has the shortcoming that it is not possible to add an important information we know about the velocity field, that is the incompressibility $\nabla \cdot \mathbf{u} = 0$, since working plane by plane we cannot add constraints on the vertical derivative of the velocity $\partial_z w$. This leads to values for the maximum and average divergence of \mathbf{u} reported in Tab. 6.2, where we can see that even if on average the condition is well satisfied in the reconstructed fields, locally

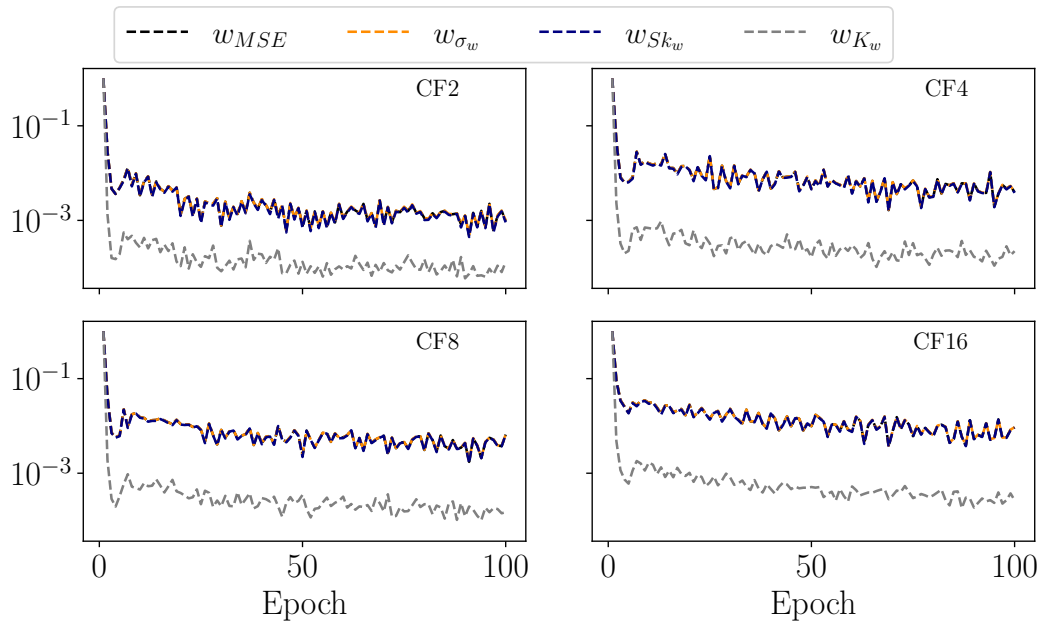


Figure 6.2. History of the loss function weights (detailed in the legend) for the four Convolutional Autoencoders during the training phase.

this is not true while the condition is satisfied also point-wise for the original field.

6.1.2 Statistical-aware loss function

The learning process of a neural networks is performed through an optimization algorithm, which looks for the best weights and biases for the network by minimizing what is called a *loss function* (or cost function). This represents the metric that evaluates, during the training phase, how good is the reconstruction made by the CAE, in our case, and in general represents the objective function for a machine learning algorithm to minimize to have optimal performance in the required task. Indeed, in general loss functions are very specific for the problem formulation: many different losses have been adopted in the literature for problems involving "real" numbers, such as the (root) mean squared error (R)MSE, the mean absolute error MAE, the cross-entropy and many others.

As we already mentioned in the introduction, there exist many applications of CAEs, but also other neural networks, such as generative adversarial networks (GAN) [113, 36] and fully-connected networks [185, 186] largely adopted for dimen-

	Id	MSE [$\times 10^{-4}$]	σ_w err. [$\times 10^{-5}$]	Sk_w err. [$\times 10^{-4}$]	K_w err. [$\times 10^{-2}$]	Loss [$\times 10^{-4}$]
1st stage						
“standard loss”						
	CF2	0.39	0.13	10.9	18.4	0.39
	CF4	0.55	0.45	13.2	22.4	0.55
	CF8	0.54	0.82	19.1	19.0	0.54
	CF16	1.1	5.3	44.9	41.7	1.1
2nd stage						
“statistical-informed loss”						
	CF2	0.67	1.03	1.9	0.04	0.44
	CF4	1.0	1.0	3.2	1.4	4.0
	CF8	1.3	0.074	3.6	1.7	2.3
	CF16	2.3	0.32	12.0	5.9	10.0

Table 6.3. Results of the four CAE on the test set for both the first (top) and second (bottom) training phase.

sionality reduction or reduced order representation of turbulent systems; however, in most cases the goal is to reproduce the dynamics of fully-developed turbulent flows which obviously are characterized by multi-scale structures and a complex dynamics, but still manifest a stable statistics with Gaussian or quasi-Gaussian PDF at large scales and fat tails with extreme gradients at smaller ones. These features are almost constant over time and space once the flow is in a completely developed turbulent state. Nevertheless, this is not the case when dealing with numerical simulations of stably stratified flows as those we analyze in this work. Indeed, we widely observed how the statistics, as well as the dynamics and energetics, of these flows can drastically change in time and space, but also with the governing parameters, such as the different regimes explored varying the Froude number (the buoyancy Reynolds alternatively). The presence of large tails in the vertical velocity w and temperature θ distributions likely represent an additional challenge for the reconstruction of the physical fields through CAEs, and with machine learning techniques in general. As an example, if we evaluate the reconstruction made by

the implemented CAEs with a standard MSE as loss function we may obtain a very low reconstruction error, but by looking locally at the point-wise error in areas where vertical drafts develop the low-dimensional representation is not sufficient to correctly capture the particular behavior of the flow. Since vertical drafts are rare and extreme, the flow is dominated by regions with Gaussian distributions and therefore drafts do not have a significant weight on the global loss function. Yet, we know that they are fundamental for some aspects of the dynamics of stratified flows. For these reasons we introduce a statistical-aware loss function which contains four different terms,

$$\begin{aligned} \mathcal{L} &= \frac{1}{D} \left(w_1 \sum_{\alpha}^{[u,v,w,\theta]} \sum_{i=1}^N \frac{(\alpha_i - \alpha_i^r)^2}{N} + w_2 \sum_{i=1}^N \frac{(\sigma_{w_i} - \sigma_{w_i^r})^2}{N} \right. \\ &\quad \left. + w_3 \sum_{i=1}^N \frac{(Sk_{w_i} - Sk_{w_i^r})^2}{N} + w_4 \sum_{i=1}^N \frac{(K_{w_i} - K_{w_i^r})^2}{N} \right) \quad (6.1) \\ &= \frac{1}{D} \sum_{j=1}^4 w_j R_j \end{aligned}$$

where $D = 3(w_1 + w_2 + w_3 + w_4)$, α^r is the field reconstructed by the CAE, whereas α the original corresponding one. The second, third and fourth term in (6.1) are the quadratic mean errors between the moments of the original and the reconstructed vertical velocity w computed over horizontal planes (x,y) , namely the standard deviation σ_w , the skewness Sk_w and kurtosis K_w respectively. We recall that for a normal distribution the reference values are: $\sigma = 1$, $Sk = 0$ and $K = 3$. Each term is properly weighted with values w_i varying at each epoch during the training phase. In order to obtain a loss function with terms having the same order of magnitude during the whole training procedure at a given epoch m , the weight of the i th term w_i is proportional to the sum of the other three terms at the previous epoch $m - 1$, e.g. $w_i^m = \sum_{j \neq i} w_j^{(m-1)} R_j^{(m-1)}$ (and normalized such that their sum is equal to 1). The behavior of the different terms of the loss function during one hundred epochs of training is shown in Fig. 6.2. We can appreciate from the four panels how there are essentially three weights (w_{MSE} , w_{σ_w} and w_{Sk_w}) which are nearly equal for the entire training phase, whereas the coefficient weighting the kurtosis term is significantly smaller indicating a larger error on the fourth-order moment, as

expected. Even though the various terms of the statistical-informed loss function are well balanced, the training procedure with additional constraints either coming from the knowledge of the physical system, as it happens for physical-informed neural networks, or from statistical information can be difficult, slower and sometimes very noisy. Therefore, in many situations a two stage training approach is adopted [see for example, 41]. Indeed, during the first stage the algorithm is trained using a standard MSE loss function (meaning that $w_1 \equiv 1$ and $w_2 = w_3 = w_4 \equiv 0$) for the first 50 epochs (see panel (a) in Fig. 6.3). The first stage of training is necessary to create a robust model which is able to obtain the best average reconstruction of the physical fields, without accounting for specific features of the flow. During the second stage of training we switch on all the terms of the loss, proceeding for one hundred more epochs in creating a model with the addition of statistical constraints on the first four moments of the vertical velocity PDF (see panels (b)-(f) in Fig. 6.3).

6.2 SI-CAE Performance

We analyze in details the output of run S8 (see Tab. 3.1) for more than $45\tau_{NL}$ corresponding to one-hundred time steps. Since in our approach we divide each simulation cube in planes along the vertical direction, the data set we use for training and testing our CAEs comprises $N = 51,200$ samples, with dimension $512^2 \times 4$ (512^2 grid-points for four variables u , v , w and θ). We divided the data set in training and test set on a temporal basis, taking the first 70% for the training phase and the remaining 30% for testing the performance. Fig. 6.3 shows the history of the various terms of the loss function during the two phases of training. Panel (a) (yellow) shows the first 50 epochs where the only term in the loss is the mean squared error, while panel (b) shows the total loss \mathcal{L} for the next 100 epochs of the second training stage. The other panels, from (c) to (f), show the evolution of the four terms in Eq. (6.1) which determine the behavior of the curves in (a). Obviously a trend with the compression factor is observed, and as expected the higher CF, the higher the reconstruction error both on the mean field and the statistical moments. This is not related to the newly introduced loss function since already during the first training stage (panel (a)) this trend can be clearly observed. We see from the

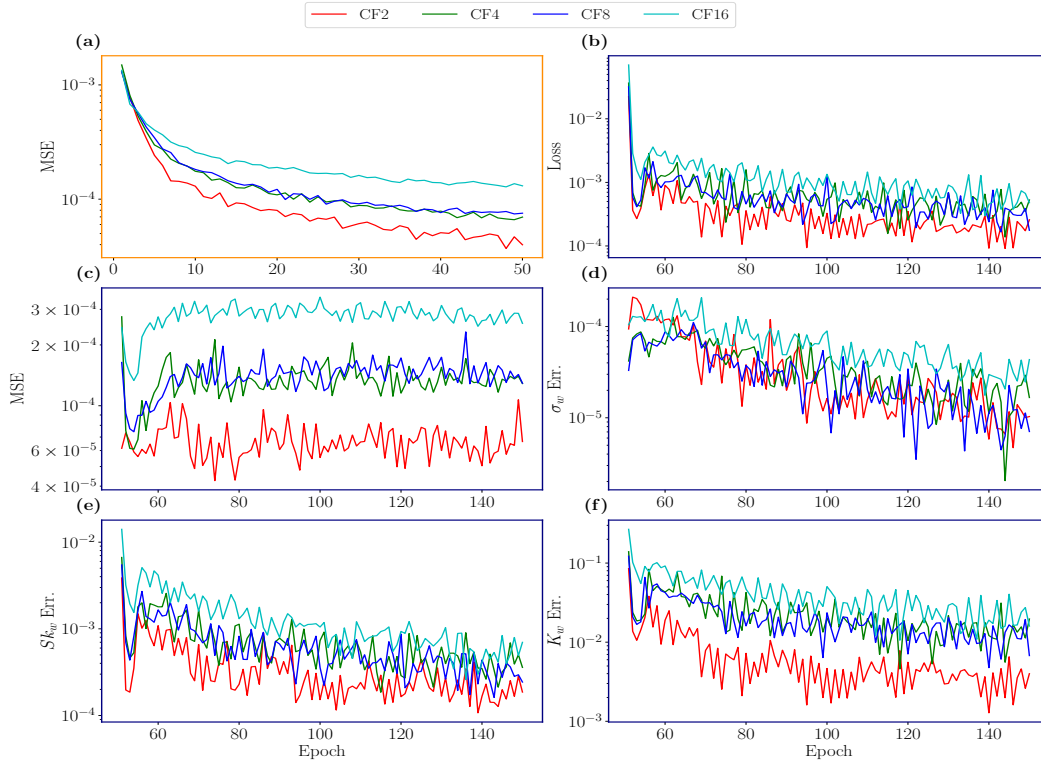


Figure 6.3. Loss function trend during the training phase. Panel (a) shows the MSE during the first training stage (orange panel), whereas for the second phase (blue panels) we show the details of all the terms composing the statistical-informed loss function: MSE in panel (c), standard deviation error in (d), the error on the skewness (panel (e)) and kurtosis (panel (f)). The total statistical-informed loss as a function of the epoch is represented in panel (b).

behavior of the MSE when other terms are accounted in the objective function in panel (c) that essentially the CAE during the second training stage stop improving the average reconstruction of the average physical fields, since all the curves in such panel are nearly constant for the entire phase. On the contrary there is a significant improvement of the error on all the statistical moments (panels (d)-(f)), even though the rate of decreasing of the error seems to be inversely proportional to the order of moment, meaning that in the same amount of epochs the improvement on the reconstructed standard deviation (2nd-order moment) is significantly higher than what obtained for the kurtosis (4th-order moment). As also confirmed by the trend of the loss weights (Fig. 6.2), the error on the kurtosis is nearly between one and two

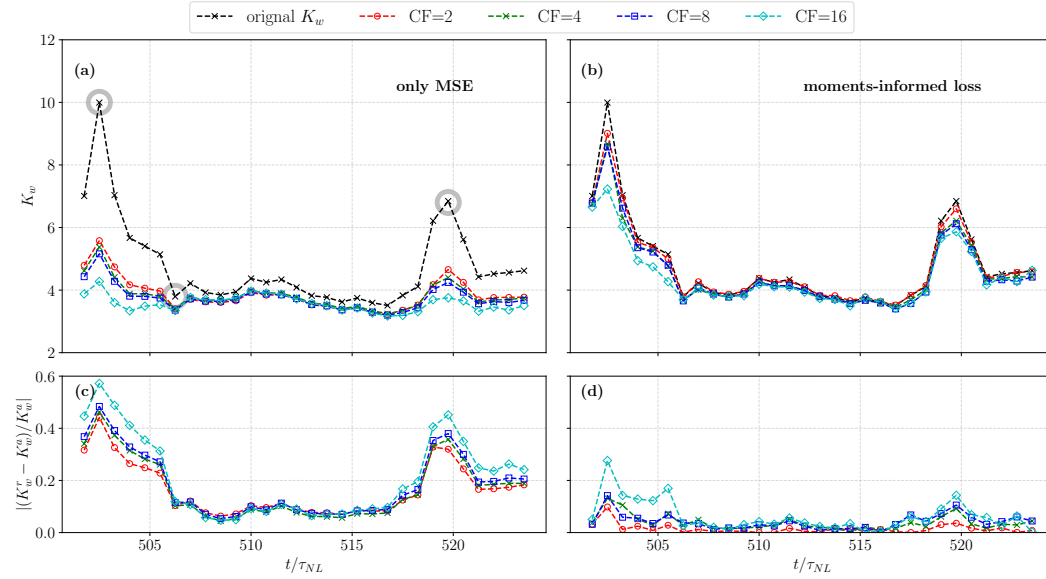


Figure 6.4. In panel (a), the reconstruction of the volume kurtosis obtained with the four CAE (colored curves) with respect to the original values of K_w (black dashed line), obtained with standard CAE. Panel (b) shows the same for the statistical-informed Convolutional Autoencoder (SI-CAE). Panels (c) and (d) show, for each colored curve, the relative error between the original K_w^a and reconstructed K_w^r values of kurtosis.

orders of magnitude greater than the others. The huge difference with respect to the error on the other statistical moments may be due to the high variability of K_w (as we have often seen in this manuscript), whereas standard deviation and skewness are expected to vary less and to be closer to values of a Gaussian distribution. The details of the results obtained on the test set for the various terms involved in the loss function during the two training stages are summarized in Tab. 6.3. We can see that including other terms into the loss function results in an average reconstruction error 2-3 times greater than what obtained after the first training stage (see MSE in Tab. 6.3), even though it remains on the order of $\text{MSE} \sim 10^{-4}$, consistent with other results found in literature [87, 154]. In addition, when constraints on the statistical moments are added to the model, we observe that the reconstruction of high-order moments improves up to 10 times for any compression factor.

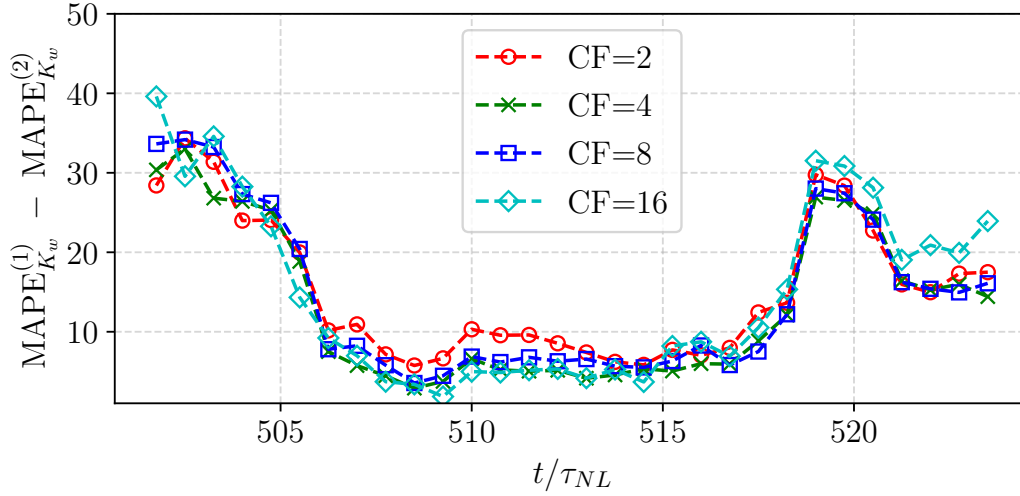


Figure 6.5. Difference between the mean absolute percentage error (MAPE) obtained after the first training phase $\text{MAPE}_{K_w}^{(1)}$ and after that the statistical-informed loss is introduced $\text{MAPE}_{K_w}^{(2)}$ MAPE, for the four different CAE, evidenced by colored curves.

6.2.1 Low-dimensional representation of extreme vertical drafts

We selected an interval of run S8 where isolated extreme bursts occur, producing evident peaks of the kurtosis K_w . In Fig. 6.4 the values computed on the original data (black dashed curve) are reported as a function of the turnover time for the entire test set. This figure clearly highlights how the second stage of training improves the forth-order moment of the reconstructed velocity, not only if computed by planes but also considering the whole simulation volume. Indeed, after the reconstruction made by the CAE we are able to rearrange data into simulation cubes 512^3 allowing also to compute statistics on the entire domain; therefore for each time step in the test set, we computed the vertical velocity kurtosis both of the original and of the reconstructed data, and the results of such a comparison are shown in the four panels of Fig. 6.4. Panels (a) and (c) show the trend of kurtosis obtained with the CAEs after the first training stage and the mean absolute percentage error (MAPE) computed with respect to the original values, respectively; the same quantities are shown in panels (b) and (d) after that the statistical-informed loss has been used. All the CAEs show a significant reduction of the percentage error, with a particular improvement in times where volume averaged K_w exhibits highly non-Gaussian values ($t \approx 503\tau_{NL}$

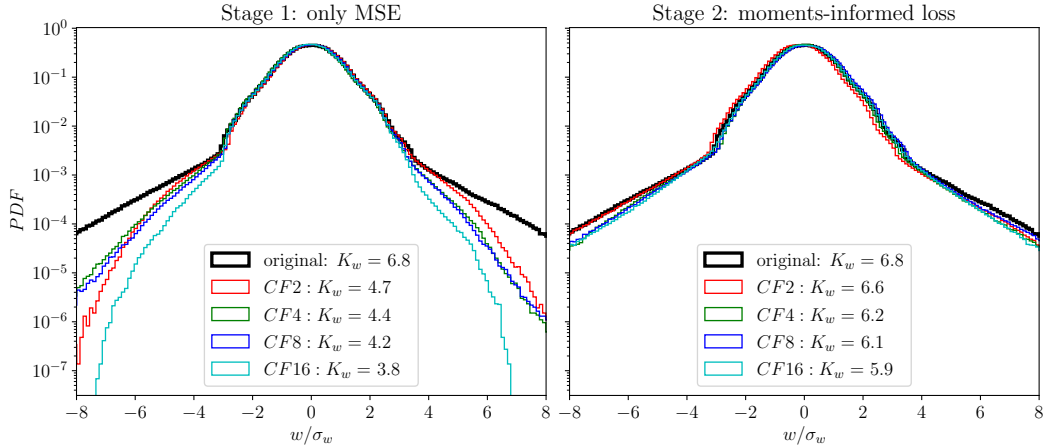


Figure 6.6. Left: PDFs of w computed at $t/\tau \approx 520$ (black curve) and the same obtained from the field reconstructed with the networks (colored curves), when only MSE is used as loss function. Right: the same as the left panel but using the statistical-informed loss.

and $t \approx 520\tau_{NL}$). In addition, with the application of the modified loss we are able to obtain percentage errors on the kurtosis smaller than 10% on average. However, the improvement in the reconstruction of the forth-order moment is obtained also for values close to the Gaussian reference ($K_w \approx 3$). Indeed, it is evident that our approach can be successfully extended to other situations where the PDFs are far from Gaussian shape as it is the case for the concentration of a passive scalar [183] or for the velocity in the boundary layer [32]. The statistical moments up to the forth-order embedded into the loss function guarantee an optimal reconstruction of the statistical properties of the physical fields without any prior knowledge about the shape or variability of their distribution function. The improvement we obtain with the custom loss is quantified in Fig. 6.5 where we show the difference between the MAPE computed on K_w after the first and second training stage, as a function of time. The improvement reaches up to $\approx 40\%$ at times with high values of K_w but in general an increasing of nearly 10% is observed at all times. In Fig. 6.6 we show the probability distribution functions (PDFs) computed on the entire volume at time $t \approx 520\tau_{NL}$ (third gray circle in Fig. 6.4), when $K_w \simeq 6.8$, using both the original (black) and data obtained from the four Convolutional Autoencoders. We notice how after the first training stage (left panel) the PDF core is already reliably mapped by the reconstructed data, even though the tails significantly differ, and

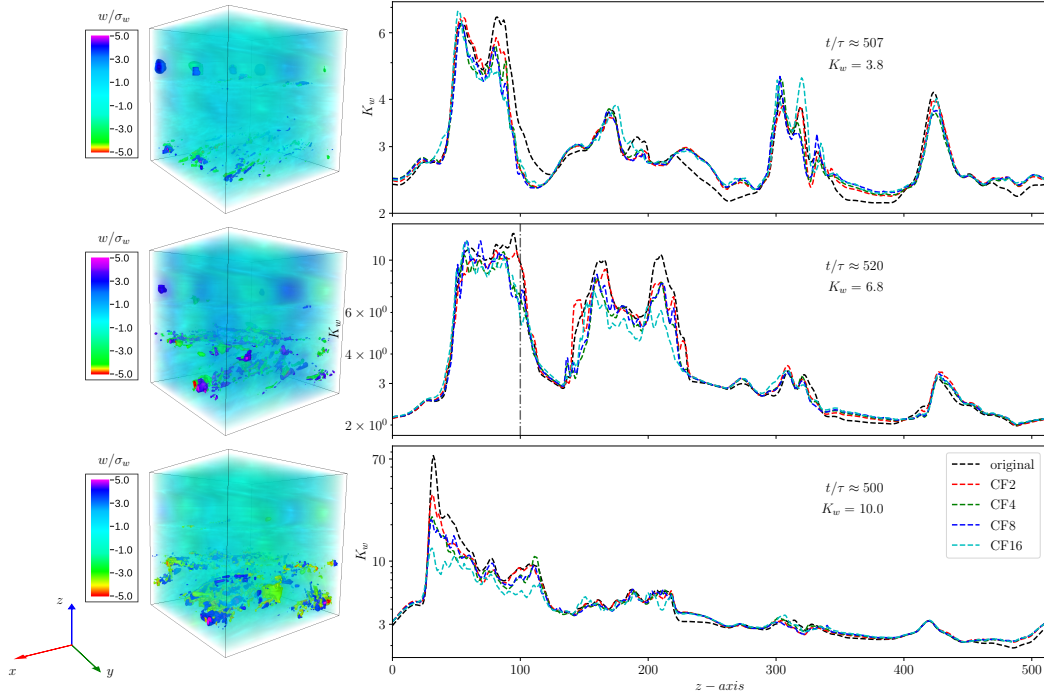


Figure 6.7. Right panels show the vertical profile of the vertical velocity kurtosis K_w (black dashed lines) at times: $t/\tau \approx 507$ (top), $t/\tau \approx 520$ (middle) and $t/\tau \approx 500$. Colored dashed curves are the same profile of K_w obtained from the reconstructed fields. Right 3D renderings highlight that higher values of K_w indicates more extreme events, which are represented as solid regions ($|w/\sigma_w| > 4$) while the rest of the domain is shaded.

in particular the departure seems increasing for higher $|w|$. The PDF in the right panel of Fig. 6.6, after the second training stage, completely resemble the original ones, confirming that if the distribution moments are the same up to the fourth-order the shape of the PDF is equal with good approximation.

In Fig. 6.7 we show an example of large-scale intermittency observed at three different times, indicated by the gray circles in Fig. 6.4. The three-dimensional renderings represent the vertical velocity field w at low (top, $t \simeq 506\tau_{NL}$), middle (center, $t \simeq 520\tau_{NL}$) and high kurtosis K_w (bottom, $t \simeq 502.5\tau_{NL}$), where values $|w/\sigma_w| > 4$ are highlighted in solid color while smaller values are depicted as a transparent blue. Aside each rendering the vertical profile of the kurtosis K_w computed plane-by-plane with the original data (black), as well as with the reconstructed (colored for the different CAEs) is shown. Also for the top panel, when the kurtosis

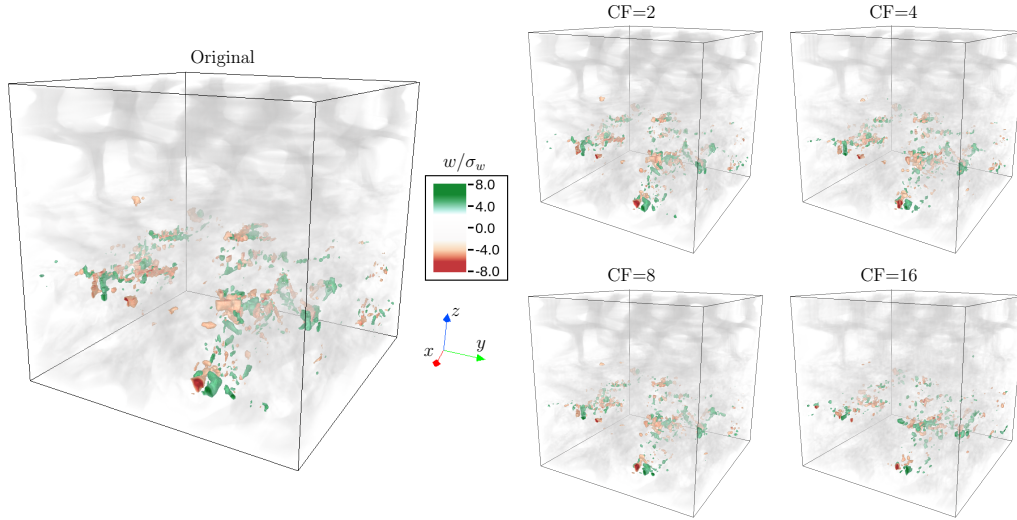


Figure 6.8. Larger three-dimensional rendering is the original vertical velocity w fields where values $|w/\sigma_w| > 4$ are represented with solid colors while other points are in transparency. The same for the reconstruction obtained with the four CAEs.

is small $K_w \simeq 3.8$ there are planes reaching values of $K_w \approx 6$, and in general an high level of variability is observed. These effects are enhanced when more vertical drafts develop within the flow (center and bottom) with kurtosis more than one order greater than the Gaussian reference values, as it shown in logarithmic scale in Fig. 6.7.

6.2.2 Physical fields 3D reconstruction

We saw that the statistical properties, and in particular the kurtosis, of the vertical velocity are well recovered by the developed CAEs. However we already mentioned that the presence of large-scale extreme events represents a challenge for their intermittency in time but also in space, creating patches of enhanced turbulence where the flow may explore completely different regimes. In addition, the low-dimensional representation of turbulent flows would represent a valuable result if the reconstruction produces truthful physical fields with local features which realistically resemble the quantities produced by the evolution of the governing equations. Therefore in this last part of the results we analyze how the introduction of large-scale terms to the loss function locally affect the reconstruction of the entire

velocity field \mathbf{u} as well as the potential temperature θ . In Fig. 6.8 we report a three-dimensional visualization of the vertical velocity w obtained with the four CAEs, as well as the original field for comparison. Data are taken at time $t \simeq 520\tau_{NL}$, with relatively high kurtosis $K_w \approx 6.8$. Clear extreme vertical drafts, identified as values with $|w| > 4\sigma_w$, have developed in the mid-bottom part of the domain. The same kind of structures can be noted in cubes reconstructed with the CAEs up to the maximum compression; only at $CF = 16$ their shape starts being more noisy. The gray transparent shading, representing velocity values below the threshold of $4\sigma_w$, and therefore the majority of the volume, is consistent for the recovered data which confirms the small values of MSE observed earlier. However, the reconstruction made by the implemented CAEs involves also the other components of the velocity field (u and v) as well as the (potential) temperature fluctuations θ . To have a general overview of how the neural networks recover all the physical quantities interested in the analyzed DNSs we represent them with several panels in Fig. 6.9. This figure shows an horizontal cut (x,y) of the simulation domain taken at the same time of the previous figure (Fig. 6.8 at the height z^* indicated with a dash-dotted line in Fig. 6.7 (middle panel)). The columns of Fig. 6.9 refer to the three components of the velocity field $\mathbf{u} = (u, v, w)$ and the temperature θ . All the images are represented by the same color bar which is not shown since the main objective of this figure is the comparison between the first row, the original data, and the others, being the reconstructed physical fields for increasing values of the compression factor. Since we are looking the domain from top (gravity is a vector entering the page), it is correct to have horizontal components strongly dominated by a nearly constant positive (red) for v and negative (blue) for u mean wind; this is indeed the effect of vertically sheared horizontal winds (VSHWs) which are ubiquitous in stratified flows. Nevertheless, also the horizontal components of the velocity show small-scale perturbations where extreme vertical drafts develop, as already seen throughout this manuscript. The extreme events developed in this snapshot are clearly visible from the vertical velocity and partially from the temperature renderings (third and forth columns in Fig. 6.9), and the same detail is captured also by the field reconstructions. Indeed, as already noticed for the three-dimensional visualization, the reconstruction is very reliable up

to $CF = 16$ where a significant checkerboard effect starts developing everywhere in the domain. This is probably due to the combined effect of the high compression factor and of the statistical-informed loss function presenting large-scale statistical constraints. In fact, by looking at the reconstructed fields after the first stage of training (not shown here), we can observe the same artifact at high compression but it is slightly reduced for the absence of other terms into the loss function.

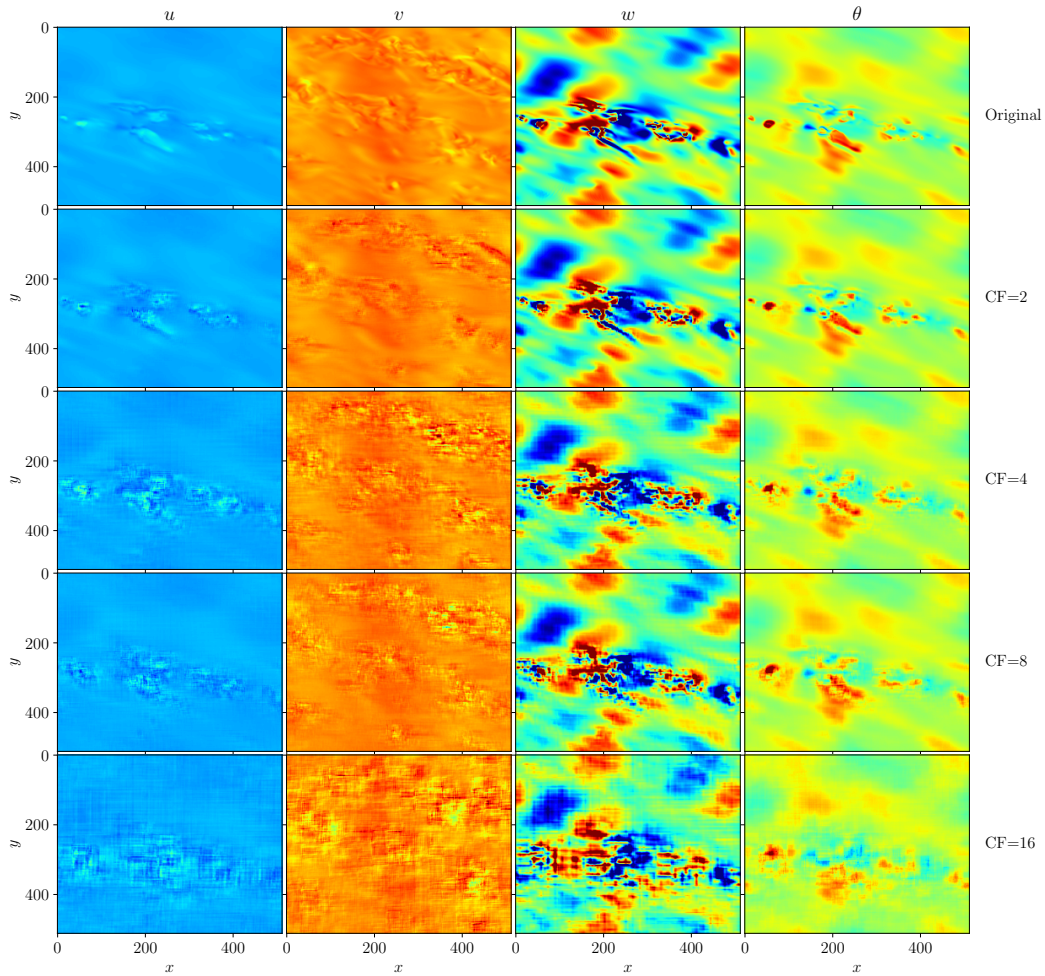


Figure 6.9. Horizontal 2D slice of the original physical fields under analysis: the three velocity component (u, v, w) and the (potential) temperature θ . Other rows represent the same fields reconstructed after the compression by a factor 2 (second line), 4 (third line), 8 (forth line) and 16 (fifth line).

Chapter 7

Conclusions and discussion

7.1 Conclusions

In this thesis we worked on implementing and further developing a well-established data analysis tool, known as space-filtering (SF) or coarse-graining (CG) technique, already employed for the analysis of neutral and conductive turbulent flows in a variety of physical contexts, to characterize the dynamics of stratified flows. The SF approach proved to be a valuable tool to provide information on the energy distribution in both physical and spectral space, as testified by many results appeared in the literature concerning the study of turbulent structures and instabilities in geophysical [9, 59, 37] and astrophysical flows [40, 133, 132, 238, 237]. One of our main contributions to this method is the extension to the use of filter functions with a generic shape, beyond the classical filtering kernel with isotropic support (i.e., $G_\ell(k)$ with $k = \sqrt{k_x^2 + k_y^2 + k_z^2}$). In particular, here we implemented the axisymmetric ($k_\perp = \sqrt{k_x^2 + k_y^2}$) and parallel ($k_\parallel = |k_z|$) versions of the filtering approach which are particularly helpful for the analysis of anisotropic turbulent systems, such as the Earth's atmosphere and oceans, where the effect of gravity and rotation determines a dynamics which significantly differs in the parallel and perpendicular directions. This framework has been validated against classical reduced energy fluxes [137, 1], directly obtained from the transfer functions, showing an excellent agreement in terms of the average spectral features recovered (e.g., inertial range, injection scale, intensity of the transfer rate and others). The analysis performed in this thesis and

their outcome can be summarized in four main points:

1. In stratified fluids large-scale intermittent events developing in the form of sudden enhancement of the vertical component of the velocity (w) and of the temperature (θ) do locally generate turbulence, determining enhanced downscale energy transfer and dissipation. These events make stratified flows as efficient as in homogeneous isotropic turbulence (HIT) flows Marino et al. [139] in dissipating energy, whereas in general they would be less dissipative due to the strong stratification. Our space-filtering analysis unveiled that the enhanced energy transfer observed in a certain parameters range, is mainly due to the coupling between the small-scale Reynolds stress tensor \mathcal{T}_{uu} and the large-scale strain tensor $\nabla\tilde{\mathbf{u}}$. We emphasized how, in presence of extreme drafts, the mechanism involved in the energy transfer to small-scale structures is through generation of vorticity and therefore the creation of strong gradients, especially in the velocity field. Indeed, we observed that in the same range of Froude numbers in which the kurtosis of the vertical velocity K_w peaks ($\text{Fr} \approx 0.06 - 0.1$), the same happens to the kurtosis of some of the components of the velocity gradient $\partial_i u_j$, pointing to the connection between large- and small-scale intermittency.
2. What we found in our simulations, where no forcing is applied to the (potential) temperature field, is that vertical drafts act as a mechanism to inject potential energy through the buoyancy term, which couples velocity and temperature fields in the Boussinesq model (see 2.2.2). All that results in a transfer of the potential energy, in the perpendicular direction (in Fourier space, k_\perp), towards both large and small scales, all that occurring within the turbulent inertial range. Such coupling affects also the mixing properties of the flow, quantified here in terms of buoyancy flux, also through the application of filters, $N\tilde{\theta}\tilde{w}$, providing both local-in-space and local-in-scale information. Variations of the local value of the buoyancy flux can be relevant for geophysical applications, especially in global models, since the trends we observe concern a range of Froude numbers close to that of the atmosphere and the oceans.

3. Further exploring the interaction between large- and small-scale structures by means of a model for the field gradients, we proposed a mechanism for the generation of extreme vertical drafts based on buoyancy-driven instabilities. The occurrence of the latter is somewhat related to the presence of vertical shears, driving small-scale instabilities, such as Kelvin-Helmholtz instability (KHI), at the interface between strata. Finally, the amplification of vertical gradients through strain interaction and the development of overturning regions, often identified in terms of Richardson number [72], results in extreme events generating small-scale vortical motions with a mechanism which resembles what happens in the atmosphere with baroclinic instabilities. Nowadays weather and climate embed complex modeling through the parameterization of the unresolved small scales, on which depends the capability of the model to make predictions of the dynamical state of the system. Therefore, a deeper understanding of the link between small-scale intermittency and large-scale enhancement of vertical velocity and buoyancy is crucial to develop more accurate sub-grid models, reproducing more phenomena, such as strong vertical shear layers, vertical drafts and others.
4. As it is shown throughout the manuscript, vertical drafts provide a direct contribution to the energy transfer in stratified flows. This behavior is pretty consistent for different values of the Froude number in a range of geophysical interest, $Fr \approx 0.04 - 0.15$, while the presence and intensity of extreme events is modulated in the same interval. The capability of stratified flows to transfer energy approximately in the same range of scale, with a mechanism mediated by the vertical drafts, is something that should be taken into account in modeling the energy transfer in geophysical flows.

In the last chapter of this manuscript we presented the preliminary results of the implementation of machine learning (ML) methods for the low-dimensional representation of the velocity and temperature fields in stratified turbulent flows, with a particular focus on the reconstruction of the statistics up to the fourth-order moment, in direct numerical simulation. The main goal of this analysis is to develop a tool combining ML algorithms with physical constraints to investigate the dynamics

of these turbulent frameworks optimizing the use of both numerical simulations and experimental data. Indeed, as we explain in the text, the possibility to extract richer information as well as of performing accurate predictions of the dynamical state of these systems, from sparse and/or heterogeneous data, is crucial in a variety of contexts such as the weather forecasting, space weather and climatology.

There is a broad range of turbulent systems, from geophysical fluids to space plasmas, with varying characteristic parameters, some involving additional physical processes and phenomena, to which the approaches and tools presented here could be successfully applied, extending the results obtained in this thesis. Some of them would require running direct numerical simulation at higher resolution, allowing for a more comprehensive analysis of the behavior of large-scale intermittency at higher Reynolds number, and therefore a larger buoyancy Reynolds $R_B = \text{ReFr}^2$, characteristic of the troposphere, for instance. Other parameters which would be worth investigating, which are relevant to the emergence of vertical drafts, are of course the forcing and the aspect ratio in the simulations domain. Among the physical processes to consider, there is certainly rotation, important to describe the dynamics of the Earths' atmosphere at large scale and of the oceans. As a reference, considering $\Omega \approx 10^{-4} \text{s}^{-1}$ as the Earths' rotation frequency at mid latitudes, the ratio of rotation-over-stratification (N/f , where $f = 2\Omega$) is 10 in the ocean, and more than one order of magnitude larger in the atmosphere (100). That means rotation at small Rossby numbers (with $Ro = U_{rms}/[fL_{int}]$) can play a role in the development of large-scale and small-scale intermittency. However, considering extra term in the equations would come with additional computational cost since, in the presence of forcing, both a direct and inverse cascade of energy develops for small Ro , and thus it may be necessary to introduce a large-scale friction mechanism to prevent the pile-up of energy at those scales, especially for long integration times as in Feraco et al. [72], Marino et al. [139] or using much larger grids. The framework we developed can be applied to study a variety of intermittent phenomena, transients and non-homogeneous turbulent flows, having potentially a vast range of applications, involving the analysis of observational and laboratory data, which did not concern this thesis. For instance, we mentioned that the SF could be use to elucidate the

dynamics of the extreme events robserved in the mesosphere-lower-thermosphere (MLT) [49], as well as that of switchbacks in the heliospheric plasma [205] and the magnetic reconnection processes developing in the Earths' magnetosphere [132].

Appendices

Appendix A

Space-Filter analysis of reconnection events in 2D3V hybrid Vlasov-Maxwell simulation

We show the versatility of the space-filtering (SF) approach to 2D3V (2 dimensions, 3 vector components) plasma simulations at kinetic scales to understand the characteristics of the processes allowing the energy cascade from large (or injection) to small (or dissipation) scales in space plasma. Turbulence in those systems is non-collisional, multi-scale and multi-physics, being able to explore a large variety of physical regimes at different scales, and therefore it is significantly different from what observed in neutral fluids and fusion plasma, for example. Particularly relevant for space plasma turbulence is the formation of local-in-space *coherent* structures, such as current sheets and magnetic islands, showing enhanced small-scale features confirmed with both observations and simulations [e.g., 194, 91, 111, 166, 206, 229, 240, 48, 144, 13, 77, 171, 176, 177, 212, 221, 92, 38, 197, 12, 223]. In particular, an increasing attention has been focused on the scale smaller than the ion cyclotron radius $\rho_i = v_{T_i}/\Omega_{ci}$, being v_{T_i} and Ω_{ci} the ion thermal speed and cyclotron frequency, respectively, also identified from phenomena faster than the

ion cyclotron period $1/\Omega_{ci}$, usually called kinetic scales. Indeed in the past decade, the study of this range has been possible thanks to increasingly accurate *in-situ* measurements [4, 192, 51, 33, 50, 224], but also with direct numerical simulation with particle-in-cell (PIC) [44, 79] and (hybrid) Vlasov-Maxwell, (H)VM [131, 211], codes being able to simultaneously solve both the MHD and kinetic regime at the cost of a huge computational impact in terms of memory and time. The commonly adopted idea of full turbulent cascade in space plasmas is that quasi-2D Alfvénic modes feed the energy transfer in the MHD regime [143, 18] whereas range dispersive fluctuations dominate at the ion kinetic range [199, 84, 54, 96, 193, 23, 24]. However, at sub-ion scales the role of current sheets and of magnetic reconnection producing non-linear interactions local in the physical space needs to be taken into account in this picture. In this context, the effect of the aforementioned structures and in particular the disruption of current sheets due to magnetic reconnection, as possible mechanism mediating the energy transfer in plasma turbulence as well as heating, accelerating particles and creating sub-ion instabilities, has been extensively studied [43, 22, 123, 129, 130, 45, 78, 40, 55, 65, 215, 170, 133, 132]. As we widely showed in this manuscript, an effective approach in order to observe the effect of particular physical mechanisms simultaneously in the physical and spectral space is provided by the space-filtering (SF) technique. Despite the large use for neutral fluid turbulence, the SF has not received the same attention in the plasma physics community, with a few exceptions in recent years [e.g., 236, 40, 68, 109]. In particular, in the context of 2D3V PIC simulations, Yang et al. [236] found, using the SF approach, a qualitative correspondence between the coherent structures and spatial location of enhanced energy transfer. In the present work we exploit the space-filtered equations provided in Cerri and Camporeale [46], representing a finer description than the original application to the MHD and Hall-MHD plasmas [e.g., 133] but coarser than the six-dimensional phase-space kinetic description [68]. The SF technique is applied to a hybrid-kinetic simulation where the Vlasov equation for the ion distribution function is coupled to a neutral fluid responsive to a generalized Ohm’s law and representing mass-less electrons. On one hand, the hybrid Vlasov-Maxwell (HVM) represents an acceptable trade-off between partially interpreting the effects due to the electron-ion

coupling and the complexity and computational impact of the various terms arising from the filtering operation. A qualitative picture of the energy transfer at sub-ion scales on the same HVM plasma simulation was originally proposed in Franci et al. [78] (see their Fig 4), while in Cerri and Califano [45] the authors partially correlate the presence of magnetic reconnection and the enhancement of small-scale turbulence. In the following analysis we will show how the occurrence and intensity of magnetic reconnection events: (i) triggers an enhanced total energy transfer across ion scales, and (ii) drives simultaneously a direct (to smaller scale) and inverse (to larger scale) energy transfer developing within the sub-ion range.

Evidence of dual energy transfer driven by magnetic reconnection at sub-ion scales

Raffaello Foldes,^{1,2,*} Silvio Sergio Cerri,^{3,†} Raffaele Marino,^{1,‡} and Enrico Camporeale^{4,§}

¹*Université de Lyon, CNRS, École Centrale de Lyon,
INSA de Lyon, Université Claude Bernard Lyon 1,
Laboratoire de Mécanique des Fluides et d'Acoustique, F-69134 Écully, France*

²*Dipartimento di Scienze Fisiche e Chimiche,
Università dell'Aquila, 67100 Coppito (AQ), Italy*

³*Université Côte d'Azur, Observatoire de la Côte d'Azur,
CNRS, Laboratoire Lagrange, Bd de l'Observatoire,
CS 34229, 06304 Nice cedex 4, France*

⁴*CIRES, University of Colorado & NOAA Space Weather Prediction Center, Boulder, CO, USA*

(Dated: February 6, 2023)

The properties of energy transfer in the kinetic range of plasma turbulence have fundamental implications on the turbulent heating of space and astrophysical plasmas. It was recently proposed that magnetic reconnection may be responsible for driving the sub-ion scale cascade, and that this process would be characterized by a direct energy transfer towards even smaller scales (until dissipation), and a simultaneous inverse transfer of energy towards larger scales, until the ion break. Here we employ the space-filter technique on high-resolution 2D3V hybrid-Vlasov simulations of continuously driven turbulence providing for the first time quantitative evidence that magnetic reconnection is indeed able to trigger a dual energy transfer originating at sub-ion scales.

Introduction.—Kinetic-scale plasma turbulence is a topic that has seen a surge of interest in the past decade, since increasingly accurate *in-situ* measurements in such range have become available[1–6]. In this context, a transition between magnetohydrodynamic and kinetic regimes occurs when the turbulent energy reaches ion scales as a result of a forward cascade process. An extensive numerical campaign has been recently performed in order to better understand the properties of turbulence and plasma heating across and below the so-called *ion break*, targeting the interplanetary medium[7–21]. Based on these recent simulation results, it has been speculated that *magnetic reconnection* might be at the origin of the observed ion-break formation driving the subsequent sub-ion scale cascade[22, 23]. Such conjecture has been supported both by theoretical arguments[24–27] and, at least partially,

by solar-wind observations[28]. Since then, *tearing-mediated turbulence* has been the subject of thorough numerical investigations[29–34]. Yet, the features of the energy transfer across and below the ion scales, in a tearing-mediated scenario, remains rather unexplored. As we show in this letter, an effective approach in order to tackle potentially relevant physical mechanisms is provided by the so-called *space-filter technique*, originally developed in the context of hydrodynamics to perform ‘large-eddy simulations’[35, 36], and later on adopted as an investigative tool in plasma turbulence[37–47].

A qualitative picture of the energy transfer in the kinetic range for the tearing-mediated regime was originally proposed in [23] (see their Fig.4). In that work, the interaction between large-scale vortices feeding the formation of strong current sheets at their boundaries, quickly destroyed by the plasmoid in-

stability, was interpreted as a non-local transfer of energy from the large scales (of the vortices) directly to sub-ion scales (of the order of the thickness of the reconnecting layer). Moreover, the continuous formation of small-scale magnetic islands (*plasmoids*) and their subsequent merging to form structures at increasingly large scales, was interpreted as a dual transfer of energy: a direct transfer of reconnection-induced fluctuations towards smaller scales until dissipation, and a simultaneous inverse transfer towards the ion break due to the plasmoid growth by island coalescence. This picture has remained a cartoon until now.

In this Letter, 2D3V hybrid-kinetic simulations of continuously driven turbulence are analyzed through the implementation of space-filter technique, which allows to investigate the (local and non-local) energy transfer through scales as a function of spatial location and time. We will show how the occurrence of magnetic reconnection: (i) triggers a consistent energy transfer across ion scales, and (ii) drives a dual (inverse and direct) transfer developing within the sub-ion range.

Method.—We analyze the 2D3V hybrid-Vlasov-Maxwell (HVM) simulation of continuously driven turbulence in a $\beta_i = \beta_e = 1$ plasma presented in Ref.[22]. The HVM model evolves fully kinetic ions, solving the Vlasov equation for their distribution function $f_i(\mathbf{x}, \mathbf{v}, t)$, and fluid electrons through a generalized Ohm's law in the quasi-neutral approximation $n_i = n_e \doteq n$ (displacement current in the Ampère's law is neglected). The simulation employs 1024^2 grid points in real space, spanning a wavenumber range (in ion inertial length units d_i) $0.1 \leq kd_i \leq 51.2$, where $k = k_\perp = (k_x^2 + k_y^2)^{1/2}$. The external forcing in the Vlasov equation continuously injects ion-momentum fluctuations in the range $0.1 \leq k_{\text{ext}}d_i \leq 0.2$; small-amplitude magnetic-field perturbations $\delta\mathbf{B}$ in the range $0.1 \leq k_{\delta B}d_i \leq 0.3$ are also initialized at $t = 0$. Results from this HVM simulation were

used to first conjecture about the existence of a sub-ion-scale tearing-mediated range[22]; they were later accompanied by the hybrid-PIC simulation of Ref.[7] to confirm such conjecture[23]. Despite fluctuations' properties have been thoroughly analyzed[48], a detailed analysis of the turbulent energy transfer based on this high-resolution numerical simulation had to await the development of proper space-filter formalism and diagnostics for hybrid-kinetic models[43].

In the following, a filtered vector field $\tilde{\mathbf{V}}(\mathbf{x}, t)$ denotes the convolution of $\mathbf{V}(\mathbf{x}, t)$ with a filter φ , i.e., $\tilde{\mathbf{V}}(\mathbf{x}, t) \doteq \int_\Omega \varphi(x - \xi)\mathbf{V}(\mathbf{x}, t)d\xi$ over the domain Ω . Here, we adopt the low-pass Butterworth filter, which in Fourier space reads $\varphi_k = 1/[1 + (k/k_*)^8]$ with k_* ($\sim \ell_*^{-1}$) being the characteristic filtering wavenumber (scale). The Favre filter of \mathbf{V} is $\hat{\mathbf{V}} \doteq \tilde{\varrho}\tilde{\mathbf{V}}/\tilde{\varrho}$, where ϱ is the mass density. Filtered equations for the energy channels in general quasi-neutral hybrid-kinetic models are presented in Ref. [43]. When dissipation and external injection can be neglected in the HVM model with massless, isothermal electrons, these equations read

$$\frac{\partial\langle\hat{\mathcal{E}}_{u_i}\rangle}{\partial t} = \langle\hat{\Phi}_{u_i,B}\rangle + \langle\hat{\Phi}_{u_i,\Pi_i}\rangle - \langle\mathcal{S}_{u_i}\rangle, \quad (1)$$

$$\frac{\partial\langle\hat{\mathcal{E}}_{\Pi_i}\rangle}{\partial t} = -\langle\hat{\Phi}_{u_i,\Pi_i}\rangle - \langle\mathcal{S}_{\Pi_i}\rangle, \quad (2)$$

$$\frac{\partial\langle\hat{\mathcal{E}}_B\rangle}{\partial t} = \langle\hat{\mathcal{I}}_e\rangle - \langle\hat{\Phi}_{u_i,B}\rangle - \langle\mathcal{S}_B\rangle, \quad (3)$$

where $\langle\dots\rangle$ denotes a spatial average, $\hat{\mathcal{E}}_{u_i} = \frac{1}{2}\tilde{\varrho}|\hat{\mathbf{u}}_i|^2$, $\hat{\mathcal{E}}_{\Pi_i} = \frac{1}{2}\text{tr}[\hat{\Pi}_i]$, and $\hat{\mathcal{E}}_B = |\hat{\mathbf{B}}|^2/8\pi$ are the ion-kinetic, ion-thermal, and magnetic energy densities at scales $\ell \geq \ell_*$, respectively ($\hat{\Pi}_i$ is the ion-pressure tensor and \mathbf{u}_i is the ion-bulk flow, both obtained as \mathbf{v} -space moments of f_i). The injection-like term $\hat{\mathcal{I}}_e \doteq \tilde{P}_e(\nabla \cdot \hat{\mathbf{u}}_e)$ involving scales $\ell \geq \ell_*$ is due to the isothermal-electron condition $P_e = nT_{0,e}$. The terms $\hat{\Phi}_{u_i,B} \doteq \hat{\mathbf{j}}_i \cdot \hat{\mathbf{E}}$ (where $\hat{\mathbf{j}}_i = e\tilde{n}\hat{\mathbf{u}}_i$) and $\hat{\Phi}_{u_i,\Pi_i} \doteq \tilde{\Pi}_i : \nabla\hat{\mathbf{u}}_i$ represent energy exchange (i.e., conversion) between different channels (occurring at scales

$\ell \geq \ell_*$). Finally, the source/sink terms representing the (local and non-local) energy transfer between large ($k < k_*$) and small ($k > k_*$) scales through the filtering scale $k_* \sim \ell_*^{-1}$ are

$$\mathcal{S}_{u_i} \doteq \widehat{\mathbf{j}}_i \cdot \boldsymbol{\epsilon}_{\text{MHD}}^* - \mathcal{T}_{uu}^{(i)} : \nabla \widehat{\mathbf{u}}_i, \quad (4)$$

$$\mathcal{S}_{\Pi_i} \doteq \mathcal{T}_{\Pi \nabla u}^{(i)}, \quad (5)$$

$$\mathcal{S}_B \doteq \widehat{\mathbf{j}}_e \cdot (\boldsymbol{\epsilon}_{\text{MHD}}^* + \boldsymbol{\epsilon}_{\text{Hall}}^*) + \mathbf{j}^* \cdot \widehat{\mathbf{E}}, \quad (6)$$

where $\widehat{\mathbf{j}}_e = -e\tilde{n}\widehat{\mathbf{u}}_e = \widetilde{\mathbf{J}} - e\tilde{n}\widehat{\mathbf{u}}_i$ (with $\widetilde{\mathbf{J}} = \frac{c}{4\pi} \nabla \times \widehat{\mathbf{B}}$), and we have introduced the ‘‘turbulent’’ electric fields and current density at scales $\ell < \ell_*$, $\boldsymbol{\epsilon}_{\text{MHD}}^* = -\mathcal{T}_{u \times B}^{(i)}$, $\boldsymbol{\epsilon}_{\text{Hall}}^* = -\mathcal{T}_{J \times B}$, and $\mathbf{j}^* = \mathcal{T}_{nu}^{(i)} - \mathcal{T}_{nu}^{(e)} = \widehat{\mathbf{J}} - \widetilde{\mathbf{J}}$. The sign convention is such that $\mathcal{S} > 0$ denotes direct energy transfer from large to small scales, while $\mathcal{S} < 0$ means inverse transfer from small to large scales. The ‘‘sub-grid’’ terms \mathcal{T} associated to nonlinearities are given by $\mathcal{T}_{uu}^{(i)} \doteq \widehat{\varrho}(\widehat{\mathbf{u}}_i \widehat{\mathbf{u}}_i - \widehat{\mathbf{u}}_i \widehat{\mathbf{u}}_i)$, $\mathcal{T}_{u \times B}^{(i)} \doteq \frac{1}{c}(\widehat{\mathbf{u}}_i \times \widehat{\mathbf{B}} - \widehat{\mathbf{u}}_i \times \widehat{\mathbf{B}})$, $\mathcal{T}_{\Pi \nabla u}^{(i)} \doteq \overline{\Pi_{i,jk} \partial_k u_{i,j}} - \widetilde{\Pi_{i,jk} \partial_k \widehat{u}_{i,j}}$, $\mathcal{T}_{J \times B} \doteq \frac{m_i}{ec} \frac{1}{\varrho}(\widehat{\mathbf{J}} \times \widehat{\mathbf{B}} - \widetilde{\mathbf{J}} \times \widetilde{\mathbf{B}})$, and $\mathcal{T}_{nu}^{(\alpha)} \doteq \widehat{n} \widehat{\mathbf{u}}_\alpha - \widetilde{n} \widehat{\mathbf{u}}_\alpha$. The corresponding equation for the (filtered) total energy $\widehat{\mathcal{E}} = \widehat{\mathcal{E}}_{u_i} + \widehat{\mathcal{E}}_{\Pi_i} + \widehat{\mathcal{E}}_B$ is $\partial_t \langle \widehat{\mathcal{E}} \rangle = \langle \widehat{\mathcal{I}}_e \rangle - \langle \mathcal{S}_{\text{tot}} \rangle$, where $\mathcal{S}_{\text{tot}} = \mathcal{S}_{u_i} + \mathcal{S}_{\Pi_i} + \mathcal{S}_B$. In the following, we focus our analysis on the terms \mathcal{S} , representing the actual transfer through scales.

Results.—The simulation exhibits two noteworthy times (in inverse ion-cyclotron frequency units $\Omega_{c,i}^{-1}$): the time of first reconnection events $t_{\text{rec}} \approx 135$, and the time marking the transition to quasi-steady turbulence $t_{\text{qst}} \approx 200$ [23]). Here we analyze the same three times belonging to the stages separated by the above-mentioned times, i.e., $t \simeq 120$, $\simeq 150$, and $\simeq 228$.

Fig.1 shows contours of the out-of-plane current density normalized to its standard deviation J_z/σ_{J_z} (first column) at the above-mentioned times (top to bottom row, respectively), alongside contours of the total energy transfer $\mathcal{S}_{\text{tot}}/\sigma_{\mathcal{S}_{\text{tot}}}$ (also normalized by its standard deviation) through three representative wavenumbers $k_\perp d_i = 1.5, = 5.5,$

and $= 13$ (second, third and fourth column, respectively). Although the normalization of \mathcal{S}_{tot} in Fig.1 prevents a quantitative analysis of how much energy is transferred during these three different stages, it allows to highlight some key qualitative features. First, as k increases, the energy transfer becomes significantly less volume filling and simultaneously more localized within strong current structures and magnetic islands [41, 42]. Second, we can observe that while at $kd_i \sim 1$ and $kd_i \sim 10$ the contribution to \mathcal{S}_{tot} is mainly positive (yellow-red colors), meaning direct transfer of total energy from the large to the small scales, at $kd_i \sim 5$ the total transfer is dominated by negative values (cyan-blue colors), which instead denotes an inverse energy flux from small to large scales.

In order to quantitatively assess the properties of energy transfer as a function of the scale, in what follows we focus on volume-averaged (i.e., global) quantities. This is shown in Fig.2, where we plot the total energy transfer and its components, i.e., $\langle \mathcal{S}_{\text{tot}} \rangle$, $\langle \mathcal{S}_B \rangle$, $\langle \mathcal{S}_{u_i} \rangle$, and $\langle \mathcal{S}_{\Pi_i} \rangle$ versus kd_i (top to bottom panel, respectively), at $t \simeq 120$, $\simeq 150$, and $\simeq 228$ (dotted, dashed and solid line, respectively). First of all, we note that the transfer \mathcal{S}_{tot} at $t \simeq 120$ (i.e., before the first reconnection events occur) is negligible with respect to the energy transfer occurring at later times (i.e., when magnetic-reconnection events continuously destroy the forming current sheets). This feature also holds for each energy channel separately and supports the interpretation of magnetic reconnection as the process that allows to achieve a fully developed turbulent state [22]. After the first reconnection events occur, there is a transitional stage (at $t \simeq 150$) over which the transfer of total energy $\langle \mathcal{S}_{\text{tot}} \rangle$ has significantly increased. This stage is overall characterized by forward flux at MHD scales ($\langle \mathcal{S}_{\text{tot}} \rangle \approx \text{const.} > 0$ for $kd_i \lesssim 0.8$) and by initial indications of a bi-directional transfer of the total energy at sub-ion scales. More precisely: a direct transfer ($\langle \mathcal{S}_{\text{tot}} \rangle > 0$) at

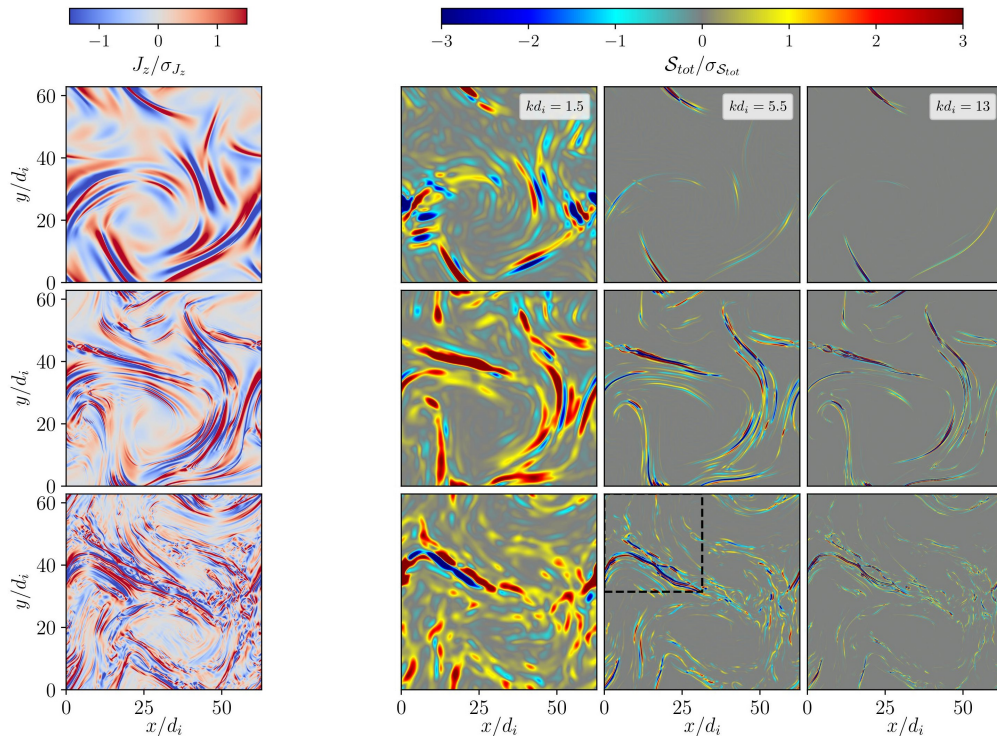


FIG. 1. Contours of the out-of-plane current density normalized to its standard deviation J_z/σ_{J_z} (first column) at times $t \simeq 120$, $\simeq 150$, and $\simeq 228$ (top to bottom row, respectively). Second, third, and fourth columns show contours of the normalized total energy transfer $\mathcal{S}_{tot}/\sigma_{\mathcal{S}_{tot}}$ through three representative wavenumbers $k_\perp d_i = 1.5$, 5.5 , and 13 , respectively. The dashed box in contour of $\mathcal{S}_{tot}/\sigma_{\mathcal{S}_{tot}}$ at $t \simeq 228$ (bottom row, third panel from the left) denotes the zoom analyzed in Fig.3.

$kd_i \gtrsim 7$ and an inverse transfer ($\langle \mathcal{S}_{tot} \rangle < 0$) in the range $4 \lesssim kd_i \lesssim 7$. In the quasi-steady state ($t > 200$) these ranges slightly adjust, settling down to a fully developed dual transfer, featuring an inverse flux at $3 \lesssim kd_i \lesssim 9$ and a direct flux at $kd_i \gtrsim 9$. Around ion scales ($0.8 \lesssim kd_i \lesssim 3$), the total-energy transfer also exhibits a peak. This feature is associated to significant conversion of ion-bulk energy $\widehat{\mathcal{E}}_{u_i}$ into ion-internal energy $\widehat{\mathcal{E}}_{\Pi_i}$ that is driven by the large-scale pressure-strain interaction $\widehat{\Phi}_{u_i, \Pi_i} = \widehat{\Pi}_i : \nabla \widehat{u}_i$ term (which has a bump at those scales; not shown) and boosts the transfer within the latter channel (mediated by the pressure-strain sub-grid nonlinearity $\mathcal{S}_{\Pi_i} = \mathcal{T}_{\Pi \nabla u}^{(i)}$; Fig.2d). This picture supports the idea that turbulent ion heating occurs mostly around $k_\perp \rho_i \sim 1$ and within the first few sub-ion scales[see, e.g.,

49, 50]. By looking at the different energy channels separately, one can notice a few interesting features. First, the actual transfer of magnetic energy $\langle \mathcal{S}_B \rangle$ is about two orders of magnitude smaller than the corresponding transfer of ion-bulk and ion-internal energy. A detailed inspection of the terms contributing to $\langle \mathcal{S}_B \rangle$ shows that this is dominated by the turbulent Hall electric field ϵ_{Hall}^* , while the turbulent current density \mathbf{j}^* is always negligible (i.e., in our simulation the ordering $|\mathbf{j}^* \cdot \widehat{\mathbf{E}}| \ll |\widehat{\mathbf{j}}_e \cdot \epsilon_{MHD}^*| \lesssim |\widehat{\mathbf{j}}_e \cdot \epsilon_{Hall}^*|$ always holds; not shown). The magnetic-energy channel is also showing only an inverse transfer of energy during the transition stage at $t \simeq 150$ (Fig.2b, dashed line), whereas in the quasi-steady state it exhibits only one sign inversion of the flux, with a direct transfer at $kd_i \gtrsim 3$ and an inverse

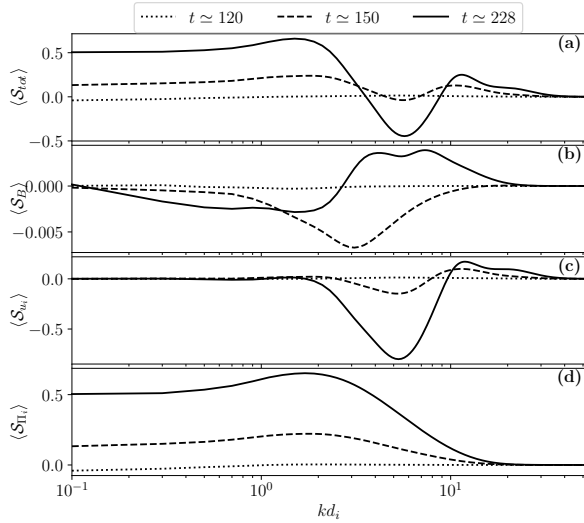


FIG. 2. Box-averaged turbulent energy transfer through scales at $t \simeq 120$ (dotted line), $t \simeq 150$ (dashed line), and $t \simeq 228$ (solid line). From top to bottom: total energy $\langle \mathcal{S}_{\text{tot}} \rangle$, magnetic energy $\langle \mathcal{S}_B \rangle$, ion-bulk energy $\langle \mathcal{S}_{u_i} \rangle$, and ion-internal energy $\langle \mathcal{S}_{\Pi_i} \rangle$, versus kd_i .

transfer at $kd_i \lesssim 3$, i.e., no direct cascade of magnetic energy is observed at large scales (Fig.2b, solid line). We attribute the direct transfer of magnetic energy towards smaller scales to the breakup of large-scale current structures by reconnection, while the negative flux of magnetic energy is likely due to the growth of magnetic-islands by coalescence. The absence of a MHD-range direct cascade of magnetic energy may be due to the limited range of fluid scales of the simulation and/or to the fact that the external forcing only injects ion-bulk energy. Another interesting feature is that the dual transfer of total energy at sub-ion scales seems to be driven by the ion-bulk-energy channel, i.e., by $\langle \mathcal{S}_{u_i} \rangle$ (Fig.2c). The only non-negligible contribution to such transfer is represented by the interaction between the “sub-grid” Reynolds stress tensor $\mathcal{T}_{uu}^{(i)}$ and the large-scale strain tensor $\hat{\Sigma} \doteq \nabla \hat{u}_i$, i.e., $\langle \mathcal{S}_{u_i} \rangle \approx \langle \mathcal{T}_{uu}^{(i)} : \nabla \hat{u}_i \rangle$ (not shown). Here we speculate that the emergence of an inverse transfer of ion-bulk energy from the above in-

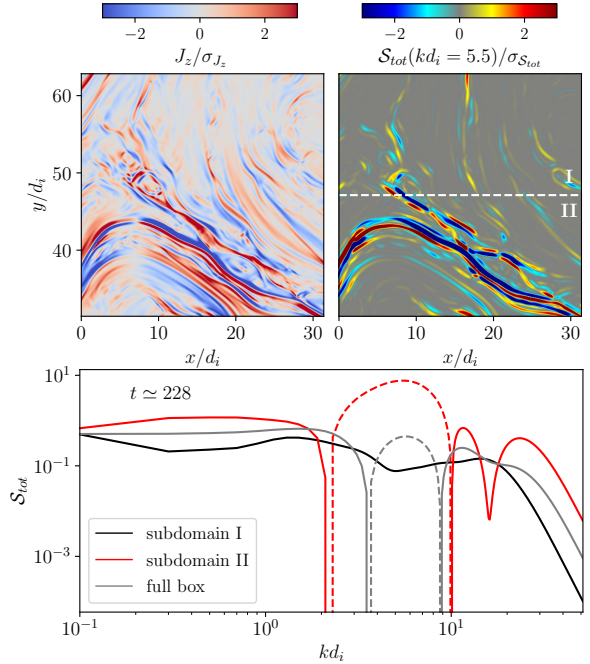


FIG. 3. Top panels: contour plots of J_z/σ_{J_z} (left panel) and of $\mathcal{S}_{\text{tot}}/\sigma_{\mathcal{S}_{\text{tot}}}$ computed at $kd_i = 5.5$ (right panel) in a sub-region of the simulation domain (dashed box in Fig.1). Bottom plot: total-energy transfer \mathcal{S}_{tot} averaged over subdomain I (black), over subdomain II (red), and over the whole simulation box (grey). Solid line means direct transfer ($\mathcal{S}_{\text{tot}} > 0$), while dashed line denotes inverse transfer ($\mathcal{S}_{\text{tot}} < 0$).

teraction might be the manifestation of the ion jets generated by “ion-coupled” magnetic reconnection[22] (as opposed to “electron-only” reconnection[51, 52]).

In order to show that the dual energy transfer is associated to reconnection events and actual magnetic-islands dynamics, we exploit the fact that \mathcal{S}_{tot} is defined in configuration space. We thus monitor the behavior of density current and flux terms in a sub-region of the entire simulation plane in the quasi-steady state, at $t \simeq 228$ (dashed box in Fig.1, bottom row, third column). The top panels of Fig.3 show the zoomed contour plots of J_z/σ_{J_z} (left panel) and of $\mathcal{S}_{\text{tot}}/\sigma_{\mathcal{S}_{\text{tot}}}$ computed at $kd_i = 5.5$ (right panel). This sub-region is then further divided into two subdo-

mains, “I” and “II”, of equal size (Fig.3, top left panel), to ensure statistical consistency. The upper subdomain I does not have significant reconnection sites and/or plasmoids, whereas the lower subdomain II includes one of the largest structure present in the simulation, showing a streak of reconnection sites and grown/merged magnetic islands. In the bottom panel of Fig.3 we then report the total-energy transfer \mathcal{S}_{tot} averaged over subdomain I (black) and subdomain II (red) separately, and over the whole simulation box (grey). Solid lines are used to denote direct transfer ($\mathcal{S}_{\text{tot}} > 0$), while dashed lines denote inverse transfer ($\mathcal{S}_{\text{tot}} < 0$). It is remarkable how, when averaged over subdomain I (Fig.3, black curve), the transfer of total energy would emerge only as a direct transfer at any k . On the contrary, when we consider subdomain II (Fig.3, red curve), the dual transfer at sub-ion scales clearly emerges and is similar to the one obtained from the global picture (Fig.3, grey curve), suggesting a dominance of the points coming from subdomain II in the overall statistics. Moreover, the transfer rate is clearly larger in subdomain II than in subdomain I, and thus represents the major contribution to the global energy transfer. An analogous result holds if the average of the total transfer \mathcal{S}_{tot} is conditioned over different intervals of $|J_z/\sigma_{J_z}|$ (not shown). This study clearly demonstrate, within the constraints of the high-resolution run analyzed, that the dual transfer observed globally is indeed an intermittent feature associated to local dynamics driven by patches of magnetic reconnection, that make the plasma non-homogeneous.

Conclusions.— Exploiting the space-filter techniques, we have shown for the first time, that magnetic reconnection and the consequent island dynamics is associated with (i) the enhancement of the energy transfer across the scales, the onset of a quasi-steady turbulent state, and (ii) the emergence of a dual (direct and inverse) transfer of energy originating from sub-ion scales. Once such quasi-

steady state is attained, the observed bidirectional energy flux is globally characterized by a direct transfer towards smaller scales at $k_{\perp}d_i \gtrsim 9$ and a simultaneous inverse transfer in the range $3 \lesssim k_{\perp}d_i \lesssim 9$. Although in our simulations the magnetic-energy channel exhibits as well a dual transfer (which is dominated by the interaction between the large-scale electron-current density and the “turbulent” Hall electric field $\hat{\mathbf{j}}_e \cdot \boldsymbol{\epsilon}_{\text{Hall}}^*$), its contribution to the total-energy transfer is negligible with respect to the one coming from the ion-bulk and ion-internal channels. The sub-ion-scale dual transfer of total energy that emerges globally is driven by the ion-bulk-energy channel, which is dominated by the interaction between the large-scale strain tensor and the “turbulent” Reynolds stress $\mathcal{T}_{uu}^{(i)} : \nabla \hat{\mathbf{u}}_i$ (and is likely a consequence of ion jets triggered by “ion-coupled” magnetic reconnection). The MHD-scale direct cascade is driven by the ion-internal-energy channel, which is dominated by the “turbulent” pressure-strain interaction $\mathcal{T}_{\text{II}\nabla u}^{(i)}$ (and shows signatures of ion turbulent heating across a limited range of scales around $k_{\perp}d_i \sim 1$).

The existence of a simultaneous direct and inverse transfer at sub-ion scales driven by magnetic reconnection may have fundamental implications on our understanding of turbulent ion heating in the solar wind, especially in the context of the so-called “helicity barrier” [20, 21, 53, 54]. Moreover, the fact that this sub-ion-scale dual transfer seems to require “ion-coupled” magnetic reconnection (in order to form ion outflows) can feed back significantly on the species’ turbulent heating in the presence of “electron-only” reconnection [51, 52] and, thus, on the heating of the Earth’s magnetosheath [55, 56].

R.M. and R.F. acknowledge support from the project “EVENTFUL” (ANR-20-CE30-0011), funded by the French “Agence Nationale de la Recherche” - ANR through the program AAPG-2020. E.C. is partially funded by NASA grant 80NSSC20K1275.

-
- * raffaello.foldes@ec-lyon.fr
† silvio.cerri@oca.eu
‡ raffaele.marino@ec-lyon.fr
§ enrico.camporeale@noaa.gov
- [1] O. Alexandrova, J. Saur, C. Lacombe, A. Mangeney, J. Mitchell, S. J. Schwartz, and P. Robert, Universality of Solar-Wind Turbulent Spectrum from MHD to Electron Scales, *PhRvL* **103**, 165003 (2009), arXiv:0906.3236 [physics.plasm-ph].
- [2] F. Sahraoui, M. L. Goldstein, P. Robert, and Y. V. Khotyaintsev, Evidence of a Cascade and Dissipation of Solar-Wind Turbulence at the Electron Gyroscale, *PhRvL* **102**, 231102 (2009).
- [3] C. H. K. Chen, T. S. Horbury, A. A. Schekochihin, R. T. Wicks, O. Alexandrova, and J. Mitchell, Anisotropy of Solar Wind Turbulence between Ion and Electron Scales, *PhRvL* **104**, 255002 (2010), arXiv:1002.2539 [physics.space-ph].
- [4] R. Bruno and D. Telloni, Spectral Analysis of Magnetic Fluctuations at Proton Scales from Fast to Slow Solar Wind, *Astrophys. J. Lett.* **811**, L17 (2015), arXiv:1509.04866 [astro-ph.SR].
- [5] C. H. K. Chen and S. Boldyrev, Nature of Kinetic Scale Turbulence in the Earth's Magnetosheath, *Astrophys. J.* **842**, 122 (2017), arXiv:1705.08558 [physics.space-ph].
- [6] T. Wang, J. He, O. Alexandrova, M. Dunlop, and D. Perrone, Observational Quantification of Three-dimensional Anisotropies and Scalings of Space Plasma Turbulence at Kinetic Scales, *Astrophys. J.* **898**, 91 (2020), arXiv:2006.02722 [physics.space-ph].
- [7] L. Franci, S. Landi, L. Matteini, A. Verdini, and P. Hellinger, High-resolution Hybrid Simulations of Kinetic Plasma Turbulence at Proton Scales, *Astrophys. J.* **812**, 21 (2015), arXiv:1506.05999 [astro-ph.SR].
- [8] T. N. Parashar, W. H. Matthaeus, M. A. Shay, and M. Wan, Transition from Kinetic to MHD Behavior in a Collisionless Plasma, *Astrophys. J.* **811**, 112 (2015).
- [9] S. S. Cerri, F. Califano, F. Jenko, D. Told, and F. Rincon, Subproton-scale Cascades in Solar Wind Turbulence: Driven Hybrid-kinetic Simulations, *Astrophys. J. Lett.* **822**, L12 (2016), arXiv:1604.07674 [physics.plasm-ph].
- [10] L. Franci, S. Landi, L. Matteini, A. Verdini, and P. Hellinger, Plasma Beta Dependence of the Ion-scale Spectral Break of Solar Wind Turbulence: High-resolution 2D Hybrid Simulations, *Astrophys. J.* **833**, 91 (2016), arXiv:1610.05158 [physics.space-ph].
- [11] S. S. Cerri, S. Servidio, and F. Califano, Kinetic Cascade in Solar-wind Turbulence: 3D3V Hybrid-kinetic Simulations with Electron Inertia, *Astrophys. J. Lett.* **846**, L18 (2017), arXiv:1707.08429 [physics.plasm-ph].
- [12] D. Grošelj, S. S. Cerri, A. Bañón Navarro, C. Willmott, D. Told, N. F. Loureiro, F. Califano, and F. Jenko, Fully Kinetic versus Reduced-kinetic Modeling of Collisionless Plasma Turbulence, *Astrophys. J.* **847**, 28 (2017), arXiv:1706.02652 [physics.plasm-ph].
- [13] S. S. Cerri, M. W. Kunz, and F. Califano, Dual Phase-space Cascades in 3D Hybrid-Vlasov-Maxwell Turbulence, *Astrophys. J. Lett.* **856**, L13 (2018), arXiv:1802.06133 [physics.plasm-ph].
- [14] D. Grošelj, A. Mallet, N. F. Loureiro, and F. Jenko, Fully Kinetic Simulation of 3D Kinetic Alfvén Turbulence, *Phys. Rev. Lett.* **120**, 105101 (2018), arXiv:1710.03581 [physics.plasm-ph].
- [15] D. Perrone, T. Passot, D. Laveder, F. Valentini, P. L. Sulem, I. Zouganelis, P. Veltri, and S. Servidio, Fluid simulations of plasma turbulence at ion scales: Comparison with Vlasov-Maxwell simulations, **25**, 052302 (2018), arXiv:1804.01312

- [physics.plasm-ph].
- [16] L. Arzamasskiy, M. W. Kunz, B. D. G. Chandran, and E. Quataert, Hybrid-kinetic Simulations of Ion Heating in Alfvénic Turbulence, *Astrophys. J.* **879**, 53 (2019), arXiv:1901.11028 [astro-ph.HE].
- [17] S. S. Cerri, D. Grošelj, and L. Franci, Kinetic plasma turbulence: recent insights and open questions from 3D3V simulations, *Front. Astron. Space Sci.* **6**, 64 (2019), arXiv:1909.11525 [astro-ph.SR].
- [18] D. Grošelj, C. H. K. Chen, A. Mallet, R. Samtaney, K. Schneider, and F. Jenko, Kinetic Turbulence in Astrophysical Plasmas: Waves and/or Structures?, *Phys. Rev. X* **9**, 031037 (2019), arXiv:1806.05741 [physics.plasm-ph].
- [19] S. S. Cerri, L. Arzamasskiy, and M. W. Kunz, On Stochastic Heating and Its Phase-space Signatures in Low-beta Kinetic Turbulence, *Astrophys. J.* **916**, 120 (2021), arXiv:2102.09654 [astro-ph.SR].
- [20] T. Passot, P. L. Sulem, and D. Laveder, Direct kinetic Alfvén wave energy cascade in the presence of imbalance, *Journal of Plasma Physics* **88**, 905880312 (2022), arXiv:2205.03292 [physics.space-ph].
- [21] J. Squire, R. Meyrand, M. W. Kunz, L. Arzamasskiy, A. A. Schekochihin, and E. Quataert, High-frequency heating of the solar wind triggered by low-frequency turbulence, *Nature Astronomy* 10.1038/s41550-022-01624-z (2022), arXiv:2109.03255 [astro-ph.SR].
- [22] S. S. Cerri and F. Califano, Reconnection and small-scale fields in 2D-3V hybrid-kinetic driven turbulence simulations, *New J. Phys.* **19**, 025007 (2017).
- [23] L. Franci, S. S. Cerri, F. Califano, S. Landi, E. Papini, A. Verdini, L. Matteini, F. Jenko, and P. Hellinger, Magnetic Reconnection as a Driver for a Sub-ion-scale Cascade in Plasma Turbulence, *Astrophys. J. Lett.* **850**, L16 (2017), arXiv:1707.06548 [physics.space-ph].
- [24] S. Boldyrev and N. F. Loureiro, Magnetohydrodynamic Turbulence Mediated by Reconnection, *Astrophys. J.* **844**, 125 (2017), arXiv:1706.07139 [physics.plasm-ph].
- [25] N. L. Loureiro and S. Boldyrev, Collisionless reconnection in magnetohydrodynamic and kinetic turbulence, *Astrophys. J.* **850**, 182 (2017).
- [26] A. Mallet, A. A. Schekochihin, and B. D. G. Chandran, Disruption of sheet-like structures in Alfvénic turbulence by magnetic reconnection, *MNRAS* **468**, 4862 (2017).
- [27] A. Mallet, A. A. Schekochihin, and B. D. G. Chandran, Disruption of Alfvénic turbulence by magnetic reconnection in a collisionless plasma, *JPIPh* **83**, 905830609 (2017), arXiv:1707.05907 [physics.plasm-ph].
- [28] D. Vech, A. Mallet, K. G. Klein, and J. C. Kasper, Magnetic Reconnection May Control the Ion-scale Spectral Break of Solar Wind Turbulence, *Astrophys. J. Lett.* **855**, L27 (2018), arXiv:1803.00065 [physics.space-ph].
- [29] C. Dong, L. Wang, Y.-M. Huang, L. Comisso, and A. Bhattacharjee, Role of the Plasmoid Instability in Magnetohydrodynamic Turbulence, *Phys. Rev. Lett.* **121**, 165101 (2018), arXiv:1804.07361 [physics.plasm-ph].
- [30] E. Papini, L. Franci, S. Landi, A. Verdini, L. Matteini, and P. Hellinger, Can Hall Magnetohydrodynamics Explain Plasma Turbulence at Sub-ion Scales?, *Astrophys. J.* **870**, 52 (2019), arXiv:1810.02210 [physics.plasm-ph].
- [31] A. Tenerani and M. Velli, Spectral signatures of recursive magnetic field reconnection, *MNRAS* **491**, 4267 (2020), arXiv:1907.05243 [physics.space-ph].
- [32] D. Borgogno, D. Grasso, B. Achilli, M. Romé, and L. Comisso, Coexistence of Plasmoid and Kelvin-Helmholtz Instabilities in Collisionless Plasma Turbulence, *Astrophys. J.* **929**, 62 (2022).
- [33] C. Dong, L. Wang, Y.-M. Huang, L. Comisso, T. A. Sandstrom, and A. Bhat-

- tacharjee, Reconnection-Driven Energy Cascade in Magnetohydrodynamic Turbulence, arXiv e-prints , arXiv:2210.10736 (2022), arXiv:2210.10736 [astro-ph.SR].
- [34] S. S. Cerri, T. Passot, D. Laveder, P. L. Sulem, and M. W. Kunz, Turbulent Regimes in Collisions of 3D Alfvén-wave Packets, *Astrophys. J.* **939**, 36 (2022).
- [35] M. Germano, Turbulence: the filtering approach, *J. Fluid Mech.* **238**, 325 (1992).
- [36] C. Meneveau and J. Katz, Scale-Invariance and Turbulence Models for Large-Eddy Simulation, *Annual Review of Fluid Mechanics* **32**, 1 (2000).
- [37] H. Aluie and G. L. Eyink, Scale locality of magnetohydrodynamic turbulence, *Phys. Rev. Lett.* **104**, 081101 (2010).
- [38] P. Morel, A. B. Navarro, M. Albrecht-Marc, D. Carati, F. Merz, T. Görler, and F. Jenko, Gyrokinetic large eddy simulations, *Physics of Plasmas* **18**, 072301 (2011), arXiv:1104.2422 [physics.plasm-ph].
- [39] M. Miesch, W. Matthaeus, A. Brandenburg, A. Petrosyan, A. Pouquet, C. Cambon, F. Jenko, D. Uzdensky, J. Stone, S. Tobias, J. Toomre, and M. Velli, Large-Eddy Simulations of Magnetohydrodynamic Turbulence in Heliophysics and Astrophysics, *Space Sci. Rev.* **194**, 97 (2015), arXiv:1505.01808 [astro-ph.SR].
- [40] Y. Yang, W. H. Matthaeus, T. N. Parashar, P. Wu, M. Wan, Y. Shi, S. Chen, V. Roytershteyn, and W. Daughton, Energy transfer channels and turbulence cascade in Vlasov-Maxwell turbulence, *Phys. Rev. E* **95**, 061201 (2017).
- [41] Y. Yang, W. H. Matthaeus, T. N. Parashar, C. C. Haggerty, V. Roytershteyn, W. Daughton, M. Wan, Y. Shi, and S. Chen, Energy transfer, pressure tensor, and heating of kinetic plasma, **24**, 072306 (2017), arXiv:1705.02054 [physics.plasm-ph].
- [42] E. Camporeale, L. Sorriso-Valvo, F. Califano, and A. Retinò, Coherent Structures and Spectral Energy Transfer in Turbulent Plasma: A Space-Filter Approach, *Physical Review Letters* **120**, 125101 (2018), arXiv:1711.00291 [physics.plasm-ph].
- [43] S. S. Cerri and E. Camporeale, Space-filter techniques for quasi-neutral hybrid-kinetic models, *Physics of Plasmas* **27**, 082102 (2020), arXiv:2005.03130 [physics.plasm-ph].
- [44] S. Adhikari, T. N. Parashar, M. A. Shay, W. H. Matthaeus, P. S. Pyakurel, S. Fordin, J. E. Stawarz, and J. P. Eastwood, Energy transfer in reconnection and turbulence, *Phys. Rev. E* **104**, 065206 (2021), arXiv:2104.12013 [physics.plasm-ph].
- [45] A. Alexakis and S. Chibbaro, Local fluxes in magnetohydrodynamic turbulence, *Journal of Plasma Physics* **88**, 905880515 (2022).
- [46] G. Arró, F. Califano, and G. Lapenta, Spectral properties and energy transfer at kinetic scales in collisionless plasma turbulence, *A&A* **668**, A33 (2022), arXiv:2112.12753 [physics.plasm-ph].
- [47] D. Manzini, F. Sahraoui, and F. Califano, Sub-ion scale turbulence driven by magnetic reconnection, arXiv e-prints , arXiv:2208.00855 (2022), arXiv:2208.00855 [physics.plasm-ph].
- [48] S. S. Cerri, L. Franci, F. Califano, S. Landi, and P. Hellinger, Plasma turbulence at ion scales: a comparison between particle in cell and Eulerian hybrid-kinetic approaches, *J. Plasma Phys.* **83**, 705830202 (2017), arXiv:1703.02443 [physics.plasm-ph].
- [49] A. A. Schekochihin, S. C. Cowley, W. Dorland, G. W. Hammett, G. G. Howes, E. Quataert, and T. Tatsuno, Astrophysical Gyrokinetics: Kinetic and Fluid Turbulent Cascades in Magnetized Weakly Collisional Plasmas, *Astrophys. J. Suppl. Series* **182**, 310 (2009), arXiv:0704.0044.
- [50] B. D. G. Chandran, B. Li, B. N. Rogers, E. Quataert, and K. Germaschewski, Perpendicular Ion Heating by Low-frequency Alfvén-wave Turbulence in the Solar Wind, *Astrophys. J.* **720**, 503 (2010), arXiv:1001.2069 [astro-ph.SR].

- [51] P. Sharma Pyakurel, M. A. Shay, T. D. Phan, W. H. Matthaeus, J. F. Drake, J. M. TenBarge, C. C. Haggerty, K. G. Klein, P. A. Cassak, T. N. Parashar, M. Swisdak, and A. Chasapis, Transition from ion-coupled to electron-only reconnection: Basic physics and implications for plasma turbulence, *Physics of Plasmas* **26**, 082307 (2019), arXiv:1901.09484 [physics.space-ph].
- [52] F. Califano, S. S. Cerri, M. Faganello, D. Laveder, M. Sisti, and M. W. Kunz, Electron-only reconnection in plasma turbulence, *Front. Phys.* **8**, 317 (2020).
- [53] T. Passot and P. L. Sulem, Imbalanced kinetic Alfvén wave turbulence: from weak turbulence theory to nonlinear diffusion models for the strong regime, arXiv e-prints (2019), arXiv:1902.04295 [physics.plasm-ph].
- [54] R. Meyrand, J. Squire, A. A. Schekochihin, and W. Dorland, On the violation of the zeroth law of turbulence in space plasmas, *Journal of Plasma Physics* **87**, 535870301 (2021), arXiv:2009.02828 [physics.space-ph].
- [55] T. D. Phan, J. P. Eastwood, M. A. Shay, J. F. Drake, B. U. Ö. Sonnerup, M. Fujimoto, P. A. Cassak, M. Øieroset, J. L. Burch, R. B. Torbert, A. C. Rager, J. C. Dorelli, D. J. Gershman, C. Pollock, P. S. Pyakurel, C. C. Haggerty, Y. Khotyaintsev, B. Lavraud, Y. Saito, M. Oka, R. E. Ergun, A. Retino, O. Le Contel, M. R. Argall, B. L. Giles, T. E. Moore, F. D. Wilder, R. J. Strangeway, C. T. Russell, P. A. Lindqvist, and W. Magnes, Electron magnetic reconnection without ion coupling in Earth's turbulent magnetosheath, *Nature (London)* **557**, 202 (2018).
- [56] J. E. Stawarz, J. P. Eastwood, T. D. Phan, I. L. Gingell, M. A. Shay, J. L. Burch, R. E. Ergun, B. L. Giles, D. J. Gershman, O. Le Contel, P. A. Lindqvist, C. T. Russell, R. J. Strangeway, R. B. Torbert, M. R. Argall, D. Fischer, W. Magnes, and L. Franci, Properties of the Turbulence Associated with Electron-only Magnetic Reconnection in Earth's Magnetosheath, *Astrophys. J. Lett.* **877**, L37 (2019).

Appendix B

Deep-FLRID: Machine Learning Algorithms for Automated Field Line Resonance Identification

The near-Earth environment is composed of different plasma populations that cover an energy range of several orders of magnitude. The plasmasphere is the innermost layer of the Earth's magnetosphere and it is composed of dense cold plasma ($\sim 1eV$), and it typically extends from the top of the ionosphere up to 4–6 Earth radii (R_E). Because of its preponderant contribution to the mass density in the magnetosphere, it plays a crucial role in exciting plasma-waves and driving their interaction with energetic particles [117, 207]. This makes the plasmasphere central in the space weather context, and therefore the real-time monitoring of the cold plasma in the inner magnetosphere would be an essential task to achieve. Several systems and tools have been developed, in particular, for monitoring the plasmaspheric mass density using ground-based magnetometers measurements, and all of them are based on the gradient method proposed by Baransky et al. [16] and further developed by Waters et al. [226]. This represents the most adopted and reliable technique to estimate the Field Line Resonance (FLR) frequency of magnetic field lines, based on the Fourier cross-spectral analysis of the magnetic signal recorded by two stations slightly separated in latitude. In this configuration,

it is possible to estimate the resonance frequency of the field line whose footprint is halfway between the stations. Indeed, around the FLR frequency and its higher harmonics the cross-phase presents a maximum and the amplitude ratio crosses one with a positive slope. One or both these characteristics can be used to identify FLR frequencies which, in turn, depend on the magnetic field strength and plasma mass density distribution along the field line. The importance of the FLR frequencies is that it allows, by making assumptions on the magnetic field topology and the field line plasma distribution, to solve the governing wave equation [196], providing an estimate of the plasma mass density in the equatorial crossing point of the field line. Based on the gradient method, several authors in the past developed algorithms to automatically detect FLRs based on the cross-phase and/or cross-amplitude or both. In these works, either statistical or morphological properties of the cross-spectra were used to individuate the resonance peaks. Berube et al. [17] and Chi et al. [53] used very similar statistical arguments to select eigenfrequencies based both on the phase difference and amplitude ratio, employing a t -statistic test to detect the peak associated with the most significant eigenfrequencies. In Lichtenberger et al. [115], the authors combine several features of the cross-spectra, such as the location of the inflection point in the amplitude ratio, the amplitude ratio at the inflection point, the magnitude of the phase difference, and others that all help to identify the FLR and to estimate the uncertainty in the detected frequency. Many of these procedures exploit the ultra-low frequency wave data measured by the magnetometer stations developed inside the PLASMON FP7 European project [115] during which the European quasi-Meridional Magnetometer Array (EMMA) was established (see Del Corpo et al. [61] and reference therein for more specifications on the EMMA network). EMMA consists of 27 ground-based magnetic stations approximately located along the same magnetic meridian and mapping into magnetic L -shells in the range 1.6–6.1, where L is the McIlwain parameter evaluated using the IGRF, providing a real-time monitoring of the plasmasphere dynamics. Using ULF signals simultaneously observed by pairs of stations it is possible to infer the radial distribution of the equatorial plasma mass density in the longitudinal sector identified by the network [61, 115].

Del Corpo et al. [61] created a data set of validated fundamental frequencies employing a semi-automated algorithm which require in the final steps the intervention of a trained user to select the best FLR. They used the TS05 model [208] to represent the geomagnetic field lines and assumed a power-law dependence of the plasma mass density along them. The validation procedure, manually performed, takes care of possible failures of the automated part. Indeed, the gradient technique presents critical situations which may yield to a difficult identification of resonances. The first issue concerns the computation of Fourier cross-spectra; according to the latitude of the pair of stations, to the separation between them and other factors, also dependent on the geomagnetic conditions, the cross-spectra need to be computed with proper parameters in order to maximize the information within them. The other major critical situations concerns the detection of FLR frequencies at high latitudes. They can be very close to the spectral resolution, so the fundamental harmonic could be hard to detect, especially during prolonged quiet period, when the FLR frequency usually decreases. In this case higher harmonics could be accidentally picked up by a fully automated procedure [61]. Other issues can emerge when a pair is sounding the region near the PBL where the selected FLR frequency can be mismatched or can even disappear [80, 146, 147].

In the last thirty years, the increasing amount and quality of both space- and ground-based data has allowed an exponential development of data-driven technique, such as machine learning, deep learning and artificial intelligence. These approaches became one of the most powerful tool for understanding the dynamics of complex systems involving several degrees of freedom and multiple non-linear interactions, especially in the space weather context. Nowadays machine learning methods are adopted for the most varied space weather applications [see 39, for a review], ranging from algorithms for event identification, such as solar image classification [11], near-Earth plasma regions classification [31] and the classification of periods with ultra-low frequency (ULF) waves activity [15]; to methods for revealing causality between high dimensional data sets and specific events, see Wing et al. [228] and Heidrich-Meisner and Wimmer-Schweingruber [93], and forecasting algorithms, widely used for predicting solar flares [142], the arrival time of coronal mass ejections [121] and the behavior

of various geomagnetic indices [47]; and even algorithms for modeling non-linear relationships which try to reveal the physical action of the system starting from first principles [28].

In this work, by employing multiple supervised Machine Learning (ML) algorithms, we develop a completely automated procedure for the identification of FLR frequencies using ground-based measurements from the EMMA network. At first, we tested several ML regression algorithms to find the optimal in the estimation of FLR frequencies starting from 1D cross-phase spectra. The implemented method needs to be combined with an additional step, based on classification algorithms, for the discrimination of quiet and active periods, being the presence of FLRs not a continuous phenomenon. Machine Learning methods proved to be sometimes more accurate, but certainly more efficient than other methods, in automating the recognition and estimation of FLR frequency in the Earths' plasmasphere using ULF magnetometer measurements.

JGR Space Physics

RESEARCH ARTICLE

10.1029/2020JA029008

Special Section:

Probing the Magnetosphere through Magnetoseismology and Ultra-Low-Frequency Waves

Key Points:

- We investigated the performances of several machine learning algorithms to identify geomagnetic Field Line Resonance (FLR) frequencies from ultralow frequency signals detected at European quasi-Meridional Magnetometer Array
- Tree-based methods have higher performance than kernel-based methods and they result a robust technique to estimate FLR frequencies
- The estimation error of our approach shows a dependence on the station latitude, but it is stable on highly variable geomagnetic conditions

Correspondence to:

R. Foldes,
raffaello.foldes@graduate.univaq.it

Citation:





Foldes, R., Del Corpo, A., Pietropaolo, E., & Vellante, M. (2021). Assessing machine learning techniques for identifying field line resonance frequencies from cross-phase spectra. *Journal of Geophysical Research: Space Physics*, 126, e2020JA029008. <https://doi.org/10.1029/2020JA029008>

Received 7 DEC 2020
 Accepted 4 MAY 2021

© 2021. The Authors.

This is an open access article under the terms of the [Creative Commons Attribution License](https://creativecommons.org/licenses/by/4.0/), which permits use, distribution and reproduction in any medium, provided the original work is properly cited.

Assessing Machine Learning Techniques for Identifying Field Line Resonance Frequencies From Cross-Phase Spectra

Raffaello Foldes¹ , Alfredo Del Corpo¹ , Ermanno Pietropaolo¹ , and Massimo Vellante¹ 

¹Department of Physical and Chemical Sciences, University of L'Aquila, L'Aquila, Italy

Abstract Monitoring the plasmasphere is an important task to achieve in the Space Weather context. A consolidated technique consists of remotely inferring the equatorial plasma mass density in the inner magnetosphere using Field Line Resonance (FLR) frequencies estimates. FLR frequencies can be obtained via cross-phase analysis of magnetic signals recorded from pairs of latitude separated stations. In the last years, machine learning (ML) has been successfully applied in Space Weather, but this is the first attempt to estimate FLR frequencies with these techniques. We survey several supervised ML algorithms for identifying FLR frequencies by using measurements of the European quasi-Meridional Magnetometer Array. Our algorithms take as input the 2-hour cross-phase spectra of magnetic signals and return the FLR frequency as output; we evaluate the algorithm performance on four different station pairs from $L = 2.4$ to $L = 5.5$. Results show that tree-based algorithms are robust and accurate models to achieve this goal. Their performance slightly decreases with increasing latitude and tend to deteriorate during nighttime. The estimation error does not seem to depend on the geomagnetic activity, although at high latitudes the error increases during highly disturbed geomagnetic conditions such as the main phase of a storm. Our approach may represent a prominent space weather tool included into an automatic monitoring system of the plasmasphere. This work represents only a preliminary step in this direction; the application of this technique on a more extensive data set and on more pairs of stations is straightforward and necessary to create more robust and accurate models.

1. Introduction

The near-Earth environment is composed of different plasma populations that cover an energy range of several orders of magnitude. The plasmasphere is the coldest one (~ 1 eV) and typically extends from the top of the ionosphere up to 4–6 Earth radii (R_E). Its shape, composition and extension change in response to geomagnetic activity variation and, due to its preponderant contribution to the mass density, plays a crucial role in exciting plasma-waves and driving their interaction with more energetic particles (Liemohn, 2006; Thorne, 2010). During major storms the outer boundary, the plasmopause, also defined as the plasmasphere boundary layer (PBL, Carpenter & Lemaire, 2004), can move earthward as near as 1.5–2 R_E , and the recovery to the pre-storm conditions can last for several days.

For its central role in the space weather context, a real-time monitoring of the cold plasma in the inner magnetosphere would be an essential task to achieve. A prototype of such system was developed inside the PLASMON FP7 European project (Lichtenberger et al., 2013) during which the European quasi-Meridional Magnetometer Array (EMMA) was established. EMMA provides a unique opportunity to monitor the plasmasphere dynamics in near real-time. It consists of 27 ground-based magnetic stations approximately located along the same magnetic meridian and mapping into magnetic L -shells in the range 1.6–6.1, where L is the McIlwain parameter evaluated using the IGRF. Using Ultra Low Frequency (ULF) signals simultaneously observed by pairs of stations it is possible to infer the radial distribution of the equatorial plasma mass density in the longitudinal sector identified by the network (Del Corpo et al., 2019; Lichtenberger et al., 2013).

The core of this monitoring system is the gradient method proposed by Baransky et al. (1985) and further developed by Waters et al. (1991): By performing Fourier cross-spectral analysis of the magnetic signal recorded by two stations slightly separated in latitude, it is possible to estimate the resonance frequency of the field line whose footprint is halfway between the stations. Around the field line resonance (FLR) frequency and its higher harmonics the cross-phase presents a maximum and the amplitude ratio crosses one with a positive slope. One or both these characteristics can be used to identify FLR frequencies which, in turn, depend on the magnetic field strength and plasma mass density distribution along the field line. By making assumptions on the magnetic field

topology and the field line plasma distribution, the governing wave equation (Singer et al., 1981) can be numerically solved, providing an estimate of the plasma mass density in the equatorial crossing point of the field line.

Using EMMA observations, Del Corpo et al. (2019) created a data set of validated frequencies considering only the fundamental harmonic and employing a semi-automated algorithm which performs the above procedure. They used the TS05 model (Tsyganenko & Sitnov, 2005) to represent the geomagnetic field lines and assumed a power-law dependence of the plasma mass density along them. The validation procedure takes care of possible failures of the automated part. One of the most critical situations concerns the detection of FLR frequencies at high latitudes. They can be very close to the spectral resolution, so the fundamental harmonic could be hard to detect, especially during prolonged quiet period, when the FLR frequency usually decreases. In this case higher harmonics could be accidentally picked up by a fully automated procedure (Del Corpo et al., 2019). Other issues can emerge when a pair is sounding the region near the PBL where the selected FLR frequency can be mismatched or can even disappear (Fraser et al., 2005; Menk et al., 2004; Milling et al., 2001).

Based on the gradient method, mentioned above, a few authors in the past developed algorithms to automatically detect FLRs (Berube et al., 2003; Chi et al., 2013; Lichtenberger et al., 2013; Wharton et al., 2018). In these works, either statistical or morphological properties of the cross-phase spectra were used to individuate the resonance peaks. In this study, we propose an alternative approach based on machine learning methods, using the cross-phase spectra by Del Corpo et al. (2019) as input data and their data set of validated frequencies to train the algorithms.

Machine learning techniques represent a subset of artificial intelligence and they have turned into one of the most powerful tools for addressing space weather problems. Since the early 90s machine learning has benefited from the high amount and quality of both space and ground-based data. Nowadays machine learning methods are applied to the most varied space weather topics, and they can be identified according to their final goal into four macro categories (Camporeale et al., 2018): (i) algorithms for event identification, such as solar image classification (Armstrong & Fletcher, 2019), near-Earth plasma regions classification (Breuillard et al., 2020) and the classification of periods with ULF waves activity (Balasis et al., 2019); (ii) methods for revealing causality between high dimensional data sets and specific events, see Wing et al. (2018) and Heidrich-Meisner and Wimmer-Schweingruber (2018); (iii) forecasting algorithms, widely used for predicting solar flares (Massone et al., 2018), the arrival time of coronal mass ejections (Liu et al., 2018) and the behavior of various geomagnetic indices (Chandorkar & Camporeale, 2018); and (iv) algorithms for modeling non-linear relationships which try to reveal the physical action of the system starting from first principles (Boynton et al., 2018).

Despite the wide application, machine learning techniques were applied to the characterization of plasmasphere regions only in the past few years. Main contribution is from Zhelavskaya et al. (2016, 2017) who applied a convolutional neural network for estimating electron mass density. To the best of our knowledge, the only attempt of estimating FLR frequencies using a ML approach has been developed by Fujimoto et al. (2019) for a pair of stations in New Zealand (mid-latitude).

In this work, we assess various machine learning methods for addressing the challenging task of identifying FLR frequencies by using ground-based measurements.

In Section 2 we briefly introduce the machine learning algorithms adopted for this analysis. Section 3 widely explains the set of data obtained from the EMMA network. Section 4 focuses on pre-processing, feature and model selection procedure which compose the whole machine learning process. Finally, in Section 5 we discuss the results and in Section 6 we outline the significant breakthrough and development produced by this analysis.

2. Machine Learning Algorithms

Machine Learning (ML) algorithms can be principally divided into three macro categories: supervised (labeled data set y_i), unsupervised (not labeled data set y_i) and reinforcement learning (goal-oriented algorithms). Since our analysis is the first attempt to identify ULF wave resonance frequencies from ground-based measurements using a ML approach, we assess several different algorithms, widely used for regression problems, that is, identification and/or prediction. A general regression problem within this framework can be expressed as the estimation of a real-valued function $F(X)$, where X is a d -dimensional input variable defined by an input/output pair (X_i, y_i) . It is possible to divide regression algorithms into three main groups: classification and regression trees

(CART, i.e., Decision Tree by Breiman et al., 1984), ensemble methods (i.e., Random Forest and Gradient Boosting algorithms) and kernel methods (linear methods using the “kernel trick,” that is, Support Vector Machines and Kernel Ridge).

2.1. Kernel Methods

Ridge regression employs ordinary least squares (OLS) for minimizing the error between predictions \hat{y}_i and targets y_i , by adding a penalty term ($\alpha \geq 0$) that controls the complexity of the learned model (Hoerl & Kennard, 1970).

Kernel Ridge Regression (KRR) combines such a described method with the kernel trick (Theodoridis & Koutroumbas, 2008). Kernel functions transform data into higher dimensional space, by computing the inner product in the input space. There exist several different kernel functions; the Gaussian radial basis function (RBF), polynomial and sigmoid kernels are the most used, just to cite a few.

As well as KRR, several ML algorithms can operate with the kernel method; among them, *support vector machines* (SVMs, Cortes & Vapnik, 1995) are the best known, though they were initially used for classification.

SVM models employ the so called *support vectors* (i.e., data points nearest the division boundary) for identifying the optimal hyperplane in the feature d -dimensional space, which divides the points by maximizing the margin around the hyperplane itself. Because of its universality and robustness many variants were developed (see Kumar et al., 2019, for a review), and they have been widely used also for regression problems (Bao et al., 2020; Yang et al., 2009). In particular, the so-called ϵ -SVM addresses regression problems by employing an ϵ -range which represents the approximation region of the real-valued target function.

After the training process SVM and KRR have learned the same model shape, though they use different cost functions, that is, quadratic for KRR and ϵ -insensitive for SVM. Another difference between these two algorithms is the execution time; since KRR can be computed in a closed form, it results faster with medium-sized (less than 10^4 samples) data sets, but SVM can learn sparse models resulting in faster performance with massive sets (Murphy, 2012).

2.2. Decision Trees

Differently from single-stage algorithms, like those described in the previous section, decision trees (DTs) are multi-step models which recursively divide data in two partitions (binary split). Starting from the root node, containing all data, the tree structure is composed by intermediate nodes (called splits) and terminal nodes (leaves).

The process involves two macro phases: the splitting procedure and the pruning phase. The main objective of pruning techniques (see Esposito et al., 1997, for a review) is to generalize the tree structure and hence avoid over-fitting, see Figure 1. Pruning techniques can be controlled by various parameters which drive the growth of DTs, such as the minimum number of samples in a split/leaf or the maximum number of features to consider for the best split.

The splitting procedure determines the growth of a DT; at each iteration the central operation is finding the best split for the data set according to some error measures (Buntine & Niblett, 1992). The tree growth continues until no more splitting produces a significant gain in the error measure or a stopping criterion is satisfied. DTs represent optimal algorithms in processing massive data sets, handling missing values and mixed data (ordinal, categorical and continuous), performing features selection, ignoring redundant features, but even for their user-friendly final structure.

One of the major shortcoming is a poorness of generalization which make this kind of algorithms prone to over-fitting and highly unstable with respect of slight variation in the input data (Li & Belford, 2002). This error, namely variance error, can be addressed using ensemble (or “forest”) models which combine results from numerous trees (usually averaging, i.e., Random Forest), or combine various DTs during the growth phase (i.e., Gradient Boosting methods).

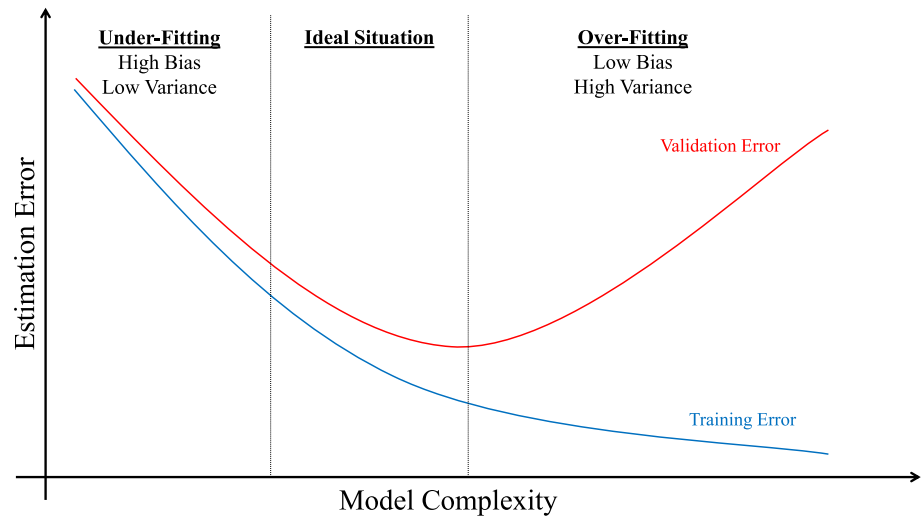


Figure 1. Illustration of a typical scenario occurring during the procedure of hyperparameter tuning for every machine learning method. As the model complexity increases the estimation error for the training set decreases; still, the model parameters are too specific and hence they are not able to reproduce the same high performance with unseen data (i.e., validation set), namely over-fitting.

2.3. Ensemble Methods

The central concept besides ensemble methods is that multiple weak estimators can achieve better results than a single complex model; they result more efficient than DTs in reducing the variance error (Breiman, 1996).

Let us consider many shallow DT regressors (usually hundreds) which give K solutions of a real-valued function, $\hat{F}_1(X), \hat{F}_2(X), \dots, \hat{F}_K(X)$. We can build the final prediction using a linear combination of the estimation:

$$\hat{F}_{Ens}(X) = \sum_{j=1}^K a_j \hat{F}_j(X)$$

where the coefficients, a_j , determine the type of procedure adopted in constructing the ensemble. Two main approaches are commonly used: bootstrap aggregating (or Bagging) methods use the average as an estimator, that is, $a_j \equiv 1/K$, and boosting techniques, which employs coefficients dependent on the number of estimators (Buhlmann, 2012).

Similarly to bagging methods, the Random Forest (RF) algorithm averages the solutions of many estimators; still, it considers for splitting data only a subset of features, $d < D$, producing highly varied estimators and resulting in faster performance with high dimensional data sets. In RF, each tree grows independently, while boosting algorithms create one tree at a time to improve the prediction of the previous model recursively. Usually, RF obtains better performance than bagging methods but worse than boosting ones.

A wide group of boosting methods are those related to the gradient descent technique, widely known as Gradient boosting models. Considering, for instance, a quadratic loss function $L = \sum (y_i - \hat{F}(x_i))^2 / 2$, these methods act to minimize L by adding further estimators according to the value of the negative gradient, $r(x_n) = y_n - F(x_n) = -\partial L / \partial F(x_n)$, which represents how far the model is from a reliable estimation. Gradient boosting algorithm can be directly generalized to different loss functions, without modifying any part of their procedure.

In this analysis, we focus our attention on two particular boosting algorithms: eXtreme Gradient Boost (XGB, Chen & Guestrin, 2016) and Light Gradient Boost Model (LGBM, Ke et al., 2017). Both methods have shown in the last years to address regression/classification problems with high and robust performance.

More in detail, XGB is a recent algorithm resulted in being highly efficient in regression/classification competition (see www.kaggle.com) and many real-world applications (Ivanov et al., 2020; Kunte & Panicker, 2020;

Luckner et al., 2017). XGB employs second-order derivative during gradient descent resulting in faster and more refined performance. It results particularly reliable in handling massive data sets because of its parallel implementation. Despite the numerous novelties and improvements of XGB, this algorithm can result barely efficient with high dimensional data set, because of its splitting method which turns out very time-consuming.

For speeding up the splitting procedure, LGBM combines two additional methods, namely Gradient-based One-Side Sampling (GOSS) and Exclusive Features Bundling (EFB). GOSS, in combination with EFB, picks (usually randomly) only a small portion of data having small gradients for estimating the information gain, since these points give minor contributions to the gradient descent. LGBM, in comparison to XGB, can simply handle with categorical data without requiring any pre-processing phase.

3. Data

The plasmaspheric mass density can change drastically during active geomagnetic periods and the associated field line resonance frequencies change accordingly. Therefore, a good data set, suitable to train ML algorithms, should cover the most comprehensive range of geomagnetic disturbance levels. The data set by Del Corpo et al. (2019) was created following this idea and covers 165 days along 5 years: 2012 (DoY 266–336), 2013 (DoY 72–86 and 145–162), 2014 (DoY 45–68), 2015 (DoY 72–90 and 169–178), and 2017 (DoY 146–153). It comprises prolonged quiet geomagnetic periods as well as disturbances of different intensity, including 13 geomagnetic storms, nine of them having a minimum Dst value less than -100 nT. For each period, the analysis has been carried out over a variable number of station pairs, depending on the data coverage. About 20 pairs were analyzed for each period, but only eight were common to all the data set.

This work aims to test the viability of a machine learning algorithm to pick up trusted FLR frequencies from magnetic field cross-phase spectra collected by a network like EMMA. Since the frequency generally decreases with latitude, such algorithm should be tested not only in different geomagnetic conditions, but also for data collected at different latitudes. For this reason, we selected four pairs among the eight common to the entire data set, that cover at the same time the largest range of latitudes. Figure 2 shows the position of the selected pairs inside the EMMA network: Suwalki-Belsk (SUW-BEL) in black, Tartu-Birzai (TAR-BRZ) in green, Oulujärvi-Hankasalmi (OUJ-HAN) in red and Muonio-Pello (MUO-PEL) in blue. More details about coordinates and the L -parameters are reported in Table 1.

The data set consists of daily Fourier cross-phase spectra computed with a 2-h moving window every half an hour (Del Corpo & Vellante, 2020). Each 2-h window is divided into a variable number of sub-intervals that depends on the latitude (increasing from 1 to 7 with decreasing latitude). The spectra are evaluated for each sub-interval and successively averaged. This implies a spectral resolution that increases with increasing latitude, a condition necessary to detect FLR frequencies that vary by more than a factor of 10, moving from the lowest to the highest latitude station pair. Each final spectrum is smoothed over 9–11 samples and the fundamental resonance frequency is eventually provided following a selection and validation process composed of both automated and manual steps.

The fundamental resonance frequencies are provided with a time resolution of 30 min, although the coverage is not continuous. In fact, for several reasons, it is not always possible to detect FLR frequencies from cross-phase spectra: (i) data gaps in one or both stations; (ii) noise in the magnetic signals that inhibits the appearance of the resonance signatures in the spectra; (iii) quiescent LF wave periods that prevent the excitation of standing Alfvén waves (Balasis et al., 2019). Statistical works have shown that the FLR detection rate changes also with latitude and local time with a broad peak around noon; in particular, during nighttime it can be as low as 10% (Chi et al., 2013; Del Corpo et al., 2019).

To efficiently sustain a standing Alfvén wave, the field line should be fixed at the footprints, which implies an infinite conductivity. This approximation is generally satisfied during daytime, when the ionospheric conductivity is sufficiently high, but after sunset the conductivity decreases due to the predominant role of recombination processes and it should be assumed finite (Allan & Knox, 1979). Whether the ionosphere conditions are able to sustain normal modes also during nighttime, is still under debate. If the conductivity is sufficiently small, the observed modes should be interpreted as free-end ones. Recently Takahashi et al. (2020) observed FLRs across the midnight sector compatible with a fixed-end mode configuration. In some cases, only one footprint is

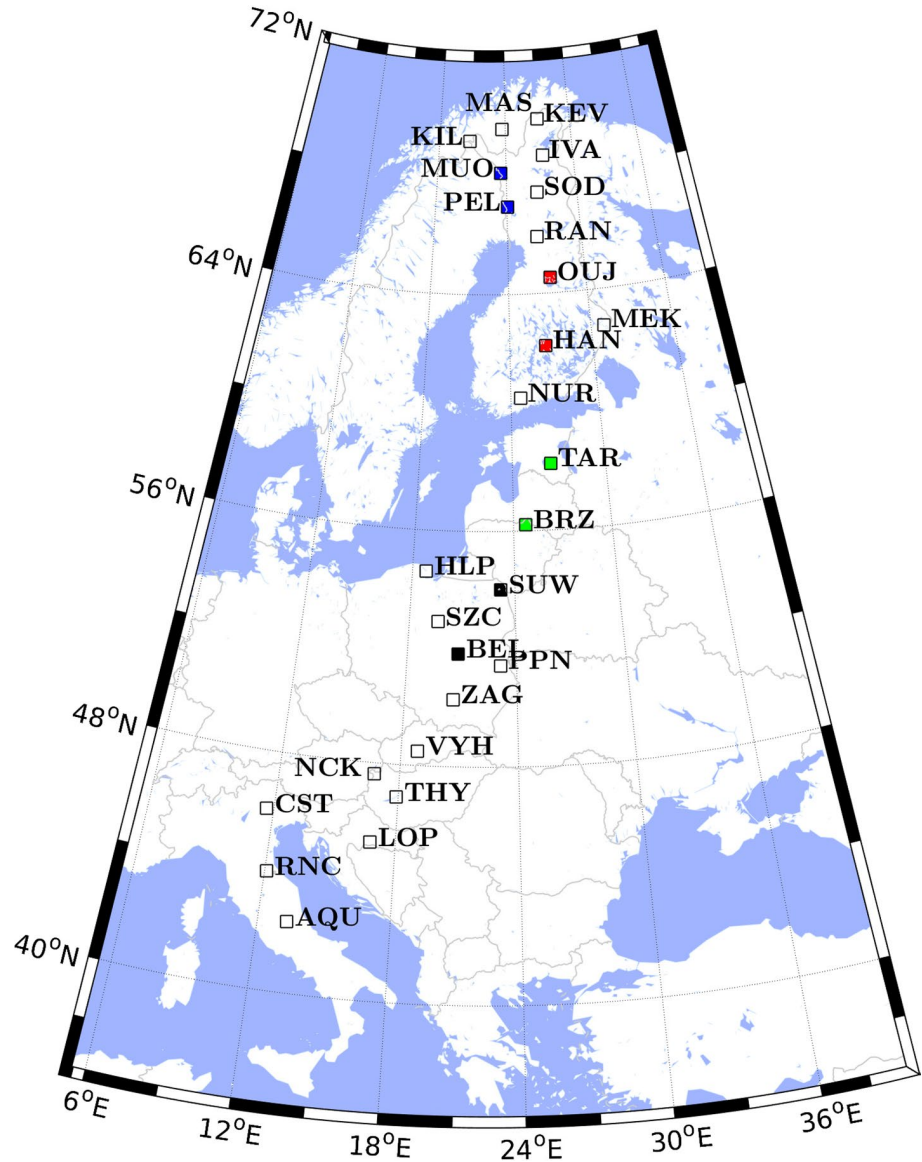


Figure 2. The European quasi-Meridional Magnetometer Array network map in geographic coordinates. The four pairs used in this analysis are highlighted in different colors.

Table 1

Station Pairs of the EMMA Network Considered in This Work With Their Mid-Point Geographic Coordinates and the Corresponding McIllwan Parameter

Pair code	Stations name	Latitude (deg.)	Longitude (deg.)	<i>L</i>
MUO-PEL	Muonio-Pello	67.5	23.8	5.5
OUI-HAN	Oulujärvi-Hankasalmi	63.4	26.9	4.1
TAR-BRZ	Tartu-Birzai	57.2	25.6	2.9
SUW-BEL	Suwalki-Belsk	52.9	22.0	2.4

Abbreviation: EMMA, European quasi-Meridional Magnetometer Array.

sunlit while the other is in darkness, generating quarter-wave modes (Obana et al., 2008, 2015). These situations make less reliable the nighttime validated frequencies.

Despite the data set contains some dubious frequencies, that is, especially during nighttime hours, we kept all the frequencies for the training and used sunrise and sunset information to interpret the results according to the reliability of validated frequencies; the main reason is that we want to maximize the number of samples for the training phase.

Excluding times without selected frequencies, we eventually obtain 3514 samples for SUW-BEL, 4721 for TAR-BRZ, 3270 for OUI-HAN and 3112 for MUO-PEL.

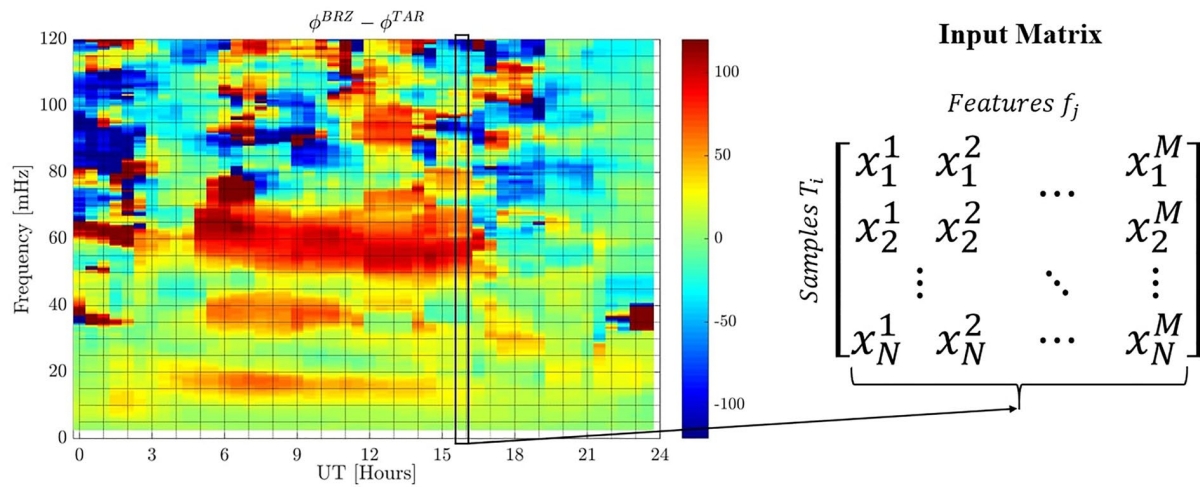


Figure 3. Graphical representation of the input matrix preparation. Every entry x_i^j represents the cross-phase value at a specific time and frequency value.

3.1. Input and Output Data

Every ML algorithm adopted in this analysis requires a so-called features matrix as input data, where rows represent different samples and columns are the input features. As previously stated, following the well-established cross-phase technique, our input for the ML algorithm is the cross-spectrum, as shown in Figure 3. The output will be the estimated value of the resonance frequency f_i for that sample.

Since we would like to test our ML algorithms on different pairs of stations, the input matrix is created separately for each couple. Typically, the resonance frequency decreases with increasing latitude except across the PBL where the behavior is the opposite. Thus, to obtain reasonable average spectral resolutions ($\Delta f / \bar{f} \sim 3\%$) at every latitude along the EMMA network, different pairs of stations have a different length of cross-phase spectra, resulting in features matrix with different dimensions: TAR-BRZ and SUW-BEL spectra are composed by 212 frequency bins (between 0 and 120 mHz), while OUI-HAN and MUO-PEL have both 285 input features, but for OUI-HAN they vary between 0 and 80 mHz while for MUO-PEL between 0 and 40 mHz.

Input data are transformed using two subsequent operations to improve the performance of ML algorithms: standardization, $(x - \mu) / \sigma$ and normalization, $(x - x_{\min}) / (x_{\max} - x_{\min})$. The same procedure is applied to the output frequencies.

As can be observed in Figure 4, the first transformation gives a more Gaussian-like shape to the distribution of frequency, while the second one forces values between 0 and 1. Both operations are commonly adopted in various ML applications resulting in higher accuracy with every algorithm. After these transformation data are split in training and test set with roughly a 7:1 ratio (Figure 4); the former will be used to create the ML model, while the latter will evaluate the model performance.

4. Methods

In Figure 5 is depicted the entire ML pipeline built for FLR frequencies identification. After the stage of data pre-processing, described in the previous section, our ML procedure involves the application of typical ML techniques for creating the optimal model and subsequently improving its performance: feature selection and model selection.

Every ML algorithm is then trained via the cross-validation technique to further avoid over-fitting, producing a final model which is used to estimate frequencies from the test set.

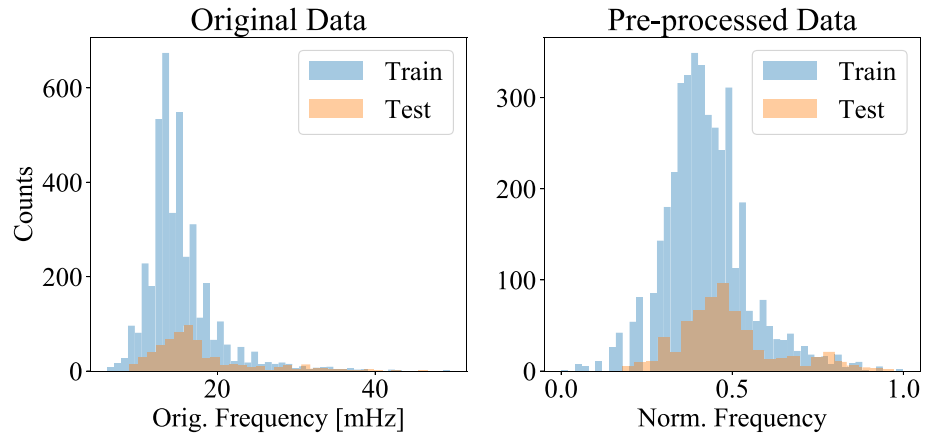


Figure 4. The left panel shows the original data set, while the right panel represents the same data after the pre-processing stage for Tartu-Birzai. In both panels distributions are divided in training (blue) and test (orange) set. This division is performed before the pre-processing procedure.

4.1. Feature Selection

Feature selection techniques are one of the central concept in ML methods, since the data set dimensionality, as well as the feature choice, severely affects the algorithm performance. Various works showed that numerous and redundant features may result in decreasing the algorithm accuracy and robustness (Guyon & Elisseeff, 2003; Hua et al., 2004; Kapetanios, 2007; Peng et al., 2005). The reasons for implementing and including feature selection routines in a ML pipeline can be summarized in four main points: lower dimensional data sets are simpler to interpret and visualize for end-users (the curse of dimensionality), increasing the model generalization (avoid over-fitting), improving the algorithm accuracy and shortening data processing times. For all these reasons we include two different feature selection techniques for reducing the data set dimensionality as well as evaluating additional features.

Feature selection methods can be categorized in embedded, filters, and wrapper methods (Guyon & Elisseeff, 2003). Embedded methods are ML models which implement feature selection using different regularization techniques, that is, l_1/l_2 -norm for linear models and a feature sub-sampling for DTs (Lal et al., 2006). Filters are model-independent methods which simply employ some correlation measure to find the optimal subset of features. Commonly known correlation measures are mutual information, point-wise mutual information and the Pearson's R correlation coefficient. Filters are computationally cheaper than other methods. Eventually, wrapper methods use model performance (accuracy and robustness) as a metric for evaluating feature subsets.

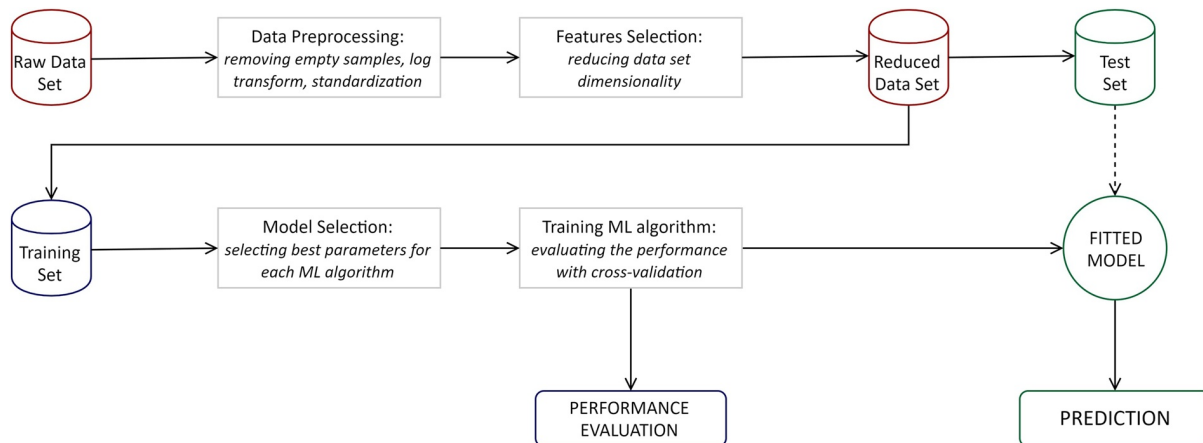


Figure 5. Graphical representation of the entire machine learning pipeline we built.

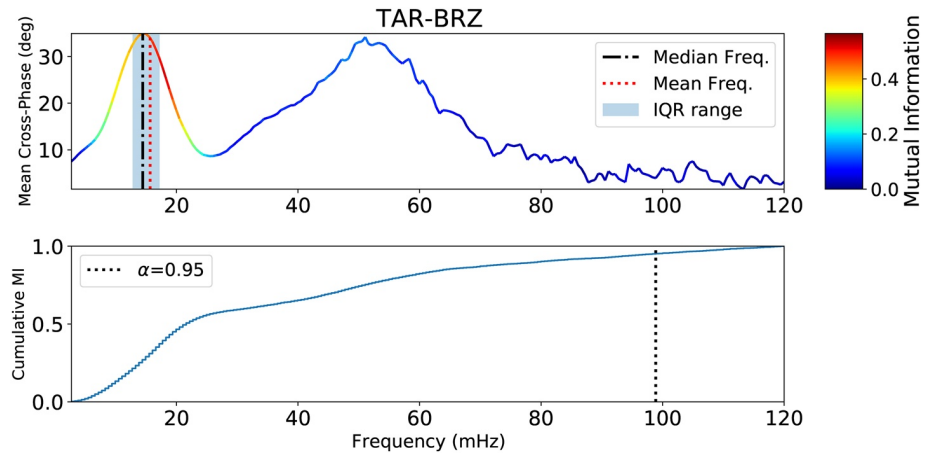


Figure 6. Results from the first feature selection technique. The upper panel represents the average cross-phase spectrum over the entire data set of Tartu-Birzai; black dash-dotted and red dotted vertical lines are the median and the average value of the validated frequency, respectively, while the blue interval is built with the first and third quartile of the distribution of frequencies. The average spectrum shows a peak close to the median value of the frequency, with a highly right-skewed distribution (high frequencies). The bottom panel is the cumulative mutual information (MI) indicating the 95% (vertical dotted line) of information subsisting between inputs and output. This confidence level is reached around 100 mHz.

These methods are computationally heavy, especially with high-dimensional data set, and often they allow only a random (or sparse) search between all the possible subsets.

For reducing the initial matrix dimensionality, we first compute the mutual information (MI) at every frequency bin and for the whole data set. Mutual information can be interpreted as a correlation measure between inputs and outputs, and it represents a powerful tool to identify even non-linear and non-monotonic correlations. Then we apply a time average over the entire period and compare mutual information values, represented in Figure 6 as a color scale, with the average cross-phase spectrum (Figure 6, top panel). By imposing a confidence level over the cumulative function of the mutual information (bottom panel of Figure 6) at $\alpha = 0.95$ (vertical dotted line), we can keep only frequencies below this threshold value. In this way, we ensure that, despite the lower number of features, the data set contains at least 95% of the information to estimate the output frequencies.

Figure 6 summarizes the results of this procedure for TAR-BRZ. As expected, highest values of mutual information correspond to the first peak of the average cross-phase spectrum, meaning that, on average, this is the most informative part of the spectrum for predicting the frequencies. The first peak occurs at $f_1 \approx 14$ mHz and is related to the first harmonic since it perfectly overlaps with the blue interval (top panel in Figure 6) which represents the 0.25 and 0.75 percentile of the validated FLR frequency distribution (i.e., interquartile range, IQR). The second peak occurs at $f_2 \sim 50$ mHz; the frequency ratio between the first and second peak is $f_2/f_1 \sim 3.6$ which is compatible with the expected ratio between the third and fundamental harmonics (Schulz, 1996).

Applying this procedure to the four pairs, we found that, independently from the couple of stations, the 95% threshold is reached using only the 80% of the initial number of features, resulting in 170 for TAR-BRZ and SUW-BEL, and 230 for OIJ-HAN and MUO-PEL.

The second part of the feature selection stage is the evaluation of additional features using wrapper methods. These novel features are spatio-temporal information, solar activity proxies, and geomagnetic activity indicators derived from geomagnetic indices. All the additional features analyzed in this section are summarized in Table 2. Temporal features are represented by the day of year (DoY) to highlight the seasonal variation of the resonance frequency (Vellante et al., 2007) and the decimal hour, because is commonly known that resonance frequencies show a diurnal modulation (e.g., Chi et al., 2013; Del Corpo et al., 2019).

To consider the effects of solar activity, mostly for its impact on the production of ion-electron pairs at ionospheric height, we take into account the daily radio solar flux at 10.7 cm (F107, see Table 2) as provided by OMNIWeb. From the same database we also consider the y-component of the solar wind electric field (EField in Table 2) to investigate any impact of the convection electric field.

Table 2
Summary of all the Other Features Evaluated During the Features Assessment Procedure

Col. Name	Description
DoY	Day of Year
Hour	Decimal hour with a resolution of 0.5 h
Kp	Instantaneous <i>Kp</i> value
Kp_w_XX	<i>Kp</i> index weighted at different intervals 12, 24, ..., 72 h
Kp_m_XX	Maximum value of <i>Kp</i> index during last 12, 24, ..., 72 h
DST	Instantaneous <i>Dst</i> value (nT)
DST_m_XX	Minimum value of <i>Dst</i> index during last 12, 24, ..., 72 h (nT)
AE Index	Auroral Electrojet index
F107	Radio flux emitted from the entire solar disc at 10.7 cm (sfu or $W m^{-2} Hz^{-1}$)
EField	Convection electric field ($mV m^{-1}$)
r_{eq}	Field line equatorial crossing point (in Earth radii) with the Tsyganenko and Sitnov (2005, TS05) model

Notes. The geomagnetic indexes, the solar radio flux, and the convection electric field are derived from the OMNIWeb database.

Since the frequency also depends on the geomagnetic field line length we consider the equatorial crossing (r_{eq}) using the TS05 models to map the field line from the station pair position.

Geomagnetic activity indicators are evaluated to consider the FLR frequency variations due to the geomagnetic activity. The use of such indicators is widespread in the literature (e.g., Carpenter & Anderson, 1992; Del Corpo et al., 2019, 2020; Gallagher et al., 1988; Moldwin et al., 2002; Sheeley et al., 2001; Takahashi et al., 2006). The simplest indicators are the geomagnetic indices themselves. For this analysis, we consider the *Kp*, the *Dst* and the *AE* indices provided by the OMNIWeb database (<https://omniweb.gsfc.nasa.gov/>). More sophisticated indicators that take into account some effects of the magnetospheric dynamics can be derived from the *Kp* and *Dst* indices. In this work we consider two main different approaches: in the first, following the work by Moldwin et al. (2002), the maximum/minimum *Kp*/*Dst* are evaluated over a period τ preceding the time analyzed t_0 ; the second is made by following the work by Gallagher et al. (1988) and by evaluating the average *Kp* over a period τ preceding t_0 , weighted with an exponential function of the form $w(t) = \exp[-(t - t_0)/\tau]$. Both the procedures are applied to values of τ in the range 12–72 h with a step of 12 h, producing three groups of indices. The first is related to the *Kp* maximum in the preceding period and is reported in Table 2 and Figure 7 as *Kp_m_XX*, where *XX* are the τ values expressed in hours. The second group is related to the minimum *Dst* in the preceding period and it is indicated as *DST_m_XX*. The third one consists of *Kp* weighted averages and are represented as *Kp_w_XX*.

Figure 7 summarizes the evaluation of the additional features for all the six ML methods applied to the TAR-BRZ data set. Method performance, obtained using only the cross-phase as input, is reported as the initial value of the coefficient of determination, namely R_0^2 (reported in the lower right side of each panel of Figure 7). The additional features are evaluated by adding recursively the quantity which produces the best variation of the R^2 -score with respect to the previous value. This technique, commonly known as Sequential Forward Selection (SFS, Ferri et al., 1994), represents the most powerful tool to investigate medium and low-dimensional data sets. At each step, the selected feature is evaluated multiple times using the cross-validation technique; in this way we can produce a confidence interval defined by the standard deviation of the cross-validation score (orange area in Figure 7).

From the six panels in Figure 7 we can observe that the additional features have lower influence as the method complexity (and model performance) increases. Except for KRR and SVR, which result in poor performance, the other ML methods considered for this analysis (DTR, RF, LGBM, and XGB) basically express the same behavior. Algorithms that reach higher performance tend to return similar results also adding novel features, meaning that for these algorithms information from the cross-phase is sufficient to achieve the best accuracy. Another aspect is that it is impossible to select optimal quantities resulting in best performance for all the considered methods. Similar results are found for the other pairs of stations.

Hence, since no additional feature results in a significant improvement of the algorithms performance, we consider as input the cross-phase spectra only.

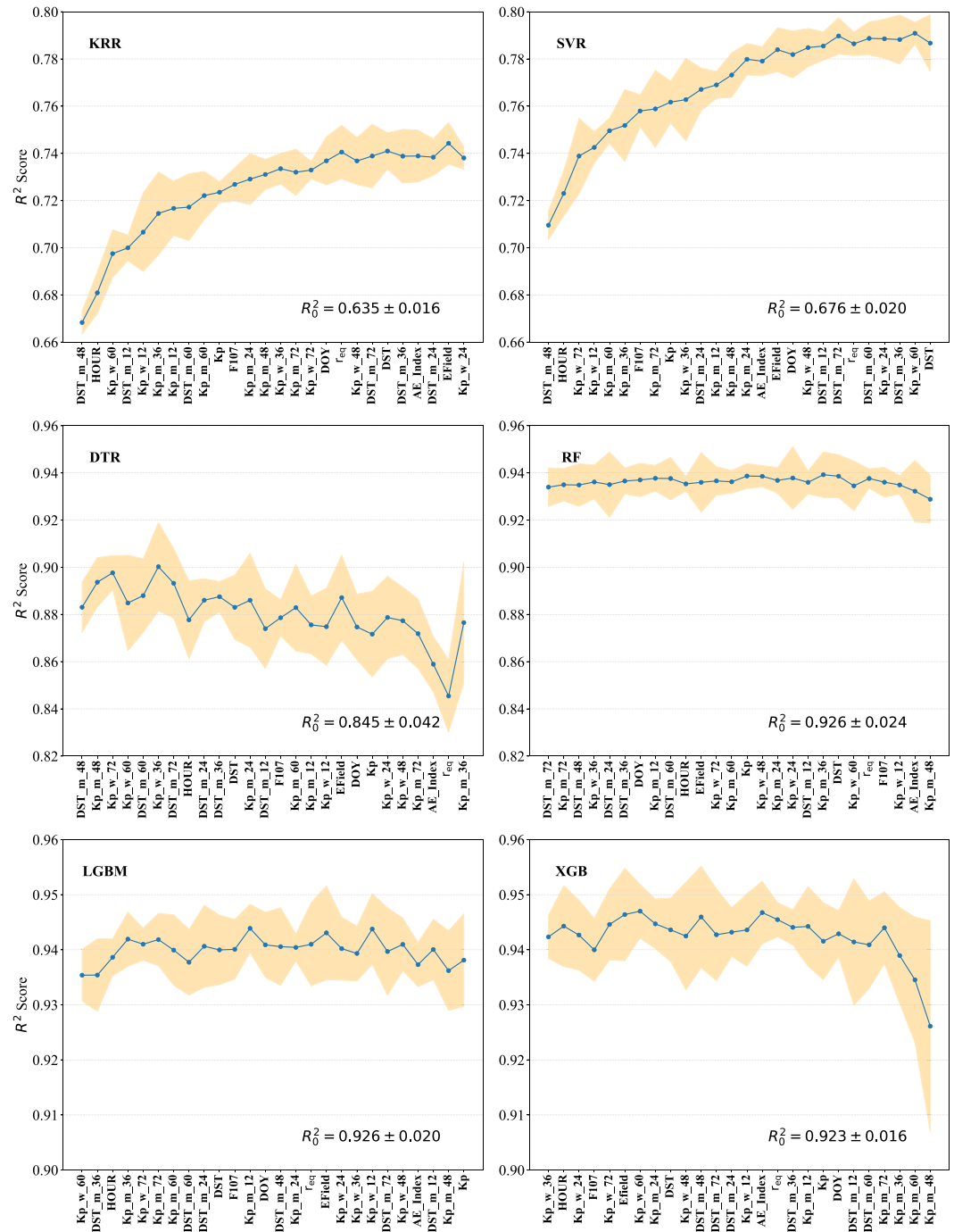


Figure 7. Results of the performance evaluation of all the additional features for Tartu-Birzai. The behavior for the other station pairs is the same. R_0^2 is the score obtained using only the cross-phase as input features. Methods with lower performance (Kernel Ridge Regression and Support Vector Regression) have an improvement with additional features while, as the model accuracy increases, they become less relevant. A comparison of these panels makes difficult to conclude which features could be more relevant for improving predictions.

4.2. Model Selection

The choice of the optimal ML method for a specific task and the procedure for tuning the model hyperparameters are both objectives of model selection. In Section 5.1 we will address the choice of the most suitable ML method for predicting resonance frequencies, by observing the model complexity and the accuracy for all the four

Table 3
Table of the Hyperparameters Optimized During Model Selection for Every Pair of Stations

Method	Hyperparameters	SUW-BEL	TAR-BRZ	OUI-HAN	MUO-PEL
KRR (w. RBF)	α	$7 \cdot 10^{-3}$	0.06	0.23	0.06
	γ	0.01	0.1	0.1	0.1
SVR (w. RBF)	C	1.5	1.5	1.5	1.5
	γ	0.1	0.1	0.5	0.5
DTR	Max. depth	19	17	17	5
	Min. samp. leaf	19	4	12	6
	Min. samp. split	14	8	19	8
RF	Max. depth	15	19	19	19
	# estimators	400	500	200	500
	Max. features	0.2	0.2	0.2	0.2
LGBM	# estimators	1,500	1,500	1,000	1,000
	# leaves	19	18	19	19
XGB	# estimators	1,000	200	300	200
	Max. depth	5	6	5	6
	Learn. rate	0.1	0.1	0.1	0.1

Abbreviations: KRR, Kernel Ridge Regression; LGBM, Light Gradient Boost Model; SVR, Support Vector Regression; XGB, eXtreme Gradient Boost.

station pairs. In this section we focus the attention on the selection of the best hyperparameters which control the model complexity of the six ML methods described in Section 2.

The number, typology and value of these parameters determine the model complexity and its performance. It is worth noting that hyperparameters, optimized in this step, are significantly different for the various methods; their optimal values are summarized in Table 3.

The first two rows in Table 3 are kernel methods which control the model complexity via the regularization terms, α for KRR and C for SVM. Higher values of α reduce collinearity between coefficients leading in higher generalization, while as α approaches zero KRR reverts to a simple OLS. In SVMs applied to regression problems (Support Vector Regression, SVR), the regularization parameter, C , controls the tolerance region width around the division boundary; increasing C results in more points close to the boundaries and hence more support vectors are required. Conversely, higher values of C mean a narrower tolerance and thus fewer points near boundaries.

In both methods input data are transformed using an RBF kernel for creating non-linear regression models (see Section 2.1). The hyperparameter γ for kernel methods refers to the standard deviation adopted for the Gaussian kernel (RBF kernel).

For decision trees and ensemble methods the main hyperparameters controlling the tree structure and the ensemble population are the maximum depth (i.e., Max. depth) and the number of estimators (i.e., # estimators), as briefly explained in Section 2.3.

Since the hyperparameter space is not too wide, for selecting the optimal values we perform a random search ($N = 3,000$ points) over the hyperparameter grid of each ML method. Real-valued hyperparameters are sampled using a logarithmic scale with $M = 1,000$ points, except for the maximum number of features which is picked from the values [0.0, 0.2, 0.5, 0.7, 1.0]. Kernel methods hyperparameters, α , C , and γ , vary in the range $[10^{-5}, 10]$, and the learning rate in the $[10^{-5}, 0.5]$ interval. Discrete-valued hyperparameters are all selected from specific lists of values: the maximum depth, the number of leaves and minimum samples in leaf/split are selected in the interval $[0, 1, \dots, 20]$, and the number of estimators is picked between $[100, 200, 500, 700, 1000, 1500, 2000]$.

The selection of optimal model hyperparameters is essential into the ML pipeline for avoiding model over-fitting, reducing the variance error and increasing model accuracy. We select the best method and model for identifying resonance frequencies by considering two main aspects: the accuracy of the method and the ability to create a common model for all the four station pairs, reflected by more stable hyperparameters across the pairs (see Table 3).

After this stage, the next step is training/validation, during which all the ML models are trained using the cross-validation (CV) technique, with a number of CV folds, $k_{CV} = 5$. CV divides the training set into k_{CV} partitions; at each step one of the partition is excluded from the training phase, and it will be only used for validation. By optimizing results obtained with the validation set model, over-fitting is avoided and the model generalization increases.

The training set for each pair of stations is selected using two main criteria: all the station pairs must have the same proportion between training and test set, and the four pairs must share periods in the test set for a comparison. In particular, we selected DoY 148–162 (2013) as common test for the extremely varied geomagnetic conditions, consisting of a geomagnetic storm (June 2013, Stepanova et al., 2019; Thaller et al., 2015; Zou et al., 2017) preceded by prolonged quiescent days. It follows that the test set ($\sim 13\%$ of the whole data set) consists of DoY 78–82 and 145–162 (2013) for TAR-BRZ, DoY 148–162 (2013) for OUI-HAN, and DoY 145–162 (2013) for SUW-BEL and MUO-PEL. The remaining portion, 87%, composes the training set.

5. Results and Discussions

5.1. Models Evaluation

The first part of the results focuses on the performance comparison of the various ML methods. The accuracy of regression problems can be evaluated by using various estimators, the coefficient of determination (R^2), the mean absolute error (MAE), the mean absolute percentage error (MAPE) and the root mean squared error (RMSE):

$$R^2 = 1 - \frac{\sum_{i=1}^N (y_i - \hat{y}_i)^2}{\sum_{i=1}^N (y_i - \bar{y})^2}, \quad MAE = \frac{1}{N} \sum_{i=1}^N |y_i - \hat{y}_i|,$$

$$MAPE = \frac{1}{N} \sum_{i=1}^N \left| \frac{y_i - \hat{y}_i}{y_i} \right|, \quad RMSE = \sqrt{\frac{1}{N} \sum_{i=1}^N (y_i - \hat{y}_i)^2},$$

where y_i are the actual frequencies, \hat{y}_i the predicted frequencies and \bar{y} the average value of y_i .

For the CV procedure we use R^2 , since it weakly depends on the distribution function of data and therefore it is more reliable for regression problems. The results from the CV procedure are shown in the boxplot of Figure 8 for TAR-BRZ, the other station pairs show a similar behavior; hence we show only one pair for the sake of simplicity. The first aspect of this graph is a significant difference in accuracy between kernel-based (KRR and SVR) and tree-based models. The main reason for such a difference could rely on data: by using discrete cross-phase spectra the validated frequencies can assume only a discrete set of values and, for their implementation, tree-based methods are more suitable, and therefore accurate, to estimate discrete-like data.

From Figure 8 we can also argue that DTR has a high variance error, meaning that the model is too simple for the specific task. This statement is also supported by the high variability of hyperparameters across the station pairs (see Table 3). On the other hand, RF results in high accuracy, but it does not appear sufficiently robust with high frequency outliers, as highlighted by a large skewness and the presence of a flier point out of the ends of the whiskers. LGBM and XGB show a similar behavior even in their performance, resulting in robust algorithms which avoid over-fitting and reduce the variance error. These two methods also result in similar hyperparameter variability between the four station pairs (see Table 3), the main difference relies on the execution time (see Table 4); XGB processes the same number of sample in half the time with respect of LGBM.

After the CV stage each ML method is applied to the prediction of resonance frequencies of the test set for each station pair. The frequencies obtained during both the training and the test phase are available from <https://doi.org/10.5281/zenodo.4304911> (Foldes et al., 2020). The results for TAR-BRZ (DoY 78–82 and 145–162, 2013,

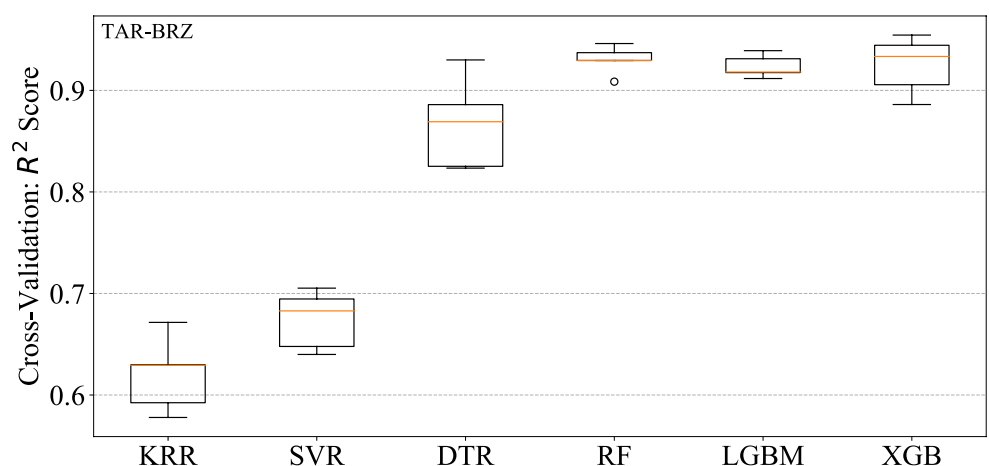


Figure 8. Comparison of the 6 ML methods trained in this analysis for Tartu-Birzai. Results for other station pairs have the same tendency. At first glance, we observe a substantial difference between kernel-based (Kernel Ridge Regression and Support Vector Regression) and tree-based models. Light Gradient Boost Model (LGBM) and eXtreme Gradient Boost (XGB) are quite similar methods as we see even from results, but XGB tends to be more robust for all the four pairs of stations since it reaches performances comparable with LGBM and RF using a lower number of estimators (i.e., simpler model, see Table 3); hence we consider XGB as the best-performed algorithm for this task.

Table 4
The General Performance of the Six ML Algorithms for TAR-BRZ

	R^2	MAE (mHz)	MAPE	RMSE (mHz)	CV time (s)
KRR	0.613	2.4	0.128	3.9	2.83
SVR	0.688	2.0	0.106	3.5	17.8
DTR	0.828	1.0	0.057	2.6	1.82
RF	0.840	0.93	0.042	2.5	32.7
LGBM	0.878	0.98	0.052	2.3	46.6
XGB	0.875	0.95	0.046	2.2	24.3

Abbreviations: KRR, Kernel Ridge Regression; LGBM, Light Gradient Boost Model; ML, machine learning; SVR, Support Vector Regression; TAR-BRZ, Tartu-Birzai; XGB, eXtreme Gradient Boost.

Notes. These results are obtained on the test set, $N_{\text{test}} = 619$. The best results for each metric are in bold. XGB does not show the best performances even though they are always close to the best results.

$N_{\text{test}} = 619$) are summarized in Table 4. By observing parameter stability in Table 3 and the algorithm performance in Table 4, we can observe that XGB and LGBM show almost the same robustness and accuracy. For these reasons, we choose XGB as most performing algorithm between them by considering two main aspects: it always employs fewer estimators than LGBM to reach the same performance, resulting as a simpler model, and because of its faster execution time it is more suitable for real-time applications.

To further explore the performance of the six ML methods we show, as an example, the relative error as a function of time (Figure 9) for a particular case study: 2013, DoY 151 (31 May). The relative error is the difference between the estimated frequency (f_{meth}) and the observed one (f_{obs}), normalized to f_{obs} . The intervals in which one or both the field line footprints are in darkness are represented as light or dark shadowed areas, respectively. The sunrise and sunset times (edges of the shadowed area) are evaluated at the height of 120 km as suggested by Del Corpo et al. (2020). The error increases during nighttime for all the methods, probably because, as stated above, the night frequencies are harder to detect and the relative cross-phase spectra can result poorly informative. During daytime the prediction error is remarkably

low for ensemble methods (especially LGBM and XGB), as previously pointed out in Table 4, and their fluctuations show a Gaussian-like behavior.

As stated above, XGB is the most suitable method to estimate FLR frequencies, hence, starting from this point, we perform further analysis using only the XGB method.

In Figure 10, we show an overview of the results obtained on the test set of TAR-BRZ. The first scatter plot (left panel) contains the median value of the predicted frequencies with the interquartile range (IQR) represented with bars. To compute the uncertainty of the model estimation we use two different approaches; for single estimator algorithms (i.e., KRR, SVR, and DTR) the uncertainty is computed using $N = 1,000$ different runs, while for multi-estimator algorithms (i.e., RF, LGBM, and XGB) the IQR is derived from the distribution of the estimators. The error increases when we observe a broader spread of the estimators; the uncertainty seems to increase slightly with frequency, but surely the error is greater when points are farther from the actual frequency value.

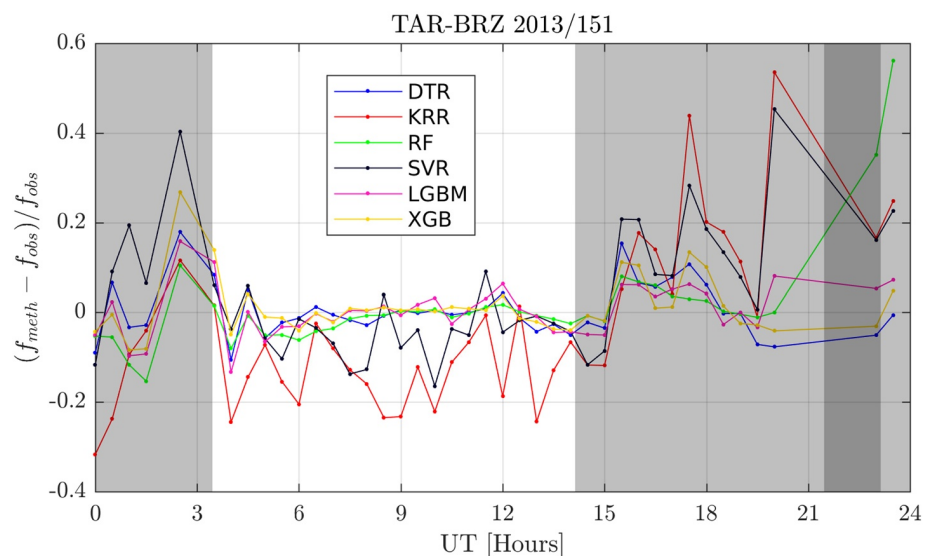


Figure 9. Comparison of the six machine learning methods for a quiescent day, 31 May. The light-gray area indicates when only one of the field line footprints is in the night-side. The dark-gray area occurs when both footprints are in darkness. In the daily part of the graph the relative error is significantly low ($\leq \pm 10\%$) for ensemble methods.

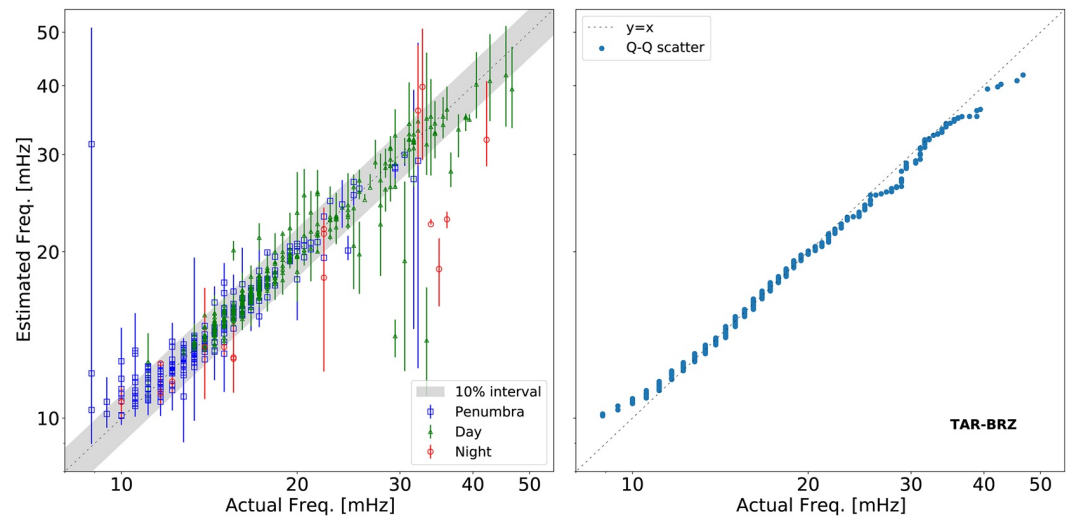


Figure 10. Global results from the test set of Tartu-Birzai. The left panel shows the median value of all the 619 test frequencies with their interquartile range as error bars; colors distinguish between diurnal (green), nocturnal (red) and penumbral (blue) frequencies. Right panel is the quantile-quantile (Q-Q) plot; it summarizes simultaneously several aspects of the target (actual frequencies) and obtained (estimated frequencies) distribution. The dashed line is the bisector and it indicates that the two sets come from a population with the same distribution.

Colors of the scatter plot represent the day, night and penumbral frequencies; the latter are those selected when only one footprint of the field line is sunlit. The division is made using the same criteria of Figure 9. Night and penumbral frequencies are harder to be observed (Balasis et al., 2019; Del Corpo et al., 2019) and indeed they are less numerous. The main reason is that cross-phase spectra are barely informative and hence FLR identification results more difficult. During penumbra, frequencies could correspond to quarter-wave mode events (Del Corpo et al., 2019; Obana et al., 2015). Right panel in Figure 10 represents a quantile-quantile plot (Q-Q plot). The Q-Q plot describes various distributional aspects of the two set of frequencies, actual and estimated; since points in Figure 10 (right panel) accurately follow the identity line (dashed line), the mean value of the two distributions does not show a significant shift. At frequency values higher than 38 mHz, and between 25 and 32 mHz, points move below the bisector, which means that estimated frequencies are slightly lower than actual frequencies in these ranges. As can be noticed from the left panel in Figure 10, the lack of points at higher frequencies (≥ 40 mHz) produces higher errors which nevertheless can be considered as statistical fluctuations.

5.2. The June 2013 Geomagnetic Storm: A Case Study

As already stated in Section 4.2, the geomagnetic storm occurred in June 2013 offers an excellent opportunity to test the algorithm performance since it comprises highly variable geomagnetic conditions with comprehensive data coverage for all the considered station pairs. The two top panels of Figure 11 show the time variations of the Dst and Kp indices, respectively. The main phase starts at the beginning of DoY 152 and proceeds until noon when Dst reaches a minimum value of about -120 nT and Kp rises up to 7. The recovery phase lasts for a few days during which both geomagnetic indices slowly recover to quiet time values. A peculiarity of this event is the prolonged very low geomagnetic activity conditions that characterize the days preceding the storm, allowing us to test the efficiency of the algorithm also in such an unusual situation.

The last four panels in Figure 11 show, from top to bottom, the relative error of the estimated frequency for the four station pairs arranged in decreasing latitude order. As for Figure 9, light and dark shadowed areas correspond to periods in which the field lines have one or both footprint in dark, respectively. The average relative error at $L = 2.4, 2.9, 4.1$ is about $+1-2\%$ suggesting that the distribution of the deviations has a Gaussian-like shape. At $L = 5.5$ the average relative error is about $+4.5\%$ suggesting a systematic overestimation of the algorithm, even if this larger value might be due to a preponderance of positive deviations on DoY 152 during which the main phase of the storm took place. To further evaluate the performance of the algorithm we can look at the average deviation

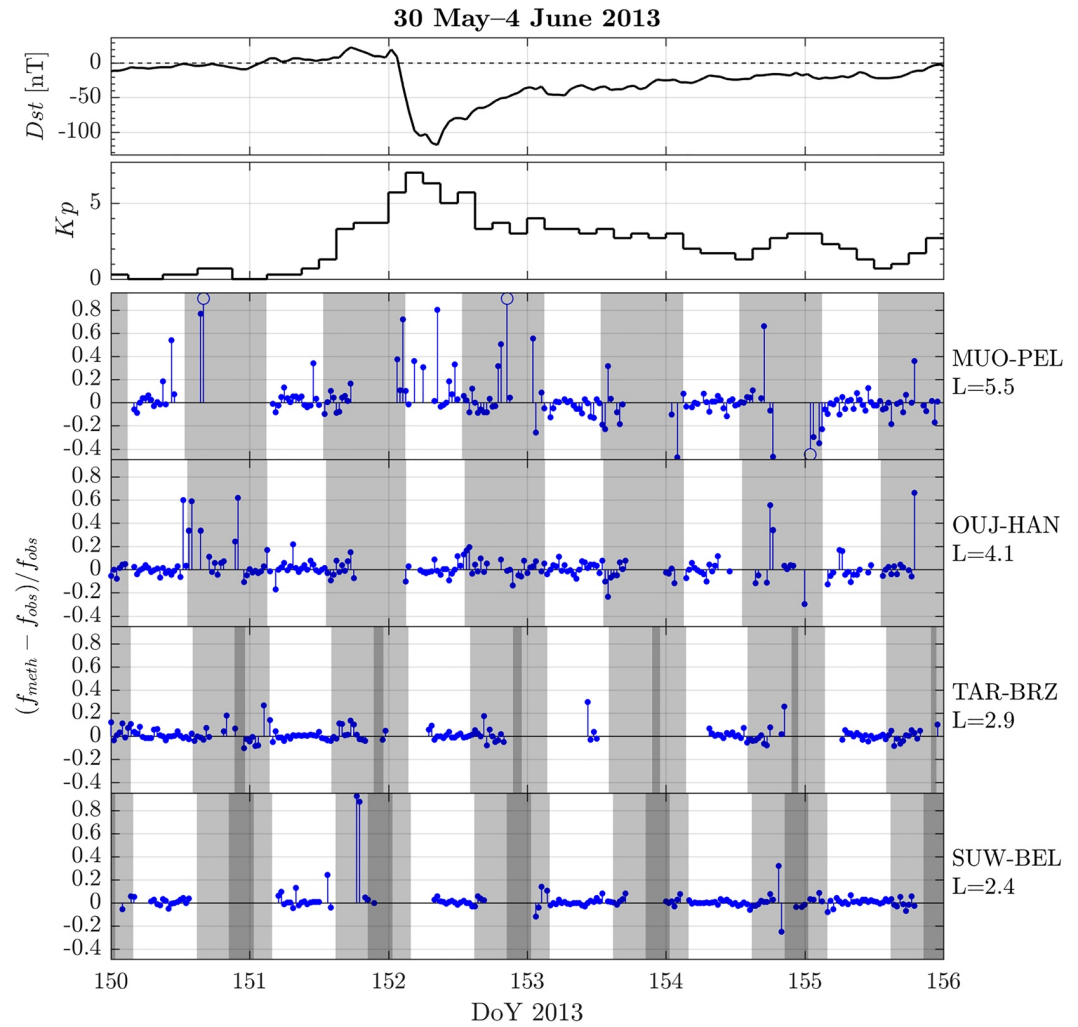


Figure 11. From top to bottom. First two panels represent the Kp and Dst indices respectively during DoY 150–155 of 2013 (30 May to 4 June). It is possible to clearly distinguish between the pre-storm phase (DoY 150 and 151), the main phase (DoY 152) and the recovery phase (DoY 153 and subsequent). The other four panels represent the evolution of the relative error during these six days with the station latitude in descending order. In this representation the difference between stations, the behavior with variable geomagnetic conditions and various data gaps are well evidenced. Points out of graph limits are represented as open circles.

from zero (the MAPE) that does not exceed 13%, although it increases from 4% to 13% with increasing latitude. As already pointed out, this could be due to the signal-to-noise ratio in the cross-phase spectra that becomes lower as the latitude increases. During daytime hours the MAPE assumes the values 2.4%, 2.7%, 4.7%, and 6.9% at $L = 2.4, 2.9, 4.1,$ and $5.5,$ respectively, suggesting that the method performs significantly better in these conditions. Again, there is the exception on DoY 152 at $L = 5.5$ for which the daytime MAPE is 17.5%, indicating that, at least for high latitude pairs, the performance of the method deteriorates during highly dynamical geomagnetic conditions. Also during the extreme quiet conditions on DoY 150 there are some important deviations at $L = 4.1$ and $5.5,$ mainly during nighttime. Other than that, there is no evidence of any dependence of the relative error from the geomagnetic activity. It is important to note that almost all the situations in which the algorithm does not perform well are associated to fuzzy or low signal-to-noise ratio cross-phase spectra for which also the supervised selection can be sometimes questionable. These issues can be better understood looking at Figure 12 which shows the dynamic cross-phase spectra of the four pairs on DoY 151 (panels a–d) and 152 (panels e–h). Black open squares are the frequencies estimated by the algorithm while magenta open circles are the frequencies validated by Del Corpo et al. (2019). The shadowed regions represent dark and light hours as in Figures 9 and 11. The main phase of the storm starts at the beginning of DoY 152, however the magnetosphere is already perturbed in the

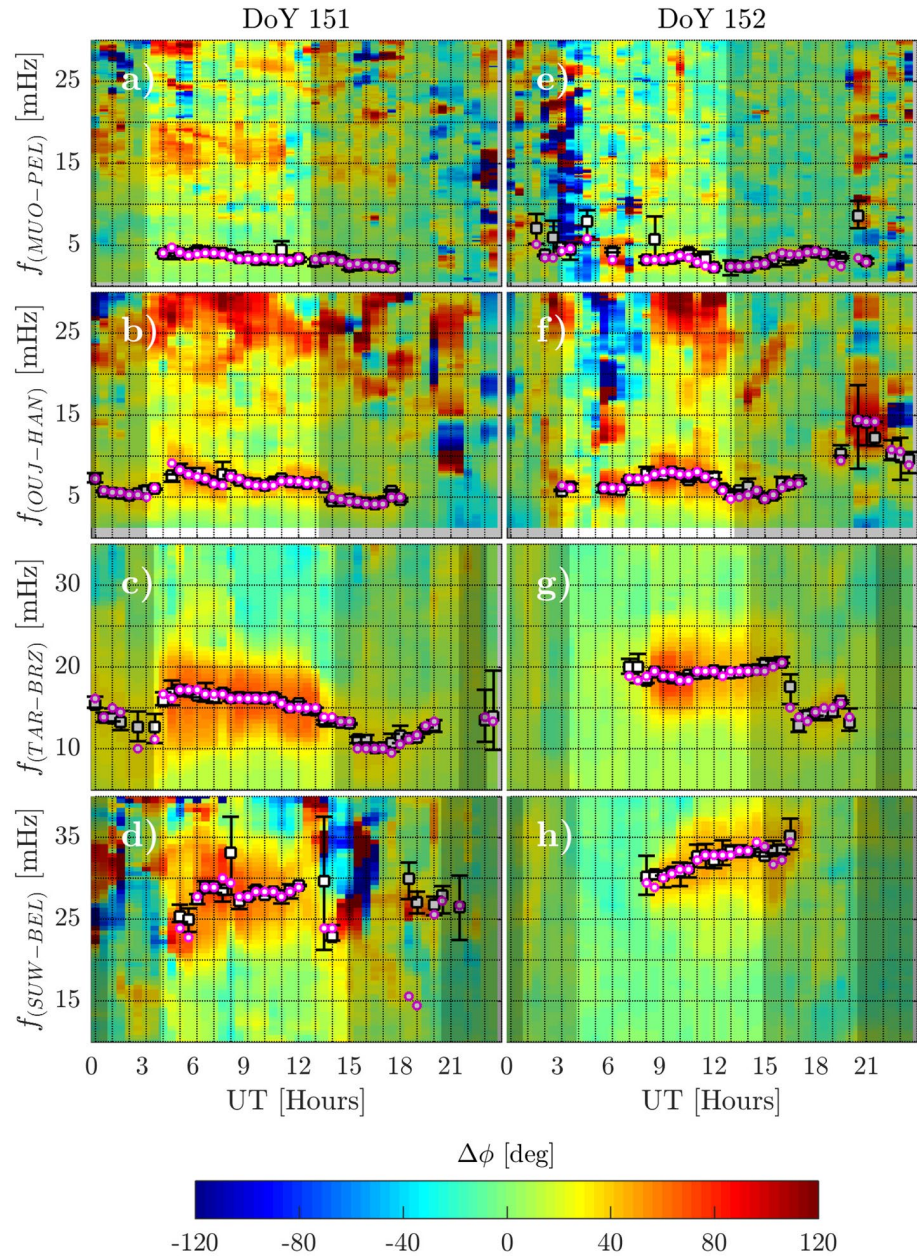


Figure 12. Panel of results obtained with eXtreme Gradient Boost for DoY 151 and 152 (2013). Black points with error bars are the predicted frequencies while the magenta ones are the observed frequencies. DoY 151 is a quiescent day while during DoY 152 (1 June) the main phase of a geomagnetic storm occurs. Such a difference is highlighted by slightly different resonance frequencies between the two days. Predictions show high accordance with observed frequencies in most cases, especially during daytime.

afternoon of DoY 151 as clearly visible from the growing of the K_p index (see Figure 11). During this period the spectra are fuzzy for all the pairs but TAR-BRZ, and important mismatches between the estimated and validated frequencies occur at SUW-BEL on DoY 151 and at MUO-PEL on DoY 152. Such mismatches could not depend exclusively from the algorithm efficacy, but also from the presence of questionable points in the data set by Del Corpo et al. (2019), as is the case for the above mentioned points at SUW-BEL. They created the data set taking particular care to daytime hours when the physical assumptions made in the entire procedure are expected to be applicable, but keeping also nighttime frequencies to study the efficiency of the procedure during these conditions; occasionally, they kept also some unclear points as the ones just described. In this preliminary work we

used the entire data set as it was, analyzing also nocturnal frequencies, but to obtain an operative space weather tool the reliability of the selected night frequencies should be investigated and all questionable data points should be excluded. It is worth noting that, also during nighttime or disturbed geomagnetic conditions, the algorithm performs well when the spectra have smooth and clear traces of the resonance peak. A good example are the spectra of TAR-BRZ (panels c and g) in which the only notable deviations from the validated frequencies arise during discontinuities as in the interval 02:30–03:30 of DoY 151 and at 16:30 on DoY 152, when a quarter wave event and a PBL crossing probably happened. In general, the good performances of the algorithm, mainly during daytime hours, are confirmed.

6. Conclusions

Our work represents a preliminary result in the direction of building a tool for monitoring the plasmasphere dynamics using the whole EMMA network.

We have evaluated several ML algorithms, commonly adopted for regression problems, to estimate FLR frequencies in cross-phase spectra among magnetic field measurements. This survey has proved that ML techniques can be successfully applied for addressing this challenging task; in our particular case tree-based methods have resulted the most reliable algorithms of those considered.

Results have shown a slight dependence of the estimation error with the station latitude, that is, MAPE increases from 4% to 13% passing from $L = 2.4$ to $L = 5.5$, so it remains acceptable even at high latitude. In fact, the percentage of points with an absolute relative error ≤ 0.1 is about 70% for MUO-PEL ($L = 5.5$), and it increases rapidly at OUJ-HAN ($L = 4.1$), 82%, reaching 90% for TAR-BRZ ($L = 2.9$) and SUW-BEL ($L = 2.4$). An interesting aspect evidenced in this analysis is that results generally do not depend on geomagnetic activity, except for high latitude pairs for which extreme geomagnetic conditions (i.e., storm main phase, prolonged quiet conditions) could produce a higher estimation error. We have considered the June 2013 geomagnetic storm as case study; except for $L = 5.5$, when the MAPE reaches values greater than 15% in some points, during this event the estimation error remains around its average value passing from quiescent days to the main phase of the geomagnetic storm, and eventually to the recovery phase. This feature makes our ML procedure particularly reliable for space weather purposes within the framework of the plasmaspheric density nowcast.

However, since we have trained our models only on times with observed FLR frequencies, our procedure is unable to distinguish whether a resonance is triggered. To create a complete automated ML procedure suitable for real-time monitoring, it may be required an additional ML step placed before the one we have already built. To classify times when the FLR frequency can be observed or not, we could follow an approach similar to Balasis et al. (2019), who adopted a fuzzy-logic neural network for classifying periods with ULF activity in geomagnetic field time series.

The present analysis could be mainly improved by extending our training set. First, a larger data set means a more balanced proportion between the number of samples, N , and the number of features, M , that in our case is represented by the number of frequencies in the cross-phase spectra. Then, by extending the data set, we could remove from the training data those FLR frequencies which present an unclear trace on the cross-phase spectrum and hence are considered less reliable (e.g., nighttime frequencies, quarter-waves). Lastly, a larger data set would allow to test our procedure on most varied geomagnetic conditions.

Our approach may be extended to all the EMMA station pairs, and in principle to any magnetometer network, like CARISMA (Mann et al., 2008) and McMAC (Chi et al., 2005). Testing this method on other pairs of stations, even longitudinally separated from EMMA, would allow to obtain more information about the accuracy and the robustness of our technique.

Data Availability Statement

Cross-phase spectra and FLR resonances used to train the ML methods are available from Zenodo (<https://doi.org/10.5281/zenodo.4304662>). The output of the various ML methods are available from Zenodo (<https://doi.org/10.5281/zenodo.4304911>).

Acknowledgments

This work is partially supported by Italian MIUR-PRIN grant 2017APKP7T_004 on *Circumterrestrial Environment: Impact of Sun-Earth Interaction*. We thank the Finnish Meteorological Institute (FMI), the University of Oulu (Finland), the Institute of Geophysics of the Polish Academy of Sciences (IGF-PAS), the Mining and Geological Survey of Hungary (MBFSZ) and the University of L'Aquila for contributing to EMMA. We also acknowledge use of NASA/GSFC's Space Physics Data Facility's OMNIWeb service, and OMNI data. Open Access Funding provided by Università degli Studi dell'Aquila within the CRUI-CARE Agreement.

References

- Allan, W., & Knox, F. B. (1979). A dipole field model for axisymmetric Alfvén waves with finite ionosphere conductivities. *Planetary and Space Science*, 27(1), 79–85. [https://doi.org/10.1016/0032-0633\(79\)90149-1](https://doi.org/10.1016/0032-0633(79)90149-1)
- Armstrong, J. A., & Fletcher, L. (2019). Fast solar image classification using deep learning and its importance for automation in solar physics. *Solar Physics*, 294(80). <https://doi.org/10.1007/s1207-019-1473-z>
- Balasis, G., Ainalragia-Giamini, S., Papadimitriou, C., Daglis, I. A., Anastasiadis, A., & Haagmans, R. (2019). A machine learning approach for automated ulf wave recognition. *Journal of Space Weather and Space Climate*, 9, A13. <https://doi.org/10.1051/swsc/2019010>
- Bao, X., Jiang, D., Yang, X., & Wang, H. (2021). An improved deep belief network for traffic prediction considering weather factors. *Alexandria Engineering Journal*, 60, 413–420. <https://doi.org/10.1016/j.aej.2020.09.003>
- Baransky, L. N., Borovkov, J. E., Gokhberg, M. B., Krylov, S. M., & Troitskaya, V. A. (1985). High resolution method of direct measurement of the magnetic field lines' Eigen frequencies. *Planetary and Space Science*, 33(12), 1369–1374. [https://doi.org/10.1016/0032-0633\(85\)90112-6](https://doi.org/10.1016/0032-0633(85)90112-6)
- Berube, D., Moldwin, M. B., & Weygand, J. M. (2003). An automated method for the detection of field line resonance frequencies using ground magnetometer techniques. *Journal of Geophysical Research*, 108(A9), 1348. <https://doi.org/10.1029/2002JA009737>
- Boynton, R., Balikhin, M., Wei, H.-L., & Lang, Z.-Q. (2018). Applications of NARMAX in space weather. In E. Camporeale, J. Johnson, & S. Wing (Eds.), *Machine learning techniques for space weather* (p. 203 - 236). Elsevier. <https://doi.org/10.1016/B978-0-12-811788-0.00008-1>
- Breiman, L. (1996). Bagging predictors. *Machine Learning*, 24, 123–140. <https://doi.org/10.1023/A:1018054314350>
- Breiman, L., Friedman, J. H., Olshen, R. A., & Stone, C. J. (1984). *Classification and regression trees*. Wadsworth. <https://doi.org/10.1201/9781315139470>
- Breuillard, H., Dupuis, R., Retino, A., Le Contel, O., Amaya, J., & Lapenta, G. (2020). Automatic classification of plasma regions in near-Earth space with supervised machine learning: Application to magnetospheric multi scale 2016–2019 observations. *Frontiers in Astronomy and Space Sciences*, 7, 55. <https://doi.org/10.3389/fspas.2020.00055>
- Buhlmann, P. (2012). *Bagging, boosting and ensemble learning*. Springer-Verlag. https://doi.org/10.1007/978-3-642-21551-3_33
- Buntine, W., & Niblett, T. (1992). A further comparison of splitting rules for decision-tree induction. *Machine Learning*, 8, 75–85. <https://doi.org/10.1007/BF00994006>
- Camporeale, E., Wing, S., & Johnson, J. R. (2018). Introduction. In E. Camporeale, J. Johnson, & S. Wing (Eds.), *Machine learning techniques for space weather* (pp. XIII–XVIII). Elsevier. <https://doi.org/10.1016/B978-0-12-811788-0.09987-x>
- Carpenter, D. L., & Anderson, R. R. (1992). An ISEE/whistler model of equatorial electron density in the magnetosphere. *Journal of Geophysical Research*, 97(A2), 1097–1108. <https://doi.org/10.1029/91JA01548>
- Carpenter, D. L., & Lemaire, J. (2004). The plasmasphere boundary layer. *Annales Geophysicae*, 22(12), 4291–4298. <https://doi.org/10.5194/angeo-22-4291-2004>
- Chandorkar, M., & Camporeale, E. (2018). Probabilistic forecasting of geomagnetic indices using Gaussian process models. In E. Camporeale, J. Johnson, & S. Wing (Eds.), *Machine learning techniques for space weather* (pp. 237–258). Elsevier. <https://doi.org/10.1016/B978-0-12-811788-0.00009-3>
- Chen, T., & Guestrin, C. (2016). XGBoost. In *Proceedings of the 22nd ACM SIGKDD international conference on knowledge discovery and data mining*. <https://doi.org/10.1145/2939672.2939785>
- Chi, P. J., Engebretson, M. J., Moldwin, M. B., Russell, C. T., Mann, I. R., Hairston, M. R., et al. (2013). Sounding of the plasmasphere by Mid-continent MAGnetoseismic Chain (McMAC) magnetometers. *Journal of Geophysical Research: Space Physics*, 118(6), 3077–3086. <https://doi.org/10.1002/jgra.50274>
- Chi, P. J., Engebretson, M. J., Moldwin, M. B., Russell, C. T., Mann, I. R., Samson, J. C., & Lee, D. H. (2005). Mid-continent magnetoseismic chain (McMAC): A meridional magnetometer chain for magnetospheric sounding. In *Proceedings of the environment modeling workshop* (pp. 17–22).
- Cortes, C., & Vapnik, V. (1995). Support-vector networks. *Machine Learning*, 20(3), 273–297. <https://doi.org/10.1007/BF00994018>
- Del Corpo, A., & Vellante, M. (2020). *Field line resonances observed by EMMA*. ver. 1.0.0 [Data set] Zenodo. <https://doi.org/10.5281/zenodo.4304662>
- Del Corpo, A., Vellante, M., Heilig, B., Pietropaolo, E., Reda, J., & Lichtenberger, J. (2019). Observing the cold plasma in the Earth's magnetosphere with the EMMA network. *Annals of Geophysics*, 61(4). <https://doi.org/10.4401/ag-7751>
- Del Corpo, A., Vellante, M., Heilig, B., Pietropaolo, E., Reda, J., & Lichtenberger, J. (2020). An empirical model for the dayside magnetospheric plasma mass density derived from EMMA magnetometer network observations. *Journal of Geophysical Research: Space Physics*, 125(2), e2019JA027381. <https://doi.org/10.1029/2019JA027381>
- Esposito, F., Malerba, D., Semeraro, G., & Kay, J. (1997). A comparative analysis of methods for pruning decision trees. *IEEE Transactions on Pattern Analysis and Machine Intelligence*, 19(5), 476–491. <https://doi.org/10.1109/34.589207>
- Ferri, F., Pudil, P., Hatf, M., & Kittler, J. (1994). Comparative study of techniques for large-scale feature selection. In E. S. Gelsema & L. S. Kanal (Eds.), *Pattern recognition in practice iv* (Vol. 16, pp. 403–413). North-Holland. <https://doi.org/10.1016/B978-0-444-81892-8.50040-7>
- Foldes, R., Del Corpo, A., Pietropaolo, E., & Vellante, M. (2020). *Field line resonances estimated using machine learning methods*. ver. 1.0.0 [Data set] Zenodo. <https://doi.org/10.5281/zenodo.4304911>
- Fraser, B., Horwitz, J., Slavin, J., Dent, Z., & Mann, I. (2005). Heavy ion mass loading of the geomagnetic field near the plasmopause and ULF wave implications. *Geophysical Research Letters*, 32(4), L04102. <https://doi.org/10.1029/2004GL021315>
- Fujimoto, A., Obana, Y., & Saita, S. (2019). Seasonal variation in plasmaspheric mass density in the New Zealand meridian. In (Vol. 2019, pp. SM51B–3186).
- Gallagher, D., Craven, P., & Comfort, R. (1988). An empirical model of the Earth's plasmasphere. *Advances in Space Research*, 8(8), 15–24. [https://doi.org/10.1016/0273-1177\(88\)90258-X](https://doi.org/10.1016/0273-1177(88)90258-X)
- Guyon, I., & Elisseeff, A. (2003). An introduction to variable and feature selection. *Journal of Machine Learning Research*, 3, 1157–1182. <https://doi.org/10.1162/15324430322753616>
- Heidrich-Meisner, V., & Wimmer-Schweingruber, R. F. (2018). Chapter 16—Solar wind classification via k-means clustering algorithm. In E. Camporeale, J. Johnson, & S. Wing (Eds.), *Machine learning techniques for space weather* (pp. 397–424). Elsevier. <https://doi.org/10.1016/B978-0-12-811788-0.00016-0>
- Hoerl, A. E., & Kennard, R. W. (1970). Ridge regression: Biased estimation for nonorthogonal problems. *Technometrics*, 12(1), 55–67. <https://doi.org/10.1080/00401706.1970.10488634>
- Hua, J., Xiong, Z., Lowey, J., Suh, E., & Dougherty, E. R. (2004). Optimal number of features as a function of sample size for various classification rules. *Bioinformatics*, 21(8), 1509–1515. <https://doi.org/10.1093/bioinformatics/bti171>

- Ivanov, S., Tsizh, M., Ullmann, D., Panos, B., & Voloshynovskiy, S. (2020). Solar activity classification based on mg ii spectra: Toward classification on compressed data. *arXiv*. Retrieved From <https://arxiv.org/abs/2009.07156>
- Kapetanios, G. (2007). Variable selection in regression models using nonstandard optimisation of information criteria. *Computational Statistics & Data Analysis*, *52*(1), 4–15. <https://doi.org/10.1016/j.csda.2007.04.006>
- Ke, G., Meng, Q., Finley, T., Wang, T., Wei, C., Ma, W., et al. (2017). Lightgbm: A highly efficient gradient boosting decision tree. In *Nips'17: Proceedings of the 31st international conference on neural information processing systems* (pp. 3149–3157).
- Kumar, B., Vyas, O. P., & Vyas, R. (2019). A comprehensive review on the variants of support vector machines. *Modern Physics Letters B*, *33*(25). <https://doi.org/10.1142/S0217984919503032>
- Kunte, A., & Panicker, S. (2020). Personality prediction of social network users using ensemble and xgboost. In H. Das, P. K. Pattnaik, S. S. Rautaray, & K.-C. Li (Eds.), *Progress in computing, analytics and networking* (pp. 133–140). Springer Singapore. https://doi.org/10.1007/978-981-15-2414-1_14
- Lal, T. N., Chapelle, O., Weston, J., & Elisseeff, A. (2006). Embedded methods. In I. Guyon, M. Nikravesh, S. Gunn, & L. A. Zadeh (Eds.), *Feature extraction: Foundations and applications* (pp. 137–165). Springer Berlin Heidelberg. https://doi.org/10.1007/978-3-540-35488-8_6
- Li, R.-H., & Belford, G. G. (2002). Instability of decision tree classification algorithms. In *Proceedings of ACM SIGKDD international conference on knowledge discovery and data mining*. <https://doi.org/10.1145/775047.775131>
- Lichtenberger, J., Clilverd, M. A., Heilig, B., Vellante, M., Manninen, J., Rodger, C. J., et al. (2013). The plasmasphere during a space weather event: First results from the PLASMON project. *Journal of Space Weather and Space Climate*, *3*, A23. <https://doi.org/10.1051/swsc/2013045>
- Liemohn, M. W. (2006). Introduction to special section on “results of the national science foundation geospace environment modeling inner magnetosphere/storms assessment challenge”. *Journal of Geophysical Research*, *111*, A11S01. <https://doi.org/10.1029/2006JA011970>
- Liu, J., Ye, Y., Shen, C., Wang, Y., & Erdélyi, R. (2018). A new tool for CME arrival time prediction using machine learning algorithms: CAT-PUMA. *The Astrophysical Journal*, *855*(2), 109. <https://doi.org/10.3847/1538-4357/aaac69>
- Luckner, M., Topolski, B., & Mazurek, M. (2017). Application of xgboost algorithm in fingerprinting localisation task. https://doi.org/10.1007/978-3-319-59105-6_57
- Mann, I., Milling, D., Rae, I. J., Ozeke, L., Kale, A., Kale, Z., et al. (2008). The upgraded CARISMA magnetometer array in the THEMIS era. *Space Science Reviews*, *141*, 413–451. <https://doi.org/10.1007/s11214-008-9457-6>
- Massone, A. M., Piana, M., & Consortium, F. (2018). Chapter 14—Machine learning for flare forecasting. In E. Camporeale, J. Johnson, & S. Wing (Eds.), *Machine learning techniques for space weather* (pp. 355–364). Elsevier. <https://doi.org/10.1016/B978-0-12-811788-0.00014-7>
- Menk, F. W., Mann, I. R., Smith, A. J., Waters, C. L., Clilverd, M. A., & Milling, D. K. (2004). Monitoring the plasmapause using geomagnetic field line resonances. *Journal of Geophysical Research*, *109*, A04216. <https://doi.org/10.1029/2003JA010097>
- Milling, D. K., Mann, I. R., & Menk, F. W. (2001). Diagnosing the plasmapause with a network of closely spaced ground-based magnetometers. *Geophysical Research Letters*, *28*(1), 115–118. <https://doi.org/10.1029/2000GL011935>
- Moldwin, M. B., Downward, L., Rassoul, H., Amin, R., & Anderson, R. (2002). A new model of the location of the plasmapause: CRRES results. *Journal of Geophysical Research*, *107*(A11), 1339. <https://doi.org/10.1029/2001JA009211>
- Murphy, K. P. (2012). *Machine learning: A probabilistic perspective*. The MIT Press. <https://doi.org/10.1109/iroso.2012.6386118>
- Obana, Y., Menk, F. W., Sciffer, M. D., & Waters, C. L. (2008). Quarter-wave modes of standing Alfvén waves detected by cross-phase analysis. *Journal of Geophysical Research*, *113*(A8). <https://doi.org/10.1029/2007JA012917>
- Obana, Y., Waters, C. L., Sciffer, M. D., Menk, F. W., Lysak, R. L., Shiokawa, K., et al. (2015). Resonance structure and mode transition of quarter-wave ULF pulsations around the dawn terminator. *Journal of Geophysical Research: Space Physics*, *120*(6), 4194–4212. <https://doi.org/10.1002/2015JA021096>
- Peng, H., Long, F., & Ding, C. (2005). Feature selection based on mutual information criteria of max-dependency, max-relevance, and min-redundancy. *IEEE Transactions on Pattern Analysis and Machine Intelligence*, *27*(8), 1226–1238. <https://doi.org/10.1109/TPAMI.2005.159>
- Schulz, M. (1996). Eigenfrequencies of geomagnetic field lines and implications for plasma-density modeling. *Journal of Geophysical Research*, *101*(A8), 17385–17397. <https://doi.org/10.1029/95JA03727>
- Sheeley, B., Moldwin, M., Rassoul, H., & Anderson, R. (2001). An empirical plasmasphere and trough density model: CRRES observations. *Journal of Geophysical Research*, *106*(A11), 25631–25641. <https://doi.org/10.1029/2000JA000286>
- Singer, H., Southwood, D., Walker, R., & Kivelson, M. (1981). Alfvén wave resonances in a realistic magnetospheric magnetic field geometry. *Journal of Geophysical Research*, *86*(A6), 4589–4596. <https://doi.org/10.1029/JA086iA06p04589>
- Stepanova, M., Antonova, E. E., Moya, P. S., & Pinto, J. A. (2019). Multisatellite analysis of plasma pressure in the inner magnetosphere during the 1 June 2013 geomagnetic storm. *Journal of Geophysical Research: Space Physics*, *124*. <https://doi.org/10.1029/2018JA025965>
- Takahashi, K., Denton, R. E., Anderson, R. R., & Hughes, W. J. (2006). Mass density inferred from toroidal wave frequencies and its comparison to electron density. *Journal of Geophysical Research*, *111*, A01201. <https://doi.org/10.1029/2005JA011286>
- Takahashi, K., Vellante, M., Del Corpo, A., Claudepierre, S. G., Kletzing, C., Wygant, J., & Koga, K. (2020). Multiharmonic toroidal standing Alfvén waves in the midnight sector observed during a geomagnetically quiet period. *Journal of Geophysical Research: Space Physics*, *125*(3), e2019JA027370. <https://doi.org/10.1029/2019JA027370>
- Thaller, S. A., Wygant, J. R., Dai, L., Breneman, A. W., Kersten, K., Cattell, C. A., et al. (2015). Van Allen probes investigation of the large-scale duskward electric field and its role in ring current formation and plasmasphere erosion in the 1 June 2013 storm. *Journal of Geophysical Research: Space Physics*, *120*(6), 4531–4543. <https://doi.org/10.1002/2014JA020875>
- Theodoridis, S., & Koutroumbas, K. (2008). *Pattern recognition* (4th ed.). Academic Press, Inc. <https://doi.org/10.1016/B978-1-59749-272-0.X0001-2>
- Thorne, R. M. (2010). Radiation belt dynamics: The importance of wave-particle interactions. *Geophysical Research Letters*, *37*, L22107. <https://doi.org/10.1029/2010GL044990>
- Tsyganenko, N. A., & Sitnov, M. I. (2005). Modeling the dynamics of the inner magnetosphere during strong geomagnetic storms. *Journal of Geophysical Research*, *110*(A3). <https://doi.org/10.1029/2004JA010798>
- Vellante, M., Förster, M., Villante, U., Zhang, T. L., & Magnes, W. (2007). Solar activity dependence of geomagnetic field line resonance frequencies at low latitudes. *Journal of Geophysical Research: Space Physics*, *112*, A02205. <https://doi.org/10.1029/2006JA011909>
- Waters, C. L., Menk, F. W., & Fraser, B. J. (1991). The resonance structure of low latitude Pc3 geomagnetic pulsations. *Geophysical Research Letters*, *18*(12), 2293–2296. <https://doi.org/10.1029/91GL02550>
- Wharton, S. J., Wright, D. M., Yeoman, T. K., James, M. K., & Sandhu, J. K. (2018). Cross-phase determination of ultralow frequency wave harmonic frequencies and their associated plasma mass density distributions. *Journal of Geophysical Research: Space Physics*, *123*(8), 6231–6250. <https://doi.org/10.1029/2018JA025487>

- Wing, S., Johnson, J. R., Camporeale, E., & Reeves, G. D. (2018). Chapter 6 - Untangling the solar wind drivers of the radiation belt: An information theoretical approach. In E. Camporeale, J. Johnson, & S. Wing (Eds.), *Machine learning techniques for space weather* (pp. 149–175). Elsevier. <https://doi.org/10.1016/B978-0-12-811788-0.00006-8>
- Yang, H., Huang, K., King, I., & Lyu, M. R. (2009). Localized support vector regression for time series prediction. *Neurocomputing*, 72(10), 2659–2669. (Lattice Computing and Natural Computing (JCIS 2007)/Neural Networks in Intelligent Systems Design (ISDA 2007)) <https://doi.org/10.1016/j.neucom.2008.09.014>
- Zhelavskaya, I. S., Shprits, Y. Y., & Spasojević, M. (2017). Empirical modeling of the plasmasphere dynamics using neural networks. *Journal of Geophysical Research: Space Physics*, 122(11), 11227–11244. <https://doi.org/10.1002/2017JA024406>
- Zhelavskaya, I. S., Spasojevic, M., Shprits, Y. Y., & Kurth, W. S. (2016). Automated determination of electron density from electric field measurements on the van Allen probes spacecraft. *Journal of Geophysical Research: Space Physics*, 121(5), 4611–4625. <https://doi.org/10.1002/2015JA022132>
- Zou, S., Ridley, A., Jia, X., Boyd, E., Nicolls, M., Coster, A., et al. (2017). PFISR observation of intense ion upflow fluxes associated with an SED during the 1 June 2013 geomagnetic storm. *Journal of Geophysical Research: Space Physics*, 122(2), 2589–2604. <https://doi.org/10.1002/2016JA023697>

Appendix C

FLAME: Fast Lattice Boltzmann Algorithm for Magnetohydrodynamics (MHD) Experiments

In this chapter, we briefly introduce the theoretical background, the context and the reasoning behind the development of a Lattice-Boltzmann (LB) solver for plasmas in the magneto-hydrodynamics (MHD) and Hall magneto-hydrodynamics (Hall-MHD) regimes. The implemented code, Fast Lattice-Boltzmann Algorithm for MHD Experiments (FLAME) relies on a multi-GPU (Graphic Processing Unit) implementation of the LB scheme to reach high resolution with acceptable computational times. In the frame of ideal MHD turbulence, plasma is treated as a single species quasi-neutral conductive fluid responsive to the effect of the magnetic field [83]; ions and electrons are tied to the magnetic field, moving with the same velocity. The Hall magneto-hydrodynamics (Hall-MHD) model is a finer representation of plasma, taking into account smaller-scale effects. Indeed, it relaxes the MHD hypotheses assuming ions disentangled from the magnetic field due to their inertia, while electrons remain bound to it [168]. In this framework, the resistive Ohm's law is generalized through the introduction of the Hall term, proportional to $\mathbf{J} \times \mathbf{B}$,

where \mathbf{J} and \mathbf{B} denote the current density and the magnetic field, respectively. The Hall electric field acts on the plasma dynamics at length scales shorter than the ion inertial length $d_i = c/\omega_{pi}$ (with ω_{pi} the ion plasma frequency and c the speed of light), even identified as time scales shorter than the ion cyclotron period $1/\omega_{ci}$ [97]. Hall-MHD has been successfully adopted in literature to describe a variety of astrophysical, space and laboratory environments to study how the introduction of the Hall current affects the plasma dynamics in different scenarios. In the astrophysical context, their applications span from the star formation [164, 134, 231], and the solar atmosphere and the solar wind at Earth distance [85, 90], to the dynamo action [149, 151, 89] and the Earth and planetary magnetospheres [120, 66, 233, 210]. Several studies show that the Hall effect is central in enhancing the rate of magnetic reconnection [225, 156, 126, 125]. Moreover, its effect can also be employed to explain the steepening of the power spectrum of the magnetic field, showing otherwise a power-law slope close to $-5/3$ (as in the Kolmogorov hydrodynamic theory) at large scale (MHD scale). Indeed, at scales above the ion inertial length the spectrum shows a steeper trend, even though the value of the spectral index and the nature of this additional inertial range are strongly debated. Some theoretical and numerical works predicted a value close to $-7/3$ [85, 96], due to either the Hall term or the effect of faster wave modes on the non-linear interactions. However, most spacecrafts observations (principally in the near-Earth solar wind) suggest a steeper value, between -2.6 and -3 [100, 3], also reported in other numerical studies [76, 44].

A major difficulty in simulating Hall-MHD is related to the need to resolve fast phenomena such as whistler and Hall-drift waves, evolving on faster dynamics than Alfvén waves and requiring smaller time steps. To properly account for the propagation of the perturbations caused by the Hall effect, it is necessary to capture those plasma waves with $\max(c_w) \propto 1/\Delta x$, at the smallest resolved wavelength Δx . The Courant-Friedrichs-Lewy (CFL) condition then yields $\Delta t \propto \Delta x^2$. This scaling implies a rapid decrease in the time step as the spatial resolution increases, which poses severe limitations in terms of computational cost. Nevertheless, several different numerical schemes performing Hall-MHD simulations have been developed over the years; pseudo-spectral methods [150] are commonly recognized as having the most ac-

curate representation of the fields at the resolved dynamical scales [173], however also finite-volume [209, 135] or hybrid particle-in-cell codes [125, 170] have been widely adopted. Here, we propose a Lattice-Boltzmann (LB) implementation of the Hall magneto-hydrodynamics (Hall-MHD) equations representing a valuable alternative to more established algorithms and providing a convenient trade-off between accuracy and computational efficiency. Indeed, unlike more traditional methods that solve the dynamics of flows at the macroscopic level, Lattice-Boltzmann method (LBM) operate at an underlying mesoscopic level, in which the flow complexity emerges from re-iterating simple rules of collision and streaming of populations of particles moving along the links of a regular cubic lattice [108]. Therefore, its intrinsically discrete nature and focus on the local dynamics, makes it computationally extremely efficient [104]. Also, these reasons encouraged us to pursue the LB modeling to simulate Hall-MHD turbulence, an effort that has never been undertaken. The development of FLAME was also strongly motivated by the need of the community for innovative numerical tools for the study of space plasma turbulent dynamics at scales that are by now within reach of high-resolution on-board spacecraft's instruments, such as the ESA mission Solar Orbiter [158].

In this work, the implemented code, FLAME, is validated at first against an analytical solution of the dissipative Hall-MHD equations [232], and then against MHD simulations performed with the Geophysical High-Order Suite for Turbulence (GHOST) code, providing optimal results of FLAME in terms of stability and accuracy. As an example, in a regime of high Reynolds numbers, we show that LB simulations are able to reproduce the break in the magnetic energy spectrum at sub-ion scales, in perfect agreement with solar-wind measurements. Numerical simulations of MHD and Hall-MHD turbulence performed with FLAME have been used for comparisons of high-order statistics with magnetic field measurements in the solar wind, showing also in this case a good agreement.

Efficient kinetic Lattice Boltzmann simulation of three-dimensional Hall-MHD Turbulence

Raffaello Foldes^{†1,2}, Emmanuel Lévêque², Raffaele Marino², Ermanno Pietropaolo¹, Alessandro De Rosis³, Daniele Telloni⁴ and Fabio Feraco²

¹Dipartimento di Scienze Fisiche e Chimiche, Università dell'Aquila, 67100 Coppito (AQ), Italy

²Univ Lyon, CNRS, École Centrale de Lyon, INSA Lyon, Univ Claude Bernard Lyon I, LMFA UMR 5509, F-69134 Ecully cedex, France

³Department of Mechanical, Aerospace and Civil Engineering, The University of Manchester, Manchester M13 9PL, United Kingdom

⁴National Institute for Astrophysics - Astrophysical Observatory of Torino, Via Osservatorio 20, I-10025 Pino Torinese, Italy

(Received xx; revised xx; accepted xx)

For the purpose of Open Access, a CC-BY public copyright licence has been applied by the authors to the present document and will be applied to all subsequent versions up to the Author Accepted Manuscript arising from this submission

Simulating plasmas in the Hall-MagnetoHydroDynamics (Hall-MHD) regime represents a valuable approach for the investigation of complex non-linear dynamics developing in astrophysical frameworks and fusion machines. Taking into account the Hall electric field is computationally very challenging as it involves the integration of an additional term, proportional to $\nabla \times ((\nabla \times \mathbf{B}) \times \mathbf{B})$ in the Faraday's induction law. The latter feeds back on the magnetic field \mathbf{B} at small scales (between the ion and electron inertial scales), requiring very high resolutions in both space and time in order to properly describe its dynamics. The computational advantage provided by the kinetic Lattice Boltzmann (LB) approach is exploited here to develop a new code, the **F**ast **L**attice-**B**oltzmann **A**lgorithm for **M**HD **E**xperiments (**FLAME**). The **FLAME** code integrates the plasma dynamics in lattice units coupling two kinetic schemes, one for the fluid protons (including the Lorentz force), the other to solve the induction equation describing the evolution of the magnetic field. Here, the newly developed algorithm is tested against an analytical wave-solution of the dissipative Hall-MHD equations, pointing out its stability and second-order convergence, over a wide range of the control parameters. Spectral properties of the simulated plasma are finally compared with those obtained from numerical solutions from the well-established pseudo-spectral code **GHOST**. Furthermore, the LB simulations we present, varying the Hall parameter, highlight the transition from the MHD to the Hall-MHD regime, in excellent agreement with the magnetic field spectra measured in the solar wind.

1. Introduction

In the frame of the MHD model, plasma is treated as a single species quasi-neutral fluid with conductive properties sensitive to the action of the magnetic field (Galtier

[†] Email address for correspondence: raffaello.foldes@ec-lyon.fr

2016). In the ideal MHD description, ions and electrons are tied to the magnetic field, moving with the same velocity. The Hall-MHD model relaxes the MHD prescriptions assuming ions disunite from the magnetic field due to their inertia, while electrons remain bound to it (Pandey & Wardle 2008). In this framework, the resistive Ohm's law is generalized through the introduction of the Hall electric field, proportional to $\mathbf{J} \times \mathbf{B}$, where \mathbf{J} and \mathbf{B} denote the current density and the magnetic field, respectively. The Hall electric field has an effect on the magnetic field at length scales shorter than the ion inertial length $d_i = c/\omega_{pi}$ (ω_{pi} being the ion plasma frequency, c the speed of light) as well as at time scales shorter than the ion cyclotron period $1/\omega_{ci}$ (Huba 2003). The scale d_i corresponds to the scale at which ions and electrons decouple, and the magnetic field becomes frozen into the electron fluid rather than in the bulk plasma. Hall-MHD has been already adopted in literature to describe a variety of astrophysical, space and laboratory environments, and to provide a detailed description of plasma dynamics. Its applications span from the star formation (Norman & Heyvaerts 1985; Marchand, P. *et al.* 2018) to the solar atmosphere and the solar wind (Galtier & Buchlin 2007; González-Morales *et al.* 2019), and it has been used also to investigate magnetic reconnection processes (Wang *et al.* 2001; Morales *et al.* 2005; Ma *et al.* 2018) and the dynamo action (Mininni *et al.* 2002, 2005; Gómez *et al.* 2010). A major difficulty in simulating Hall-MHD is related to the need to resolve whistler waves, evolving on fast dynamics with a phase speed $c_w(k) \propto k$ increasing linearly with the wavenumber k . In order to properly account for the propagation of the perturbations caused by the Hall effect, it is, therefore, necessary to capture those plasma waves with $\max(c_w) \propto 1/\Delta x$, at the smallest resolved wavelength Δx . The Courant-Friedrichs-Lewy (CFL) condition then yields $\Delta t \propto \Delta x^2$. This scaling implies a rapid decrease of the time-step as the spatial resolution increases, which poses severe limitations in terms of computational cost. Nevertheless, Hall-MHD simulations have been proposed over the years in numerous studies, through the integration of the equations with pseudo-spectral (Mininni *et al.* 2003), finite-volume (Tóth *et al.* 2008; Marchand, P. *et al.* 2018) or hybrid particle-in-cell codes (Ma *et al.* 2018; Papini *et al.* 2019). When dealing with turbulent flows, pseudo-spectral methods are usually recognized as the best option that allows for an equally-accurate representation of the fields at the resolved dynamical scales (Patterson & Orszag 1971). On the other hand, their computational cost can be prohibitive (as mentioned before) when it comes to the integration of simulations in three dimensions and for many turnover times (Huba 2003). The main purpose of the novel code that we developed here, FLAME (**F**ast **L**attice-**B**oltzmann **A**lgorithm for **M**HD **E**xperiments), is to overcome this issue. Indeed, the Lattice Boltzmann (LB) implementation provides an alternative to achieve a convenient trade-off between accuracy and computational efficiency. Unlike more traditional methods that solve the dynamics of flows at the macroscopic level, LB methods operate at an underlying mesoscopic kinetic level. The flow complexity emerges from re-iterating simple rules of collision and streaming of populations of particles moving along the links of a regular cubic lattice (Krueger *et al.* 2016). The connection between such an idealized representation and the macroscopic dynamics is by now well-established and accepted, placing the method on a solid theoretical and mathematical ground (Shan & He 1998). Furthermore, due to its intrinsically discrete nature and its focus on the local dynamics, it is also computationally extremely efficient (Körner *et al.* 2006). A decisive contribution to make possible the simulation of ideal MHD plasmas by means of LB methods was made by Dellar (2002), who showed that the native LB framework based on the Bhatnagar-Gross-Krook (BGK) collision (Bhatnagar *et al.* 1954) could be consistently extended to encompass both the fluid dynamics driven by the Lorentz force and the induction equation for the magnetic field. The scheme introduced by Dellar

overcomes the major limitations of previous efforts (Montgomery & Doolen 1987; Chen *et al.* 1991; Succi *et al.* 1991; Martínez *et al.* 1994) and fully complies with the macroscopic MHD equations in a weakly-compressible formulation (see §3). Nevertheless, it is prone to develop numerical instabilities when strong gradients emerge in the flow, thus delaying in the community its implementation for the simulation of turbulent fluid frameworks. More recently, De Rosis *et al.* (2018) have shown that it is possible to prevent the simulation to become unstable by replacing the original BGK collision with an operator defined in the space of moments, allowing the explicit damping of the *non-hydrodynamic modes* responsible for the onset of spurious instabilities. An entropic stabilization has also been proposed by Flint & Vahala (2018), though leading to a more complicated scheme. These advances encouraged us to pursue the LB modeling to simulate Hall-MHD turbulence, an effort that has never been undertaken previously. The development of FLAME was also strongly motivated by the need of the community for innovative numerical tools for the study of space plasma turbulent dynamics at scales that are by now within the reach of high-resolution instruments on board spacecrafts, such as the ESA mission Solar Orbiter (Müller *et al.* 2020a).

The paper is organized as follows. In §2, the Hall-MHD equations are presented in a form that is relevant for LB developments. The LB scheme implemented in FLAME is introduced and discussed in §3. The coupling between the fluid and the magnetic lattices is explained, as well as the inclusion of the Hall effect in the collision operator. The conversion from physical to lattice units is discussed in great detail. §4 is devoted to the validation of the code against an analytical solution of the dissipative Hall-MHD equations (Xia & Yang 2015). This section provides an assessment of the numerical stability and a quantitative estimation of the dispersion and dissipation errors. The computational efficiency is discussed in §5, where GPU-accelerated simulations of the three-dimensional Orszag-Tang vortex problem are considered (Orszag & Tang 1979). In a regime of high Reynolds numbers, we show that LB simulations are able to reproduce the break in the magnetic energy spectrum at sub-ion scales, in perfect agreement with solar-wind measurements. Finally, we outline potential applications for the investigation of space plasmas in §6, and draw conclusions in §7.

2. The Hall-MHD equations

In this section, the Hall-MHD equations are introduced in the standard incompressible approximation and in a weakly-compressible formulation, suitable for LB developments.

2.1. Incompressible formulation

In this context, when we refer to the macroscopic description of the plasma what we mean is the description of the prognostic fields appearing in the model equations. Thus, at the macroscopic level, the incompressible resistive MHD equations for an electrically conductive quasi-neutral fluid consist of the incompressible Navier-Stokes equations with the addition of the Lorentz force, coupled with the resistive induction equation for the magnetic field:

$$\nabla \cdot \mathbf{U} = 0 \quad (2.1)$$

$$\partial_t \mathbf{U} + (\mathbf{U} \cdot \nabla) \mathbf{U} = \frac{1}{\rho_0} \mathbf{J} \times \mathbf{B} - \frac{1}{\rho_0} \nabla p + \nu \nabla^2 \mathbf{U} \quad (2.2)$$

$$\partial_t \mathbf{B} = \nabla \times (\mathbf{U} \times \mathbf{B} - \eta \nabla \times \mathbf{B}) \quad (2.3)$$

$$\nabla \cdot \mathbf{B} = 0 \quad (2.4)$$

where t is the time, ρ_0 is the mass density of the fluid, ν is the kinematic viscosity and η it the magnetic resistivity. The electric current density is expressed as $\mathbf{J} = 1/\mu_0 \nabla \times \mathbf{B}$, where μ_0 is the magnetic permeability in the vacuum. To account for the Hall effect, it is necessary to take a step back in the mathematical developments and resort to a two-fluid description that includes the fluid equations for both ions and electrons separately. For a fully ionized plasma in which the masses of ions (mainly protons) and electrons (hereafter i and e) are $m_e \ll m_i \approx m$, the momentum equations read as

$$\rho[\partial_t \mathbf{U} + (\mathbf{U} \cdot \nabla) \mathbf{U}] = en(\mathbf{E} + \mathbf{U} \times \mathbf{B}) - \nabla p_i + \nabla \cdot \boldsymbol{\sigma} + \mathbf{R} \quad (2.5)$$

$$0 = -en(\mathbf{E} + \mathbf{U}_e \times \mathbf{B}) - \nabla p_e - \mathbf{R} \quad (2.6)$$

where e is the unit electric charge, $\boldsymbol{\sigma}$ is the viscous stress tensor, n is the particle density with $\rho = mn$, and \mathbf{R} is the rate (per unit volume) of momentum exchange due to collisions between protons and electrons. The latter is given by $\mathbf{R} = -mnf_{ie}(\mathbf{U} - \mathbf{U}_e)$ where f_{ie} denotes the collision frequency and can be reformulated as $\mathbf{R} = -(mf_{ie}/e) \mathbf{J}$, with the density current $\mathbf{J} = en(\mathbf{U} - \mathbf{U}_e)$. By summing (2.5) and (2.6) and assuming $\sigma_{\alpha\beta} = \rho\nu(\partial_\alpha U_\beta + \partial_\beta U_\alpha)$, one obtains

$$\partial_t \mathbf{U} + (\mathbf{U} \cdot \nabla) \mathbf{U} = \frac{1}{\rho} \mathbf{J} \times \mathbf{B} - \frac{1}{\rho} \nabla p + \nu \nabla^2 \mathbf{U}. \quad (2.7)$$

On the other hand, by replacing \mathbf{U}_e by $\mathbf{U} - \mathbf{J}/ne$ and the expression for the rate of momentum exchange into (2.6), the Ohm's law becomes

$$\mathbf{E} = -(\mathbf{U} - \frac{1}{en} \mathbf{J}) \times \mathbf{B} + \frac{1}{en} \nabla p_e + \frac{mf_{ie}}{e^2 n} \mathbf{J}. \quad (2.8)$$

Taking the curl of this equation gives in the end an induction equation with Hall's current correction in standard physical units as

$$\partial_t \mathbf{B} = \nabla \times [(\mathbf{U} - \alpha_H \mathbf{J}) \times \mathbf{B}] + \eta \nabla^2 \mathbf{B} \quad (2.9)$$

where $\alpha_H = 1/en$ is usually referred to as the Hall parameter and the magnetic resistivity $\eta = mf_{ie}/(e^2 n \mu_0)$.

2.2. Weakly-compressible formulation

Incompressibility is an assumption made at the macroscopic level and cannot be implemented in the mesoscopic representation as this would imply that fluid particles move at infinite speed, in order to adapt instantaneously the pressure. Incompressibility can nevertheless be approached in the so-called *weakly-compressible* limit, in which the speed of sound waves c_s becomes much larger than the typical fluid velocity U_0 , or equivalently, the pressure field adapts in a time shorter than the time over which the flow evolves. This regime is attained for vanishing Mach number, $\text{Ma} \equiv U_0/c_s$. Consequently, the incompressible equations should be replaced with the compressible formulation

$$\partial_t \rho + \nabla \cdot (\rho \mathbf{U}) = 0 \quad (2.10)$$

$$\partial_t (\rho \mathbf{U}) + \nabla \cdot \left(\rho \mathbf{U} \otimes \mathbf{U} + p \mathbb{I} + \frac{1}{2} |\mathbf{B}|^2 \mathbb{I} - \mathbf{B} \otimes \mathbf{B} \right) = \rho \nu \nabla^2 \mathbf{U} \quad (2.11)$$

in which the Lorentz force has been rewritten in a conservative form, since the divergence of the Maxwell stress tensor $M_{\alpha\beta} = \frac{1}{2} |\mathbf{B}|^2 \delta_{\alpha\beta} - B_\alpha B_\beta$ and μ_0 has been absorbed by replacing \mathbf{B} with $\mu_0^{1/2} \mathbf{B}$. This (standard) normalization will be assumed hereafter, which

† The notation $\mathbf{a} \otimes \mathbf{b} \equiv a_\alpha b_\beta$ is adopted

allows simplifying the Lorentz force as $(\nabla \times \mathbf{B}) \times \mathbf{B}$. Compressibility requires resorting to an *equation of state* linking pressure, mass density and temperature. Here, the low-Mach limit justifies the use of a simple isothermal relation

$$p = \rho c_s^2 \quad (2.12)$$

which is consistent with $O(\text{Ma}^2)$ mass-density fluctuations. The induction equation describing the evolution of the magnetic field can be rewritten in the same fashion as

$$\partial_t \mathbf{B} + \nabla \cdot ((\mathbf{U} - \alpha_H \mathbf{J}) \otimes \mathbf{B} - \mathbf{B} \otimes (\mathbf{U} - \alpha_H \mathbf{J})) = \eta \nabla^2 \mathbf{B}. \quad (2.13)$$

Let us remark that following the normalization of \mathbf{B} by $\mu_0^{1/2}$, the Hall current $\alpha_H \mathbf{J}$ reads as $\alpha_H / \mu_0^{1/2} \nabla \times \mathbf{B}$. In the next sections, the developed LB scheme will conform to the set of equations (2.10), (2.11), (2.12) and (2.13). The divergence-free condition on \mathbf{B} is preserved by (2.13), justifying that it is sufficient to impose $\nabla \cdot \mathbf{B} = 0$ initially. In the numerical modelling, particular attention will be paid to verify that this condition is indeed preserved with accuracy.

3. Hall-MHD Lattice Boltzmann scheme

In this section, the standard LB method for classical fluid dynamics is briefly introduced, focusing on key steps, then it is extended to encompass Hall-MHD. Further details are provided in the appendix A. A central-moment collision operator (De Rosi *et al.* 2018) and a high-connectivity D3Q27 lattice are used to integrate the dynamics of the fluid protons, while the evolution of the magnetic field is accounted by a Bhatnagar-Gross-Krook (BGK) collision operator (Bhatnagar *et al.* 1954) and a low-connectivity D3Q7 lattice. Our original contribution to these developments is the self-consistent integration of the Hall term in the LB scheme by suitably redefining the equilibrium state for the magnetic field.

3.1. Lattice Boltzmann scheme for the fluid dynamics

3.1.1. Standard BGK Lattice Boltzmann scheme

The LB method (Krueger *et al.* 2016) is based on the idea that fluid motions can be represented by the collective behavior of fictitious (introduced in the frame of the LB integration strategy) particle populations evolving along the links of a cubic lattice. When the lattice connectivity, which accounts for the discrete directions of propagation of the particles, is high enough to satisfy sufficient isotropy, weakly-compressible Navier-Stokes dynamics can be reproduced with an $O(\text{Ma}^3)$ error. The macroscopic variables such as the fluid density ρ , momentum $\rho \mathbf{U}$, or stress tensor Σ are obtained as statistical moments of the particle distributions, *i.e.*

$$\rho = \sum_{i=0}^{N-1} f_i \quad (3.1)$$

$$\rho \mathbf{U} = \sum_{i=0}^{N-1} f_i \mathbf{c}_i \quad (3.2)$$

$$\Sigma = \sum_{i=0}^{N-1} f_i \mathbf{c}_i \otimes \mathbf{c}_i \quad (3.3)$$

by summing over the local mass densities f_0, \dots, f_{N-1} of particles moving with velocities $\mathbf{c}_0, \dots, \mathbf{c}_{N-1}$, respectively. The sums replace here the integrals over \mathbf{c} of the classical

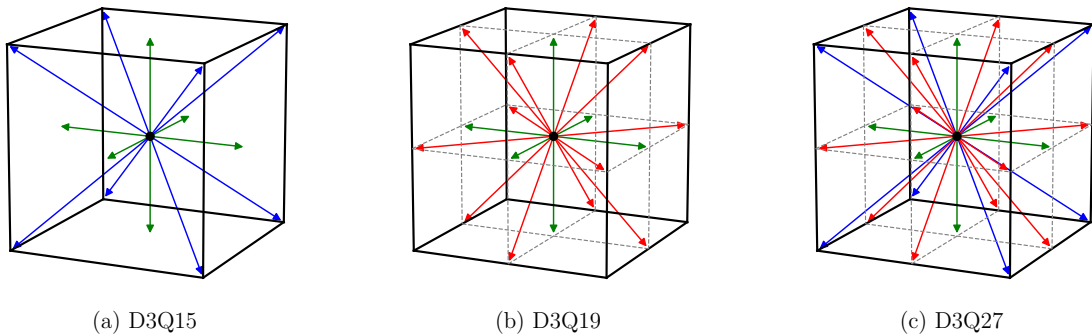


FIGURE 1. Typical cubic lattices with 15, 19 and 27 velocities, respectively. At each lattice node, the microscopic velocities point towards the centre (black), the 6 centres of faces (green), the 12 centres of the edges (red) or the 8 corners (blue) of a cube. The arrows represent the local displacements $\mathbf{c}_i \Delta t$ of particles from a lattice node to a neighbouring node during exactly one time-step. In the present study, a D3Q27 lattice that is more appropriate to simulate strongly non-linear fluid dynamics is considered (Silva & Semiao 2014).

kinetic theory as the result of a drastic decimation in velocity of the phase space. From a theoretical viewpoint, the LB method is derived by expanding the solution of the continuum Boltzmann equation onto a finite basis of Hermite polynomials in velocity, and by resorting to a Gaussian quadrature formula to express the statistical moments (He & Luo 1997). As a consequence, the particle densities $f_i(\mathbf{x}, t)$ evolve according to a discrete-velocity analogue of the Boltzmann equation, which reads as

$$\partial_t f_i + (\mathbf{c}_i \cdot \nabla) f_i = -\frac{1}{\tau} \left(f_i - f_i^{(0)}(\rho, \mathbf{U}) \right) \quad (3.4)$$

under the BGK approximation (Bhatnagar *et al.* 1954). The latter assumes that collisions are responsible for the relaxation of the particle densities towards their equilibrium state $f_i^{(0)}(\rho, \mathbf{U})$, with a unique relaxation time $\tau = \nu/c_s^2$.

The *Lattice* keyword refers to the discretization in space and time of (3.4) with a set of microscopic velocity $\mathbf{c}_0, \dots, \mathbf{c}_{N-1}$ chosen in a way such that particles travel from a lattice node to a neighbour lattice node in exactly one time-step (see Fig. 1).

The LB scheme then expresses simply as

$$\bar{f}_i(\mathbf{x} + \mathbf{c}_i \Delta t, t + \Delta t) = \bar{f}_i(\mathbf{x}, t) - \omega \left(\bar{f}_i(\mathbf{x}, t) - f_i^{(0)}(\rho, \mathbf{U})(\mathbf{x}, t) \right) \quad (3.5)$$

where the discrete distribution functions $\bar{f}_i(\mathbf{x}, t)$ depend on the three spatial coordinates \mathbf{x} and on time t , and stems from the change of variables $\bar{f}_i = f_i + \Delta t/2\tau(f_i - f_i^{(0)})$. This change of variable comes from the trapezoidal rule used to approximate the integral of the collision operator (right-hand side of (3.4)) between t and $t + \Delta t$ (Krueger *et al.* 2016). It also calls for a redefinition of the relaxation time as $\tau + \Delta t/2$ so that

$$\frac{1}{\omega} = \left(\frac{\nu}{c_s^2 \Delta t} + \frac{1}{2} \right) \quad (3.6)$$

where the speed of sound c_s is linked to the lattice spacing by $\Delta x/\Delta t = \sqrt{3}c_s$ for the D3Q27 lattice. The expressions of the mass density and fluid momentum as statistical moments remain unchanged with

$$\rho = \sum_{i=0}^{N-1} \bar{f}_i \quad (3.7)$$

$$\text{and } \rho \mathbf{U} = \sum_{i=0}^{N-1} \bar{f}_i \mathbf{c}_i. \quad (3.8)$$

In practice, (3.5) is divided into a two-step algorithm with a streaming step consecutive to a local collision operation, *i.e.*

$$\bar{f}_i(\mathbf{x} + \mathbf{c}_i \Delta t, t + \Delta t) = \bar{f}_i^*(\mathbf{x}, t) \quad (3.9)$$

$$\bar{f}_i^*(\mathbf{x}, t) = \bar{f}_i(\mathbf{x}, t) - \omega \left(\bar{f}_i(\mathbf{x}, t) - f_i^{(0)}(\rho, \mathbf{U})(\mathbf{x}, t) \right). \quad (3.10)$$

To complete the algorithm, the particle densities at the equilibrium $f_i^{(0)}$ need to be specified. By construction, $f_i^{(0)}$ is defined as a truncated Hermite expansion of the continuous Maxwell-Boltzmann distribution evaluated in \mathbf{c}_i , which reads as

$$f_i^{(0)}(\rho, \mathbf{U}) = w_i \rho \left(1 + \frac{\mathbf{c}_i \cdot \mathbf{U}}{c_s^2} + \frac{(\mathbf{c}_i \cdot \mathbf{U})^2}{2c_s^4} - \frac{\mathbf{U} \cdot \mathbf{U}}{2c_s^2} + \dots \right) \quad (3.11)$$

with the weights $w_{\text{center}} = 8/27$, $w_{\text{face}} = 2/27$, $w_{\text{edge}} = 1/54$ and $w_{\text{corner}} = 1/216$ for the D3Q27 lattice. An expansion truncated at the second order is enough to recover the Navier-Stokes equations with an $O(\text{Ma}^3)$ error. However, several groups (Malaspinas 2015; Coreixas *et al.* 2017, 2019; De Rosi & Luo 2019) have recently shown that accounting for high-order terms results in a gain in accuracy and stability. In our code, $f_i^{(0)}$ has been developed up to the sixth order. The extension of the standard LB algorithm to encompass the Lorentz force is straightforward and relies on the fundamental property that the second-order statistical moment at equilibrium gives the conservative part of the stress tensor. Therefore, incorporating the Lorentz force in the equation describing the fluid dynamics, or equivalently, the Maxwell tensor in the stress tensor amounts to upgrading the equilibrium state as

$$f_i^{\text{mhd}(0)}(\rho, \mathbf{U}, \mathbf{B}) = f_i^{(0)}(\rho, \mathbf{U}) + \frac{w_i}{2c_s^4} \left((\mathbf{B} \cdot \mathbf{B})(\mathbf{c}_i \cdot \mathbf{c}_i) - (\mathbf{c}_i \cdot \mathbf{B})^2 \right) \quad (3.12)$$

so that the second-order moment becomes,

$$\boldsymbol{\Sigma}^{\text{mhd}(0)} = \sum_{i=0}^{N-1} f_i^{\text{mhd}(0)} \mathbf{c}_i \otimes \mathbf{c}_i = \rho \mathbf{U} \otimes \mathbf{U} + p \mathbb{I} + \frac{1}{2} |\mathbf{B}|^2 \mathbb{I} - \mathbf{B} \otimes \mathbf{B}. \quad (3.13)$$

This concludes the introduction of the standard BGK-LB algorithm for MHD.

3.1.2. Central-moment Lattice Boltzmann scheme

Despite its simplicity, effectiveness and large popularity, the BGK-LB scheme is known to suffer from numerical instability when large velocity gradients develop in the flow. This issue made it necessary to adapt either the numerical discretization of (3.4) or the collision operator (Krueger *et al.* 2016). If the former leads to more stable schemes, accuracy is also considerably degraded. This drawback motivated the remarkable efforts made towards developing collision operators with improved stability, as recently reviewed by Coreixas *et al.* (2019). Moment-based collision operators rely on relaxing statistical moments rather than distributions. In addition, different relaxation times can be chosen to individually

over-damp non-hydrodynamic moments (mainly responsible for instabilities) while ensuring the correct relaxation of hydrodynamic moments, *e.g.* density, velocity or stress tensor. By doing so stability can be considerably enhanced while preserving physical consistency. Nevertheless, due to the strongly nonlinear character of turbulent dynamics, spurious dissipative effects can occur as a result of the numerical integration of fluid-like equations over a very large number of grid points and of time-steps, as is the case for Hall-MHD turbulence.

A significant reduction of dissipation artifacts developing in turbulence simulations can be obtained by considering statistical moments expressed in the reference frame of the moving fluid rather than in the laboratory inertial frame, referring to a class of so-called central-moment (CM) collision operators (Geier *et al.* 2007, 2015; De Rosis *et al.* 2018). This is the very framework adopted in lay-outing our code (details are given in the appendix A). A key ingredient of CM-LB schemes is the shift of the particle velocities by the local fluid velocity that defines a new set of local microscopic velocities $\bar{\mathbf{c}}_i = \mathbf{c}_i - \mathbf{U}$ used for the CMs evaluation. Here, we consider the set of CMs as formally defined by

$$|k\rangle \equiv [k_0 \cdots k_{26}]^\top = \mathbf{T}^\top |f\rangle \quad (3.14)$$

where the transformation matrix \mathbf{T} applies to the set of distributions $|f\rangle \equiv [\bar{f}_0 \cdots \bar{f}_{26}]^\top$ and is explicitly defined by the column vectors

$$\begin{aligned} |T_0\rangle &= |1\rangle \\ |T_1\rangle; |T_2\rangle; |T_3\rangle &= [\bar{c}_{ix}]^\top; [\bar{c}_{iy}]^\top; [\bar{c}_{iz}]^\top \\ |T_4\rangle; |T_5\rangle; |T_6\rangle &= [\bar{c}_{ix}\bar{c}_{iy}]^\top; [\bar{c}_{ix}\bar{c}_{iz}]^\top; [\bar{c}_{iy}\bar{c}_{iz}]^\top \\ |T_7\rangle; |T_8\rangle; |T_9\rangle &= [\bar{c}_{ix}^2 - \bar{c}_{iy}^2]^\top; [\bar{c}_{ix}^2 - \bar{c}_{iz}^2]^\top; [\bar{c}_{ix}^2 + \bar{c}_{iy}^2 + \bar{c}_{iz}^2]^\top \\ |T_{10}\rangle; |T_{11}\rangle; |T_{12}\rangle &= [\bar{c}_{ix}\bar{c}_{iy}^2 + \bar{c}_{ix}\bar{c}_{iz}^2]^\top; [\bar{c}_{ix}\bar{c}_{iy}^2 + \bar{c}_{iy}\bar{c}_{iz}^2]^\top; [\bar{c}_{ix}^2\bar{c}_{iy} + \bar{c}_{iy}^2\bar{c}_{iz}]^\top \\ |T_{13}\rangle; |T_{14}\rangle; |T_{15}\rangle &= [\bar{c}_{ix}\bar{c}_{iy}^2 - \bar{c}_{ix}\bar{c}_{iz}^2]^\top; [\bar{c}_{ix}\bar{c}_{iy}^2 - \bar{c}_{iy}\bar{c}_{iz}^2]^\top; [\bar{c}_{ix}^2\bar{c}_{iy} - \bar{c}_{iy}^2\bar{c}_{iz}]^\top \\ |T_{16}\rangle &= [\bar{c}_{ix}\bar{c}_{iy}\bar{c}_{iz}]^\top \\ |T_{17}\rangle; |T_{18}\rangle; |T_{19}\rangle &= [\bar{c}_{ix}^2\bar{c}_{iy}^2 + \bar{c}_{ix}^2\bar{c}_{iz}^2 + \bar{c}_{iy}^2\bar{c}_{iz}^2]^\top; [\bar{c}_{ix}^2\bar{c}_{iy}^2 + \bar{c}_{ix}^2\bar{c}_{iz}^2 - \bar{c}_{iy}^2\bar{c}_{iz}^2]^\top; [\bar{c}_{ix}^2\bar{c}_{iy}^2 - \bar{c}_{ix}^2\bar{c}_{iz}^2]^\top \\ |T_{20}\rangle; |T_{21}\rangle; |T_{22}\rangle &= [\bar{c}_{ix}^2\bar{c}_{iy}\bar{c}_{iz}]^\top; [\bar{c}_{ix}\bar{c}_{iy}^2\bar{c}_{iz}]^\top; [\bar{c}_{ix}\bar{c}_{iy}\bar{c}_{iz}^2]^\top \\ |T_{23}\rangle; |T_{24}\rangle; |T_{25}\rangle &= [\bar{c}_{ix}\bar{c}_{iy}^2\bar{c}_{iz}^2]^\top; [\bar{c}_{ix}^2\bar{c}_{iy}\bar{c}_{iz}^2]^\top; [\bar{c}_{ix}^2\bar{c}_{iy}^2\bar{c}_{iz}]^\top \\ |T_{26}\rangle &= [\bar{c}_{ix}^2\bar{c}_{iy}^2\bar{c}_{iz}^2]^\top. \end{aligned}$$

This set of vectors forms a simple relevant basis (\mathbf{T} is reversible) allowing for a suitable separation between hydrodynamic and non-hydrodynamic moments (De Rosis 2017). In the space of CMs, the collision step (3.10) now generalizes as

$$|k^*\rangle = |k\rangle - S \left(|k\rangle - |k^{(0)}\rangle \right) \quad \text{with} \quad |k^{(0)}\rangle = \mathbf{T}^\top |f^{\text{mhd}(0)}\rangle \quad (3.15)$$

where S is a diagonal matrix applied to each moment individually. Let us point out that the BGK collision is recovered by taking $S = \omega \mathbb{I}$. A proper choice for S is given by

$$S = \text{diag}[1, 1, 1, 1, \omega, \omega, \omega, \omega, \omega, 1, \dots, 1] \quad (3.16)$$

which ensures that mass and momentum are conserved by the collision operator and that viscosity is suitably taken into account. On the other hand, higher-order moments are set equal to equilibrium. Eventually, the post-collision distributions are obtained by

returning to the space of the distributions through

$$|\bar{f}^*\rangle = \mathbb{T}^{-1\top} |\mathbf{k}^*\rangle \quad (3.17)$$

before moving on to the streaming step (3.9).

3.2. Vector-valued Lattice Boltzmann scheme for the magnetic field

We now present the LB scheme for the magnetic field introduced by Dellar (2002), here extended to encompass the Hall effect in simulating MHD turbulent plasmas. Following the works previously done by Croisille *et al.* (1995) and Bouchut (1999), Dellar (2002) proposed a decomposition of the magnetic field as:

$$\mathbf{B}(\mathbf{x}, t) = \sum_{i=0}^{M-1} \bar{\mathbf{g}}_i(\mathbf{x}, t) \quad (3.18)$$

where the sum spans a set of vector-valued densities $\mathbf{g}_0, \dots, \mathbf{g}_{M-1}$ associated with the microscopic velocities $\boldsymbol{\xi}_0, \dots, \boldsymbol{\xi}_{M-1}$.

The magnetic field \mathbf{B} is here provided by the zeroth-order moment of $\bar{\mathbf{g}}_i$ hinting that a lattice with low connectivity should suffice to simulate its dynamics. In practice, a D3Q7 lattice with only seven velocities (see green arrows in Fig. 1) shall prove to be satisfactory in reproducing the magnetic field of Hall-MHD turbulent plasmas. Analogously to the fluid case, a LB scheme can be derived in order to simulate the induction equation in the form

$$\bar{\mathbf{g}}_i(\mathbf{x} + \boldsymbol{\xi}_i \Delta t, t + \Delta t) = \bar{\mathbf{g}}_i(\mathbf{x}, t) - \omega_B \left(\bar{\mathbf{g}}_i(\mathbf{x}, t) - \mathbf{g}_i^{(0)}(\mathbf{U}, \mathbf{B})(\mathbf{x}, t) \right) \quad (3.19)$$

where the relaxation parameter ω_m is now related to the magnetic resistivity η by

$$\frac{1}{\omega_B} = \left(\frac{\eta}{C^2 \Delta t} + \frac{1}{2} \right) \quad (3.20)$$

with $\Delta x / \Delta t = 2C$ for the D3Q7 lattice. In practice, it is desirable that the nodes of the D3Q7 and D3Q27 lattices coincide so that the macroscopic quantities such as \mathbf{u} , \mathbf{B} or \mathbf{J} may be exchanged between the two lattices without interpolation. This constraint imposes that

$$2C = \sqrt{3}c_s. \quad (3.21)$$

In the context of ideal MHD, the densities at equilibrium are given by

$$g_{i\alpha}^{(0)}(\mathbf{U}, \mathbf{B}) = W_i \left(B_\alpha + \frac{1}{C^2} \xi_{i\beta} (U_\beta B_\alpha - B_\beta U_\alpha) \right) \quad (3.22)$$

with $W_{\text{center}} = 1/4$ and $W_{\text{face}} = 1/8$ for a D3Q7 lattice. By doing so, the first-order moment

$$\sum_{i=0}^{M-1} \xi_{i\alpha} g_{i\beta}^{(0)} = \mathbf{U} \otimes \mathbf{B} - \mathbf{B} \otimes \mathbf{U} \quad (3.23)$$

would suitably reconstruct the transport term of the induction equation. Including the Hall correction in this equation is thus equivalent to upgrading the equilibrium densities, so that

$$\mathbf{A}_{\alpha\beta}^{(0)} = \sum_{i=0}^{M-1} \xi_{i\alpha} g_{i\beta}^{\text{Hall}(0)} = (\mathbf{U} - \alpha_H \mathbf{J}) \otimes \mathbf{B} - \mathbf{B} \otimes (\mathbf{U} - \alpha_H \mathbf{J}) \quad (3.24)$$

which is obviously possible by now considering

$$g_{i\alpha}^{\text{Hall}(0)}(\mathbf{U}, \mathbf{B}, \mathbf{J}) = W_i \left(B_\alpha + \frac{1}{C^2} \xi_{i\beta} ((U_\beta - \alpha_H J_\beta) B_\alpha - B_\beta (U_\alpha - \alpha_H J_\alpha)) \right). \quad (3.25)$$

Nevertheless, \mathbf{J} needs to be computed, possibly from the densities, in this expression.

An essential benefit of the LB framework is that the spatial derivatives of the magnetic field, thus \mathbf{J} , are self-consistently obtained (within an $O(\text{Ma}^3)$ error) from the first-order moment of the densities as

$$\mathbf{J}_\gamma = \varepsilon_{\alpha\beta\gamma} \frac{\partial B_\alpha}{\partial x_\beta} = -\varepsilon_{\alpha\beta\gamma} \frac{\omega_B}{C^2} \left(\mathbf{A}_{\alpha\beta} - \mathbf{A}_{\alpha\beta}^{(0)} \right) \quad (3.26)$$

where $\varepsilon_{\alpha\beta\gamma}$ is the Levi-Civita tensor and $\mathbf{A}_{\alpha\beta} = \sum_{i=0}^{M-1} \xi_{i\alpha} \bar{g}_{i\beta}$ (Dellar 2002).

By replacing (3.24) in (3.26) we obtain a linear system readily solvable to obtain the current density \mathbf{J} , namely

$$\left(\mathbb{I} + \frac{2\alpha_H \omega_B}{C^2} \mathbf{M} \right) \mathbf{J} = \mathbf{J}_0 \quad (3.27)$$

where

$$\mathbf{M} = \begin{bmatrix} 0 & B_z & -B_y \\ -B_z & 0 & B_x \\ B_y & -B_x & 0 \end{bmatrix} \text{ and } \mathbf{J}_0 = \begin{bmatrix} \mathbf{A}_{yz} - \mathbf{A}_{zy} - 2(U_y B_z - U_z B_y) \\ \mathbf{A}_{zx} - \mathbf{A}_{xz} - 2(U_z B_x - U_x B_z) \\ \mathbf{A}_{xy} - \mathbf{A}_{yx} - 2(U_x B_y - U_y B_x) \end{bmatrix}. \quad (3.28)$$

Obviously, a solution exists only if it is possible to invert $\widetilde{\mathbf{M}} = \mathbb{I} + (2\alpha_H \omega_B / C^2) \mathbf{M}$. It can be easily verified that $\det(\widetilde{\mathbf{M}}) \neq 0$, which proves this solution exists and is unique. The current density obtained by solving (3.27) can then be used to compute the equilibrium densities (3.25) and proceed to the collision operation.

The expression of (3.26) also provides a consistent approximation of the divergence of the magnetic field. Indeed by taking the trace of the magnetic tensor, one obtains

$$\nabla \cdot \mathbf{B} \simeq -\frac{\omega_B}{C^2} \text{Tr}(\mathbf{A}_{\alpha\beta}) \quad (3.29)$$

by noticing that $\text{Tr}(\mathbf{A}_{\alpha\beta}^{(0)}) = 0$. Furthermore, the $O(\text{Ma}^3)$ correction cancels out by taking the trace. Therefore, this correction is pushed to a higher order, so that the divergence-free $\nabla \cdot \mathbf{B} = 0$ corresponds with high accuracy to the condition $\text{Tr}(\mathbf{A}_{\alpha\beta}) = 0$ in the LB framework (Dellar 2002). In practice, we have checked in our LB simulations that this condition was maintained throughout the runs, to machine round-off error.

3.3. Dimensionless formulation

In the following, the Hall-MHD equations are re-arranged in a dimensionless form in terms of the control parameter ϵ_H , associated with the Hall parameter $\alpha_H = 1/ne$. This control parameter is then recast in lattice units for practical LB purposes. Physical quantities in lattice units are hereafter indicated with the superscript ^{lbm}. In lattice units, the lattice spacing Δx and the time-step Δt of the scheme define the units of length and time, respectively. In order to obtain a dimensionless induction equation, let us normalise the magnetic field with a reference value, B_0 , the fluid velocity with U_0 , the current density with B_0/L_0 , the length with L_0 and the time with L_0/U_0 . Leveraging these characteristic quantities, (2.9) can be written in a dimensionless form as

$$\left(\frac{U_0 B_0}{L_0} \right) \partial_t \mathbf{b} = \frac{1}{L_0} \nabla \times \left[\left(U_0 \mathbf{u} - \frac{\alpha_H B_0}{\sqrt{\mu_0} L_0} \nabla \times \mathbf{b} \right) \times (B_0 \mathbf{b}) \right] + \frac{\eta B_0}{L_0^2} \nabla^2 \mathbf{b} \quad (3.30)$$

Dimensionless fields are here indicated by lowercase letters. This equation can be reduced to

$$\partial_t \mathbf{b} = \nabla \times \left[\left(\mathbf{u} - \epsilon_H \nabla \times \mathbf{b} \right) \times \mathbf{b} \right] + \frac{1}{\text{Re}_m} \nabla^2 \mathbf{b} \quad (3.31)$$

by defining the magnetic Reynolds number $\text{Re}_m = U_0 L_0 / \eta$ and the dimensionless Hall parameter

$$\epsilon_H = \frac{\alpha_H B_0}{\sqrt{\mu_0} L_0 U_0}. \quad (3.32)$$

We can treat in the same fashion the fluid momentum equation, where the reference scales are the same as those used to adimensionalize the induction equation. Therefore,

$$\rho \frac{U_0^2}{L_0} [\partial_t \mathbf{u} + (\mathbf{u} \cdot \nabla) \mathbf{u}] = -\frac{1}{L_0} \nabla \rho c_s^2 + \rho \nu \frac{U_0}{L_0^2} \nabla^2 \mathbf{u} + \frac{B_0^2}{L_0} (\nabla \times \mathbf{b}) \times \mathbf{b} \quad (3.33)$$

which gives

$$\partial_t \mathbf{u} + (\mathbf{u} \cdot \nabla) \mathbf{u} = -\frac{1}{\text{Ma}^2} \frac{1}{\rho} \nabla \rho + \frac{1}{\text{Re}} \nabla^2 \mathbf{u} + \left(\frac{V_A}{U_0} \right)^2 (\nabla \times \mathbf{b}) \times \mathbf{b} \quad (3.34)$$

where the control parameters are the Mach number $\text{Ma} = U_0 / c_s$, the (fluid) Reynolds number $\text{Re} = U_0 L_0 / \nu$ and V_A / U_0 , the Alfvén velocity being $V_A = B_0 / \sqrt{\rho}$. The Hall number ϵ_H is given in lattice units by

$$\epsilon_H^{\text{lbm}} = \frac{\alpha_H}{\sqrt{\mu_0}} \frac{[B_0 / B_0^{\text{lbm}}]}{[L_0 / L_0^{\text{lbm}}] [U_0 / U_0^{\text{lbm}}]} = \epsilon_H \frac{U_0^{\text{lbm}} L_0^{\text{lbm}}}{B_0^{\text{lbm}}}. \quad (3.35)$$

If one considers that the reference velocity U_0 corresponds to the Alfvén velocity ($U_0 = V_A$) and $\rho \simeq 1$ for simplicity, one obtains that $U_0^{\text{lbm}} = B_0^{\text{lbm}}$ and

$$\epsilon_H^{\text{lbm}} = \epsilon_H L_0^{\text{lbm}} = \epsilon_H N \quad (3.36)$$

with $N = L_0 / \Delta x$ being the number of lattice points per reference length L_0 . The Hall parameter ϵ_H can also be obtained as the ratio of two reference scales as

$$\epsilon_H = \frac{V_A}{U_0 L_0} \sqrt{\frac{m}{\mu_0 n e^2}} = \frac{L_H}{L_0} \quad (3.37)$$

with

$$L_H = \frac{V_A}{U_0} \sqrt{\frac{m}{\mu_0 n e^2}}. \quad (3.38)$$

In lattice units,

$$\epsilon_H^{\text{lbm}} = \frac{L_H}{L_0} \frac{U_0^{\text{lbm}} L_0^{\text{lbm}}}{B_0^{\text{lbm}}} = \frac{L_H}{\Delta x} \frac{U_0^{\text{lbm}}}{B_0^{\text{lbm}}} = \frac{U_0^{\text{lbm}} L_H^{\text{lbm}}}{B_0^{\text{lbm}}}. \quad (3.39)$$

If $U_0 = V_A$, L_H is equal to the ion inertial length d_i (or ion skin depth). In that case, $\epsilon_H^{\text{lbm}} = L_H^{\text{lbm}}$ and this corresponds to the number of lattice points per ion inertial length. It is assumed that the dynamics of a MHD plasma develops under the influence of the Hall effect at scales ℓ smaller than L_H .

3.4. CFL condition for Hall-MHD turbulence

The Courant–Friedrichs–Lewy (CFL) condition (Lewy *et al.* 1928) determines, for an explicit time-marching scheme, the maximum time-step for convergence, as

$$\Delta t \leq \Delta x / c_{\text{max}} \quad (3.40)$$

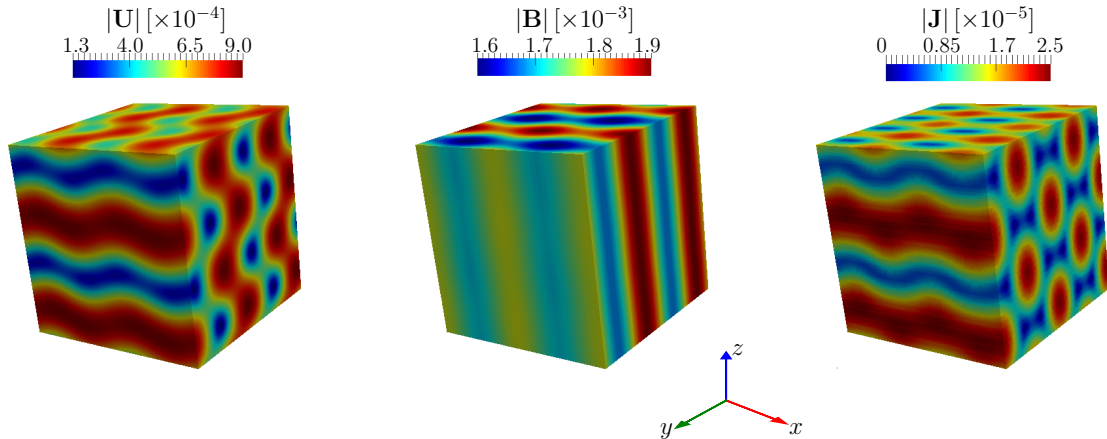


FIGURE 2. Three-dimensional rendering of the initial condition as indicated in (4.5) and (4.6). The magnitudes of the fluid velocity (left), magnetic field (center) and density of electric current (right) are here displayed for $N = 128$.

where c_{\max} refers to the largest speed at which a signal propagates in the solution. In the context of Hall-MHD, c_{\max} should be identified with the largest phase speed of the whistler waves. When the plasma dynamics in the direction of the magnetic field B is dominant, the phase speed of the whistler waves varies as $c_w(k) = kV_A^2/\omega_{ci}$ with the wavenumber k ; V_A is the Alfv en velocity, while ω_{ci} is the ion cyclotron frequency. In physical units, $\omega_{ci} = eB/m_i$ and $V_A = B/\sqrt{\mu_0 n m_i}$, m_i being the mass of ions and the Hall parameter being $\alpha_H = 1/ne$. Therefore, one obtains that the time-step decreases quadratically with the grid spacing, as

$$\Delta t \leq \frac{\mu_0(\Delta x)^2}{\pi \alpha_H B} \quad (3.41)$$

assuming the largest attainable wavenumber to be $k_{\max} = \pi/\Delta x$ in the context of the Hall-MHD turbulence. This condition can be rewritten accounting for the rescaling of the magnetic field by $\mu_0^{1/2}$

$$\Delta t \leq \frac{(\Delta x)^2}{\pi (\alpha_H/\sqrt{\mu_0}) B_0} \quad (3.42)$$

which finally yields in lattice units to

$$1 \leq \frac{1}{\pi \epsilon_H^{\text{lbm}} L_0^{\text{lbm}} U_0^{\text{lbm}}} = \frac{1}{\pi} \frac{B_0^{\text{lbm}}}{\epsilon_H (N U_0^{\text{lbm}})^2} \quad (3.43)$$

where (3.32) is used to retrieve $\alpha_H/\sqrt{\mu_0}$, and $N = L_0^{\text{lbm}}$. If $U_0 = V_A$, the CFL condition for whistler waves can be reformulated as a condition on the Mach number $\text{Ma} = \sqrt{3}U_0^{\text{lbm}}$, which is in turn written as

$$\text{Ma} \leq \left(\frac{\sqrt{3}}{\pi} \right) \frac{1}{\epsilon_H N^2}. \quad (3.44)$$

This condition reminds the quadratic dependence of the time step on the resolution obtained with conventional CFD methods (G omez *et al.* 2010). It also confirms that Hall-MHD turbulence is computationally very demanding due to the presence of whistler waves.

Parameters	Values
Resolution: N	32, 64, 96, 128
Mach number: Ma [$\times 10^{-2}$]	1.0, 0.7, 0.5, 0.3
Kinematic viscosity: ν [$\times 10^{-3}$]	1.0, 0.5, 0.33, 0.25, 0.2, 0.17, 0.14, 0.13, 0.11

TABLE 1. Parameters of LB simulations. The magnetic Prandtl number is kept unitary. The kinematic viscosity is given in dimensionless units, *i.e.* normalised by $U_0 L_0$, which means that the Reynolds number $\text{Re} = 1/\nu$.

4. Results

Our LB scheme and code FLAME is now validated against the analytical solution of the incompressible and dissipative Hall-MHD equations proposed in (Xia & Yang 2015). The latter is used as a benchmark to evaluate accuracy and convergence of the numerical solutions for different values of the control parameters (in a regime of low Reynolds numbers in which the aforementioned analytical solution holds). A further validation was done focusing on the MHD range of scales, this time in a regime of high Reynolds numbers. The solutions of the MHD dynamics produced by FLAME were compared in this case with those obtained with a well-established pseudo-spectral solver, widely used for turbulent plasma simulations, namely the Geophysical High-Order Suite for Turbulence (GHOST, Mininni *et al.* (2011); Rosenberg *et al.* (2020)). Finally, the physical consistency of the output and the computational performance were evaluated when accounting explicitly for the Hall effect in the turbulent regime. This allowed us to assess the reliability of our code in simulating the multi-scale dynamics generated by turbulent flows at high Reynolds numbers, and in reproducing the transition from the MHD to the Hall-MHD spectral range (at sub-ion scales).

4.1. Exact solution of the dissipative Hall-MHD

Due to their high computational cost, the availability in the literature of plasma simulations reproducing the Hall-MHD range of scales (in three dimensions) is much less than for the MHD case. Moreover, Hall-MHD simulations are in general performed using pseudo-spectral codes (Ferrand *et al.* 2022; Meyrand & Galtier 2012; Gómez *et al.* 2010; Yadav *et al.* 2022), which integrate of course the dynamical equations in the Fourier space. Interestingly, Mahajan & Krishan (2005) derived an analytical solution for the non-dissipative Hall-MHD equations, then extended by Xia & Yang (2015) with the inclusion of dissipative effects. This solution is used in the following to test the stability and convergence of FLAME. Encompassing dissipative effects Xia & Yang (2015), this analytical solution allowed us to quantify as well the numerical dissipation spuriously introduced by our scheme.

The solution provided by Xia & Yang (2015) is rewritten in a dimensionless form (see §3.3) as

$$\mathbf{u}(\mathbf{x}, t) = \mathbf{u}'(\mathbf{x}, t) \quad \text{and} \quad \mathbf{b}(\mathbf{x}, t) = \hat{\mathbf{e}}_z + \mathbf{b}'(\mathbf{x}, t) \quad (4.1)$$

where the fluctuating velocity and magnetic fields are damped circular polarized waves given respectively by

$$\begin{aligned} \mathbf{u}'(\mathbf{x}, t) = & [B(\hat{\mathbf{e}}_x + i\hat{\mathbf{e}}_y) \exp(ikz - i\omega_{\pm}t) \\ & + C(\hat{\mathbf{e}}_y + i\hat{\mathbf{e}}_z) \exp(ikx) \\ & + A(\hat{\mathbf{e}}_z + i\hat{\mathbf{e}}_x) \exp(iky)] e^{-\nu \mathbf{k}^2 t} \end{aligned} \quad (4.2)$$

and

$$\mathbf{b}'(\mathbf{x}, t) = \alpha_{\pm} \mathbf{u}'(\mathbf{x}, t) \quad (4.3)$$

in complex notations. The amplitudes A , B , and C are arbitrary real values. The ambient magnetic field here is assumed to be oriented along the unit vector $\hat{\mathbf{e}}_z$. Since the dynamical equations only consist of real variables, either the imaginary part or the real part is a solution. The pulsation $\omega_{\pm} = -\alpha_{\pm}k$, where α_{\pm} depends itself on the wavenumber k as

$$\alpha_{\pm} = -\frac{1}{2}\epsilon_H k \pm \sqrt{\frac{\epsilon_H^2 k^2}{4} + 1}. \quad (4.4)$$

The magnetic Prandtl number is assumed unitary in obtaining this solution and the reference velocity is assumed as corresponding to the Alfv en velocity, *i.e.* $U_0 = V_A$ in (3.34). Finally, it is worth mentioning that this analytical solution holds in a strictly incompressible framework, which, given the intrinsically compressible nature of the LB scheme, prescribes that our simulations must be run at a (very) low Mach number so that relative density fluctuations generated by the code remain negligible. In our investigations, the Hall-MHD equations have been integrated in a cubic box of size $L_0 = 2\pi$. The evolution of the velocity field is deterministic from the initial condition

$$\begin{aligned} u_x^{\text{lbm}}(\mathbf{x}, 0) &= U_0^{\text{lbm}} \left(B \sin\left(\frac{4\pi z_k}{N}\right) + A \cos\left(\frac{4\pi y_j}{N}\right) \right) \\ u_y^{\text{lbm}}(\mathbf{x}, 0) &= U_0^{\text{lbm}} \left(B \cos\left(\frac{4\pi z_k}{N}\right) + C \sin\left(\frac{4\pi x_i}{N}\right) \right) \\ u_z^{\text{lbm}}(\mathbf{x}, 0) &= U_0^{\text{lbm}} \left(C \cos\left(\frac{4\pi x_i}{N}\right) + A \sin\left(\frac{4\pi y_j}{N}\right) \right) \end{aligned} \quad (4.5)$$

expressed in lattice units with $A = 0.3$, $B = 0.2$, $C = 0.1$ and N being the number of lattice nodes per reference length L_0 . The reference velocity U_0^{lbm} is related by construction to the Mach number through $U_0^{\text{lbm}} = \text{Ma}/\sqrt{3}$. The magnetic field is initially proportional to the fluid velocity with

$$\begin{aligned} b_x^{\text{lbm}}(\mathbf{x}, 0) &= \alpha_+ u_x^{\text{lbm}}(\mathbf{x}, 0) \\ b_y^{\text{lbm}}(\mathbf{x}, 0) &= \alpha_+ u_y^{\text{lbm}}(\mathbf{x}, 0) \\ b_z^{\text{lbm}}(\mathbf{x}, 0) &= \alpha_+ u_z^{\text{lbm}}(\mathbf{x}, 0) + U_0^{\text{lbm}} \end{aligned} \quad (4.6)$$

since $U_0 = V_A$. For sake of simplicity, the initial density is set to one everywhere in the space. The (normalized) Hall parameter is fixed at $\epsilon_H = 1$, that is $\epsilon_H^{\text{lbm}} = N$ according to (3.36). This value ensures that the solution is affected by the Hall effect with $L_H = L_0$ from (3.37). A three-dimensional rendering of the initial conditions expressed in (4.5) and (4.6) is displayed in Fig. 2. With this initialization, the current density $\mathbf{J} = \nabla \times \mathbf{B}$ is non-zero at $t = 0$. The parameters used in the different simulations are reported in Tab. 1. The Mach number is always small enough for the plasma to approach the incompressible limit and in order to reduce the intrinsic discretization error of the LB method. The CFL condition imposed by this solution is also satisfied. Finally, let us mention that analogous simulations were performed with the phase speed α_- yielding very similar results on accuracy and stability. However, the phase speed is much larger in the latter case, requiring a significant reduction of the Mach number (with $\epsilon_H = 1$). Results obtained for α_+ and the velocity field only ($\mathbf{b} = \alpha_+ \mathbf{u} + \hat{\mathbf{e}}_z$) are presented in the following.

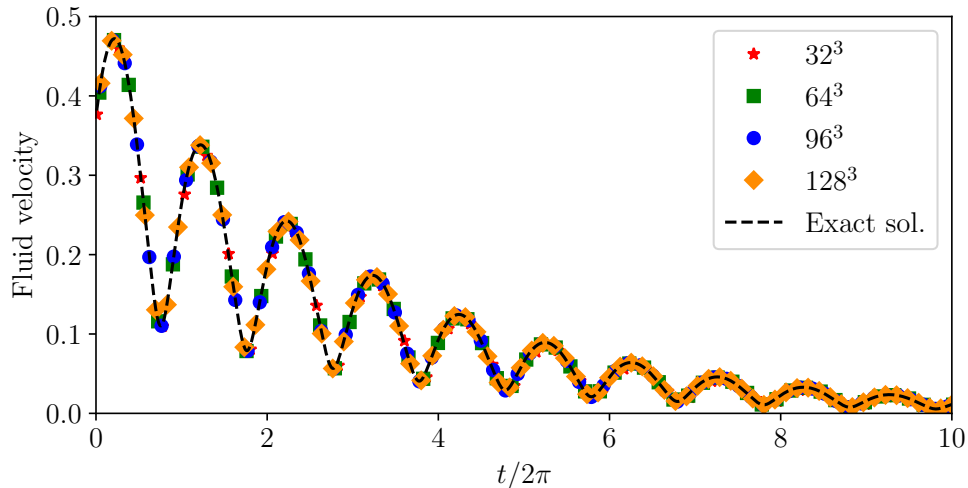


FIGURE 3. Temporal evolution of the velocity magnitude $|\mathbf{u}|(\mathbf{0}, t)$. Comparison between the analytical (dashed line) and the numerical solutions (symbols) at different lattice resolutions. The Mach number $\text{Ma} = 0.003$ and the kinematic viscosity $\nu = 3.3 \cdot 10^{-4}$.

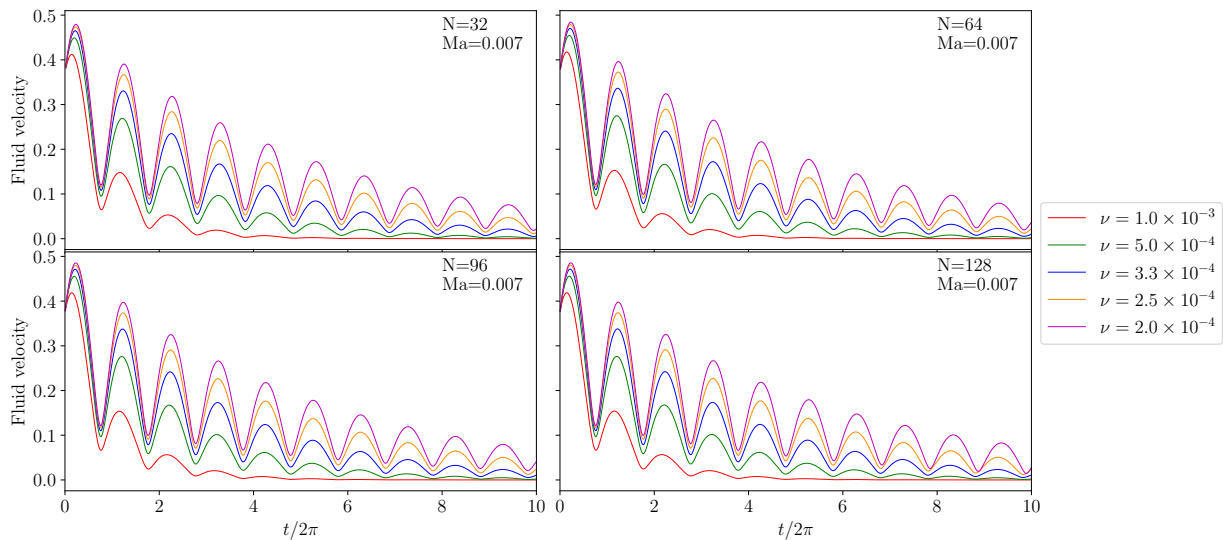


FIGURE 4. Temporal evolution of the velocity magnitude $|\mathbf{u}|(\mathbf{0}, t)$ for different values of the resolution (N) and viscosity (ν) at fixed Mach number $\text{Ma} = 0.007$.

4.2. Stability and incompressibility

The stability of the scheme was tested exploring the parameter space defined through the Mach number, the lattice resolution and the kinematic viscosity (see Tab. 1). The analytical solution introduced by Xia & Yang (2015) is such that the nonlinear terms in the incompressible dissipative Hall MHD equations are strictly zero. In practice, physical instabilities triggered by numerical errors do naturally develop and grow in time in simulations whenever the viscosity is too small, eventually inducing the transition to a turbulent state. Therefore, the numerical stability and accuracy of FLAME were assessed in runs in which the viscosity was sufficiently high to prevent such transition to turbulence. The typical temporal evolution of the velocity at a fixed location in the simulation domain is shown in Fig. 3. The solution appears as a damped wave propagating in the direction of the ambient magnetic field. The amplitude and the phase of the solution are well captured in the LB simulation. The results obtained for different resolutions and viscosity values at Mach number $\text{Ma} = 0.007$ are shown in Fig. 4 for

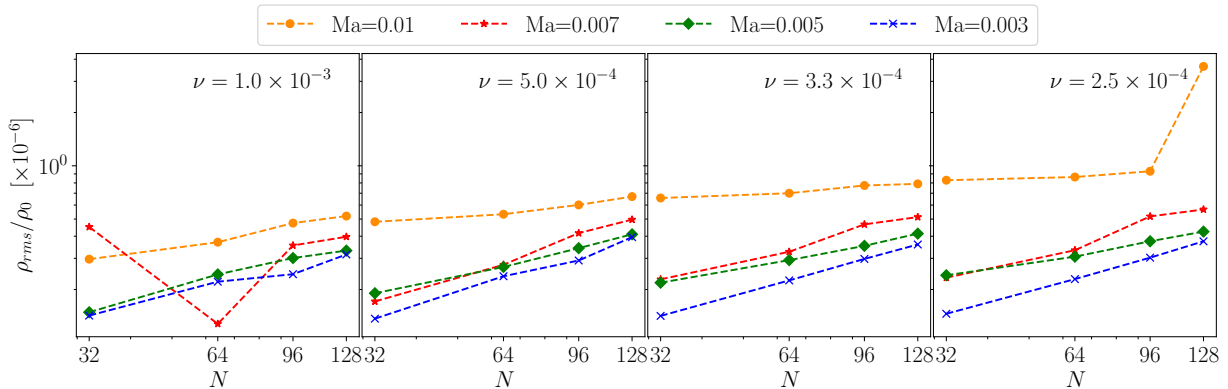


FIGURE 5. Relative density fluctuations at different values of the Mach number (Ma) and kinematic viscosity (ν) as a function of the resolution (N). In our simulations, the reference density ρ_0 is fixed at unity.

10 wave periods. All simulations remained numerically stable in the explored range of parameters. The temporal averages of relative density fluctuations at different values of Mach number and kinematic viscosity are displayed in Fig. 5. The level of these relative fluctuations is typically of order $10^{-7} - 10^{-6}$, indicating a very good convergence towards the incompressible limit in all the simulations presented. Furthermore, the results confirm that the amplitude of density fluctuations decreases with the Mach number.

4.3. Dispersion and dissipation errors

The dispersion and dissipation errors of the LB scheme implemented in FLAME are now assessed. In this analysis, the dispersion error (or phase error) is computed by evaluating the shift in time between the local maxima of the numerical solution and the analytical wave solution (see Fig. 3). Therefore, tagging as t_i^{\max} and \bar{t}_i^{\max} the positions in time of the maxima of the numerical and analytical solution (at a fixed location) respectively, the average value of the relative dispersion error can be defined as

$$\varepsilon_\phi = 1 - \frac{1}{M} \sum_{i=0}^{M-1} \frac{t_{i+1}^{\max} - t_i^{\max}}{\bar{t}_{i+1}^{\max} - \bar{t}_i^{\max}} \quad (4.7)$$

over M oscillating periods. For practical purposes we have used $M = 10$. As expected, it can be observed in Fig. 6 how the dispersion error is very small and decreases as the resolution N of the grid increases, showing a power-scaling law close to $1/N^2$. This confirms a second-order accuracy of the LB scheme. We also found that the dispersion error exhibits a rather constant behavior when changing the Mach number, and does not seem to be affected by the value of the kinematic viscosity either. Let us remark that some results differ from the global trend, certainly due to the presence of (physical) instabilities at the lowest viscosity. After synchronizing the phases of numerical and analytical solutions, the (relative) dissipation error is evaluated by comparing the velocity magnitude of the two solutions, *i.e.*

$$\varepsilon_r = \sum_{i=0}^{M-1} \frac{|u(t_i) - \bar{u}(t_i)|}{\bar{u}(t_i)}. \quad (4.8)$$

The dissipation error provides a first measure of the numerical dissipation. Two different scaling behaviors are considered, namely the so-called acoustic and diffusive scalings (Krueger *et al.* 2016). The acoustic scaling consists in keeping the Mach number fixed while monitoring the convergence rate of the error ε_r for different Reynolds numbers,

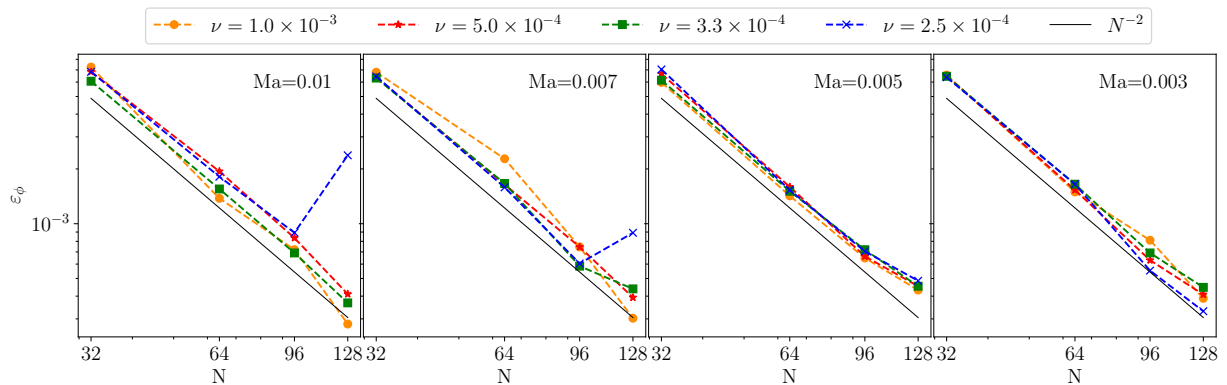


FIGURE 6. Relative dispersion error as defined by (4.7) for different values of the kinematic viscosity ν and the Mach number Ma . The error decreases as N^{-2} as expected for a LB scheme.

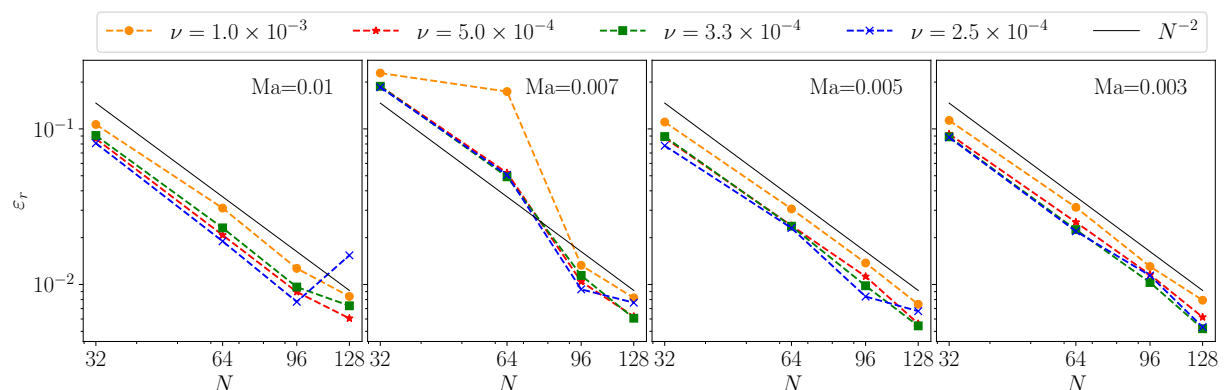


FIGURE 7. Acoustic scaling (Ma constant) of the relative dissipation error for different values of the kinematic viscosity (ν) at fixed Mach number (Ma). The error decreases as N^{-2} .

as a function of the resolution (see Fig. 7). On the other hand, the diffusive scaling is obtained by keeping the lattice viscosity fixed (see Fig. 8). The behavior of the numerical solution is consistent between the two regimes, showing a convergence of the dissipation error with respect to the grid resolution $\propto 1/N^2$, as expected for a second-order scheme.

One of the advantages of dealing with a *dissipative* solution of the Hall-MHD equations is the possibility to identify an effective viscosity $\tilde{\nu}$ related to the damping $\propto \exp(-\tilde{\nu}k^2t)$ of the numerical solution. By decomposing $\tilde{\nu}$ into the sum of a physical and a (spurious) numerical viscosity, $\tilde{\nu} = \nu + \nu_{\text{num}}$, the ratio between these two contributions reads as

$$\varepsilon_\nu = \frac{\nu_{\text{num}}}{\nu} = \frac{\tilde{\nu} - \nu}{\nu}. \quad (4.9)$$

The results obtained for the viscosity error ε_ν are shown in Fig. 9. Here, we found that the numerical viscosity represents only a small percentage of the estimated total viscosity, and it decreases as $1/N^2$ with the resolution, which is once again consistent with a second-order accuracy of the LB scheme. Interestingly, it is observed that the (relative) viscosity error is independent from the physical viscosity and the Mach number, whereas it only depends on the lattice resolution.

Finally, despite Dellar (2002) showed that a D3Q7 lattice was sufficient to reliably account for the dynamics of each component of the magnetic field, in order to check the validity of this statement, LB simulations with enhanced connectivity have been performed here to investigate whether a more isotropic representation of the magnetic densities would significantly improve the level of accuracy of the algorithm (Silva &

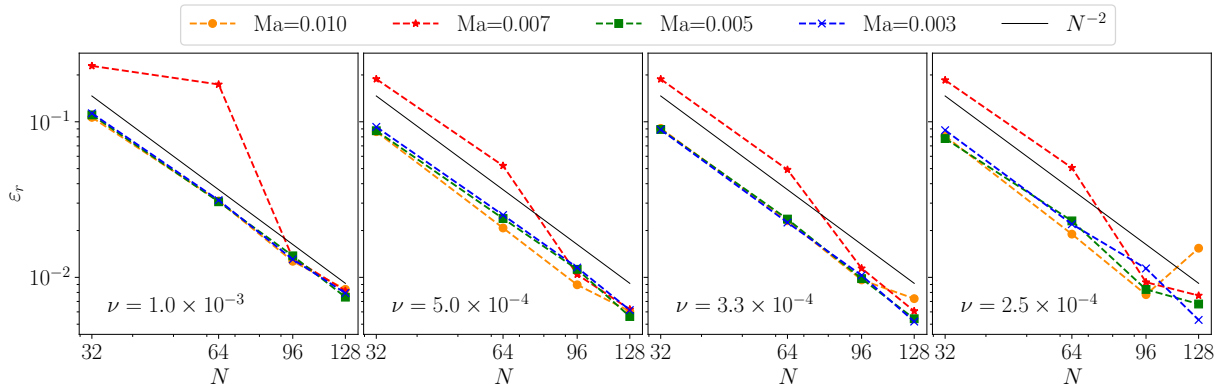


FIGURE 8. Diffusive scaling (ν constant) of the (relative) dissipation error for different values of the Mach number (Ma) at fixed kinematic viscosity (ν).

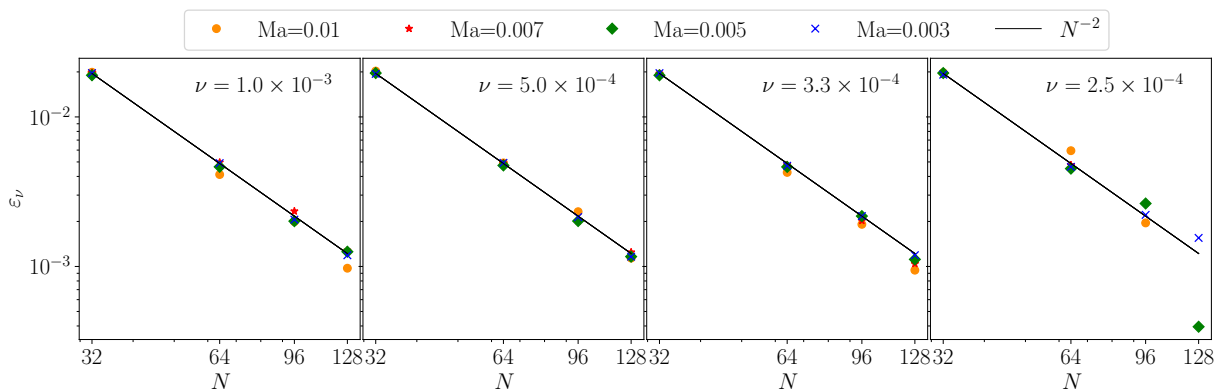


FIGURE 9. Scaling of the ratio between the numerical and kinematic viscosities $\epsilon_\nu = \nu^{\text{num}}/\nu$ with the grid resolution (N) for different Mach numbers (Ma) and kinematic viscosity. The second-order accuracy of the LB algorithm is highlighted by the black lines, *i.e.* $\epsilon_\nu \sim O(\Delta x^2)$.

Semiao 2014). Interestingly, our results showed no significant improvement when upgrading the magnetic lattice to D3Q15 or D3Q27 lattices (see Fig. 1), thus confirming what was reported in Dellar (2002). A plausible explanation of this lies on the fact that the magnetic field is represented as a zeroth order moment of densities for each component (see (3.18)). Therefore, a few degrees of freedom are certainly sufficient to accurately reconstruct the moments and describe the magnetic field dynamics.

4.4. Comparison with pseudo-spectral simulations of MHD turbulence

In this section, comparisons are made between the dynamics of MHD plasmas simulated with FLAME and the outputs obtained with the GHOST pseudo-spectral solver for high-resolution simulations, when both codes perform the same decaying test run initialized with the classical Orszag-Tang (OT) vortex problem (Orszag & Tang 1979). Indeed, the OT solution is often considered as a prototypical flow to study freely evolving MHD turbulence. The GHOST solver has been widely used to tackle a variety of problems related to both geophysical fluids and space plasmas (Marino *et al.* 2013; Pouquet & Marino 2013; Marino *et al.* 2014, 2015a; Mininni *et al.* 2002, 2003, 2006; G omez *et al.* 2010; Pouquet *et al.* 2019). It is a well-established community code available on <https://github.com/pmininni/GHOST>. GHOST is a hybrid MPI/OpenMP/CUDA-parallelized framework that hosts a variety of solvers having also GPU capability, delivering high performance, robust results and an optimal scaling up to hundreds of thousand computing cores. It relies on a second-order Runge-Kutta scheme for time integration and is de-

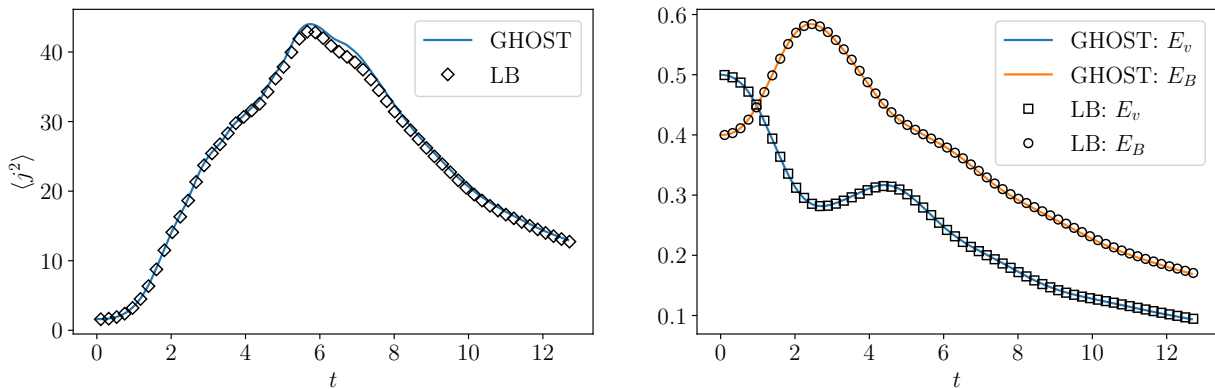


FIGURE 10. (Left) Time evolution of the mean magnetic dissipation $\propto \langle |\mathbf{J}|^2 \rangle$ in freely-evolving MHD turbulence for a LB simulation ($N = 512$) and a pseudo-spectral simulation ($N=512$) performed with the GHOST solver. (Right) Time evolution of the mean kinetic (E_v) and magnetic (E_B) energies.

aliased based on the classical two-third rule. As a pseudo-spectral de-aliased code, it provides very high accuracy in resolving the spatial scales (Patterson & Orszag 1971). The OT vortex problem prescribes the following initialization for the velocity and magnetic fields:

$$\begin{aligned} \mathbf{U}(\mathbf{x}, \mathbf{0}) &= U_0 [-2 \sin y ; 2 \sin x ; 0] \\ \mathbf{B}(\mathbf{x}, \mathbf{0}) &= B_0 [-2 \sin 2y + \sin z ; 2 \sin x + \sin z ; \sin x + \sin y] \end{aligned}$$

with $U_0 = 1$ and $B_0 = 0.8$ in a cubic box of size 2π .

In the simulation performed here, the Reynolds number attains values up to $Re = UL/\nu \simeq 1600$ when the flow reaches its peak of dissipation. The small-scale energy dissipation is defined as $\epsilon = -\nu \langle |\nabla \times \mathbf{U}|^2 \rangle - \eta \langle |\mathbf{J}|^2 \rangle$ and encompasses both the kinetic and magnetic dissipation with $\nu/\eta = 1$. In the definition of the Reynolds number, U refers to the r.m.s velocity and $L = 2\pi \int k^{-1} E_v(k) dk / \int E_v(k) dk$ is the integral length scale, where $E_v(k)$ is the energy spectrum of the velocity field. The Mach number is fixed at $Ma = 0.025$. The number of grid points in each direction is $N = 512$.

The time evolution of the mean magnetic dissipation, as well as the kinetic and magnetic energies, are shown in Fig. 10 for two realizations of LB and pseudo-spectral simulations of the same OT problem. The simple visual inspection of the runs shows that the agreement between FLAME and GHOST is very satisfactory for the cases under study. Only a slight underestimation of the magnetic dissipation in the FLAME run can be observed for a few time steps after the peak of the current density $\mathbf{J} = \nabla \times \mathbf{B}$. Let us recall at this stage that \mathbf{J} is directly obtained from the magnetic densities in the LB simulation, and is not inferred by differentiating the magnetic field.

A more detailed comparison is provided by looking at the Fourier decomposition of the fields obtained with the two codes. The kinetic and magnetic energy spectra are displayed in Fig.11 at the peak of the magnetic dissipation. The kinetic energy spectrum of the LB simulation seems over-damped at high wavenumbers. This is related to a known drawback of the moment-based collision operator, which ensures higher stability (compared to the standard BGK collision operator) but at the cost of an enhanced numerical dissipation (Coreixas *et al.* 2019). However, when increasing the spatial resolution to $N = 768$, the numerical dissipation is reduced and the spectrum of the FLAME run gets very close to that of the pseudo-spectral solution. Concerning the magnetic energy spectrum, the results from both simulations perfectly match, reflecting the fact that the BGK collision operator adopted for the magnetic scheme does not add numerical dissipation

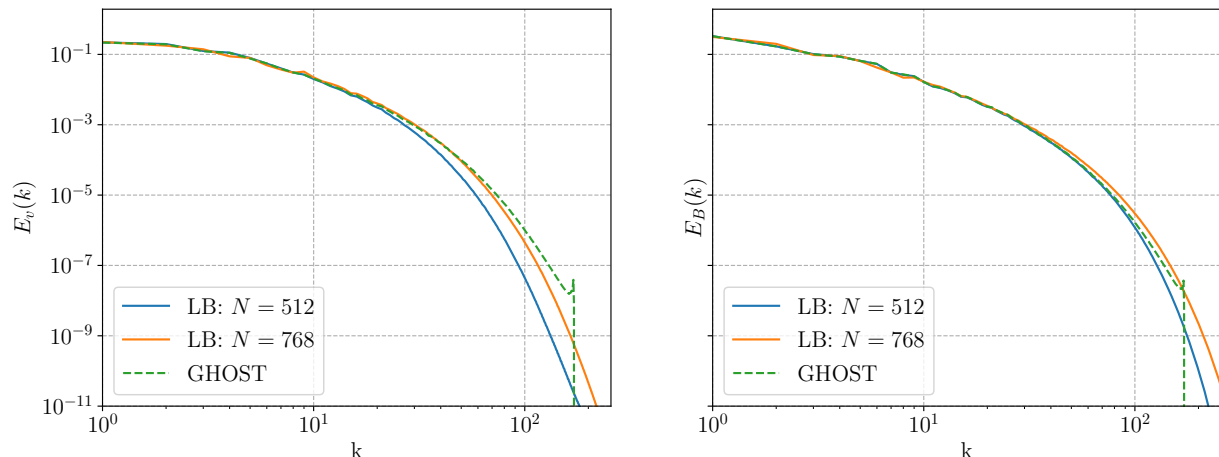


FIGURE 11. Kinetic (left) and magnetic (right) energy spectra of MHD turbulence at the peak of magnetic dissipation. The spectra are normalised by the total kinetic and magnetic energies respectively. Comparison between LB simulations at two different resolutions ($N = 512$, $N = 768$) and a de-aliased pseudo-spectral simulation ($N = 512$) performed with the GHOST solver.

(as compared to the pseudo-spectral simulation). It should also be noted that, while the maximum wave-number is $k_{\max} = N/3$ (due to the $2/3$ rule for de-aliasing) in pseudo-spectral simulations, the range of resolved scales reaches the Nyquist cut-off $k_{\max} = N/2$ in LB simulations. Particular attention is now paid to the wavenumber-by-wavenumber energy budget of the MHD equations. Starting from (2.11) and (2.13), the (total) energy flux across wavenumber k can be defined as

$$\mathcal{S}_{\text{MHD}}(k) = \sum_{|\mathbf{k}'| < k} \Re[\mathcal{F}(\mathbf{U})^* \cdot (\mathcal{F}(\mathbf{U} \cdot \nabla \mathbf{U}) - \mathcal{F}(\mathbf{J} \times \mathbf{B})) - \mathcal{F}(\mathbf{B})^* \cdot \mathcal{F}(\nabla \times (\mathbf{U} \times \mathbf{B}))] \quad (4.10)$$

whereas the (total) dissipation in the range $[0, k[$ is given by

$$\mathcal{D}(k) = \sum_{|\mathbf{k}'| < k} \nu k'^2 |\mathcal{F}(\mathbf{U})|^2 + \eta k'^2 |\mathcal{F}(\mathbf{B})|^2 \quad (4.11)$$

where $\mathcal{F}(\cdot)$ means the Fourier transform and $*$ is the complex conjugate. The wavenumber-by-wavenumber energy budget then writes

$$\partial_t \sum_{|\mathbf{k}'| < k} E(\mathbf{k}') = -\mathcal{S}_{\text{MHD}}(k) - \mathcal{D}(k). \quad (4.12)$$

We would like to mention that the contribution of the pressure term (not shown here) is negligible in the context of these simulations. The fluxes obtained for the LB and pseudo-spectral OT implementations (with $N = 512$) are displayed in detail in Fig. 12. A satisfactory agreement is observed in particular for the non-linear energy transfer terms, over the entire range of resolved wavenumbers. The slight over-dissipative nature of the LB scheme is again evidenced in the output of the dissipation term $\mathcal{D}(k)$ at very high wavenumbers.

5. High-Resolution simulations of 3D Hall-MHD plasmas

FLAME was used to simulate plasma dynamics in a regime in which the Hall-MHD term is non-negligible. In particular, the governing equations have been integrated in a triply periodic cubic lattice of size $L = 2\pi$ with resolution 512^3 and 768^3 , initialized

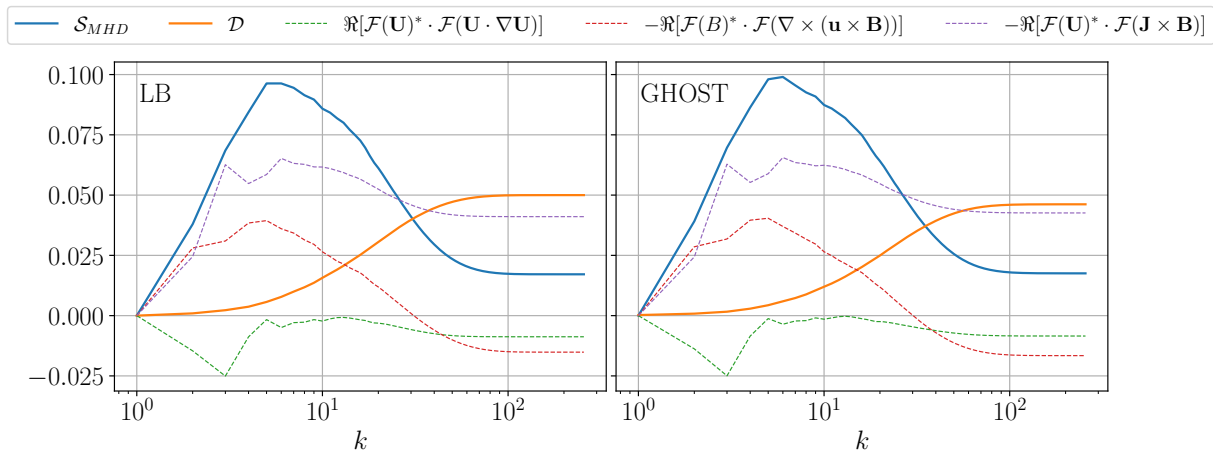


FIGURE 12. Various third-order energy fluxes across wavenumber k as reported in (4.11). Comparison is made between LB (left) and de-aliased pseudo-spectral (right) GHOST simulations. Let us notice that $\partial_t \sum_{|\mathbf{k}'| < k} E(\mathbf{k}') = -\mathcal{S}_{\text{MHD}}(k) - \mathcal{D}(k) < 0$ as expected for freely-decaying MHD turbulence.

Run	N	$\text{Ma} [\times 10^{-4}]$	Re	Pr_m	ϵ_H	t_{tot}/τ_0	t_{peak}/τ_0
I	512	7.0	4400	1	0.0025	48.2	31.8
II	512	1.0	5240	1	0.01	35.8	33.6
III	512	0.625	7150	1	0.025	29.6	26.5
IV	768	0.6	6000	1	0.015	36.6	32.0

TABLE 2. Parameters of Hall-MHD turbulence runs. Re , Ma and Pr_m denote respectively the Reynolds number (at the peak of magnetic dissipation), the initial Mach number and the magnetic Prandtl number. The (dimensionless) Hall parameter is ϵ_H . The number of grid points per dimension is N . The total duration of the run is t_{tot}/τ_0 and the time at which the peak of current density occurs is t_{peak}/τ_0 in units of the reference time scale L_0/U_0 . The Mach number satisfies the CFL condition (3.4) imposed by whistler waves.

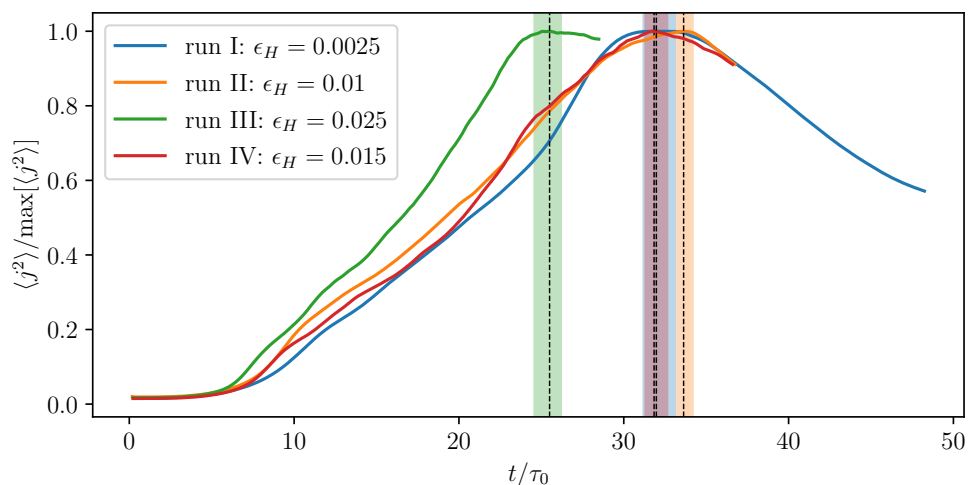


FIGURE 13. Evolution of the magnetic dissipation over time for the three simulations performed with the OT initial condition (see Tab.2). The shaded areas around the peak of the current density (black dashed line) correspond to the range over which the energy spectra in Fig. 16 have been averaged.

with the OT vortex as described in the previous section, for different values of the Hall parameter (see Tab. 2). The Mach number was adjusted to the Hall parameter in order to accommodate the CFL condition based on the time-scale of the whistler waves (see 3.4). The Reynolds number is estimated here at the peak of magnetic dissipation (indicated by the vertical dashed lines in Fig 13), at which the plasma is assumed to have reached a fully developed turbulent state. The FLAME code relies on a multi-GPU (Graphic Processing Unit) implementation of the LB scheme in order to reach high resolution that optimizes the computational times. Massive multi-threading is handled within the OpenCL (Open Computing Language) framework, allowing a high portability of the code. The spatial domain is split along a single direction and each GPU is assigned a sub-domain. A one-to-one mapping operates between the host CPU processes and the GPUs. Therefore, the exchange of boundary nodes between the GPUs is handled through memory transfers with the CPU processes and a message-passing interface (MPI) between the latter. Simulations were run on a cluster equipped with NVIDIA A100-40Gb GPU cards, hosted at the CINECA supercomputing center (Italy). For a 512^3 lattice dimension, only three GPUs were used in parallel, resulting in a computational speed of about 20 iterations per second, or equivalently, in 2.7 BLUPS (Billions of Lattice-node Updates Per Second). This led to a wall-clock computational time of 10, 55 and 69 hours respectively for the three runs indicated in Tab. 2 to pass the peak of magnetic-energy dissipation (see Fig. 13). The computational times reported above are comprehensive of the time required to transfer the three-dimensional vector fields (\mathbf{u} , \mathbf{B} and \mathbf{J}) between the CPUs and GPUs, and perform post-processing operations such as the tracking of the mean kinetic and magnetic energies, and mean energy dissipation rates. All computations were performed in double precision.

A rendering of the large-scale fields \mathbf{u} and \mathbf{B} is shown in Fig. 14 for the simulation at the highest resolution (run IV in Tab. 2), again taken at the peak of the magnetic-energy dissipation. The three-dimensional visualization is displayed together with the kinetic and magnetic energy spectra, the latter showing two regimes above and below the ion inertial length d_i . At the same time, the small-scale activity visible in Fig. 15 for the electric current density \mathbf{J} and the vorticity $\boldsymbol{\omega} = \nabla \times \mathbf{u}$, emphasizes the presence of current sheets, Kelvin-Helmholtz instabilities and vortices, emerging as the disordered structures characteristic of the Hall effect (Miura & Araki 2014). Furthermore, we have found that increasing the intensity of the Hall effect produces a faster development of turbulence in the plasmas under study due to the presence of both whistler and Hall-drift waves, propagating quicker than the Alfv en waves in the ideal MHD (Huba 2003). This is consistent with the behavior captured in Fig. 13 for the three runs, increasing the Hall parameter. The kinetic and magnetic energy spectra averaged over a time interval (around the peak of dissipation, as indicated by the shaded areas in Fig. 13) are plotted in Fig. 16 for each run at resolution 512^3 . As expected, increasing the value of the Hall parameter ϵ_H (indicated by the vertical dash-dotted line in Fig. 16) produces a shift of the Hall length-scale L_H towards larger scales, hence a shrink of the Kolmogorov's $k^{-5/3}$ power law range in both kinetic and magnetic energy spectra. A very surprising and promising feature of these simulations is the behavior of the magnetic spectra in the Hall-MHD regime. In fact, at wavenumbers $k > k_H$, the spectrum develops (as ϵ_H increases) a power-law scaling that is in perfect agreement with the $k^{-2.73}$ scaling obtained from the spectral analysis of solar wind measurements at sub-ion scales, as reported in (Kiyani et al. 2015).

In the MHD regime, the time step of the (compressible) Lattice Boltzmann runs is constrained by the need for resolving sound waves. Therefore, the time-step of an LB simulation is typically much smaller compared to the time-step of equivalent (incompress-

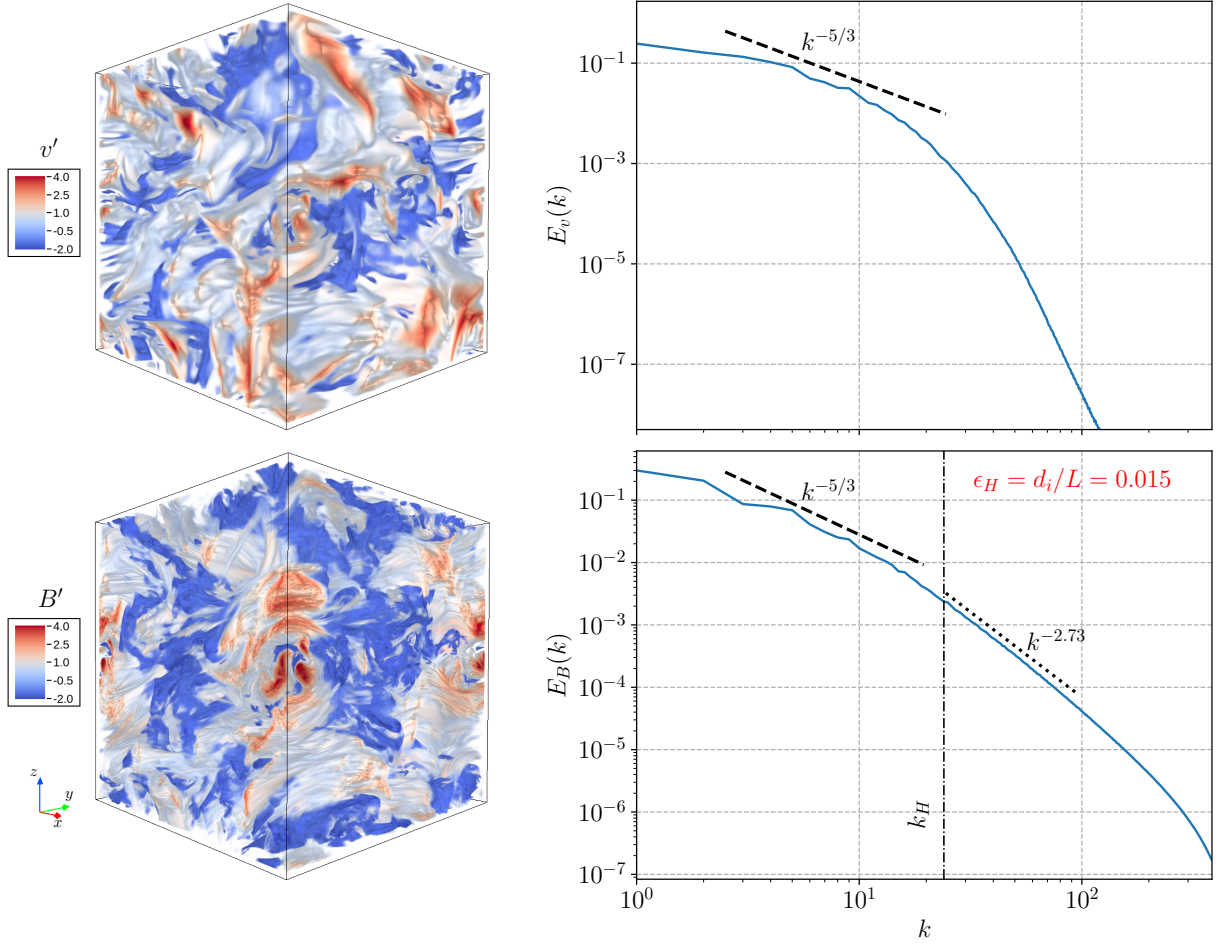


FIGURE 14. Results of a 3D Hall-MHD simulation at $N = 768^3$ taken at the peak of dissipation. The upper panels show a three-dimensional visualization of the normalized velocity field magnitude $v' = (v - \bar{v})/\sigma_v$ with $v = |\mathbf{v}|$ (upper left) and the relative power density spectrum (upper right). The same in the two bottom panels for the normalized magnetic field B' . The slopes $k^{-5/3}$ and $k^{-2.73}$ are given as a reference.

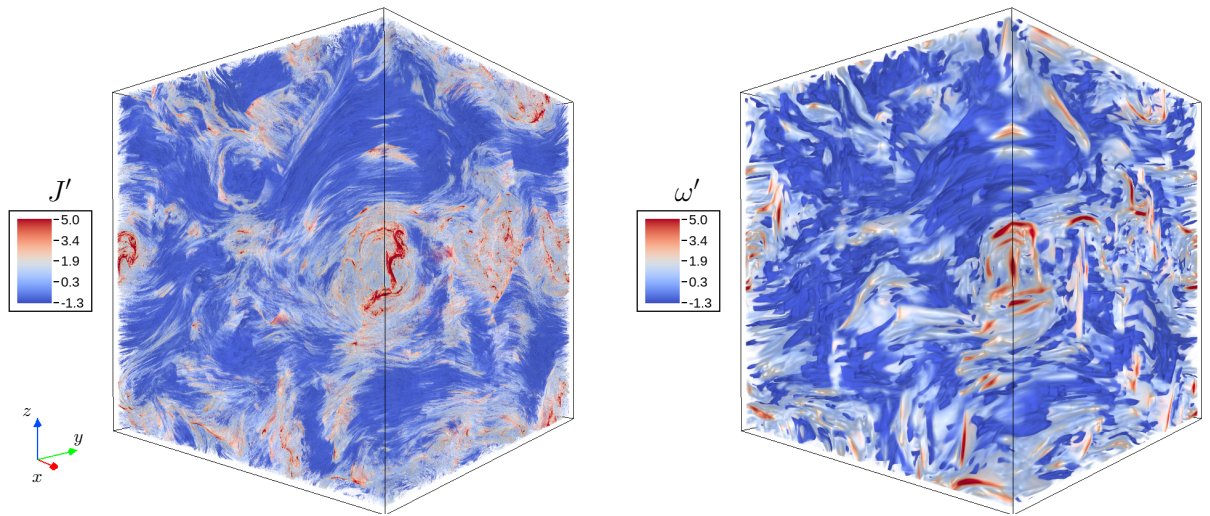


FIGURE 15. Three-dimensional rendering of the normalized current density $J' = (J - \bar{J})/\sigma_J$, with $J = |\mathbf{J}|$ (left), and vorticity ω' (right) taken at the same time as in Fig. 14.

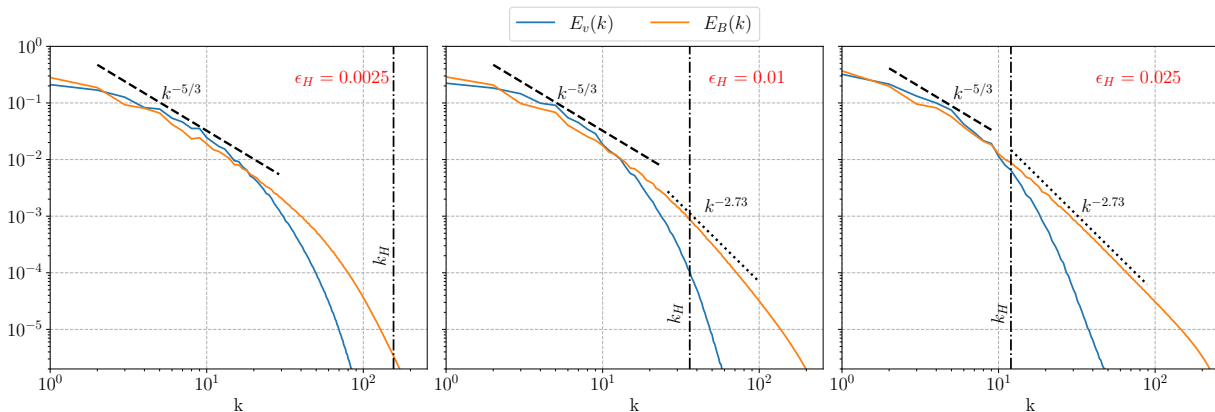


FIGURE 16. Kinetic (blue) and magnetic (orange) spectra corresponding to three different Hall-MHD turbulence regimes (see Tab. 2). The black dashed and dotted lines indicate respectively the $-5/3$ and -2.73 slopes in reference to solar wind measurements (Kiyani *et al.* 2015). All the spectra are taken at the peak of magnetic dissipation. The (black) vertical dash-dotted lines indicate the cross-over wavenumbers between MHD and Hall-MHD regimes given by $k_H = 2\pi/(\epsilon_H L_0)$ with $L_0 = 2\pi \int E_v(k)k^{-1}dk / \int E_v(k)dk$.

ible) pseudo-spectral simulation, the ratio between the two time-steps being typically the Mach number (Horstmann *et al.* 2022). Therefore, in the case of the MHD, the advantage for our LB scheme in terms of turn-around times is not that big compared to standard pseudo-spectral simulations. The situation is different when it comes to the simulation of plasmas in the Hall-MHD regime, where the time-steps of the two methods are identically constrained by the speed of whistler waves. In this case, the efficiency of the LB scheme (exploiting the computational power of GPU accelerators) is a major advantage, leading to wall-clock turn-around times that are significantly smaller for LB schemes, and for FLAME in particular. Finally, we would like to mention that an extension of FLAME allowing the simulation of the electron MHD dynamics would simply consist in modifying the equilibrium distributions for the magnetic field in the LB scheme, by neglecting the bulk velocity \mathbf{U} with respect to the Hall current $\alpha_H \mathbf{J}$ in (3.25).

6. Hall-MHD simulations for space plasma turbulence investigations

Space plasmas, whose dynamics involve a vast range of scales due to their large Reynolds numbers Matthaeus *et al.* (2008); Parashar *et al.* (2019), do actually develop well-defined MHD and Hall-MHD power-law spectral ranges, with a distinct transition between them. This clearly emerges from the observations performed with plasma and magnetic field instruments on board of two of the most recent space missions: Solar Orbiter (SO; M uller *et al.* 2020b) and Parker Solar Probe (PSP; Fox *et al.* 2016). Fig. 17 shows the trace spectra of the magnetic field fluctuations measured by the PSP/FIELDS (Bale *et al.* 2016) and SO/MAG (Horbury *et al.* 2020) magnetometers on board these state of the art spacecrafts. In particular, the PSP (red) magnetic field sample, measured on November 20, 2021, is relative to the fast solar wind plasma stream coming from an equatorial coronal hole, while the SO (blue) sample is relative to a low-speed solar wind stream measured on July 14 – 15, 2020, whose origin was identified in a coronal streamer and pseudo-streamer configuration (D’Amicis *et al.* 2021). In Tab. 3 we report the characteristic parameters of these solar wind samples. It is worth recalling that the ion gyroradius $\rho_i = v_{T,i}/\omega_{ci}$ (with $v_{T,i}$ ion thermal speed) and inertial length $d_i = c/\omega_{pi}$ are defined in terms of ion cyclotron ω_{ci} and plasma frequency ω_{pi} , respectively, the latter being in general significantly larger than the former. For values of density n , temperature

T and β typical for space plasmas, the relation $\rho_i \lesssim d_i$ is valid. However, it has been remarked by several authors how, for $\beta \sim \mathcal{O}(1)$, these characteristic length scales are comparable $\rho_i \simeq d_i$ (Alexandrova *et al.* 2008, 2009; Sahraoui *et al.* 2009; Kiyani *et al.* 2015). Thus, in the solar wind the breaking point identifying the transition between the end of the MHD range and the beginning of the range where plasma kinetic effects become relevant, in the magnetic field spectrum, at the sub-ion scales, is often referred as occurring either at the ion gyroradius or at the inertial length scale, when $\beta \sim 1$. In spite of the different speeds, both the SOLO and the PSP solar wind samples we considered here are Alfvénic, i.e., they are characterized by a high correlation between velocity and magnetic field fluctuations (see Bruno & Carbone 2013, and references therein, for a comprehensive review on the solar wind turbulence). A clear frequency break is observed at $k\rho_i \sim 1$ separating fluid and kinetic scales, as shown in Fig.17, marking the transition from the MHD turbulent inertial range (where energy is adiabatically transferred to smaller and smaller scales), that is characterized by a Kolmogorov-like spectrum Marino *et al.* (2011, 2012); Marino & Sorriso-Valvo (2023), to a range where the kinetic effects begin to dominate and in which the energy gets dissipated (at the bottom of such range), ultimately heating the solar wind plasma Marino *et al.* (2008). As is known from spacecraft observations, fluid and kinetic scales in the solar wind are characterized by different power-law spectral exponents. Features of these spectral ranges mostly depend on the distance from the Sun at which observations are made, i.e., on the observed stage of evolution of the solar wind turbulence (see, e.g., Telloni *et al.* 2021, 2022a). The physical phenomena as well as the governing parameters controlling the evolution of turbulence in the interplanetary space are still matter of investigation. Nonlinear interactions (Bruno & Carbone 2013), expansion-driven magnetic (Shi *et al.* 2021) and velocity shears Marino *et al.* (2012), as well as the parametric decay of Alfvén waves (Malara & Velli 1996), all certainly play some role. However, to date, there is not a clear consensus on how turbulence evolves from a spectrum resembling the one predicted by the Iroshnikov-Kraichnan phenomenology (Iroshnikov 1963; Kraichnan 1965) to a Kolmogorov-like spectrum (Kolmogorov 1941) as the solar wind expands from regions within the solar corona, or very close to it, to the outer heliosphere. Moreover, the slope of the magnetic-field spectrum beyond the ion skin depth (or ion inertial length) is highly variable, with power-law exponents ranging from ~ -4 to ~ -2 (Smith *et al.* 2006; Bruno *et al.* 2014), being also affected by the redistribution of the magnetic field energy at the (larger) fluid scales: in general, the larger is overall the power spectral density (PSD) within the MHD inertial range, the steeper is the spectrum at the kinetic scales. A number of dissipative wave-particle mechanisms are supposedly involved in the energy transfer and dissipation at the very small scales. Among these, cyclotron-resonant dissipation certainly plays an important role (see, e.g., Bruno & Trenchi 2014; Telloni *et al.* 2019), though the way energy is first brought to the small scales then dissipated in the collision-less solar wind plasma is still a matter of debate. Both the evolution of turbulence in the heliosphere and how energy is dissipated in the solar wind, are major open questions in the space plasma community that could be effectively targeted by means of numerical investigations produced with FLAME, which allows capturing the transition between MHD and Hall-MHD regimes (Fig.16), like the more standard pseudo-spectral codes. Another puzzle of solar and space plasma dynamics that can be tackled with our LB code is how magnetic switchbacks observed in the solar corona as well as in the solar wind do contribute to the local heating of the plasma. The switchbacks are intermittent magnetic-field polarity reversals widely observed in the heliosphere (Bale *et al.* 2019) and in the solar corona (Telloni *et al.* 2022b), that are thought to play a major role in the acceleration and heating of the solar wind. However, characterizing their

Probe	$\bar{\rho}$ [cm^3]	\bar{V} [km/s]	\bar{T} [MK]	\bar{B} [nT]	β	d_i [km]	D_{sun} [AU]
PSP	419	622	1.89	332	0.50	57.5	0.09
SO	16	429	1.50	6.76	3.59	11.1	0.64

TABLE 3. Main solar wind parameters computed at time where the solar wind samples used to produce the power spectra in Fig. 17 have been collected. Here we report solar wind density $\bar{\rho}$, solar wind bulk velocity \bar{V} , proton temperature \bar{T} , average magnetic field \bar{B} , ion inertial length d_i and the distance of the spacecraft (SO and PSP) from the Sun D_{sun} .

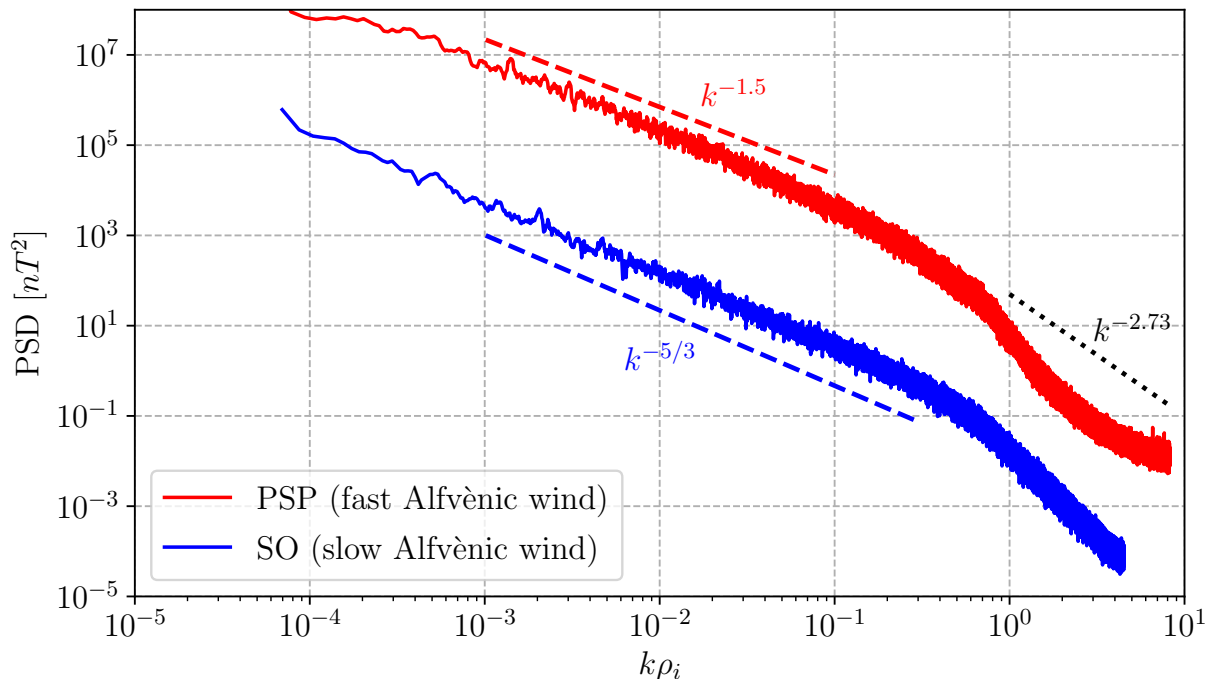


FIGURE 17. Power Spectra Density (PSD) of the magnetic field fluctuations observed by PSP (red) and SO (blue) on November 20, 2021 and July 14 – 15, 2020, respectively. The $k^{-1.67}$, $k^{-1.5}$ and $k^{-2.73}$ scalings are shown for reference as colored lines

contribution to the plasma energetics among other plasma processes is a challenging task, for which it is important to run highly accurate 3D Hall-MHD numerical simulations, able to resolve an extended dynamical range with the largest possible scale separation.

7. Conclusions

The LB approach extends the horizon for the numerical investigation of plasma dynamics. Stability issues, which have long been a handicap for the implementation of the LB method to investigate turbulent flows, are now mostly solved thanks to the use of improved collision operators that do not compromise the accuracy of the numerical solutions. Furthermore, the computational efficiency of the LB schemes on many-core devices such as GPUs allows for advantageous turn-around times. A major advantage of dealing with a kinetic representation at the level of the numerical scheme, is that the derivatives of the magnetic field are directly embedded in the solution, allowing for an intrinsically accurate description of the current density since it does not require further implementations of a differentiation scheme. The study presented here shows that the LB approach provides a valuable and efficient numerical tool to simulate Hall-MHD plasma turbulence. Furthermore, the LB approach allows us to add complexity

to the plasma, such as thermal effects, multi-species, complex geometries, etc. at the cost of new coupled lattice dynamics and boundary conditions, therefore preserving the computational performance.

The preliminary results provided by a simple benchmark based on the OT vortex problem anticipate that our code will be able to deliver excellent performances with the simulation of astrophysical and space plasmas in which the Hall term is expected to play a significant role in the dynamics of the system. Indeed, in plasmas as well as in anisotropic fluids, turbulence has to compete with waves in transferring energy across the scales (Marino *et al.* 2015c; Herbert *et al.* 2016). The interplay of waves and turbulence is responsible for the emergence of new characteristic length scales and the existence of different regimes (Marino *et al.* 2013; Feraco *et al.* 2018) in which various forms of energy can cascade to small or to large scales (Marino *et al.* 2014), or undergoing a dual energy cascade (Pouquet & Marino 2013; Marino *et al.* 2015b). The computational efficiency of our LB model will allow us to run simulations of fluids and plasmas separating regimes (in terms of spatial and temporal scales) where different physical phenomena dominate. We proved, though in a simplified configuration, that our LB model is able to capture the physical effects produced by the Hall term, such as faster dynamics due to the interplay of whistler waves and turbulence, the breakdown of the Kolmogorov spectrum at sub-ion scales and a behavior of the magnetic energy spectrum at that scales which has been already observed in solar wind measurements. All that provides FLAME with the potential to become a powerful tool for the investigation of magnetohydrodynamic plasmas in a variety of configurations of interest for heliospheric and magnetospheric studies. The present analysis and tests were performed using a benchmark configuration (OT vortex problem) which is isotropic, hence does not embed the anisotropy introduced by the ambient magnetic field in which the solar wind develops its dynamics. However, LB simulations of Hall-MHD flows performed with FLAME will be suitable to investigate plasmas immersed in a background magnetic field, at scales that are nowadays within the reach of the high-resolution instruments on board of the latest solar and magnetospheric missions, such as Solar Orbiter or Parker Solar Probe.

Acknowledgements

We gratefully thank Dr. Emmanuel Quemener for his technical support in the development of our multi-GPU code on the Centre Blaise Pascal’s computer testing platform at ENS de Lyon (France). Most simulations were run on the local HPC facilities at École Centrale de Lyon (PMCS2I) supported by the Auvergne-Rhône-Alpes region (GRANT CPRT07-13 CIRA) and the national Equip@Meso grant (ANR-10-EQPX-29-01). Finally, we acknowledge the CINECA computing center under the ISCRA initiative, for the availability of HPC resources necessary for high-resolution simulations of Hall-MHD turbulence, and support within the project LaB-HMHD - HP10C4HXCB. R.M., R.F. and F.F. also acknowledge support from the project “EVENTFUL” (ANR-20-CE30-0011), funded by the French “Agence Nationale de la Recherche” - ANR through the program AAPG-2020.

Appendix A. Central-moment-based LB scheme for fluid dynamics

For the fluid, the discretization (in velocity) of the phase space refers to the D3Q27 lattice. The set of adopted microscopic velocities $\{\mathbf{c}_i\}_{i=0,\dots,26}$ is defined in Cartesian

components by

$$\begin{aligned} |c_x\rangle &= [0, -1, 0, 0, -1, -1, -1, -1, 0, 0, -1, -1, -1, -1, 1, 0, 0, 1, 1, 1, 1, 0, 0, 1, 1, 1, 1]^\top \\ |c_y\rangle &= [0, 0, -1, 0, -1, 1, 0, 0, -1, -1, -1, -1, 1, 1, 0, 1, 0, 1, -1, 0, 0, 1, 1, 1, 1, -1, -1]^\top \\ |c_z\rangle &= [0, 0, 0, -1, 0, 0, -1, 1, -1, 1, -1, 1, -1, 1, 0, 0, 1, 0, 0, 1, -1, 1, -1, 1, -1, 1, -1]^\top \end{aligned}$$

The equilibrium densities (without accounting for the Lorentz force) are developed up to the sixth-order as

$$\begin{aligned} f_i^{(0)}(\rho, \mathbf{U}) &= w_i \rho \left\{ 1 + \frac{\mathbf{c}_i \cdot \mathbf{U}}{c_s^2} + \frac{1}{2c_s^4} \left[H_{ixx}^{(2)} U_x^2 + H_{iyy}^{(2)} U_y^2 + H_{izz}^{(2)} U_z^2 + 2 \left(H_{ixy}^{(2)} U_x U_y + \right. \right. \right. \\ &\quad \left. \left. + H_{ixz}^{(2)} U_x U_z + H_{iyz}^{(2)} U_y U_z \right) \right] + \frac{1}{2c_s^6} \left[H_{ixxy}^{(3)} U_x^2 U_y + H_{ixxz}^{(3)} U_x^2 U_z + H_{ixyy}^{(3)} U_x U_y^2 + \right. \\ &\quad \left. + H_{ixzz}^{(3)} U_x U_z^2 + H_{iyzz}^{(3)} U_y U_z^2 + H_{iyyz}^{(3)} U_y^2 U_z + 2H_{ixyz}^{(3)} U_x U_y U_z \right] + \frac{1}{4c_s^8} \left[H_{ixxyy}^{(4)} U_x^2 U_y^2 + \right. \\ &\quad \left. + H_{ixxzz}^{(4)} U_x^2 U_z^2 + H_{iyyzz}^{(4)} U_y^2 U_z^2 + 2 \left(H_{ixyzz}^{(4)} U_x U_y U_z^2 + H_{ixyzy}^{(4)} U_x U_y^2 U_z + \right. \right. \\ &\quad \left. \left. + H_{ixxyz}^{(4)} U_x^2 U_y U_z \right) \right] + \frac{1}{4c_s^{10}} \left[H_{ixxyzz}^{(5)} U_x^2 U_y U_z^2 + H_{ixxyyz}^{(5)} U_x^2 U_y^2 U_z + \right. \\ &\quad \left. + H_{ixyyz}^{(5)} U_x U_y^2 U_z^2 \right] + \frac{1}{8c_s^{12}} H_{ixxyyzz}^{(6)} U_x^2 U_y^2 U_z^2 \left. \right\} \end{aligned}$$

where the weights w_i are related to the lattice connectivity with $w_{\text{center}} = 8/27$, $w_{\text{face}} = 2/27$, $w_{\text{edge}} = 8/27$ and $w_{\text{corner}} = 1/216$ for the D3Q27 lattice (see Fig. 1), and $H_i^{(n)}$ refers to the n^{th} -order Hermite polynomial tensor in velocity \mathbf{c}_i . The Lorentz force is eventually taken into account by upgrading the densities as

$$f_i^{\text{mhd}(0)}(\rho, \mathbf{U}, \mathbf{B}) = f_i^{(0)}(\rho, \mathbf{U}) + \frac{w_i}{2c_s^4} ((\mathbf{B} \cdot \mathbf{B})(\mathbf{c}_i \cdot \mathbf{c}_i) - (\mathbf{c}_i \cdot \mathbf{B})^2).$$

The set of central moments \mathbf{k}_i is computed by applying the (invertible) transformation matrix \mathbf{T} with the column vectors

$$\begin{aligned} |\mathbf{T}_0\rangle &= |1\rangle \\ |\mathbf{T}_1\rangle; |\mathbf{T}_2\rangle; |\mathbf{T}_3\rangle &= [\bar{c}_{ix}]^\top; [\bar{c}_{iy}]^\top; [\bar{c}_{iz}]^\top \\ |\mathbf{T}_4\rangle; |\mathbf{T}_5\rangle; |\mathbf{T}_6\rangle &= [\bar{c}_{ix}\bar{c}_{iy}]^\top; [\bar{c}_{ix}\bar{c}_{iz}]^\top; [\bar{c}_{iy}\bar{c}_{iz}]^\top \\ |\mathbf{T}_7\rangle; |\mathbf{T}_8\rangle; |\mathbf{T}_9\rangle &= [\bar{c}_{ix}^2 - \bar{c}_{iy}^2]^\top; [\bar{c}_{ix}^2 - \bar{c}_{iz}^2]^\top; [\bar{c}_{ix}^2 + \bar{c}_{iy}^2 + \bar{c}_{iz}^2]^\top \\ |\mathbf{T}_{10}\rangle; |\mathbf{T}_{11}\rangle; |\mathbf{T}_{12}\rangle &= [\bar{c}_{ix}\bar{c}_{iy}^2 + \bar{c}_{ix}\bar{c}_{iz}^2]^\top; [\bar{c}_{ix}\bar{c}_{iy}^2 + \bar{c}_{iy}\bar{c}_{iz}^2]^\top; [\bar{c}_{ix}^2\bar{c}_{iy} + \bar{c}_{iy}^2\bar{c}_{iz}]^\top \\ |\mathbf{T}_{13}\rangle; |\mathbf{T}_{14}\rangle; |\mathbf{T}_{15}\rangle &= [\bar{c}_{ix}\bar{c}_{iy}^2 - \bar{c}_{ix}\bar{c}_{iz}^2]^\top; [\bar{c}_{ix}\bar{c}_{iy}^2 - \bar{c}_{iy}\bar{c}_{iz}^2]^\top; [\bar{c}_{ix}^2\bar{c}_{iy} - \bar{c}_{iy}^2\bar{c}_{iz}]^\top \\ |\mathbf{T}_{16}\rangle &= [\bar{c}_{ix}\bar{c}_{iy}\bar{c}_{iz}]^\top \\ |\mathbf{T}_{17}\rangle; |\mathbf{T}_{18}\rangle; |\mathbf{T}_{19}\rangle &= [\bar{c}_{ix}^2\bar{c}_{iy}^2 + \bar{c}_{ix}^2\bar{c}_{iz}^2 + \bar{c}_{iy}^2\bar{c}_{iz}^2]^\top; [\bar{c}_{ix}^2\bar{c}_{iy}^2 + \bar{c}_{ix}^2\bar{c}_{iz}^2 - \bar{c}_{iy}^2\bar{c}_{iz}^2]^\top; [\bar{c}_{ix}^2\bar{c}_{iy}^2 - \bar{c}_{ix}^2\bar{c}_{iz}^2]^\top \\ |\mathbf{T}_{20}\rangle; |\mathbf{T}_{21}\rangle; |\mathbf{T}_{22}\rangle &= [\bar{c}_{ix}^2\bar{c}_{iy}\bar{c}_{iz}]^\top; [\bar{c}_{ix}\bar{c}_{iy}^2\bar{c}_{iz}]^\top; [\bar{c}_{ix}\bar{c}_{iy}\bar{c}_{iz}^2]^\top \\ |\mathbf{T}_{23}\rangle; |\mathbf{T}_{24}\rangle; |\mathbf{T}_{25}\rangle &= [\bar{c}_{ix}\bar{c}_{iy}^2\bar{c}_{iz}^2]^\top; [\bar{c}_{ix}^2\bar{c}_{iy}\bar{c}_{iz}^2]^\top; [\bar{c}_{ix}^2\bar{c}_{iy}^2\bar{c}_{iz}]^\top \\ |\mathbf{T}_{26}\rangle &= [\bar{c}_{ix}^2\bar{c}_{iy}^2\bar{c}_{iz}^2]^\top \end{aligned}$$

where $\bar{\mathbf{c}}_i = \mathbf{c}_i - \mathbf{U}$ is the set of microscopic velocities obtained by the shift of particle velocities by the local fluid velocity. The 27×27 collision matrix S for the central moments

is a diagonal matrix with the respective relaxation rates

$$S = \text{diag}[1, 1, 1, 1, \omega, \omega, \omega, \omega, \omega, 1, \dots, 1],$$

which leads to

$$\begin{aligned} \mathbf{k}_{0\dots3}^* &= \langle \mathbf{T}_{0\dots3} | f^{\text{mhd}(0)} \rangle \\ \mathbf{k}_{4\dots8}^* &= \omega \langle \mathbf{T}_{4\dots8} | f^{\text{mhd}(0)} \rangle + (1 - \omega) \langle \mathbf{T}_{4\dots8} | \bar{f} \rangle \\ \mathbf{k}_{9\dots26}^* &= \langle \mathbf{T}_{9\dots26} | f^{\text{mhd}(0)} \rangle. \end{aligned}$$

Appendix B. Calculation of the electric current density

The electric current is obtained by solving the linear system (3.27). By using (3.28), this system can be re-expressed as

$$\widetilde{\mathbf{M}} \begin{bmatrix} J_x \\ J_y \\ J_z \end{bmatrix} = -\frac{1}{2\alpha_H} \begin{bmatrix} \Lambda_{yz} - \Lambda_{zy} - 2(U_y B_z - U_z B_y) \\ \Lambda_{zx} - \Lambda_{xz} - 2(U_z B_x - U_x B_z) \\ \Lambda_{xy} - \Lambda_{yx} - 2(U_x B_y - U_y B_x) \end{bmatrix}$$

where $\Lambda_{\alpha\beta} = \sum_{i=0}^{M-1} \xi_{i\alpha} \bar{g}_{i\beta}$ and $\widetilde{\mathbf{M}}$ is the invertible matrix

$$\widetilde{\mathbf{M}} = \begin{bmatrix} C^2/2\alpha_H\omega_B & B_z & -B_y \\ -B_z & C^2/2\alpha_H\omega_B & B_x \\ B_y & -B_x & C^2/2\alpha_H\omega_B \end{bmatrix}$$

where C represents the characteristic speed of *magnetic* particles on the D3Q7 lattice and ω_B is the relaxation pulsation (3.20) associated with the BGK collision operator for the magnetic field. The expression for the three components of the electric current density obtained by solving the previous linear system reads as

$$\begin{aligned} J_x &= \frac{1}{D} (-2C^4\omega_B B_y U_z + 2C^4\omega_B B_z U_y - C^4\omega_B \Lambda_{yz} + C^4\omega_B \Lambda_{zy} - 4C^2\alpha_H\omega_B^2 B_x B_y U_y - \\ &\quad - 4C^2\alpha_H\omega_B^2 B_x B_z U_z + 4C^2\alpha_H\omega_B^2 B_y^2 U_x - 2C^2\alpha_H\omega_B^2 \Lambda_{xy} B_y + 2C^2\alpha_H\omega_B^2 \Lambda_{yx} B_y + \\ &\quad + 4C^2\alpha_H\omega_B^2 B_z^2 U_x - 2C^2\alpha_H\omega_B^2 \Lambda_{xz} B_z + 2C^2\alpha_H\omega_B^2 \Lambda_{zx} B_z - 4\alpha_H^2\omega_B^3 \Lambda_{yz} B_x^2 + \\ &\quad + 4\alpha_H^2\omega_B^3 \Lambda_{zy} B_x^2 + 4\alpha_H^2\omega_B^3 \Lambda_{xz} B_x B_y - 4\alpha_H^2\omega_B^3 \Lambda_{zx} B_x B_y - 4\alpha_H^2\omega_B^3 \Lambda_{xy} B_x B_z + \\ &\quad + 4\alpha_H^2\omega_B^3 \Lambda_{yx} B_x B_z) \\ J_y &= \frac{1}{D} (2C^4\omega_B B_x U_z + 2C^4\omega_B B_z U_x + C^4\omega_B \Lambda_{xz} - C^4\omega_B \Lambda_{zx} + 4C^2\alpha_H\omega_B^2 B_x^2 U_y - \\ &\quad - 4C^2\alpha_H\omega_B^2 B_x B_y U_x + 2C^2\alpha_H\omega_B^2 \Lambda_{xy} B_x - 2C^2\alpha_H\omega_B^2 \Lambda_{yx} B_x - 4C^2\alpha_H\omega_B^2 B_y B_z U_z + \\ &\quad + 4C^2\alpha_H\omega_B^2 B_z^2 U_y - 2C^2\alpha_H\omega_B^2 \Lambda_{yz} B_z + 2C^2\alpha_H\omega_B^2 \Lambda_{zy} B_z - 4\alpha_H^2\omega_B^3 \Lambda_{yz} B_x B_y + \\ &\quad + 4\alpha_H^2\omega_B^3 \Lambda_{zy} B_x B_y + 4\alpha_H^2\omega_B^3 \Lambda_{xz} B_y^2 - 4\alpha_H^2\omega_B^3 \Lambda_{zx} B_y^2 - 4\alpha_H^2\omega_B^3 \Lambda_{xy} B_y B_z + \\ &\quad + 4\alpha_H^2\omega_B^3 \Lambda_{yx} B_y B_z) \end{aligned}$$

$$\begin{aligned}
J_z = \frac{1}{D} & (-2C^4\omega_B B_x U_y + 2C^4\omega_B B_y U_x - C^4\omega_B \Lambda_{xy} + C^4\omega_B \Lambda_{yx} + 4C^2\alpha_H\omega_B^2 B_x^2 U_z - \\
& - 4C^2\alpha_H\omega_B^2 B_x B_z U_x + 2C^2\alpha_H\omega_B^2 \Lambda_{xz} B_x - 2C^2\alpha_H\omega_B^2 \Lambda_{zx} B_x + 4C^2\alpha_H\omega_B^2 B_y^2 U_z - \\
& - 4C^2\alpha_H\omega_B^2 B_y B_z U_y + 2C^2\alpha_H\omega_B^2 \Lambda_{yz} B_y - 2C^2\alpha_H\omega_B^2 \Lambda_{zy} B_y - 4\alpha_H^2\omega_B^3 \Lambda_{yz} B_x B_z + \\
& + 4\alpha_H^2\omega_B^3 \Lambda_{zy} B_x B_y + 4\alpha_H^2\omega_B^3 \Lambda_{xz} B_y B_z - 4\alpha_H^2\omega_B^3 \Lambda_{zx} B_y B_z - 4\alpha_H^2\omega_B^3 \Lambda_{xy} B_z^2 + \\
& + 4\alpha_H^2\omega_B^3 \Lambda_{yx} B_z^2)
\end{aligned} \tag{B1}$$

where $D = C^6 + 4C^2\alpha_H^2\omega_B^2|\mathbf{B}|^2 > 0$.

REFERENCES

- ALEXANDROVA, O., LACOMBE, C. & MANGENEY, A. 2008 Spectra and anisotropy of magnetic fluctuations in the earth's magnetosheath: Cluster observations. *Annales Geophysicae* **26** (11), 3585–3596.
- ALEXANDROVA, O., SAUR, J., LACOMBE, C., MANGENEY, A., MITCHELL, J., SCHWARTZ, S. J. & ROBERT, P. 2009 Universality of solar-wind turbulent spectrum from mhd to electron scales. *Phys. Rev. Lett.* **103**, 165003.
- BALE, S. D., BADMAN, S. T., BONNELL, J. W., BOWEN, T. A., BURGESS, D., CASE, A. W., CATTELL, C. A., CHANDRAN, B. D. G., CHASTON, C. C., CHEN, C. H. K., DRAKE, J. F., DE WIT, T., DUDOK, EASTWOOD, J. P., ERGUN, R. E., FARRELL, W. M., FONG, C., GOETZ, K., GOLDSTEIN, M., GOODRICH, K. A., HARVEY, P. R., HORBURY, T. S., HOWES, G. G., KASPER, J. C., KELLOGG, P. J., KLIMCHUK, J. A., KORRECK, K. E., KRASNOSELSKIKH, V. V., KRUCKER, S., LAKER, R., LARSON, D. E., MACDOWALL, R. J., MAKSIMOVIC, M., MALASPINA, D. M., MARTINEZ-OLIVEROS, J., MCCOMAS, D. J., MEYER-VERNET, N., MONCUQUET, M., MOZER, F. S., PHAN, T. D., PULUPA, M., RAOUAFI, N. E., SALEM, C., STANSBY, D., STEVENS, M., SZABO, A., VELLI, M., WOOLLEY, T. & WYGANT, J. R. 2019 Highly structured slow solar wind emerging from an equatorial coronal hole. *Nature* **576** (7786), 237–242.
- BALE, S. D., GOETZ, K., HARVEY, P. R., TURIN, P., BONNELL, J. W., DUDOK DE WIT, T., ERGUN, R. E., MACDOWALL, R. J., PULUPA, M., ANDRE, M., BOLTON, M., BOUGERET, J. L., BOWEN, T. A., BURGESS, D., CATTELL, C. A., CHANDRAN, B. D. G., CHASTON, C. C., CHEN, C. H. K., CHOI, M. K., CONNERNEY, J. E., CRANMER, S., DIAZ-AGUADO, M., DONAKOWSKI, W., DRAKE, J. F., FARRELL, W. M., FERGEAU, P., FERMIN, J., FISCHER, J., FOX, N., GLASER, D., GOLDSTEIN, M., GORDON, D., HANSON, E., HARRIS, S. E., HAYES, L. M., HINZE, J. J., HOLLWEG, J. V., HORBURY, T. S., HOWARD, R. A., HOXIE, V., JANNET, G., KARLSSON, M., KASPER, J. C., KELLOGG, P. J., KIEN, M., KLIMCHUK, J. A., KRASNOSELSKIKH, V. V., KRUCKER, S., LYNCH, J. J., MAKSIMOVIC, M., MALASPINA, D. M., MARKER, S., MARTIN, P., MARTINEZ-OLIVEROS, J., MCCAULEY, J., MCCOMAS, D. J., McDONALD, T., MEYER-VERNET, N., MONCUQUET, M., MONSON, S. J., MOZER, F. S., MURPHY, S. D., ODOM, J., OLIVERSON, R., OLSON, J., PARKER, E. N., PANKOW, D., PHAN, T., QUATAERT, E., QUINN, T., RUPLIN, S. W., SALEM, C., SEITZ, D., SHEPPARD, D. A., SIY, A., STEVENS, K., SUMMERS, D., SZABO, A., TIMOFEEVA, M., VAIVADS, A., VELLI, M., YEHLE, A., WERTHIMER, D. & WYGANT, J. R. 2016 The FIELDS Instrument Suite for Solar Probe Plus. Measuring the Coronal Plasma and Magnetic Field, Plasma Waves and Turbulence, and Radio Signatures of Solar Transients. *Space Sci. Rev.* **204** (1-4), 49–82.
- BHATNAGAR, P. L., GROSS, E. P. & KROOK, M. 1954 A model for collision processes in gases. i. small amplitude processes in charged and neutral one-component systems. *Phys. Rev.* **94**, 511–525.
- BOUCHUT, FRANÇOIS 1999 Construction of bgk models with a family of kinetic entropies for a given system of conservation laws. *J. Stat. Phys.* **95**, 113–170.
- BRUNO, ROBERTO & CARBONE, VINCENZO 2013 The Solar Wind as a Turbulence Laboratory. *Living Rev. Sol. Phys.* **10** (1), 2.
- BRUNO, R. & TRENCHI, L. 2014 Radial Dependence of the Frequency Break between Fluid and Kinetic Scales in the Solar Wind Fluctuations. *Astrophys. J., Lett.* **787** (2), L24.

- BRUNO, R., TRENCHI, L. & TELLONI, D. 2014 Spectral Slope Variation at Proton Scales from Fast to Slow Solar Wind. *Astrophys. J., Lett.* **793** (1), L15.
- CHEN, SHIYI, CHEN, HUDONG, MARTNEZ, DANIEL & MATTHAEUS, WILLIAM 1991 Lattice boltzmann model for simulation of magnetohydrodynamics. *Phys. Rev. Lett.* **67**, 3776–3779.
- COREIXAS, CHRISTOPHE, CHOPARD, BASTIEN & LATT, JONAS 2019 Comprehensive comparison of collision models in the lattice boltzmann framework: Theoretical investigations. *Phys. Rev. E* **100**, 033305.
- COREIXAS, CHRISTOPHE, WISSOCQ, GAUTHIER, PUIGT, GUILLAUME, BOUSSUGE, JEAN-FRANÇOIS & SAGAUT, PIERRE 2017 Recursive regularization step for high-order lattice boltzmann methods. *Phys. Rev. E* **96** (3), 033306.
- CROISILLE, JP., KHANFIR, R. & CHANTEU, G. 1995 Numerical simulation of the mhd equations by a kinetic-type method. *J. Sci. Comput.* **10**, 81–92.
- D’AMICIS, R., BRUNO, R., PANASENCO, O., TELLONI, D., PERRONE, D., MARCUCCI, M. F., WOODHAM, L., VELLI, M., DE MARCO, R., JAGARLAMUDI, V., COCO, I., OWEN, C., LOUARN, P., LIVI, S., HORBURY, T., ANDRÉ, N., ANGELINI, V., EVANS, V., FEDOROV, A., GENOT, V., LAVRAUD, B., MATTEINI, L., MÜLLER, D., O’BRIEN, H., PEZZI, O., ROUILLARD, A. P., SORRISO-VALVO, L., TENERANI, A., VERSCHAREN, D. & ZOUGANELIS, I. 2021 First Solar Orbiter observation of the Alfvénic slow wind and identification of its solar source. *Astron. Astrophys.* **656**, A21.
- DE ROSIS, ALESSANDRO 2017 Nonorthogonal central-moments-based lattice boltzmann scheme in three dimensions. *Phys. Rev. E* **95**, 013310.
- DE ROSIS, ALESSANDRO & LUO, KAI H. 2019 Role of higher-order hermite polynomials in the central-moments-based lattice boltzmann framework. *Phys. Rev. E* **99** (1), 013301.
- DE ROSIS, ALESSANDRO, LÉVÊQUE, EMMANUEL & CHAHINE, ROBERT 2018 Advanced lattice boltzmann scheme for high-reynolds-number magneto-hydrodynamic flows. *J. Turb.* **19** (6), 446–462.
- DELLAR, PAUL J. 2002 Lattice kinetic schemes for magnetohydrodynamics. *Journal of Computational Physics* **179** (1), 95–126.
- FERACO, FABIO, MARINO, RAFFAELE, PUMIR, ALAIN, PRIMAVERA, LEONARDO, MININNI, PABLO, POUQUET, ANNICK & ROSENBERG, DUANE 2018 Vertical drafts and mixing in stratified turbulence: Sharp transition with froude number. *EPL (Europhysics Letters)* **123**, 44002.
- FERRAND, R., SAHRAOUI, F., GALTIER, S., ANDRÉS, N., MININNI, P. & DMITRUK, P. 2022 An in-depth numerical study of exact laws for compressible hall magnetohydrodynamic turbulence. *The Astrophysical Journal* **927** (2), 205.
- FLINT, CHRISTOPHER & VAHALA, GEORGE 2018 A partial entropic lattice boltzmann mhd simulation of the orszag–tang vortex. *Radiation Effects and Defects in Solids* **173** (1-2), 55–65, arXiv: <https://doi.org/10.1080/10420150.2018.1442460>.
- FOX, N. J., VELLI, M. C., BALE, S. D., DECKER, R., DRIESMAN, A., HOWARD, R. A., KASPER, J. C., KINNISON, J., KUSTERER, M., LARIO, D., LOCKWOOD, M. K., MCCOMAS, D. J., RAOUAFI, N. E. & SZABO, A. 2016 The Solar Probe Plus Mission: Humanity’s First Visit to Our Star. *Space Sci. Rev.* **204** (1-4), 7–48.
- GALTIER, SÉBASTIEN 2016 *Introduction to Modern Magnetohydrodynamics*. Cambridge University Press.
- GALTIER, SEBASTIEN & BUCHLIN, ERIC 2007 Multiscale hall-magnetohydrodynamic turbulence in the solar wind. *Astrophysical Journal* **656** (1), 560–566.
- GEIER, M., GREINER, A. & KORVINK, J.G. 2007 Properties of the cascaded lattice Boltzmann automaton. *Int. J. Mod. Phys. C* **18** (04), 455–462.
- GEIER, MARTIN, SCHÖNHERR, MARTIN, PASQUALI, ANDREA & KRAFCZYK, MANFRED 2015 The cumulant lattice boltzmann equation in three dimensions: Theory and validation. *Computers & Mathematics with Applications* **70** (4), 507–547.
- GÓMEZ, DANIEL O., MININNI, PABLO D. & DMITRUK, PABLO 2010 Hall-magnetohydrodynamic small-scale dynamos. *Phys. Rev. E* **82**, 036406.
- GONZÁLEZ-MORALES, P. A., KHOMENKO, E. & CALLY, P. S. 2019 Fast-to-alfvén mode conversion mediated by hall current. II. application to the solar atmosphere. *Astrophysical Journal* **870** (2), 94.

- HE, XIAOYI & LUO, LI-SHI 1997 Theory of the lattice boltzmann method: From the boltzmann equation to the lattice boltzmann equation. *Phys. Rev. E* **56**, 6811–6817.
- HERBERT, C., MARINO, R., ROSENBERG, D. & POUQUET, A. 2016 Waves and vortices in the inverse cascade regime of stratified turbulence with or without rotation. *Journal of Fluid Mechanics* **806**, 165–204.
- HORBURY, T. S., O'BRIEN, H., CARRASCO BLAZQUEZ, I., BENDYK, M., BROWN, P., HUDSON, R., EVANS, V., ODDY, T. M., CARR, C. M., BEEK, T. J., CUPIDO, E., BHATTACHARYA, S., DOMINGUEZ, J. A., MATTHEWS, L., MYKLEBUST, V. R., WHITESIDE, B., BALE, S. D., BAUMJOHANN, W., BURGESS, D., CARBONE, V., CARGILL, P., EASTWOOD, J., ERDÖS, G., FLETCHER, L., FORSYTH, R., GIACALONE, J., GLASSMEIER, K. H., GOLDSTEIN, M. L., HOEKSEMA, T., LOCKWOOD, M., MAGNES, W., MAKSIMOVIC, M., MARSCH, E., MATTHAEUS, W. H., MURPHY, N., NAKARIAKOV, V. M., OWEN, C. J., OWENS, M., RODRIGUEZ-PACHECO, J., RICHTER, I., RILEY, P., RUSSELL, C. T., SCHWARTZ, S., VAINIO, R., VELLI, M., VENNERSTROM, S., WALSH, R., WIMMER-SCHWEINGRUBER, R. F., ZANK, G., MÜLLER, D., ZOUGANELIS, I. & WALSH, A. P. 2020 The Solar Orbiter magnetometer. *Astron. Astrophys.* **642**, A9.
- HORSTMANN, JAN, TOUIL, HATEM, VIENNE, LUCIEN, RICOT, DENIS & LÉVÊQUE, EMMANUEL 2022 Consistent time-step optimization in the lattice boltzmann method. *Journal of Computational Physics* **462**, 111224.
- HUBA, J. D. 2003 Hall Magnetohydrodynamics - A Tutorial. In *Space Plasma Simulation*, , vol. 615, pp. 166–192. Büchner, J. and Dum, C. and Scholer, M.
- IROSHNIKOV, P. S. 1963 Turbulence of a Conducting Fluid in a Strong Magnetic Field. *Astron. Zh.* **40**, 742.
- KIYANI, KHUROM H., OSMAN, KAREEM T. & CHAPMAN, SANDRA C. 2015 Dissipation and heating in solar wind turbulence: from the macro to the micro and back again. *Philosophical Transactions of the Royal Society A: Mathematical, Physical and Engineering Sciences* **373** (2041), 20140155.
- KOLMOGOROV, A. 1941 The Local Structure of Turbulence in Incompressible Viscous Fluid for Very Large Reynolds' Numbers. *Dokl. Akad. Nauk SSSR* **30**, 301–305.
- KÖRNER, CAROLIN, POHL, THOMAS, RÜDE, ULRICH, THÜREY, NILS & ZEISER, THOMAS 2006 Parallel lattice boltzmann methods for cfd applications. In *Numerical Solution of Partial Differential Equations on Parallel Computers* (ed. Are Magnus Bruaset & Aslak Tveito), pp. 439–466. Berlin, Heidelberg: Springer Berlin Heidelberg.
- KRAICHNAN, ROBERT H. 1965 Inertial-Range Spectrum of Hydromagnetic Turbulence. *Phys. Fluids* **8** (7), 1385–1387.
- KRUEGER, TIMM, KUSUMAATMAJA, HALIM, KUZMIN, ALEXANDR, SHARDT, OREST, SILVA, GONCALO & VIGGEN, ERLEND MAGNUS 2016 *The Lattice Boltzmann Method: Principles and Practice*. Springer.
- LEWY, H, FRIEDRICHS, K & COURANT, R 1928 Über die partiellen differenzgleichungen der mathematischen physik. *Mathematische annalen* **100**, 32–74.
- MA, YINGJUAN, RUSSELL, CHRISTOPHER T., TOTH, GABOR, CHEN, YUXI, NAGY, ANDREW F., HARADA, YUKI, MCFADDEN, JAMES, HALEKAS, JASPER S., LILLIS, ROB, CONNERNEY, JOHN E. P., ESLEY, JARED, DIBRACCIO, GINA A., MARKIDIS, STEFANO, PENG, IVY BO, FANG, XIAOHUA & JAKOSKY, BRUCE M. 2018 Reconnection in the martian magnetotail: Hall-mhd with embedded particle-in-cell simulations. *Journal of Geophysical Research: Space Physics* **123** (5), 3742–3763.
- MAHAJAN, S. M. & KRISHAN, V. 2005 Exact solution of the incompressible Hall magnetohydrodynamics. *Monthly Notices of the Royal Astronomical Society: Letters* **359** (1), L27–L29.
- MALARA, F. & VELLI, M. 1996 Parametric instability of a large-amplitude nonmonochromatic Alfvén wave. *Phys. Plasmas* **3** (12), 4427–4433.
- MALASPINAS, ORESTIS 2015 Increasing stability and accuracy of the lattice boltzmann scheme: recursivity and regularization. *arXiv preprint arXiv:1505.06900* .
- MARCHAND, P., COMMERÇON, B. & CHABRIER, G. 2018 Impact of the hall effect in star formation and the issue of angular momentum conservation. *A&A* **619**, A37.
- MARINO, R., MININNI, P. D., ROSENBERG, D. & POUQUET, A. 2013 Inverse cascades in rotating stratified turbulence: Fast growth of large scales. *EPL (Europhysics Letters)* **102** (4), 44006.

- MARINO, R., MININNI, P. D., ROSENBERG, D. L. & POUQUET, A. 2014 Large-scale anisotropy in stably stratified rotating flows. *Phys. Rev. E* **90**, 023018.
- MARINO, R., POUQUET, A. & ROSENBERG, D. 2015a Resolving the paradox of oceanic large-scale balance and small-scale mixing. *Phys. Rev. Lett.* **114**, 114504.
- MARINO, R., POUQUET, A. & ROSENBERG, D. 2015b Resolving the paradox of oceanic large-scale balance and small-scale mixing. *Phys. Rev. Lett.* **114**, 114504.
- MARINO, RAFFAELE, ROSENBERG, DUANE, HERBERT, CORENTIN & POUQUET, ANNICK 2015c Interplay of waves and eddies in rotating stratified turbulence and the link with kinetic-potential energy partition. *EPL (Europhysics Letters)* **112**.
- MARINO, R. & SORRISO-VALVO, L. 2023 Scaling laws for the energy transfer in space plasma turbulence. *Physics Reports (IN PRESS)*.
- MARINO, R., SORRISO-VALVO, L., CARBONE, V., NOULLEZ, A., BRUNO, R. & BAVASSANO, B. 2008 Heating the Solar Wind by a Magnetohydrodynamic Turbulent Energy Cascade. *Astroph. Journal Lett.* **677** (1), L71.
- MARINO, RAFFAELE, SORRISO-VALVO, LUCA, CARBONE, VINCENZO, VELTRI, PIERLUIGI, NOULLEZ, ALAIN & BRUNO, ROBERTO 2011 The magnetohydrodynamic turbulent cascade in the ecliptic solar wind: Study of Ulysses data. *Planetary and Space Science* **59** (7), 592–597.
- MARINO, R., SORRISO-VALVO, L., D'AMICIS, R., CARBONE, V., BRUNO, R. & VELTRI, P. 2012 On the Occurrence of the Third-order Scaling in High Latitude Solar Wind. *Astroph. Journal* **750** (1), 41.
- MARTÍNEZ, DANIEL O., CHEN, SHIYI & MATTHAEUS, WILLIAM H. 1994 Lattice boltzmann magnetohydrodynamics. *Physics of Plasmas* **1** (6), 1850–1867, arXiv: <https://doi.org/10.1063/1.870640>.
- MATTHAEUS, W. H., WEYGAND, J. M., CHUYCHAI, P., DASSO, S., SMITH, C. W. & KIVELSON, M. G. 2008 Interplanetary Magnetic Taylor Microscale and Implications for Plasma Dissipation. *Astroph. Journal Lett.* **678** (2), L141.
- MEYRAND, ROMAIN & GALTIER, SÉBASTIEN 2012 Spontaneous chiral symmetry breaking of hall magnetohydrodynamic turbulence. *Phys. Rev. Lett.* **109**, 194501.
- MININNI, PABLO D., GÓMEZ, DANIEL O. & MAHAJAN, SWADESH M. 2002 Dynamo action in hall magnetohydrodynamics. *Astrophysical Journal* **567** (1), L81–L83.
- MININNI, PABLO D., GÓMEZ, DANIEL O. & MAHAJAN, SWADESH M. 2003 Dynamo action in magnetohydrodynamics and hall-magnetohydrodynamics. *Astrophysical Journal* **587** (1), 472–481.
- MININNI, PABLO D., GÓMEZ, DANIEL O. & MAHAJAN, SWADESH M. 2005 Direct simulations of helical hall-MHD turbulence and dynamo action. *Astrophysical Journal* **619** (2), 1019–1027.
- MININNI, P. D., POUQUET, A. G. & MONTGOMERY, D. C. 2006 Small-scale structures in three-dimensional magnetohydrodynamic turbulence. *Phys. Rev. Lett.* **97**, 244503.
- MININNI, PABLO D., ROSENBERG, DUANE, REDDY, RAGHU & POUQUET, ANNICK 2011 A hybrid mpi–openmp scheme for scalable parallel pseudospectral computations for fluid turbulence. *Parallel Computing* **37** (6), 316–326.
- MIURA, H. & ARAKI, K. 2014 Structure transitions induced by the hall term in homogeneous and isotropic magnetohydrodynamic turbulence. *Physics of Plasmas* **21** (7), 072313.
- MONTGOMERY, DAVID & DOOLEN, GARY D. 1987 Magnetohydrodynamic cellular automata. *Physics Letters A* **120**, 229–231.
- MORALES, LAURA, DASSO, S. & GÓMEZ, DANIEL 2005 Hall effect in incompressible magnetic reconnection. *Journal of Geophysical Research* **110**.
- MÜLLER, D., ST. CYR, O. C., ZOUGANELIS, I., GILBERT, H. R., MARSDEN, R., NIEVES-CHINCHILLA, T., ANTONUCCI, E., AUCHÈRE, F., BERGHMANS, D., HORBURY, T. S., HOWARD, R. A., KRUCKER, S., MAKSIMOVIC, M., OWEN, C. J., ROCHUS, P., RODRIGUEZ-PACHECO, J., ROMOLI, M., SOLANKI, S. K., BRUNO, R., CARLSSON, M., FLUDRA, A., HARRA, L., HASSLER, D. M., LIVI, S., LOUARN, P., PETER, H., SCHÜHLE, U., TERIACA, L., DEL TORO INIESTA, J. C., WIMMER-SCHWEINGRUBER, R. F., MARSCH, E., VELLI, M., DE GROOF, A., WALSH, A. & WILLIAMS, D. 2020a The Solar Orbiter mission. Science overview. *Astronomy & Astrophysics* **642**, A1.
- MÜLLER, D., ST. CYR, O. C., ZOUGANELIS, I., GILBERT, H. R., MARSDEN, R., NIEVES-

- CHINCHILLA, T., ANTONUCCI, E., AUCHÈRE, F., BERGHMANS, D., HORBURY, T. S., HOWARD, R. A., KRUCKER, S., MAKSIMOVIC, M., OWEN, C. J., ROCHUS, P., RODRIGUEZ-PACHECO, J., ROMOLI, M., SOLANKI, S. K., BRUNO, R., CARLSSON, M., FLUDRA, A., HARRA, L., HASSLER, D. M., LIVI, S., LOUARN, P., PETER, H., SCHÜHLE, U., TERIACA, L., DEL TORO INIESTA, J. C., WIMMER-SCHWEINGRUBER, R. F., MARSCH, E., VELLI, M., DE GROOF, A., WALSH, A. & WILLIAMS, D. 2020b The Solar Orbiter mission. Science overview. *Astron. Astrophys.* **642**, A1.
- NORMAN, C. & HEYVAERTS, J. 1985 Anomalous magnetic field diffusion during star formation. *Astronomy & Astrophysics* **147** (2), 247–256.
- ORSZAG, S. A. & TANG, C. M. 1979 Small-scale structure of two-dimensional magnetohydrodynamic turbulence. *Journal of Fluid Mechanics* **90**, 129–143.
- PANDEY, B. P. & WARDLE, MARK 2008 Hall magnetohydrodynamics of partially ionized plasmas. *Monthly Notices of the Royal Astronomical Society* **385** (4), 2269–2278.
- PAPINI, EMANUELE, FRANCI, LUCA, LANDI, SIMONE, VERDINI, ANDREA, MATTEINI, LORENZO & HELLINGER, PETR 2019 Can hall magnetohydrodynamics explain plasma turbulence at sub-ion scales? *Astrophysical Journal* **870** (1), 52.
- PARASHAR, T. N., CUESTA, M. & MATTHAEUS, W. H. 2019 Reynolds Number and Intermittency in the Expanding Solar Wind: Predictions Based on Voyager Observations. *Astroph. Journal Lett.* **884** (2), L57.
- PATTERSON, G. S. & ORSZAG, STEVEN A. 1971 Spectral calculations of isotropic turbulence: Efficient removal of aliasing interactions. *The Physics of Fluids* **14** (11), 2538–2541.
- POUQUET, A. & MARINO, R. 2013 Geophysical turbulence and the duality of the energy flow across scales. *Phys. Rev. Lett.* **111**, 234501.
- POUQUET, A., ROSENBERG, D., STAWARZ, J. & MARINO, R. 2019 Helicity dynamics, inverse, and bidirectional cascades in fluid and magnetohydrodynamic turbulence: A brief review. *Earth Space Sci.* **6**, 1–19.
- ROSENBERG, D., MININNI, P.D., REDDY, R. & POUQUET, A. 2020 GPU parallelization of a hybrid pseudospectral geophysical turbulence framework using CUDA. *Atmosphere* **11**, 178.
- SAHRAOUI, F., GOLDSTEIN, M. L., ROBERT, P. & KHOTYAINTEV, YU. V. 2009 Evidence of a cascade and dissipation of solar-wind turbulence at the electron gyroscale. *Phys. Rev. Lett.* **102**, 231102.
- SHAN, XIAOWEN & HE, XIAOYI 1998 Discretization of the velocity space in the solution of the boltzmann equation. *Phys. Rev. Lett.* **80**, 65–68.
- SHI, C., VELLI, M., PANASENCO, O., TENERANI, A., RÉVILLE, V., BALE, S. D., KASPER, J., KORRECK, K., BONNELL, J. W., DUDOK DE WIT, T., MALASPINA, D. M., GOETZ, K., HARVEY, P. R., MACDOWALL, R. J., PULUPA, M., CASE, A. W., LARSON, D., VERNIERO, J. L., LIVI, R., STEVENS, M., WHITTLESEY, P., MAKSIMOVIC, M. & MONCUQUET, M. 2021 Alfvénic versus non-Alfvénic turbulence in the inner heliosphere as observed by Parker Solar Probe. *Astron. Astrophys.* **650**, A21.
- SILVA, GONCALO & SEMIAO, VIRIATO 2014 Truncation errors and the rotational invariance of three-dimensional lattice models in the lattice boltzmann method. *Journal of Computational Physics* **269**, 259–279.
- SMITH, CHARLES W., HAMILTON, KATHLEEN, VASQUEZ, BERNARD J. & LEAMON, ROBERT J. 2006 Dependence of the Dissipation Range Spectrum of Interplanetary Magnetic Fluctuations on the Rate of Energy Cascade. *Astrophys. J., Lett.* **645** (1), L85–L88.
- SUCCI, S., VERGASSOLA, M. & BENZI, R. 1991 Lattice boltzmann scheme for two-dimensional magnetohydrodynamics. *Phys. Rev. A* **43**, 4521–4524.
- TELLONI, DANIELE, ADHIKARI, LAXMAN, ZANK, GARY P., HADID, LINA Z., SÁNCHEZ-CANO, BEATRIZ, SORRISO-VALVO, LUCA, ZHAO, LINGLING, PANASENCO, OLGA, SHI, CHEN, VELLI, MARCO, SUSINO, ROBERTO, VERSCHAREN, DANIEL, MILILLO, ANNA, ALBERTI, TOMMASO, NARITA, YASUHITO, VERDINI, ANDREA, GRIMANI, CATIA, BRUNO, ROBERTO, D’AMICIS, RAFFAELLA, PERRONE, DENISE, MARINO, RAFFAELE, CARBONE, FRANCESCO, CALIFANO, FRANCESCO, MALARA, FRANCESCO, STAWARZ, JULIA E., LAKER, RONAN, LIBERATORE, ALESSANDRO, BALE, STUART D., KASPER, JUSTIN C., HEYNER, DANIEL, DE WIT, THIERRY DUDOK, GOETZ, KEITH, HARVEY, PETER R., MACDOWALL, ROBERT J., MALASPINA, DAVID M., PULUPA, MARC, CASE, ANTHONY W., KORRECK, KELLY E., LARSON, DAVIN, LIVI, ROBERTO, STEVENS,

- MICHAEL L., WHITTLESEY, PHYLLIS, AUSTER, HANS-ULRICH & RICHTER, INGO 2022a Observation and Modeling of the Solar Wind Turbulence Evolution in the Sub-Mercury Inner Heliosphere. *Astrophys. J., Lett.* **938** (2), L8.
- TELLONI, DANIELE, CARBONE, FRANCESCO, BRUNO, ROBERTO, ZANK, GARY P., SORRISO-VALVO, LUCA & MANCUSO, SALVATORE 2019 Ion Cyclotron Waves in Field-aligned Solar Wind Turbulence. *Astrophys. J., Lett.* **885** (1), L5.
- TELLONI, DANIELE, SORRISO-VALVO, LUCA, WOODHAM, LLOYD D., PANASENCO, OLGA, VELLI, MARCO, CARBONE, FRANCESCO, ZANK, GARY P., BRUNO, ROBERTO, PERRONE, DENISE, NAKANOTANI, MASARU, SHI, CHEN, D'AMICIS, RAFFAELLA, DE MARCO, ROSSANA, JAGARLAMUDI, VAMSEE K., STEINVALL, KONRAD, MARINO, RAFFAELE, ADHIKARI, LAXMAN, ZHAO, LINGLING, LIANG, HAOMING, TENERANI, ANNA, LAKER, RONAN, HORBURY, TIMOTHY S., BALE, STUART D., PULUPA, MARC, MALASPINA, DAVID M., MACDOWALL, ROBERT J., GOETZ, KEITH, DE WIT, THIERRY DUDOK, HARVEY, PETER R., KASPER, JUSTIN C., KORRECK, KELLY E., LARSON, DAVIN, CASE, ANTHONY W., STEVENS, MICHAEL L., WHITTLESEY, PHYLLIS, LIVI, ROBERTO, OWEN, CHRISTOPHER J., LIVI, STEFANO, LOUARN, PHILIPPE, ANTONUCCI, ESTER, ROMOLI, MARCO, O'BRIEN, HELEN, EVANS, VINCENT & ANGELINI, VIRGINIA 2021 Evolution of Solar Wind Turbulence from 0.1 to 1 au during the First Parker Solar Probe-Solar Orbiter Radial Alignment. *Astrophys. J., Lett.* **912** (2), L21.
- TELLONI, DANIELE, ZANK, GARY P., STANGALINI, MARCO, DOWNS, COOPER, LIANG, HAOMING, NAKANOTANI, MASARU, ANDRETTA, VINCENZO, ANTONUCCI, ESTER, SORRISO-VALVO, LUCA, ADHIKARI, LAXMAN, ZHAO, LINGLING, MARINO, RAFFAELE, SUSINO, ROBERTO, GRIMANI, CATIA, FABI, MICHELE, D'AMICIS, RAFFAELLA, PERRONE, DENISE, BRUNO, ROBERTO, CARBONE, FRANCESCO, MANCUSO, SALVATORE, ROMOLI, MARCO, DEPO, VANIA DA, FINESCHI, SILVANO, HEINZEL, PETR, MOSES, JOHN D., NALETTO, GIAMPIERO, NICOLINI, GIANALFREDO, SPADARO, DANIELE, TERIACA, LUCA, FRASSATI, FEDERICA, JERSE, GIOVANNA, LANDINI, FEDERICO, PANCRAZZI, MAURIZIO, RUSSANO, GIULIANA, SASSO, CLEMENTINA, BIONDO, RUGGERO, BURTOVOI, ALEKSANDR, CAPUANO, GIUSEPPE E., CASINI, CHIARA, CASTI, MARTA, CHIOETTO, PAOLO, LEO, YARA DE, GIARRUSSO, MARINA, LIBERATORE, ALESSANDRO, BERGHMANS, DAVID, AUCHÈRE, FRÉDÉRIC, CUADRADO, REGINA AZNAR, CHITTA, LAKSHMI P., HARRA, LOUISE, KRAAIKAMP, EMIL, LONG, DAVID M., MANDAL, SUDIP, PARENTI, SUSANNA, PELOUZE, GABRIEL, PETER, HARDI, RODRIGUEZ, LUCIANO, SCHÜHLE, UDO, SCHWANITZ, CONRAD, SMITH, PHIL J., VERBEECK, CIS & ZHUKOV, ANDREI N. 2022b Observation of a Magnetic Switchback in the Solar Corona. *Astrophys. J., Lett.* **936** (2), L25.
- TÓTH, GÁBOR, MA, YINGJUAN & GOMBOSI, TAMAS I. 2008 Hall magnetohydrodynamics on block-adaptive grids. *Journal of Computational Physics* **227** (14), 6967–6984.
- WANG, XIAOGANG, BHATTACHARJEE, A. & MA, Z. W. 2001 Scaling of collisionless forced reconnection. *Phys. Rev. Lett.* **87**, 265003.
- XIA, ZHENWEI & YANG, WEIHONG 2015 Exact solutions of the incompressible dissipative hall magnetohydrodynamics. *Physics of Plasmas* **22** (3), 032306, arXiv: <https://doi.org/10.1063/1.4914931>.
- YADAV, SHARAD K., MIURA, HIDEAKI & PANDIT, RAHUL 2022 Statistical properties of three-dimensional Hall magnetohydrodynamics turbulence. *Physics of Fluids* **34** (9), 095135.

Helios 2 observations of solar wind turbulence decay in the inner heliosphere

L. Sorriso-Valvo^{1,2,3,*}, R. Marino⁴, R. Foldes^{4,5}, E. Lévêque⁴, R. D'Amicis⁶, R. Bruno⁶, D. Telloni⁷ and E. Yordanova¹

¹ Swedish Institute of Space Physics (IRF), Ångström Laboratory, Lägerhyddsvägen 1, 75121 Uppsala, Sweden

² CNR, Istituto per la Scienza e la Tecnologia dei Plasmi, via Amendola 122/D, 70126, Bari, Italy

³ Space and Plasma Physics, School of Electrical Engineering and Computer Science, KTH Royal Institute of Technology, Teknikringen 31, SE-11428 Stockholm, Sweden

⁴ Université de Lyon, CNRS, École Centrale de Lyon, INSA Lyon, Université Claude Bernard Lyon 1, Laboratoire de Mécanique des Fluides et d'Acoustique, UMR5509, F-69134 Écully, France

⁵ Dipartimento di Scienze Fisiche e Chimiche, Università degli Studi dell'Aquila, Via Vetoio 42, I-67100 Coppito AQ, Italy

⁶ National Institute for Astrophysics (INAF) — Institute for Space Astrophysics and Planetology (IAPS), Via Fosso del Cavaliere, 100, 00133 Rome, Italy

⁷ National Institute for Astrophysics (INAF) – Astrophysical Observatory of Torino, Via Osservatorio 20, I-10025 Pino Torinese, Italy

Received September 15, 1996; accepted March 16, XXX

ABSTRACT

Aims. The linear scaling of the mixed third-order moment of the magnetohydrodynamic fluctuations is used to estimate the energy transfer rate of the turbulent cascade in the expanding solar wind.

Methods. In 1976 the Helios 2 spacecraft measured three samples of fast solar wind originating from the same coronal hole, at different distance from the sun. Along with the adjacent slow solar wind streams, these represent a unique database for studying the radial evolution of turbulence in samples of undisturbed solar wind. A set of direct numerical simulations of the MHD equations performed with the Lattice-Boltzmann code FLAME is also used for interpretation.

Results. We show that the turbulence energy transfer rate decays approximately as a power law of the distance, and that both the amplitude and decay law correspond to the observed radial temperature profile in the fast wind case. Results from magnetohydrodynamic numerical simulations of decaying magnetohydrodynamic turbulence show a similar trend for the total dissipation, suggesting an interpretation of the observed dynamics in terms of decaying turbulence, and that multi-spacecraft studies of the solar wind radial evolution may help clarifying the nature of the evolution of the turbulent fluctuations in the ecliptic solar wind.

Key words. (Sun:) solar wind – Turbulence – magnetohydrodynamics MHD

1. Introduction

Spacecraft observations of interplanetary fields and plasma show that the solar wind is highly turbulent (Bruno & Carbone 2013). After the onset of the turbulent cascade at coronal level (Kasper et al. 2021; Bandyopadhyay et al. 2022; Zhao et al. 2022), several processes may energize the fluctuations during the solar-wind expansion (Verscharen et al. 2019): nonlinear decay of large-scale Alfvén waves of solar or coronal origin (Malara et al. 2000; Chandran 2018), expansion-related and coronal-driven shears (Velli et al. 1990; Tenerani & Velli 2017), pick-up ions interaction, magnetic switchbacks (Bale et al. 2021; Hernández et al. 2021; Telloni et al. 2022), large-scale structures and instabilities (Roberts et al. 1992; Kieokaew et al. 2021). The properties of turbulence are strongly variable (Bruno & Carbone 2013), reflecting the diversity of solar coronal sources, which modulate density, velocity, temperature and ion composition of the plasma (von Steiger et al. 2000). Solar wind intervals are often classified according to their bulk speed, V_{sw} , as fast ($V_{sw} \gtrsim 600 \text{ km s}^{-1}$) or slow ($V_{sw} \lesssim 500 \text{ km s}^{-1}$). However, turbulence properties more clearly depend on the Alfvénic nature of the

fluctuations, for example measured using the normalized cross-helicity, $\sigma_c = \langle \delta \mathbf{v} \cdot \delta \mathbf{b} \rangle / (\langle \delta \mathbf{v} \rangle^2 + \langle \delta \mathbf{b} \rangle^2)$, where the magnetic field \mathbf{B} is transformed in velocity units through the mass density ρ , $\mathbf{b} = \mathbf{B} / (4\pi\rho)^{1/2}$ (Matthaeus & Goldstein 1982), δ indicates fluctuations with respect to the mean, and brackets indicate sample average. For example, large-scale Alfvénic fluctuations may reduce the nonlinear energy transfer by sweeping apart the interacting structures (Kraichnan 1965; Dobrowolny et al. 1980).

In non-Alfvénic solar wind (often observed in slow intervals), the turbulence generates broadband power-law magnetic spectra, $E(f) \sim f^{-\alpha}$. Scaling exponents α , close to Kolmogorov's 5/3 (Kolmogorov 1941), are observed from the injection scales of solar wind structure (\sim hours), to the characteristic ion scales ($\sim 10 \text{ s}$ at 1 au) (Bruno & Trenchi 2014), where field-particle effects become relevant and the spectral exponents increase (Leamon et al. 1998). Within such broad inertial range, strong intermittency is observed (Sorriso-Valvo et al. 1999), revealing inhomogeneously distributed small-scale structures, such as vortices and current sheets, generated by the nonlinear interactions (Salem et al. 2009; Greco et al. 2016). These characteristics are robustly observed at any distance from the

* Corresponding author: lucasorriso@gmail.com

Sun beyond 0.3 au, with no or limited radial evolution of spectral range extension or intermittency (Bruno et al. 2003).

On the other hand, in typically fast Alfvénic wind strongly aligned low-frequency velocity and magnetic fluctuations produce a $1/f$ magnetic spectral range (Matthaeus & Goldstein 1986; Verdini et al. 2012; Chandran 2018; Matteini et al. 2018). The classical turbulence inertial range is narrower, with spectral exponents between $5/3$ and the Kraichnan’s $3/2$ (Kraichnan 1965). Note that Alfvénic slow solar wind was recently abundantly observed close to the Sun (Chen et al. 2020), and less frequently near 1 au (D’Amicis et al. 2021). In the Alfvénic wind, turbulence shows a clearer evolution as the wind radially expands, with the $1/f$ break drifting towards lower frequencies (Bavassano et al. 1982b). The inertial range broadening is interpreted as the growing Reynolds’ number (Frisch 1995; Parashar et al. 2019), which together with the observed increasing intermittency (Bruno et al. 2003; Bruno et al. 2014), would suggest an evolution of the solar wind dynamics towards more developed turbulence states. (Tu & Marsch 1995; Bavassano et al. 2002; Burlaga 2004; Macek et al. 2012; Bruno & Carbone 2013; Fraternali et al. 2016; Chen et al. 2020; Bandyopadhyay et al. 2020). Such evolution corresponds to the observed gradual decrease of the Alfvénic alignment between velocity and magnetic fluctuations (Bavassano et al. 1998, 2002). Alternatively, observations could result from the competing action between a coherent component (the intermittent inertial range structures generated by turbulence) with a stochastic component ($1/f$ -range propagating Alfvénic fluctuations, Bruno et al. 2001, 2003; Borovsky 2008). In both interpretations, the slow solar wind milder evolution is therefore associated with the reduced presence of Alfvénic fluctuations (Tu & Marsch 1995; Bruno & Carbone 2013). Recent observations of Alfvénic solar wind closer to the Sun confirmed the radial evolution properties briefly described above (Chen et al. 2020; Bourouaine et al. 2020; Hernández et al. 2021). The above observations of spectra and intermittency are generally used to support the evolving nature of the solar wind turbulence in the inner heliosphere, and to constrain global solar wind models and their energy budget.

As an alternative to spectra, the turbulent cascade can be examined using the scaling properties of the third-order moments of the fluctuations (Marino & Sorriso-Valvo 2023). Based on robust theoretical predictions (Politano & Pouquet 1998), third-order laws allow to estimate the energy transfer rate of turbulence (Sorriso-Valvo et al. 2007). Under specific assumptions, this quantity represents a more fundamental measure of the state of turbulence, in comparison to power spectra and intermittency. Furthermore, studies of radial evolution of turbulence mostly rely on a statistical approach, so that different samples may include plasma from different originating coronal regions or solar activity, resulting in different initial energy injection, nonlinear coupling efficiency, or in-situ energy injection from instabilities or large-scale structures. These can all diversely contribute determining the properties and energetic content of the turbulent cascade. One possible way to mitigate such inhomogeneity is to measure the same plasma with two spacecraft that are occasionally radially aligned at different distance from the sun (D’Amicis et al. 2010; Telloni et al. 2021a). Alternatively, under optimal orbital configurations, plasma from a steady solar source can be measured by the same spacecraft at different times (see, e.g., Bruno et al. 2003).

In this article, we study the status of the turbulence at different radial distances from the Sun using the third-order moment law and intermittency, as measured in a set of recurrent streams of solar wind measured by the Helios 2 spacecraft. Based on a

qualitative comparison with the plasma generated with a magnetohydrodynamic simulation in the spin-down phase, we interpret the observed trend of the energy transfer rate in the solar wind as to be determined, among other process, by a decay of turbulence occurring with the heliocentric distance. In Sections 2 and 3 we describe the dataset and the methodology used to investigate the status of turbulence. Section 4 provides the results of the analysis of Helios 2 data, while in Section 5 results of a lattice-Boltzmann numerical simulations are shown. Finally, conclusions are given in Section 6.

2. Helios 2 Data

One popular case of measurements of solar wind from the same source occurred in 1976, when Helios 2 measured plasma and fields of three fast solar wind streams at different distances (0.9, 0.7 and 0.3 au) originated from a persistent polar coronal hole, which was reasonably stable during nearly two solar rotations (Bavassano et al. 1982a; Bruno et al. 2003). Similarly, three preceding slow, non Alfvénic wind streams were used as samples of evolving slow solar wind. These streams have provided outstanding information about the radial evolution of turbulence, since the initial conditions were statistically steady and no stream interactions were included. Note, however, that the more dynamical solar source of the slow streams might not be as steady as in the case of the coronal hole generating the fast wind. Figure 1 shows an overview of solar wind bulk speed V_{sw} , spacecraft radial distance from the sun R , proton density n_p , and magnetic field magnitude B during the days 45 to 110 of 1976. Six color-shaded areas identify the selected streams, at 0.3 au (red), 0.7 au (green) and 0.9 au (blue). For each distance, lighter colors and dashed lines indicate slow streams, darker colors and full lines identify fast streams.

3. Methodology: the Politano-Pouquet law

Past studies of turbulence mainly relied on spectral and structure functions analysis (Bavassano et al. 1982a,b; Bruno et al. 1985; Bavassano et al. 2002; Bruno et al. 2003; Bruno et al. 2004; Bruno et al. 2004; Bruno et al. 2014; Perrone et al. 2018). However, the nature of the turbulent cascade is more thoroughly captured by the scaling of the third-order moments of the fluctuations, an exact relation obtained from the incompressible MHD equations under the hypothesis of stationarity, isotropy, and large Reynolds’ number (Politano & Pouquet 1998). Called Politano-Pouquet (PP) law, it prescribes that the mixed third-order moment of the MHD fields fluctuations is a linear function of the scale:

$$\begin{aligned} Y(\Delta l) &\equiv \langle \Delta v_L (|\Delta \mathbf{v}|^2 + |\Delta \mathbf{b}|^2) - 2\Delta b_L (\Delta \mathbf{v} \cdot \Delta \mathbf{b}) \rangle \\ &= \frac{4}{3} \varepsilon V_{sw} \Delta l. \end{aligned} \quad (1)$$

$\Delta \phi_L$ are longitudinal increments of the component of a generic scalar or vector component ϕ in the sampling direction, with the magnetic field \mathbf{B} in velocity units through the mass density ρ , $\mathbf{b} = \mathbf{B}/(4\pi\rho)^{1/2}$. The mean bulk speed V_{sw} allows transforming spatial lags Δl to temporal lags Δt via the Taylor hypothesis, $\Delta l = -V_{sw}\Delta t$ (Taylor 1938). Observing linear scaling ensures that a turbulent cascade is active and fully developed, and that the complex hierarchy of structures on all scales is well formed and sustains the cross-scale energy transfer leading to small-scale dissipation. Measuring the energy transfer rate ε provides a quantitative estimate of the turbulent energy flux. This is

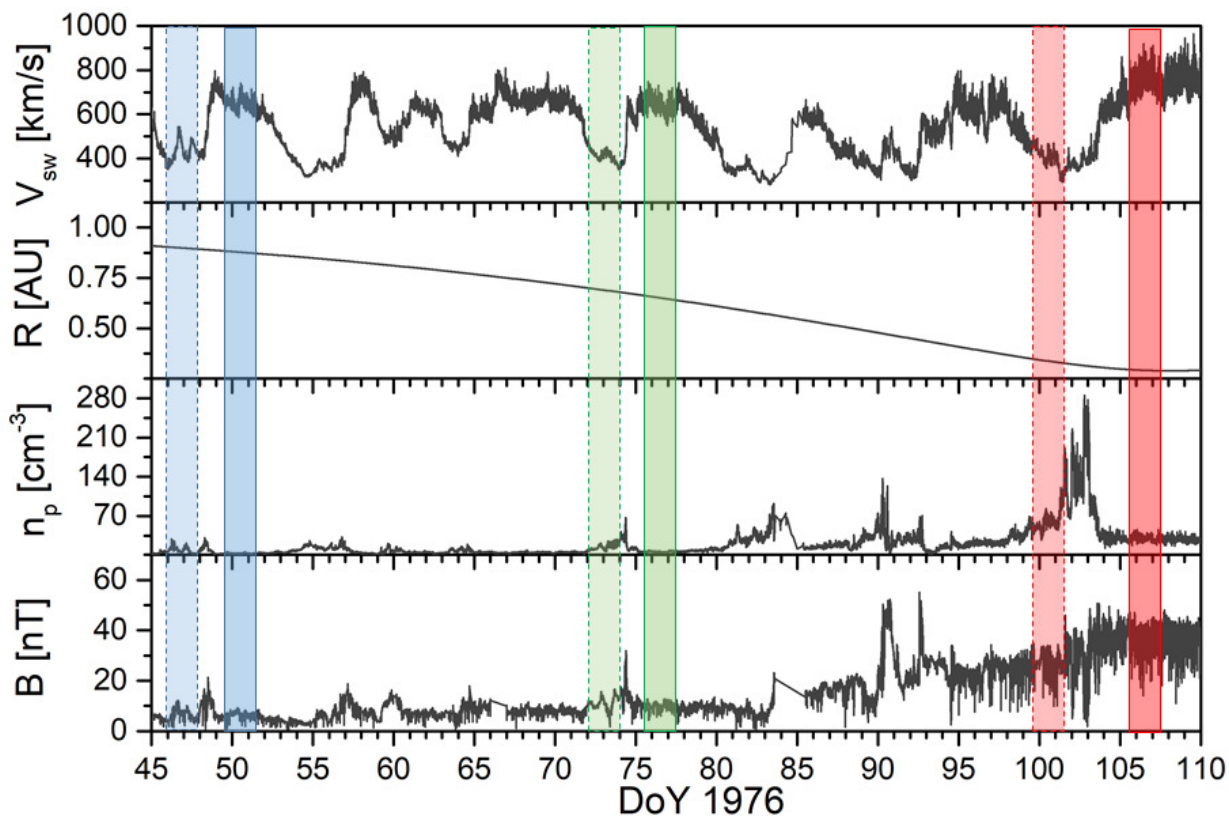


Fig. 1. Helios 2 measurements during days 45—110 of 1976. From top to bottom: solar wind bulk speed V_{sw} , distance from the sun R , proton density n_p , and magnetic field magnitude B . Colored shaded areas identify the selected streams at 0.3 au (red), 0.7 au (green) and 0.9 au (blue). Lighter (darker) colors indicate slow (fast) streams.

an invaluable information in the collisionless solar wind, where energy dissipation cannot be measured using viscous-resistive modeling. The same quantity could in principle be obtained from the (Kolmogorov) spectrum, but its evaluation includes a constant factor that can hardly be obtained in the highly variable solar wind. Third-order scaling laws (Marino & Sorriso-Valvo 2023) have been used to determine the properties of turbulence in the solar wind at 1 au (MacBride et al. 2005; Smith et al. 2009; Stawarz et al. 2010; Coburn et al. 2012), in the outer (Sorriso-Valvo et al. 2007; Marino et al. 2008; Carbone et al. 2009; Marino et al. 2012) and inner (Gogoberidze et al. 2013; Bandyopadhyay et al. 2020; Hernández et al. 2021; Wu et al. 2022) heliosphere, and in near-Earth (Hadid et al. 2017; Quijia et al. 2021) and near-Mars (Andrés et al. 2020) environments. Data from Ulysses in the polar outer heliosphere (Marino et al. 2008, 2012; Watson et al. 2022) and from Parker Solar Probe in the ecliptic inner heliosphere (Bandyopadhyay et al. 2020) suggest that the energy transfer rate statistically decreases radially. At the same time, the fraction of solar wind intervals where the linear scaling is observed increases radially (Marino et al. 2012), in agreement with the observed decrease of the cross-helicity and generally supporting the evolving nature of the turbulence in the expanding heliosphere.

4. Results: mixed third-order moment scaling laws, turbulent energy transfer rate and intermittency

Here we present the analysis of the PP scaling law in the three fast and three slow streams described above, using the 81 s resolution plasma and magnetic field measured by Helios 2. The

mixed third-order moments, Equation (1), are displayed in Figure 2 for each of the six intervals. Statistical convergence of the samples was tested using standard techniques (Dudok De Wit 2004; Kiyani et al. 2006). For both fast and slow streams, the different colors indicate different distances, as stated in the legend. The mixed third-order moments Y are mostly positive (full symbols), indicating direct energy transfer from large to small scales. Negative values, most probably due to lack of convergence or presence of large-scale velocity shears (Stawarz et al. 2011), are indicated by open symbols, and are not considered in this study. An inertial range was identified for each case, at timescales between 81 s and ~ 20 minutes, although the linear scaling is better defined and more extended in the samples at 0.3 au. The upper scales observed here are larger than, but roughly consistent with, the outer scale of the turbulence, estimated as the correlation timescale, τ_c (Greco et al. 2012), and partially include the $1/f$ range, as will be discussed below. This shows that the six intervals can be considered as samples of fully developed turbulence.

Fitting the PP law provides the mean energy transfer rate, given in colors next to each fitted line in Figure 2. The fit is performed on a range including more than one decade of scales in all cases except for the slow solar wind at 0.9 au, where a slightly shorter range is covered. It should be observed that in the two examples studied here the linear scaling range is broader closer to the sun, while the scaling becomes less clear near 1 au.

However, for the purpose of this study, the relevant information is the energy transfer rate, which is sufficiently well represented by the power-law fits shown in Figure 2. The first notable characteristic is that slow streams have smaller energy transfer

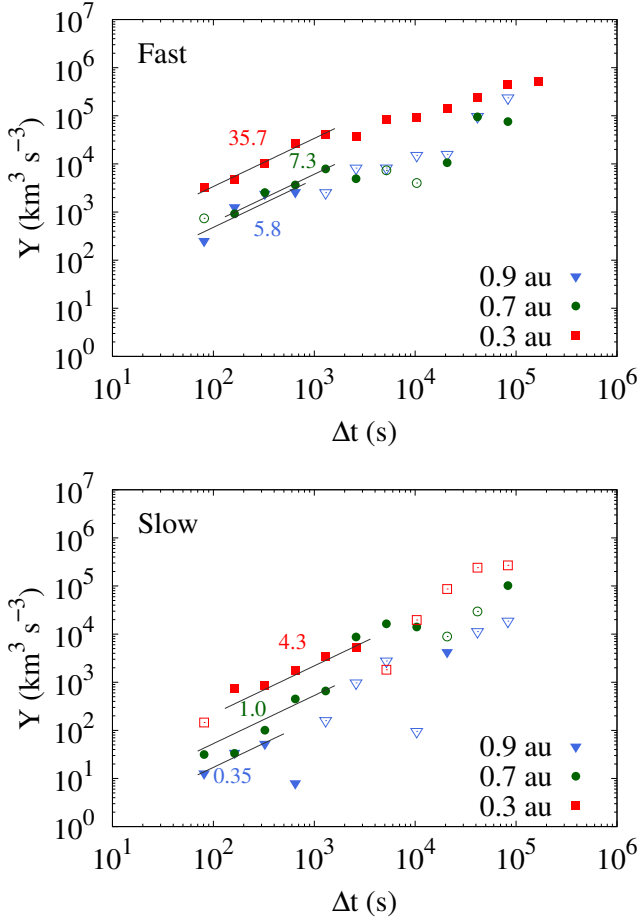


Fig. 2. PP scaling for fast (top) and slow (bottom) streams, at three different distances from the sun. Linear fits are indicated (grey lines), along with the mean energy transfer rate, ε ($\text{kJ kg}^{-1} \text{s}^{-1}$) (color coded). Full and empty symbols refer to positive and negative values of Y , respectively.

rate than fast streams at all distances, suggesting that the initial energization of the turbulence is stronger in fast wind, perhaps not systematically but in the cases under study, or that its decay is faster in slow wind. This is consistent with the known correlation between turbulence amplitude and both proton temperature and wind speed (see, e.g., Grappin et al. 1991). Furthermore, in both fast and slow wind the energy transfer rate consistently decreases with the distance, as expected from the observed decay of the turbulent fluctuations (Bruno & Carbone 2013). Such observations seem to indicate that in the fast streams, while the spectrum broadens and the small-scale intermittent structures emerge (Bavassano et al. 1982a; Bruno et al. 2003), the cascade transports less energy across the scales. The same decreasing energy transfer is observed in the otherwise steadier slow streams. In the top panel of Figure 3, the energy transfer rate is plotted versus the distance from the Sun. The measured values can be compared with standard estimates of the proton heating rate (Marino et al. 2008, 2011). This can be obtained through a simple model that, under the isotropic fluid approximation, neglecting heat fluxes, and assuming a stationary flow, uses the solar wind bulk speed and temperature radial profiles to determine the proton heating rate accounting for deviation from adiabatic cooling (Verma 2004; Vasquez et al. 2007). In particular, if the proton temperature decays as a power law of the distance, $T(R) \sim R^{-\xi}$,

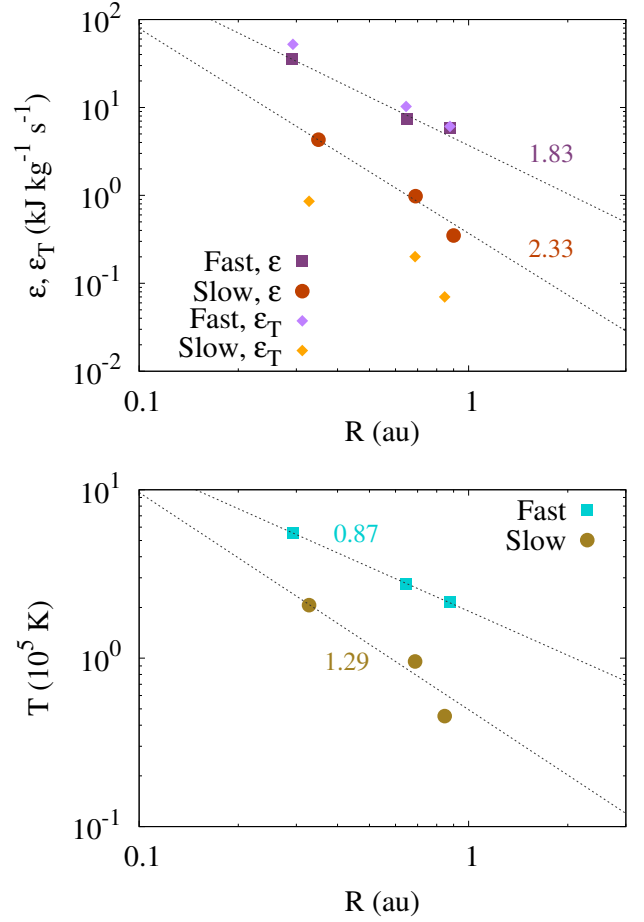


Fig. 3. Top panel: energy transfer rate, ε , versus the distance from the sun, R . Fast streams are indicated with dark purple squares, slow streams with dark orange circles. Power-law fits and the relative scaling exponents are shown. The heating rate obtained using equation (2), ε_T , is also indicated with purple diamonds (fast streams) and orange diamonds (slow wind). Bottom panel: the temperature decay for the fast (cyan squares) and slow (green circles) streams, with power-law fits and indicated exponents.

then the proton heating rate is given by

$$\varepsilon_T = \frac{3}{2} \left(\frac{4}{3} - \xi \right) \frac{k_B V_{SW}(R) T(R)}{R m_p}, \quad (2)$$

where k_B is the Boltzmann constant and m_p is the proton mass. The decay exponent ξ of the temperature can be estimated using Helios 2 data. For the two sets of fast and slow streams, the mean temperature for each stream is shown in the bottom panel of Figure 3. Assuming power-law decay, a fitting procedure provides $\xi = 0.87 \pm 0.01$ for the fast streams, and $\xi = 1.29 \pm 0.03$ for the slow streams. These considerably deviate from the expected adiabatic value ($\xi = 4/3$) for the fast wind, while for the slow streams the cooling is closer to adiabatic. Totten et al. (1995) used Helios 1 data to obtain radial profiles of the proton temperature, which was observed to consistently decay with exponent $\xi \approx 0.9$, independent of the wind speed. Note that the results shown here might be specific to the case under study, while in Totten et al. (1995) a large statistical sample was used. Similar results were found using MHD numerical simulations (Montagud-Camps et al. 2018, 2020). The Helios 2 results shown here are in good agreement with the above observations and models for the fast wind streams, but not for the slow ones.

Using the obtained temperature radial decay exponent and the mean speed and temperature of the three streams, the radial profile of the approximate heating rate can be estimated. The values obtained are shown in the top panel of Figure 3. For the fast streams, the agreement with the estimated energy transfer rate is excellent. This demonstrates that the energy transfer rate estimated using the incompressible, isotropic version of the PP law are sufficiently accurate. On the other hand, for the slow wind the required heating is nearly one order of magnitude smaller than the observed turbulent heating rate. This is a consequence of the very weak deviation from adiabatic of the power-law temperature decay. Possible reasons for this discrepancy include: (i) the relatively poor power-law profile of $T(R)$ and subsequent underestimation of the required heating rate; (ii) the possible variability in the slow wind source region, which would affect the stationarity assumption for the model and result in unaccounted for temperature variability; (iii) energy lost to heat flux and electron heating, not included in equation (2), and which might be more relevant than for the Alfvénic, fast wind. Nevertheless, even for the slow streams the decay of the predicted heating rate is close to the observed decay of the turbulent energy transfer rate.

In fact, for plasma proceeding from an approximately stationary coronal structure and far from stream interaction regions, the turbulent energy transfer can be expected to decrease as a power law of the distance. If we assume for the energy transfer rate a power-law radial decay, $\varepsilon \sim R^{-\alpha}$, the measured values can be fitted to power-laws, providing the decay exponents $\alpha_F \approx 1.8 \pm 0.2$ and $\alpha_S \approx 2.3 \pm 0.2$ for fast and slow streams, respectively. The slower decay observed in the fast streams could be the result of the local energy injection from the $1/f$ reservoir, which may partially compensate the dissipation losses and thus slightly slow down the decay in comparison with the slow wind, where no supplementary injection is provided.

The above scenario provides a quantitative estimate of the turbulence decay observed in undisturbed expanding samples, such as the Helios 2 recurrent streams. Such observation could be useful to constrain models of the radial evolution of turbulence. These may include, for example, the simple damping of both velocity and magnetic fluctuations due to the conservation of angular momentum and of magnetic flux in an expanding plasma volume advected by the radial wind (Parker 1965; Heinemann & Olbert 1980), as well as local energy injection as it results from expansion and large-scale shears (Velli et al. 1990; Grappin et al. 1993; Tenerani & Velli 2017), or modification of the timescale of nonlinear interactions associated with the radial decrease of Alfvénicity (Smith et al. 2009; Stawarz et al. 2010). Since the results presented here are based on only two case-study events, they lack generality. On the other hand, they do provide more rigorous parameters for the specific intervals. A larger study of similar events, studied individually, is however necessary to cover a broader range of parameters. In order to complete the turbulence analysis of the streams under study, we quantify the degree of intermittency of the turbulent fluctuations. Intermittency is typically described by the scaling of the statistics of the fields fluctuations, measured through probability distribution functions (Sorriso-Valvo et al. 1999; Pagel & Balogh 2003), structure functions (Carbone 1994; Kiyani et al. 2009), or multifractal analysis (Macek et al. 2012; Alberti et al. 2019). A standard estimator of intermittency is provided by the power-law scaling of the kurtosis of a magnetic field component B_i , $K(\Delta t) = \langle \Delta B_i^4 \rangle / \langle \Delta B_i^2 \rangle^2 \sim \Delta t^{-\kappa}$. The scaling exponent, κ , provides a quantitative measure of intermittency, being related to the fractal co-dimension of the intermittent structures (Castaing et al. 1990; Carbone & Sorriso-Valvo 2014; Sorriso-Valvo et al.

2015). For these intervals, the kurtosis was already presented by Bruno et al. (2003). Nevertheless, here we perform a more detailed, quantitative study that will provide additional description of the intermittency. The two panels of Figure 4 show the magnetic field kurtosis for the three fast (top panel) and slow (bottom panel) solar wind streams, computed using 6-second cadence magnetic vectors and averaging over the three field components (after verifying that all individual components displayed similar behaviour). In the fast streams, two power-law scaling ranges are identified in the inertial range, ~ 6 – 200 s, and at lower frequency, ~ 200 – 8000 s. In agreement with spectral observations, the break between the two ranges migrates towards larger scales with increasing distance from the Sun (see, e.g., Bruno & Carbone 2013, and references therein). Note that, for the streams at 0.3 and 0.7 au, the low-frequency range mostly includes the $1/f$ spectral range. Power-law fits provide the scaling exponents κ , which are indicated in the figure. The inertial-range exponents agree with previous observations (Di Mare et al. 2019; Sorriso-Valvo et al. 2021), while the smaller $1/f$ -range values are closer to fluid turbulence’s (where exponents are typically around 0.1; see, e.g., Anselmetti et al. 1984). In both ranges, the values of K and the scaling exponents quantitatively confirm the radial increase of intermittency (Bruno et al. 2003). To the best of our knowledge, the kurtosis’ power-law scaling in the $1/f$ range was not observed before. Jointly with the observation of the PP law discussed above, it suggests that, at least in the streams closer to the Sun, nonlinear interactions are effectively transferring energy across scales, even in the $1/f$ range. This observation opens interesting questions about the nature of the fluctuations in the low-frequency range, which calls for more detailed studies. On the other hand, in the slow wind streams, where no $1/f$ spectral range is observed, a single power-law covers the whole range, with no clear radial trend. The scaling exponents reveal strong intermittency at all distances.

5. Comparison with numerical simulations of unforced MHD turbulence

The power-law radial decay of the turbulent energy transfer rate and the associated increase of intermittency, highlighted in the previous section, represent a solid constraint for models of solar wind turbulence. It is interesting to notice that similar properties are also typical features of unforced fluid and magneto-fluid turbulence, as observed in numerical simulations (Biskamp 1993; Hossain et al. 1995; Miura 2019; Bandyopadhyay et al. 2019). Using a decaying direct numerical simulation integrating the incompressible MHD equations, with no mean magnetic field (Foldes et al. 2022), here we show how a simplified framework not incorporating signature features of solar wind turbulence (for example anisotropy), not accounting for effects of the solar wind expansion (Grappin et al. 1993; Verdini & Grappin 2015; Tenerani & Velli 2017), is able to qualitatively reproduce trends and statistics observed by Helios, thus can be used to decipher the phenomenology underlying the turbulent energy transfer in the solar wind. What emerged from our analysis is that the phenomenology described in the previous sections is compatible with the temporal decay of a magnetohydrodynamic unforced plasmas. In other words, the basic three-dimensional MHD simulations used here provide indications of qualitative similarity between the radial evolution of turbulence in the expanding solar wind and the temporal decay of unforced MHD turbulence via viscous-resistive dissipation. This is not in contrast with the expanding-box simulations previously suggesting that the inclusion of expansion effects results in faster energy decay

run	Re = Re _m	v_{rms}^*	v_{rms}^0/b_{rms}^0	Ma	t^*	ξ
I	~ 1500	$8.5 \cdot 10^{-4}$	~ 0.5	0.005	79.5	2.4
II	~ 900	$2.7 \cdot 10^{-3}$	~ 1.0	0.005	51.9	1.7
III	~ 800	$2.5 \cdot 10^{-3}$	~ 2.0	0.001	45.3	1.8

Table 1. Adimensional parameters at the current peak t^* (in turnover time units). Re and Re_m are respectively the Reynolds and magnetic Reynolds numbers; Ma is the Mach number; v_{rms}^0/b_{rms}^0 is the ratio between the rms velocity and magnetic fluctuations at the initial time of the simulation ($t = 0$); ξ is the fitted exponent (see Figure 6). Box size, $(2\pi)^3$, and magnetic Prandtl number, $Pr_m = 1$, are the same for all runs.

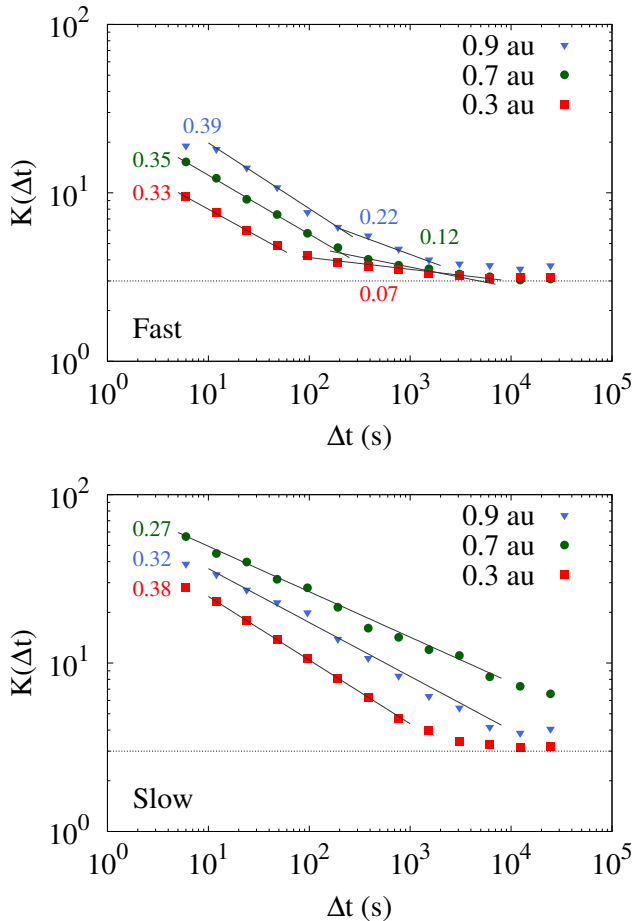


Fig. 4. Magnetic field kurtosis, K , for fast streams (top) and slow streams (bottom), averaged over the field components. Power-law fits in the $5/3$ and $1/f$ spectral ranges are indicated with the fitted scaling exponents (fitting errors are ≤ 0.01).

and in inverted cross helicity radial profile, that switches from increasing to decreasing with distance (see, e.g., Dong et al. 2014; Montagud-Camps et al. 2020, 2022). In this work, we use actually a lattice Boltzmann (LB) code, FLAME (Foldes et al. 2022), to integrate the quasi-incompressible MHD equations in a three-dimensional periodic domain, not expanding. In the LB approach, the volume discretization is operated on a gas of particles distributed on a lattice, rather than on a grid. The dynamics of the particles develops in the frame of the kinetic theory, the temporal evolution of the plasma being achieved through the recursive application of simple collision and streaming operations. The macroscopic MHD fields (e.g. fluid velocity \mathbf{v} , density ρ , and magnetic field \mathbf{B}) are then obtained through integration of the statistical moments of the particle distribution functions. Please note that the particles here are not plasma particles, they

exist at the level of the numerical scheme and are instrumental to the LB approach to obtain (in the case of FLAME) the fields of the simulated magnetohydrodynamic plasma (see details in Foldes et al. 2022). We examine three runs, whose parameters are listed in Table 1. The latter are initialized with a standard Orszag-Tang (OT) vortex (Orszag & Tang 1979; Mininni et al. 2006), using different kinetic-to-magnetic energy ratio, v_{rms}^0/B_{rms}^0 , where v_{rms}^0 and B_{rms}^0 are the initial rms values of the field fluctuations (for the Helios 2 solar wind intervals studied here, $v_{rms}/B_{rms} \sim 0.5-1$, Bruno et al. 1985). The integration is performed over a 512^3 -point three-dimensional lattice (Orszag & Tang 1979; Mininni et al. 2006), the functional form of OT being: $\mathbf{U}(\mathbf{x}, 0) = v_{rms}^0 [-2\sin(y), 2\sin(x), 0]$ and $\mathbf{B}(\mathbf{x}, 0) = B_{rms}^0 [-2\sin(2y) + \sin(z), 2\sin(x) + \sin(z), \sin(x) + \sin(y)]$. Before computing any statistics, the simulation is let to evolve until the plasma reaches a state of fully developed turbulence when the volume averaged density current $\langle j \rangle$, attains its peak value, at the time t^* . A snapshot of the vorticity field at t^* is shown for run I in Figure 5, along with the corresponding isotropic magnetic and kinetic spectral trace. For all runs, spectra exhibit the typical extended power-law inertial ranges, which enables qualitative comparison to the SW.

It must be pointed out that, since the solar wind speed is reasonably steady, the radial distance of each of the six Helios 2 streams analyzed here can be ideally converted to time of travel from an arbitrary initial position where the turbulence peaks, R_0 . We can expect this to be close to the Sun (Bandyopadhyay et al. 2020), for example at the Alfvén point (Kasper et al. 2021; Zhao et al. 2022), or it can be identified with the stream under study closest to the Sun ($R_0 = 0.3$ au). Further expressing the solar wind time of travel in units of the initial nonlinear time, t_{NL} (here taken as the average between characteristic kinetic and magnetic nonlinear times, respectively $t_v = L_{int}^v/v_{rms}^*$ and $t_B = L_{int}^B/B_{rms}^*$, where L_{int}^v and L_{int}^B are the kinetic and magnetic integral scales, whereas v_{rms}^* and B_{rms}^* are the rms values of the field fluctuations, all estimated at R_0) enables the comparison between observational and numerical estimates and statistics. This suggests the possible use of the following simple expression to determine the normalized “age” of the turbulence: $t_{turb} = (R - R_0)/(V_{sw}t_{NL})$. We will not make use of this parameter since our comparison with the numerical simulation results is only qualitative. Furthermore, determining R_0 and the integral scales is not trivial in solar wind data. However, since the parameters in the above transformation (the solar wind speed, the initial distance, and the nonlinear time at the initial position) can all be considered as constant, the power-law scaling presented will not be affected by this transformation. Computing spectral energy fluxes from numerical simulation requires the integration of quantities over extended intervals, during which the system is assumed to be stationary. This condition can hardly be attained when dealing with spin-down runs. Moreover we would like to monitor the evolution of the turbulent energy transfer rate, in all the simulations in Table 1, at different times after the plasma has reached

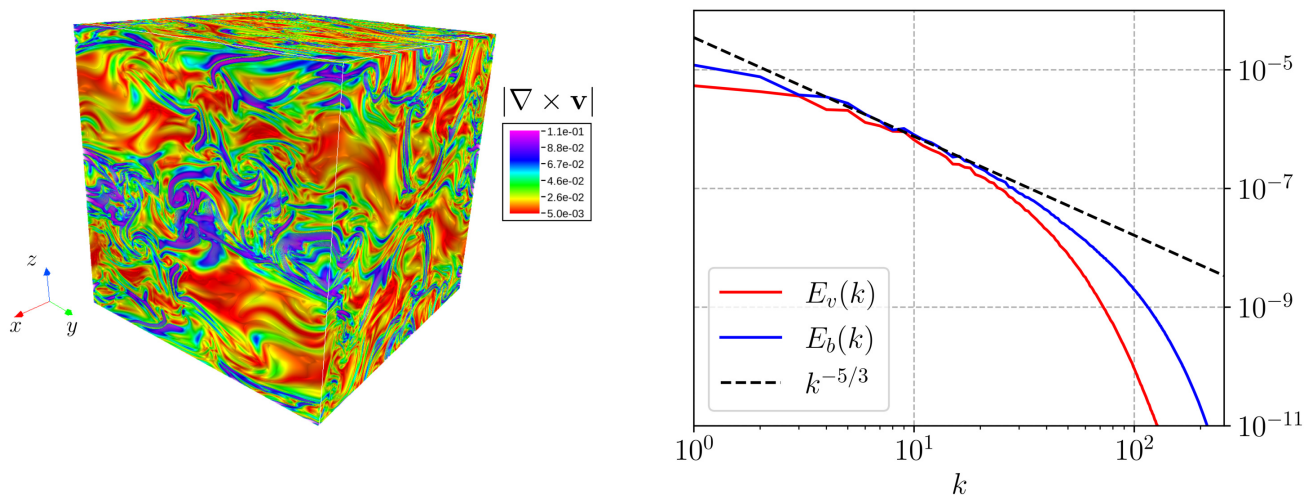


Fig. 5. Left panel: rendering of the vorticity field, at the time t^* when the peak of the density current is reached. Right panel: isotropic kinetic and magnetic energy spectra for run I in the table I of the main text at t^* .

the density current peak. For this reason, here we make the assumption (reasonable in case of fully developed turbulence) that the rate at which kinetic and magnetic energies are transferred throughout the inertial range, in subsequent time intervals, as the system relaxes due to viscous effects, does follow the same trend of the small-scale dissipation with the evolutionary time of the simulations. We have thus computed systematically the volume-averaged total dissipation rate, $\varepsilon_{tot} = \varepsilon_V + \varepsilon_B$, where $\varepsilon_V = \nu \langle (\nabla v)^2 \rangle$ and $\varepsilon_B = \eta \langle j^2 \rangle$ are the kinetic and magnetic dissipation, respectively, and $\nu = \eta$ are the kinematic viscosity and the resistivity. Figure 6 (top panel) displays the temporal evolution of the dissipation rate ε_{tot} in runs I-III, starting from the turbulence peak t^* . All times are expressed in units of the nonlinear time, t_{NL} , estimated as described above using the simulation parameter computed at the time of the peak of the density current, t^* . For all runs, a power-law time evolution of the energy transfer rate can be clearly identified (Batchelor et al. 1948; Hossain et al. 1995), with fitted scaling exponents compatible with those observed in the solar wind.

Finally, the bottom panel of Figure 6 shows the magnetic field kurtosis versus the scale Δl for Run II, at three different times $t > t^*$ in the simulation. The power-law scaling exponents indicate increasing intermittency with time (Biferale et al. 2003), similarly to observations in the fast recurrent stream studied here. The same trend is observed for all runs.

By qualitatively comparing both the energy transfer rate and intermittency, evident similarities arise between the time evolution in our simulations of decaying MHD turbulence and the radial profile in the solar wind streams. Although the numerical model used here is not intended to fully reproduce the solar wind features, such similarities suggest that the ongoing dissipation of turbulent fluctuations could concur to determine the observed radial evolution of solar wind turbulence.

6. Conclusions

We used Helios 2 measurements of the solar wind emitted from a steady coronal source and without interactions with coronal or heliospheric structures, collected at different distances from the Sun. We have shown that the turbulence energy transfer rate decays approximately as a power law of the distance, and we provided measured decay exponents that may be used to con-

strain models of solar wind expansion. It should be pointed out that the linear scaling range becomes narrow at larger distance from the Sun. In the slow wind, for example, such range covers slightly less than a decade, which is in contrast with the observed broad spectral inertial range. This is likely due to the limited statistics provided by the relatively low resolution Helios data, and more in general to the difficult observation of signed third-order scaling laws. Possible other reasons include the violation of the isotropy assumption and the presence of large-scale inhomogeneities (Stawarz et al. 2011; Verdini et al. 2015). In the Alfvénic fast wind, the turbulence decay is also associated with increasing intermittency. The observations presented here are qualitatively compared with three-dimensional direct numerical simulations of decaying MHD turbulence. Despite the simulations used here do not include important elements such as the radial expansion of the solar wind, the observed similarity between trends of energy transfer and dissipation rates (estimated from Helios 2 observations and DNS, respectively) supports the possible relevance of dissipation in the radial evolution of solar wind turbulence. Furthermore, the observation in the $1/f$ range of both the PP law and power-law scaling of the kurtosis suggests that, in fast solar wind, a turbulent cascade is active also at large scales, even in the presence of strongly Alfvénic large-scale fluctuations (Verdini et al. 2012). The behavior highlighted by our analysis, together with the observed parameters, can be relevant to constrain models of turbulence in the expanding solar wind and of the plasma heating observed in both fast and slow streams (Marino et al. 2008, 2011). Coordinated studies of PSP and Solar Orbiter measurements will add statistical significance to our observations (Velli et al. 2020; Telloni et al. 2021b).

Acknowledgements. L.S.-V. and E.Y. were supported by SNSA grants 86/20 and 145/18. L.S.-V. is supported by the Swedish Research Council (VR) Research Grant N. 2022-03352. R.M. and R.F. acknowledge support from the project “EVENTFUL” (ANR-20-CE30-0011), funded by the French “Agence Nationale de la Recherche” - ANR through the program AAPG-2020. This research was supported by the International Space Science Institute (ISSI) in Bern, through ISSI International Team project #556 (Cross-scale energy transfer in space plasmas).

References

- Alberti, T., Consolini, G., Carbone, V., et al. 2019, *Entropy*, 21
 Andrés, N., Romanelli, N., Hadid, L. Z., et al. 2020, *ApJ*, 902, 134

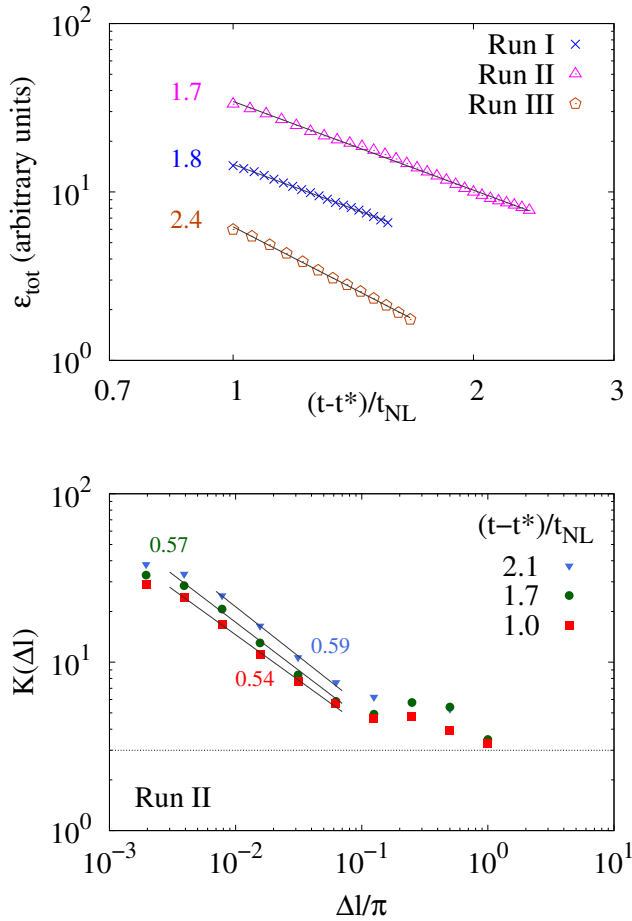


Fig. 6. Top panel: energy dissipation rate, ε_{tot} (arbitrary units), versus the rescaled simulation time, $(t-t^*)/t_{\text{NL}}$, for the three simulation runs. Bottom panel: magnetic field kurtosis, K , versus the spatial increment Δl , averaged over the field components, shown here for run II at three different times (see legend). For all plots, power-law fits and the relative fitted exponents are indicated (fitting errors ≤ 0.01).

Anselmet, F., Gagne, Y., Hopfinger, E. J., & Antonia, R. A. 1984, *J. Fluid Mech.*, 140, 63
 Bale, S. D., Horbury, T. S., Velli, M., et al. 2021, *ApJ*, 923, 174
 Bandyopadhyay, R., Goldstein, M. L., Maruca, B. A., et al. 2020, *ApJS*, 246, 48
 Bandyopadhyay, R., Matthaeus, W. H., McComas, D. J., et al. 2022, *ApJ*, 926, L1
 Bandyopadhyay, R., Matthaeus, W. H., Oughton, S., & Wan, M. 2019, *Journal of Fluid Mechanics*, 876, 5–18
 Batchelor, G. K., Townsend, A. A., & Taylor, G. I. 1948, *Proceedings of the Royal Society of London. Series A. Mathematical and Physical Sciences*, 193, 539
 Bavassano, B., Dobrowolny, M., Fanfoni, G., Mariani, F., & Ness, N. 1982a, *Solar Phys.*, 78, 373
 Bavassano, B., Dobrowolny, M., Mariani, F., & Ness, N. 1982b, *J. Geophys. Res.*, 87, 3617
 Bavassano, B., Pietropaolo, E., & Bruno, R. 1998, *J. Geophys. Res.*, 103, 6521
 Bavassano, B., Pietropaolo, E., & Bruno, R. 2002, *Journal of Geophysical Research: Space Physics*, 107, 7
 Biferale, L., Boffetta, G., Celani, A., et al. 2003, *Physics of Fluids*, 15, 2105
 Biskamp, D. 1993, *Magnetohydrodynamic Turbulence* (Cambridge University Press)
 Borovsky, J. E. 2008, *Journal of Geophysical Research: Space Physics*, 113
 Bourouaine, S., Perez, J. C., Klein, K. G., et al. 2020, *ApJ*, 904, L30
 Bruno, R., Bavassano, B., & Villante, U. 1985, *J. Geophys. Res.*, 90, 4373
 Bruno, R. & Carbone, V. 2013, *Liv. Rev. in Solar Phys.*, 10, 2
 Bruno, R., Carbone, V., Primavera, L., et al. 2004, *Annales Geophysicae*, 22, 3751
 Bruno, R., Carbone, V., Sorriso-Valvo, L., & Bavassano, B. 2003, *J. of Geophys. Res.: Space Phys.*, 108, 1130

Bruno, R., Carbone, V., Veltri, P., Pietropaolo, E., & Bavassano, B. 2001, *Planet. Space Sci.*, 49, 1201
 Bruno, R., Sorriso-Valvo, L., Carbone, V., & Bavassano, B. 2004, *Europhysics Letters (EPL)*, 66, 146
 Bruno, R., Telloni, D., Primavera, L., et al. 2014, *ApJ*, 786, 53
 Bruno, R. & Trenchi, L. 2014, *ApJ*, 787, L24
 Burlaga, L. F. 2004, *Nonlinear Processes in Geophysics*, 11, 441
 Carbone, F. & Sorriso-Valvo, L. 2014, *Eur. Phys. J. E*, 37, 61
 Carbone, V. 1994, *Annales Geophysicae*, 12, 585
 Carbone, V., Marino, R., Sorriso-Valvo, L., Noullez, A., & Bruno, R. 2009, *Phys. Rev. Lett.*, 103, 061102
 Castaing, B., Gagne, Y., & Hopfinger, E. J. 1990, *Physica D Nonlinear Phenomena*, 46, 177
 Chandran, B. D. G. 2018, *Journal of Plasma Physics*, 84, 905840106
 Chen, C. H. K., Bale, S. D., Bonnell, J. W., et al. 2020, *ApJS*, 246, 53
 Coburn, J. T., Smith, C. W., Vasquez, B. J., Stawarz, J. E., & Forman, M. A. 2012, *ApJ*, 754, 93
 D’Amicis, R., Bruno, R., Pallochia, G., et al. 2010, *ApJ*, 717, 474
 Di Mare, F., Sorriso-Valvo, L., Retinò, A., Malara, F., & Hasegawa, H. 2019, *Atmosphere*, 10, 561
 Dobrowolny, M., Mangeney, A., & Veltri, P. 1980, *Physical Review Letters*, 45, 144
 Dong, Y., Verdini, A., & Grappin, R. 2014, *The Astrophysical Journal*, 793, 118
 Dudok De Wit, T. 2004, *Phys. Rev. E*, 70, 055302(R)
 D’Amicis, R., Perrone, D., Bruno, R., & Velli, M. 2021, *Journal of Geophysical Research: Space Physics*, 126, e2020JA028996, e2020JA028996
 Foldes, R., Lévêque, E., Marino, R., et al. 2022, *Journal of Plasma Physics* (submitted)
 Fraternali, F., Gallana, L., Iovieno, M., et al. 2016, *Physica Scripta*, 91, 023011
 Frisch, U. 1995, *Turbulence: The Legacy of A.N. Kolmogorov* (Cambridge University Press)
 Gogoberidze, G., Perri, S., & Carbone, V. 2013, *ApJ*, 769, 111
 Grappin, R., Velli, M., & Mangeney, A. 1991, *Annales Geophysicae*, 9, 416
 Grappin, R., Velli, M., & Mangeney, A. 1993, *Phys. Rev. Lett.*, 70, 2190
 Greco, A., Matthaeus, W. H., D’Amicis, R., Servidio, S., & Dmitruk, P. 2012, *ApJ*, 749, 105
 Greco, A., Perri, S., Servidio, S., Yordanova, E., & Veltri, P. 2016, *ApJ*, 823, L39
 Hadid, L. Z., Sahraoui, F., & Galtier, S. 2017, *ApJ*, 838, 9
 Heinemann, M. & Olbert, S. 1980, *Journal of Geophysical Research: Space Physics*, 85, 1311
 Hernández, C. S., Sorriso-Valvo, L., Bandyopadhyay, R., et al. 2021, *ApJ*, 922, L11
 Hossain, M., Gray, P. C., Pontius, Duane H., J., Matthaeus, W. H., & Oughton, S. 1995, *Physics of Fluids*, 7, 2886
 Kasper, J. C., Klein, K. G., Lichko, E., et al. 2021, *Phys. Rev. Lett.*, 127, 255101
 Kieokaew, R., Lavraud, B., Yang, Y., et al. 2021, *arXiv e-prints*, arXiv:2103.15489
 Kiyani, K., Chapman, S., & Hnat, B. 2006, *Phys. Rev. E*, 74, 051122
 Kiyani, K. H., Chapman, S. C., & Watkins, N. W. 2009, *Phys. Rev. E*, 79, 036109
 Kolmogorov, A. N. 1941, *Dokl. Akad. Nauk SSSR*, 32, 16
 Kraichnan, R. H. 1965, *Phys. of Fluids*, 8, 1385
 Leamon, R. J., Smith, C. W., Ness, N. F., Matthaeus, W. H., & Wong, H. K. 1998, *J. Geophys. Res.*, 103, 4775
 MacBride, B. T., Forman, M. A., & Smith, C. W. 2005, in *ESA Special Publication, Vol. 592, Solar Wind 11/SOHO 16, Connecting Sun and Heliosphere*, ed. B. Fleck, T. H. Zurbuchen, & H. Lacoste, 613
 Macek, W. M., Wawrzaszek, A., & Carbone, V. 2012, *Journal of Geophysical Research (Space Physics)*, 117, 12101
 Malara, F., Primavera, L., & Veltri, P. 2000, *Physics of Plasmas*, 7, 2866
 Marino, R. & Sorriso-Valvo, L. 2023, *Physics Reports*, 1006, 1
 Marino, R., Sorriso-Valvo, L., Carbone, V., et al. 2008, *ApJ*, 677, L71
 Marino, R., Sorriso-Valvo, L., Carbone, V., et al. 2011, *Planetary and Space Science*, 59, 592
 Marino, R., Sorriso-Valvo, L., D’Amicis, R., et al. 2012, *ApJ*, 750, 41
 Matteini, L., Stansby, D., Horbury, T. S., & Chen, C. H. K. 2018, *ApJ*, 869, L32
 Matthaeus, W. H. & Goldstein, M. L. 1982, *Journal of Geophysical Research: Space Physics*, 87, 6011
 Matthaeus, W. H. & Goldstein, M. L. 1986, *Phys. Rev. Lett.*, 57, 495
 Mininni, P. D., Pouquet, A. G., & Montgomery, D. C. 2006, *Phys. Rev. Lett.*, 97, 244503
 Miura, H. 2019, *Fluids*, 4
 Montagud-Camps, V., Grappin, R., & Verdini, A. 2018, *ApJ*, 853, 153
 Montagud-Camps, V., Grappin, R., & Verdini, A. 2020, *ApJ*, 902, 34
 Montagud-Camps, V., Hellinger, P., Verdini, A., et al. 2022, *The Astrophysical Journal*, 938, 90
 Orszag, S. A. & Tang, C. M. 1979, *Journal of Fluid Mechanics*, 90, 129
 Pagel, C. & Balogh, A. 2003, *J. Geophys. Res. (Space Physics)*, 108, 1012
 Parashar, T. N., Cuesta, M., & Matthaeus, W. H. 2019, *ApJ*, 884, L57
 Parker, E. N. 1965, *Space Sci. Rev.*, 4, 666

- Perrone, D., Stansby, D., Horbury, T. S., & Matteini, L. 2018, *Monthly Notices of the Royal Astronomical Society*, 483, 3730
- Politano, H. & Pouquet, A. 1998, *Geophys. Res. Lett.*, 25, 273
- Quijia, P., Fraternali, F., Stawarz, J. E., et al. 2021, *MNRAS*, 503, 4815
- Roberts, D. A., Goldstein, M. L., Matthaeus, W. H., & Ghosh, S. 1992, *Journal of Geophysical Research: Space Physics*, 97, 17115
- Salem, C., Mangeney, A., Bale, S. D., & Veltri, P. 2009, *ApJ*, 702, 537
- Smith, C. W., Stawarz, J. E., Vasquez, B. J., Forman, M. A., & MacBride, B. T. 2009, *Phys. Rev. Lett.*, 103, 201101
- Sorriso-Valvo, L., Carbone, V., Veltri, P., Consolini, G., & Bruno, R. 1999, *Geophys. Res. Lett.*, 26, 1801
- Sorriso-Valvo, L., Marino, R., Carbone, V., et al. 2007, *Phys. Rev. Lett.*, 99, 115001
- Sorriso-Valvo, L., Marino, R., Ljoi, L., Perri, S., & Carbone, V. 2015, *ApJ*, 807, 86
- Sorriso-Valvo, L., Yordanova, E., Dimmock, A. P., & Telloni, D. 2021, *ApJ*, 919, L30
- Stawarz, J. E., Smith, C. W., Vasquez, B. J., Forman, M. A., & MacBride, B. T. 2010, *ApJ*, 713, 920
- Stawarz, J. E., Vasquez, B. J., Smith, C. W., Forman, M. A., & Klewicki, J. 2011, *ApJ*, 736, 44
- Taylor, G. I. 1938, *Royal Society of London Proceedings Series A*, 164, 476
- Telloni, D., Sorriso-Valvo, L., Woodham, L. D., et al. 2021a, *ApJ*, 912, L21
- Telloni, D., Sorriso-Valvo, L., Woodham, L. D., et al. 2021b, *ApJ*, 912, L21
- Telloni, D., Zank, G. P., Stangalini, M., Downsall, C., & al. 2022, *ApJ*
- Tenerani, A. & Velli, M. 2017, *ApJ*, 843, 26
- Totten, T. L., Freeman, J. W., & Arya, S. 1995, *Journal of Geophysical Research: Space Physics*, 100, 13
- Tu, C. Y. & Marsch, E. 1995, *Space Sci. Rev.*, 73, 1
- Vasquez, B. J., Smith, C. W., Hamilton, K., MacBride, B. T., & Leamon, R. J. 2007, *Journal of Geophysical Research (Space Physics)*, 112, A07101
- Velli, M., Grappin, R., & Mangeney, A. 1990, *Computer Physics Communications*, 59, 153
- Velli, M., Harra, L. K., Vourlidas, A., et al. 2020, *A&A*, 642, A4
- Verdini, A. & Grappin, R. 2015, *ApJ*, 808, L34
- Verdini, A., Grappin, R., Hellinger, P., Landi, S., & Müller, W. C. 2015, *ApJ*, 804, 119
- Verdini, A., Grappin, R., Pinto, R., & Velli, M. 2012, *ApJ*, 750, L33
- Verma, M. K. 2004, *Phys. Reports*, 401, 229
- Verscharen, D., Klein, K. G., & Maruca, B. A. 2019, *Living Reviews in Solar Physics*, 16, 5
- von Steiger, R., Schwadron, N. A., Fisk, L. A., et al. 2000, *Journal of Geophysical Research: Space Physics*, 105, 27217
- Watson, A. S., Smith, C. W., Marchuk, A. V., et al. 2022, *ApJ*, 927, 43
- Wu, H., Tu, C., He, J., Wang, X., & Yang, L. 2022, *ApJ*, 927, 113
- Zhao, L.-L., Zank, G. P., Telloni, D., et al. 2022, *ApJ*, 928, L15

Bibliography

- [1] A. Alexakis and S. Chibbaro. Local energy flux of turbulent flows. *Phys. Rev. Fluids*, 5:094604, Sep 2020. doi: 10.1103/PhysRevFluids.5.094604. URL <https://link.aps.org/doi/10.1103/PhysRevFluids.5.094604>.
- [2] A. Alexakis, R. Marino, P. Mininni, A. van Kan, R. Foldes, and F. Feraco. Large-scale self-organisation in dry turbulent atmospheres. *Science (SUBMITTED)*, 2023.
- [3] O. Alexandrova, V. Carbone, P. Veltri, and L. Sorriso-Valvo. Small-Scale Energy Cascade of the Solar Wind Turbulence. *The Astrophysical Journal*, 674:1153–1157, Feb. 2008. doi: 10.1086/524056.
- [4] O. Alexandrova, J. Saur, C. Lacombe, A. Mangeney, J. Mitchell, S. J. Schwartz, and P. Robert. Universality of Solar-Wind Turbulent Spectrum from MHD to Electron Scales. *PhRvL*, 103(16):165003, Oct. 2009. doi: 10.1103/PhysRevLett.103.165003.
- [5] H. Aluie and G. L. Eyink. Localness of energy cascade in hydrodynamic turbulence. ii. sharp spectral filter. *Physics of Fluids*, 21(11):115108, 2009. doi: 10.1063/1.3266948.
- [6] H. Aluie and G. L. Eyink. Scale Locality of Magnetohydrodynamic Turbulence. *Physics Review Letters*, 104(8):081101, Feb. 2010. doi: 10.1103/PhysRevLett.104.081101.
- [7] H. Aluie and S. Kurien. Joint downscale fluxes of energy and potential

- enstrophy in rotating stratified boussinesq flows. *EPL (Europhysics Letters)*, 96(4):44006, nov 2011. doi: 10.1209/0295-5075/96/44006.
- [8] H. Aluie, S. Li, and H. Li. Conservative cascade of kinetic energy in compressible turbulence. *The Astrophysical Journal*, 751(2):L29, may 2012. doi: 10.1088/2041-8205/751/2/l29.
- [9] H. Aluie, M. Hecht, and G. K. Vallis. Mapping the Energy Cascade in the North Atlantic Ocean: The Coarse-Graining Approach. *Journal of Physical Oceanography*, 48(2):225–244, Feb. 2018. doi: 10.1175/JPO-D-17-0100.1.
- [10] S. Angriman, P. Cobelli, P. Mininni, M. Obligado, and P. Leoni. Generation of turbulent states using physics-informed neural networks. *arXiv e-prints*, 09 2022.
- [11] J. A. Armstrong and L. Fletcher. Fast solar image classification using deep learning and its importance for automation in solar physics. *Solar Physics*, 294(80), 2019. doi: <https://doi.org/10.1007/s11207-019-1473-z>.
- [12] L. Arzamasskiy, M. W. Kunz, B. D. G. Chandran, and E. Quataert. Hybrid-kinetic Simulations of Ion Heating in Alfvénic Turbulence. *The Astrophysical Journal*, 879(1):53, Jul 2019. doi: 10.3847/1538-4357/ab20cc.
- [13] A. Bañón Navarro, B. Teaca, D. Told, D. Groselj, P. Crandall, and F. Jenko. Structure of Plasma Heating in Gyrokinetic Alfvénic Turbulence. *Physics Review Letters*, 117(24):245101, Dec. 2016. doi: 10.1103/PhysRevLett.117.245101.
- [14] K. Bai, C. Meneveau, and J. Katz. Experimental study of spectral energy fluxes in turbulence generated by a fractal, tree-like object. *Physics of Fluids*, 25(11):110810, 2013. doi: 10.1063/1.4819351.
- [15] G. Balasis, S. Aminalragia-Giamini, C. Papadimitriou, I. A. Daglis, A. Anastasiadis, and R. Haagmans. A machine learning approach for automated uly wave recognition. *J. Space Weather Space Clim.*, 9, 2019. doi: <https://doi.org/10.1051/swsc/2019010>.

- [16] L. Baransky, J. Borovkov, M. Gokhberg, S. Krylov, and V. Troitskaya. High resolution method of direct measurement of the magnetic field lines' eigen frequencies. *Planetary and space science*, 33(12):1369–1374, 1985. doi: [https://doi.org/10.1016/0032-0633\(85\)90112-6](https://doi.org/10.1016/0032-0633(85)90112-6).
- [17] D. Berube, M. B. Moldwin, and J. M. Weygand. An automated method for the detection of field line resonance frequencies using ground magnetometer techniques. *Journal of Geophysical Research: Space Physics*, 108(A9):1348, 2003. doi: <https://doi.org/10.1029/2002JA009737>.
- [18] J. W. Bieber, W. Wanner, and W. H. Matthaeus. Dominant two-dimensional solar wind turbulence with implications for cosmic ray transport. *Journal of Geophysical Research: Space Physics*, 101(A2):2511–2522, 1996. doi: <https://doi.org/10.1029/95JA02588>.
- [19] P. Billant and J.-M. Chomaz. Self-similarity of strongly stratified inviscid flows. *Physics of Fluids*, 13(6):1645–1651, 2001. doi: 10.1063/1.1369125.
- [20] S. P. Bishop, R. J. Small, and F. O. Bryan. The global sink of available potential energy by mesoscale air-sea interaction. *Journal of Advances in Modeling Earth Systems*, 12(10):e2020MS002118, 2020. doi: <https://doi.org/10.1029/2020MS002118>.
- [21] G. Boffetta, A. Celani, and M. Vergassola. Inverse energy cascade in two-dimensional turbulence: Deviations from gaussian behavior. *Phys. Rev. E*, 61: R29–R32, Jan 2000. doi: 10.1103/PhysRevE.61.R29.
- [22] S. Boldyrev and N. F. Loureiro. Magnetohydrodynamic Turbulence Mediated by Reconnection. *The Astrophysical Journal*, 844(2):125, Aug. 2017. doi: 10.3847/1538-4357/aa7d02.
- [23] S. Boldyrev and J. C. Perez. Spectrum of Kinetic-Alfvén Turbulence. *The Astrophysical Journal*, 758:L44, Oct. 2012. doi: 10.1088/2041-8205/758/2/L44.
- [24] S. Boldyrev, K. Horaites, Q. Xia, and J. C. Perez. Toward a Theory of

- Astrophysical Plasma Turbulence at Subproton Scales. *The Astrophysical Journal*, 777:41, Nov. 2013. doi: 10.1088/0004-637X/777/1/41.
- [25] J. Borggaard, T. Iliescu, and J. Roop. A bounded artificial viscosity large eddy simulation model. *SIAM Journal on Numerical Analysis*, 47(1):622–645, 2008. ISSN 00361429.
- [26] P. Bouruet-Aubertot, J. Sommeria, and C. Staquet. Breaking of standing internal gravity waves through two-dimensional instabilities. *Journal of Fluid Mechanics*, 285:265–301, 1995. doi: 10.1017/S0022112095000541.
- [27] P. Bouruet-Aubertot, J. Sommeria, and C. Staquet. Stratified turbulence produced by internal wave breaking: two-dimensional numerical experiments. *Dynamics of Atmospheres and Oceans*, 23(1):357–369, 1996. ISSN 0377-0265. doi: [https://doi.org/10.1016/0377-0265\(95\)00430-0](https://doi.org/10.1016/0377-0265(95)00430-0). Stratified flows.
- [28] R. Boynton, M. Balikhin, H.-L. Wei, and Z.-Q. Lang. Chapter 8 - applications of narmax in space weather. In E. Camporeale, J. Johnson, and S. Wing, editors, *Machine Learning Techniques for Space Weather*, pages 203 – 236. Elsevier, 2018. ISBN 978-0-12-811788-0. doi: <https://doi.org/10.1016/B978-0-12-811788-0.00008-1>.
- [29] M. Bramberger, A. Dörnbrack, H. Wilms, F. Ewald, and R. Sharman. Mountain-Wave Turbulence Encounter of the Research Aircraft HALO above Iceland. *Journal of Applied Meteorology and Climatology*, 59(3):567–588, Mar. 2020. doi: 10.1175/JAMC-D-19-0079.1.
- [30] G. Brethouwer, P. Billant, E. Lindborg, and J. M. Chomaz. Scaling analysis and simulation of strongly stratified turbulent flows. *J. Fluid Mech.*, 585: 343–368, 2007.
- [31] H. Breuillard, R. Dupuis, A. Retino, O. Le Contel, J. Amaya, and G. Lapenta. Automatic classification of plasma regions in near-earth space with supervised machine learning: Application to magnetospheric multi scale 2016–2019 observations. *Frontiers in Astronomy and Space Sciences*, 7:55, 2020. ISSN 2296-987X. doi: <https://doi.org/10.3389/fspas.2020.00055>.

- [32] C. Brun, S. Blein, and J.-P. Chollet. Large-eddy simulation of a katabatic jet along a convexly curved slope. part i: Statistical results. *Journal of the Atmospheric Sciences*, 74, 05 2017. doi: 10.1175/JAS-D-16-0152.1.
- [33] R. Bruno and D. Telloni. Spectral Analysis of Magnetic Fluctuations at Proton Scales from Fast to Slow Solar Wind. *The Astrophysical Journal*, 811:L17, Oct. 2015. doi: 10.1088/2041-8205/811/2/L17.
- [34] R. Bruno and L. Trenchi. Radial Dependence of the Frequency Break between Fluid and Kinetic Scales in the Solar Wind Fluctuations. *The Astrophysical Journal*, 787:L24, June 2014. doi: 10.1088/2041-8205/787/2/L24.
- [35] R. Bruno, V. Carbone, P. Veltri, E. Pietropaolo, and B. Bavassano. Identifying intermittency events in the solar wind. *Planetary and Space Science*, 49(12):1201–1210, 2001. ISSN 0032-0633. doi: [https://doi.org/10.1016/S0032-0633\(01\)00061-7](https://doi.org/10.1016/S0032-0633(01)00061-7). URL <https://www.sciencedirect.com/science/article/pii/S0032063301000617>. Nonlinear Dynamics and Fraactals in Space.
- [36] M. Buzzicotti, F. Bonaccorso, P. Clark di Leoni, and L. Biferale. Reconstruction of turbulent data with deep generative models for semantic inpainting from turbrot database. *Physical Review Fluids*, 6, 05 2021. doi: 10.1103/PhysRevFluids.6.050503.
- [37] M. Buzzicotti, B. A. Storer, S. M. Griffies, and H. Aluie. A coarse-grained decomposition of surface geostrophic kinetic energy in the global ocean. *Earth and Space Science Open Archive*, page 58, 2021. doi: 10.1002/essoar.10507290.1.
- [38] F. Califano, S. S. Cerri, M. Faganello, D. Laveder, and M. W. Kunz. Electron-only magnetic reconnection in plasma turbulence. *arXiv e-prints*, art. arXiv:1810.03957, Oct. 2018.
- [39] E. Camporeale, J. Johnson, and S. Wing. Introduction. In E. Camporeale, J. Johnson, and S. Wing, editors, *Machine Learning Techniques for Space Weather*, pages XIII–XVIII. Elsevier, 2018. ISBN 978-0-12-811788-0.

- [40] E. Camporeale, L. Sorriso-Valvo, F. Califano, and A. Retinò. Coherent Structures and Spectral Energy Transfer in Turbulent Plasma: A Space-Filter Approach. *Physical Review Letters*, 120(12):125101, Mar. 2018. doi: 10.1103/PhysRevLett.120.125101.
- [41] E. Camporeale, G. Wilkie, A. Drozdov, and J. Bortnik. Data-driven discovery of fokker-planck equation for the earth's radiation belts electrons using physics-informed neural networks. *Journal of Geophysical Research: Space Physics*, 127, 07 2022. doi: 10.1029/2022JA030377.
- [42] X. Capet, J. C. McWilliams, M. J. Molemaker, and A. F. Shchepetkin. Mesoscale to Submesoscale Transition in the California Current System. Part I: Flow Structure, Eddy Flux, and Observational Tests. *Journal of Physical Oceanography*, 38(1):29, Jan. 2008. doi: 10.1175/2007JPO3671.1.
- [43] V. Carbone, P. Veltri, and A. Mangeney. Coherent structure formation and magnetic field line reconnection in magnetohydrodynamic turbulence. *Physics of Fluids*, 2:1487–1496, Aug. 1990. doi: 10.1063/1.857598.
- [44] S. Cerri, L. Franci, F. Califano, S. Landi, and P. Hellinger. Plasma turbulence at ion scales: a comparison between particle in cell and eulerian hybrid-kinetic approaches. *Journal of Plasma Physics*, 83(2):705830202, 2017. doi: 10.1017/S0022377817000265.
- [45] S. S. Cerri and F. Califano. Reconnection and small-scale fields in 2D-3V hybrid-kinetic driven turbulence simulations. *New J. Phys.*, 19(2):025007, Feb. 2017. doi: 10.1088/1367-2630/aa5c4a.
- [46] S. S. Cerri and E. Camporeale. Space-filter techniques for quasi-neutral hybrid-kinetic models. *Physics of Plasmas*, 27(8):082102, Aug. 2020. doi: 10.1063/5.0012924.
- [47] M. Chandorkar and E. Camporeale. Chapter 9 - probabilistic forecasting of geomagnetic indices using gaussian process models. In E. Camporeale, J. Johnson, and S. Wing, editors, *Machine Learning Techniques for Space*

- Weather*, pages 237 – 258. Elsevier, 2018. ISBN 978-0-12-811788-0. doi: <https://doi.org/10.1016/B978-0-12-811788-0.00009-3>.
- [48] A. Chasapis, A. Retinò, F. Sahraoui, A. Vaivads, Y. V. Khotyaintsev, D. Sundkvist, A. Greco, L. Sorriso-Valvo, and P. Canu. Thin Current Sheets and Associated Electron Heating in Turbulent Space Plasma. *The Astrophysical Journal*, 804:L1, May 2015. doi: 10.1088/2041-8205/804/1/L1.
- [49] J. Chau, R. Marino, F. Feraco, J. Urco, G. Baumgarten, F.-J. Luebken, W. Hocking, C. Schult, T. Renkwitz, and R. Latteck. Radar observation of extreme vertical drafts in the polar summer mesosphere. *Geophysical Research Letters*, 48, 08 2021. doi: 10.1029/2021GL094918.
- [50] C. H. K. Chen and S. Boldyrev. Nature of Kinetic Scale Turbulence in the Earth’s Magnetosheath. *The Astrophysical Journal*, 842:122, June 2017. doi: 10.3847/1538-4357/aa74e0.
- [51] C. H. K. Chen, T. S. Horbury, A. A. Schekochihin, R. T. Wicks, O. Alexandrova, and J. Mitchell. Anisotropy of Solar Wind Turbulence between Ion and Electron Scales. *PhRvL*, 104(25):255002, June 2010. doi: 10.1103/PhysRevLett.104.255002.
- [52] W. Chen, Q. Wang, J. S. Hesthaven, and C. Zhang. Physics-informed machine learning for reduced-order modeling of nonlinear problems. *Journal of Computational Physics*, 446:110666, 2021. ISSN 0021-9991. doi: <https://doi.org/10.1016/j.jcp.2021.110666>.
- [53] P. J. Chi, M. J. Engebretson, M. B. Moldwin, C. T. Russell, I. R. Mann, M. R. Hairston, M. Reno, J. Goldstein, L. I. Winkler, J. L. Cruz-Abeyro, D.-H. Lee, K. Yumoto, R. Dalrymple, B. Chen, and J. P. Gibson. Sounding of the plasmasphere by Mid-continent MAgnetoseismic Chain (McMAC) magnetometers. *Journal of Geophysical Research: Space Physics*, 118(6):3077–3086, 2013. doi: <https://doi.org/10.1002/jgra.50274>.
- [54] J. Cho and A. Lazarian. The Anisotropy of Electron Magnetohydrodynamic

- Turbulence. *The Astrophysical Journal*, 615:L41–L44, Nov. 2004. doi: 10.1086/425215.
- [55] L. Comisso, Y.-M. Huang, M. Lingam, E. Hirvijoki, and A. Bhattacharjee. Magnetohydrodynamic Turbulence in the Plasmoid-mediated Regime. *The Astrophysical Journal*, 854:103, Feb. 2018. doi: 10.3847/1538-4357/aaac83.
- [56] J. A. Cover, Thomas M. and Thomas. *Entropy, Relative Entropy, and Mutual Information*, chapter 2, pages 13–55. John Wiley & Sons, Ltd, 2005. ISBN 9780471748823. doi: <https://doi.org/10.1002/047174882X.ch2>.
- [57] S. Cuomo, V. Schiano di Cola, F. Giampaolo, G. Rozza, M. Raissi, and F. Piccialli. Scientific Machine Learning through Physics-Informed Neural Networks: Where we are and What’s next. *arXiv e-prints*, art. arXiv:2201.05624, Jan. 2022.
- [58] E. A. D’Asaro, R.-C. Lien, and F. Henyey. High-Frequency Internal Waves on the Oregon Continental Shelf. *Journal of Physical Oceanography*, 37(7):1956, Jan. 2007. doi: 10.1175/JPO3096.1.
- [59] A. De Leo and A. Stocchino. Evidence of transient energy and enstrophy cascades in tidal flows: A scale to scale analysis. *Geophysical Research Letters*, 49(10):e2022GL098043, 2022. doi: <https://doi.org/10.1029/2022GL098043>.
- [60] O. Debliquy, M. K. Verma, and D. Carati. Energy fluxes and shell-to-shell transfers in three-dimensional decaying magnetohydrodynamic turbulence. *Physics of Plasmas*, 12(4):042309, 2005. doi: 10.1063/1.1867996.
- [61] A. Del Corpo, M. Vellante, B. Heilig, E. Pietropaolo, J. Reda, and J. Lichtenberger. Observing the cold plasma in the earth’s magnetosphere with the emma network. *Annals of Geophysics*, 62(4), 2019. ISSN 2037-416X. doi: <https://doi.org/10.4401/ag-7751>.
- [62] D. DeMers and G. W. Cottrell. Non-linear dimensionality reduction. In S. J. Hanson, J. D. Cowan, and C. L. Giles, editors, *Advances in Neural Information*

- Processing Systems 5*, pages 580–587. Morgan-Kaufmann, 1993. URL <http://papers.nips.cc/paper/619-non-linear-dimensionality-reduction.pdf>.
- [63] J. A. Domaradzki and D. Carati. An analysis of the energy transfer and the locality of nonlinear interactions in turbulence. *Physics of Fluids*, 19(8):085112, 2007. doi: 10.1063/1.2772248.
- [64] J. A. Domaradzki and R. S. Rogallo. Local energy transfer and nonlocal interactions in homogeneous, isotropic turbulence. *Physics of Fluids A: Fluid Dynamics*, 2(3):413–426, 1990. doi: 10.1063/1.857736.
- [65] C. Dong, L. Wang, Y.-M. Huang, L. Comisso, and A. Bhattacharjee. Role of the Plasmoid Instability in Magnetohydrodynamic Turbulence. *Physics Review Letters*, 121(16):165101, Oct. 2018. doi: 10.1103/PhysRevLett.121.165101.
- [66] J. C. Dorelli, A. Gloer, G. Collinson, and G. Tóth. The role of the Hall effect in the global structure and dynamics of planetary magnetospheres: Ganymede as a case study. *Journal of Geophysical Research: Space Physics*, 120(7): 5377–5392, 2015. doi: <https://doi.org/10.1002/2014JA020951>.
- [67] G. L. Eyink. Locality of turbulent cascades. *Physica D: Nonlinear Phenomena*, 207(1):91–116, 2005. ISSN 0167-2789. doi: <https://doi.org/10.1016/j.physd.2005.05.018>.
- [68] G. L. Eyink. Cascades and Dissipative Anomalies in Nearly Collisionless Plasma Turbulence. *Physical Review X*, 8(4):041020, Oct. 2018. doi: 10.1103/PhysRevX.8.041020.
- [69] R. L. F. *Weather Prediction by Numerical Process*. Cambridge University Press, 1922. doi: <https://doi.org/10.1017/CBO9780511618291>.
- [70] L. Fang and N. T. Ouellette. Advection and the efficiency of spectral energy transfer in two-dimensional turbulence. *Phys. Rev. Lett.*, 117:104501, Aug 2016. doi: 10.1103/PhysRevLett.117.104501.
- [71] M. Farge. Wavelet transforms and their applications to turbulence. *Annual Review of Fluid Mechanics*, 24(1):395–458, 1992. doi: 10.1146/annurev.fl.

- 24.010192.002143. URL <https://doi.org/10.1146/annurev.fl.24.010192.002143>.
- [72] F. Feraco, R. Marino, A. Pumir, L. Primavera, P. Mininni, A. Pouquet, and D. Rosenberg. Vertical drafts and mixing in stratified turbulence: Sharp transition with froude number. *EPL (Europhysics Letters)*, 123:44002, 09 2018. doi: 10.1209/0295-5075/123/44002.
- [73] F. Feraco, R. Marino, L. Primavera, A. Pumir, P. D. Mininni, D. Rosenberg, A. Pouquet, R. Foldes, E. Lévêque, E. Camporeale, S. S. Cerri, H. Charuvil Asokan, J. L. Chau, J. P. Bertoglio, P. Salizzoni, and M. Marro. Connecting large-scale velocity and temperature bursts with small-scale intermittency in stratified turbulence. *EPL (Europhysics Letters)*, 135(1):14001, July 2021. doi: 10.1209/0295-5075/135/14001.
- [74] R. Foldes, A. Del Corpo, E. Pietropaolo, and M. Vellante. Assessing machine learning techniques for identifying field line resonance frequencies from cross-phase spectra. *Journal of Geophysical Research: Space Physics*, 126(5): e2020JA029008, 2021. doi: <https://doi.org/10.1029/2020JA029008>.
- [75] R. Foldes, E. Lévêque, R. Marino, E. Pietropaolo, A. De Rosis, D. Telloni, and F. Feraco. Efficient kinetic Lattice Boltzmann simulation of three-dimensional Hall-MHD Turbulence. *arXiv e-prints*, art. arXiv:2212.11024, Dec. 2022. doi: 10.48550/arXiv.2212.11024.
- [76] L. Franci, A. Verdini, L. Matteini, S. Landi, and P. Hellinger. Solar Wind Turbulence from MHD to Sub-ion Scales: High-resolution Hybrid Simulations. *Astrophys. J. Lett.*, 804:L39, May 2015. doi: 10.1088/2041-8205/804/2/L39.
- [77] L. Franci, P. Hellinger, L. Matteini, A. Verdini, and S. Landi. Two-dimensional hybrid simulations of kinetic plasma turbulence: Current and vorticity vs proton temperature. In *American Institute of Physics Conference Series*, volume 1720 of *American Institute of Physics Conference Series*, page 040003, Mar. 2016. doi: 10.1063/1.4943814.

- [78] L. Franci, S. S. Cerri, F. Califano, S. Landi, E. Papini, A. Verdini, L. Matteini, F. Jenko, and P. Hellinger. Magnetic Reconnection as a Driver for a Sub-ion-scale Cascade in Plasma Turbulence. *The Astrophysical Journal*, 850:L16, Nov. 2017. doi: 10.3847/2041-8213/aa93fb.
- [79] L. Franci, S. Landi, A. Verdini, L. Mattini, and P. Hellinger. Solar wind turbulent cascade from MHD to sub-ion scales: large-size 3D hybrid particle-in-cell simulations. *ArXiv e-prints*, Nov. 2017.
- [80] B. Fraser, J. Horwitz, J. Slavin, Z. Dent, and I. Mann. Heavy ion mass loading of the geomagnetic field near the plasmopause and ULF wave implications. *Geophysical research letters*, 32(4):L04102, 2005. doi: <https://doi.org/10.1029/2004GL021315>.
- [81] U. Frisch. *Turbulence. The legacy of A. N. Kolmogorov*. Cambridge University Press, 1995.
- [82] K. Fukami, K. Fukagata, and K. Taira. Super-resolution reconstruction of turbulent flows with machine learning. *Journal of Fluid Mechanics*, 870:106–120, 2019. doi: 10.1017/jfm.2019.238.
- [83] S. Galtier. *Introduction to Modern Magnetohydrodynamics*. Cambridge University Press, 2016. doi: 10.1017/CBO9781316665961.
- [84] S. Galtier and A. Bhattacharjee. Anisotropic weak whistler wave turbulence in electron magnetohydrodynamics. *Physics of Plasmas*, 10:3065–3076, Aug. 2003. doi: 10.1063/1.1584433.
- [85] S. Galtier and E. Buchlin. Multiscale hall-magnetohydrodynamic turbulence in the solar wind. *The Astrophysical Journal*, 656(1):560–566, feb 2007. doi: 10.1086/510423.
- [86] M. Germano. Turbulence: the filtering approach. *Journal of Fluid Mechanics*, 238:325–336, 1992.
- [87] A. Glaws, R. King, and M. Sprague. Deep learning for in situ data compression of large turbulent flow simulations. *Phys. Rev. Fluids*, 5:114602, Nov 2020.

- doi: 10.1103/PhysRevFluids.5.114602. URL <https://link.aps.org/doi/10.1103/PhysRevFluids.5.114602>.
- [88] F. S. Godeferd and F. Moisy. Structure and Dynamics of Rotating Turbulence: A Review of Recent Experimental and Numerical Results. *Applied Mechanics Reviews*, 67(3), 05 2015. ISSN 0003-6900. doi: 10.1115/1.4029006.
- [89] D. O. Gómez, P. D. Mininni, and P. Dmitruk. Hall-magnetohydrodynamic small-scale dynamos. *Phys. Rev. E*, 82:036406, Sep 2010. doi: 10.1103/PhysRevE.82.036406.
- [90] P. A. González-Morales, E. Khomenko, and P. S. Cally. Fast-to-alfvén mode conversion mediated by hall current. II. application to the solar atmosphere. *The Astrophysical Journal*, 870(2):94, jan 2019. doi: 10.3847/1538-4357/aaf1a9.
- [91] A. Greco, F. Valentini, S. Servidio, and W. H. Matthaeus. Inhomogeneous kinetic effects related to intermittent magnetic discontinuities. *Phys. Rev. E*, 86(6):066405, Dec. 2012. doi: 10.1103/PhysRevE.86.066405.
- [92] D. Grošelj, S. S. Cerri, A. Bañón Navarro, C. Willmott, D. Told, N. F. Loureiro, F. Califano, and F. Jenko. Fully Kinetic versus Reduced-kinetic Modeling of Collisionless Plasma Turbulence. *The Astrophysical Journal*, 847:28, Sept. 2017. doi: 10.3847/1538-4357/aa894d.
- [93] V. Heidrich-Meisner and R. F. Wimmer-Schweingruber. Chapter 16 - solar wind classification via k-means clustering algorithm. In E. Camporeale, J. Johnson, and S. Wing, editors, *Machine Learning Techniques for Space Weather*, pages 397 – 424. Elsevier, 2018. ISBN 978-0-12-811788-0. doi: <https://doi.org/10.1016/B978-0-12-811788-0.00016-0>.
- [94] P. Hellinger, A. Verdini, S. Landi, L. Franci, E. Papini, and L. Matteini. On cascade of kinetic energy in compressible hydrodynamic turbulence. *arXiv e-prints*, art. arXiv:2004.02726, Apr. 2020.
- [95] J. R. Herring and O. Métais. Numerical experiments in forced stably stratified

- turbulence. *Journal of Fluid Mechanics*, 202:97–115, 1989. doi: 10.1017/S0022112089001114.
- [96] G. G. Howes, S. C. Cowley, W. Dorland, G. W. Hammett, E. Quataert, and A. A. Schekochihin. A model of turbulence in magnetized plasmas: Implications for the dissipation range in the solar wind. *J. Geophys. Res.*, 113:A05103, 2008.
- [97] J. D. Huba. Hall Magnetohydrodynamics - A Tutorial. In *Space Plasma Simulation*, volume 615, pages 166–192. Büchner, J. and Dum, C. and Scholer, M., 2003.
- [98] T. Kalmar-Nagy and B. Bak. An intriguing analogy of kolmogorov’s scaling law in a hierarchical mass–spring–damper model. *Nonlinear Dynamics*, 95, 03 2019. doi: 10.1007/s11071-018-04749-x.
- [99] H.-J. Kaltenbach, T. Gerz, and U. Schumann. Large-eddy simulation of homogeneous turbulence and diffusion in stably stratified shear flow. *Journal of Fluid Mechanics*, 280:1–40, 1994. doi: 10.1017/S0022112094002831.
- [100] K. H. Kiyani, K. T. Osman, and S. C. Chapman. Dissipation and heating in solar wind turbulence: from the macro to the micro and back again. *RSPTA*, 373(2041):20140155–20140155, Apr. 2015. doi: 10.1098/rsta.2014.0155.
- [101] M. Klema, S. Venayagamoorthy, A. Pouquet, D. Rosenberg, and R. Marino. Effect of rotation on mixing efficiency in homogeneous stratified turbulence using unforced direct numerical simulations. *Environmental Fluid Mechanics*, pages 1–16, 06 2022. doi: 10.1007/s10652-022-09869-y.
- [102] A. N. Kolmogorov. Local structure of turbulence in incompressible viscous fluid at very large Reynolds numbers. *Dokl. Akad. Nauk SSSR*, 30:299, 1941.
- [103] A. N. Kolmogorov. Dissipation of Energy in Locally Isotropic Turbulence. *Akademiia Nauk SSSR Doklady*, 32:16, Apr. 1941.
- [104] C. Körner, T. Pohl, U. Rude, N. Thürey, and T. Zeiser. Parallel lattice boltzmann methods for cfd applications. In A. M. Bruaset and A. Tveito, editors,

- Numerical Solution of Partial Differential Equations on Parallel Computers*, pages 439–466, Berlin, Heidelberg, 2006. Springer Berlin Heidelberg. ISBN 978-3-540-31619-0.
- [105] R. H. Kraichnan. Inertial-Range Spectrum of Hydromagnetic Turbulence. *Physics of Fluids*, 8:1385–1387, July 1965. doi: 10.1063/1.1761412.
- [106] R. H. Kraichnan. Inertial ranges in two-dimensional turbulence. *The Physics of Fluids*, 10(7):1417–1423, 1967. doi: 10.1063/1.1762301.
- [107] R. H. Kraichnan. Inertial-range transfer in two- and three-dimensional turbulence. *Journal of Fluid Mechanics*, 47(3):525–535, 1971. doi: 10.1017/S0022112071001216.
- [108] T. Krueger, H. Kusumaatmaja, A. Kuzmin, O. Shardt, G. Silva, and E. M. Viggen. *The Lattice Boltzmann Method: Principles and Practice*. Springer, 2016. ISBN 978-3-319-44647-9.
- [109] D. Kuzzay, O. Alexandrova, and L. Matteini. A local approach to the study of energy transfers in incompressible magnetohydrodynamic turbulence. *arXiv preprint arXiv:1812.06031*, 2018.
- [110] D. Kuzzay, O. Alexandrova, and L. Matteini. Local approach to the study of energy transfers in incompressible magnetohydrodynamic turbulence. *Phys. Rev. E*, 99:053202, May 2019. doi: 10.1103/PhysRevE.99.053202. URL <https://link.aps.org/doi/10.1103/PhysRevE.99.053202>.
- [111] A. Lazarian, G. L. Eyink, and E. T. Vishniac. Relation of astrophysical turbulence and magnetic reconnection. *Physics of Plasmas*, 19(1):012105–012105, Jan. 2012. doi: 10.1063/1.3672516.
- [112] A. Leonard. Energy cascade in large-eddy simulations of turbulent fluid flows. In F. Frenkiel and R. Munn, editors, *Turbulent Diffusion in Environmental Pollution*, volume 18 of *Advances in Geophysics*, pages 237–248. Elsevier, 1975. doi: [https://doi.org/10.1016/S0065-2687\(08\)60464-1](https://doi.org/10.1016/S0065-2687(08)60464-1).

- [113] T. Li, M. Buzzicotti, L. Biferale, and F. Bonaccorso. Generative adversarial networks to infer velocity components in rotating turbulent flows. *arXiv*, 01 2023. doi: 10.48550/arXiv.2301.07541.
- [114] Y. Liao and N. T. Ouellette. Long-range ordering of turbulent stresses in two-dimensional flow. *Phys. Rev. E*, 91:063004, Jun 2015. doi: 10.1103/PhysRevE.91.063004.
- [115] J. Lichtenberger, M. A. Clilverd, B. Heilig, M. Vellante, J. Manninen, C. J. Rodger, A. B. Collier, A. M. Jørgensen, J. Reda, R. H. Holzworth, et al. The plasmasphere during a space weather event: First results from the PLASMON project. *Journal of Space Weather and Space Climate*, 3:A23, 2013. doi: <https://doi.org/10.1051/swsc/2013045>.
- [116] L. Liechtestein, F. Godeferd, and C. Cambon. Nonlinear formation of structures in rotating stratified turbulence. *Journal of Turbulence*, 6:N24, 2005. doi: 10.1080/14685240500207407.
- [117] M. W. Liemohn. Introduction to special section on “results of the national science foundation geospace environment modeling inner magnetosphere/storms assessment challenge”. *Journal of Geophysical Research: Space Physics*, 111: A11S01, 2006. doi: <https://doi.org/10.1029/2006JA011970>.
- [118] E. Lindborg. Can the atmospheric kinetic energy spectrum be explained by two-dimensional turbulence? *Journal of Fluid Mechanics*, 388(1):259–288, June 1999. doi: 10.1017/S0022112099004851.
- [119] E. Lindborg. The energy cascade in a strongly stratified fluid. *Journal of Fluid Mechanics*, 550:207–242, 2006. doi: 10.1017/S0022112005008128.
- [120] C. Liu, X. Feng, J. Guo, and Y. Ye. Study of small-scale plasmoid structures in the magnetotail using Cluster observations and Hall MHD simulations. *Journal of Geophysical Research (Space Physics)*, 118(5):2087–2100, May 2013. doi: 10.1002/jgra.50248.

- [121] J. Liu, Y. Ye, C. Shen, Y. Wang, and R. Erdélyi. A new tool for CME arrival time prediction using machine learning algorithms: CAT-PUMA. *The Astrophysical Journal*, 855(2):109, 3 2018. doi: <https://doi.org/10.3847/1538-4357/aaae69>.
- [122] E. N. Lorenz. Available potential energy and the maintenance of the general circulation. *Tellus*, 7(2):157–167, 1955. doi: <https://doi.org/10.1111/j.2153-3490.1955.tb01148.x>.
- [123] N. L. Loureiro and S. Boldyrev. Collisionless reconnection in magnetohydrodynamic and kinetic turbulence. *The Astrophysical Journal*, 850(2):182, 2017. URL <http://stacks.iop.org/0004-637X/850/i=2/a=182>.
- [124] E. Lévêque, F. Toschi, L. Shao, and J.-P. Bertoglio. Shear-improved smagorinsky model for large-eddy simulation of wall-bounded turbulent flows. *Journal of Fluid Mechanics*, 570:491–502, 2007. doi: 10.1017/S0022112006003429.
- [125] Y. Ma, C. T. Russell, G. Toth, Y. Chen, A. F. Nagy, Y. Harada, J. McFadden, J. S. Halekas, R. Lillis, J. E. P. Connerney, J. Espley, G. A. DiBraccio, S. Markidis, I. B. Peng, X. Fang, and B. M. Jakosky. Reconnection in the martian magnetotail: Hall-mhd with embedded particle-in-cell simulations. *Journal of Geophysical Research: Space Physics*, 123(5):3742–3763, 2018. doi: <https://doi.org/10.1029/2017JA024729>.
- [126] Z. W. Ma, L. N. Wu, L. J. Li, and L. C. Wang. Bursty magnetic reconnection under slow shock-generated whistler waves. *Journal of Geophysical Research (Space Physics)*, 119(9):7495–7500, Sept. 2014. doi: 10.1002/2014JA020190.
- [127] A. Maffioli, G. Brethouwer, and E. Lindborg. Mixing efficiency in stratified turbulence. *Journal of Fluid Mechanics*, 794:R3, May 2016. doi: 10.1017/jfm.2016.206.
- [128] L. Mahrt. Intermittent of Atmospheric Turbulence. *Journal of Atmospheric Sciences*, 46(1):79–95, Jan. 1989. doi: 10.1175/1520-0469(1989)046<0079:IOAT>2.0.CO;2.

- [129] A. Mallet, A. A. Schekochihin, and B. D. G. Chandran. Disruption of Alfvénic turbulence by magnetic reconnection in a collisionless plasma. *JPLPh*, 83(6): 905830609, Nov. 2017. doi: 10.1017/S0022377817000812.
- [130] A. Mallet, A. A. Schekochihin, and B. D. G. Chandran. Disruption of sheet-like structures in Alfvénic turbulence by magnetic reconnection. *Monthly Notices of the Royal Astronomical Society*, 468:4862–4871, July 2017. doi: 10.1093/mnras/stx670.
- [131] A. Mangeney, F. Califano, C. Cavazzoni, and P. Travnicek. A Numerical Scheme for the Integration of the Vlasov-Maxwell System of Equations. *Journal of Computational Physics*, 179:495–538, July 2002. doi: 10.1006/jcph.2002.7071.
- [132] D. Manzini, F. Sahraoui, and F. Califano. Sub-ion scale turbulence driven by magnetic reconnection. *arXiv e-prints*, art. arXiv:2208.00855, Aug. 2022.
- [133] D. Manzini, F. Sahraoui, F. Califano, and R. Ferrand. Local cascade and dissipation in incompressible Hall magnetohydrodynamic turbulence: the Coarse-Graining approach. *arXiv e-prints*, art. arXiv:2203.01050, Mar. 2022.
- [134] P. Marchand, K. Tomida, B. Commerçon, and G. Chabrier. Impact of the Hall effect in star formation, improving the angular momentum conservation. *Astronomy and Astrophysics*, 631:A66, Nov. 2019. doi: 10.1051/0004-6361/201936215.
- [135] Marchand, P., Commerçon, B., and Chabrier, G. Impact of the hall effect in star formation and the issue of angular momentum conservation. *A&A*, 619: A37, 2018. doi: 10.1051/0004-6361/201832907.
- [136] R. Marino and L. Sorriso-Valvo. Scaling laws for the energy transfer in space plasma turbulence. *Physics Reports*, 1006:1–144, Mar. 2023. doi: 10.1016/j.physrep.2022.12.001.
- [137] R. Marino, P. D. Mininni, D. L. Rosenberg, and A. Pouquet. Large-scale anisotropy in stably stratified rotating flows. *Phys. Rev. E*, 90:023018, Aug

2014. doi: 10.1103/PhysRevE.90.023018. URL <https://link.aps.org/doi/10.1103/PhysRevE.90.023018>.
- [138] R. Marino, A. Pouquet, and D. Rosenberg. Resolving the paradox of oceanic large-scale balance and small-scale mixing. *Phys. Rev. Lett.*, 114:114504, Mar 2015. doi: 10.1103/PhysRevLett.114.114504. URL <https://link.aps.org/doi/10.1103/PhysRevLett.114.114504>.
- [139] R. Marino, F. Feraco, L. Primavera, A. Pumir, A. Pouquet, D. Rosenberg, and P. D. Mininni. Turbulence generation by large-scale extreme vertical drafts and the modulation of local energy dissipation in stably stratified geophysical flows. *Phys. Rev. Fluids*, 7:033801, Mar 2022. doi: 10.1103/PhysRevFluids.7.033801. URL <https://link.aps.org/doi/10.1103/PhysRevFluids.7.033801>.
- [140] J. Marshall and K. Speer. Closure of the meridional overturning circulation through southern ocean upwelling. *Nature Geoscience*, 5, 2012. doi: <https://doi.org/10.1038/ngeo1391>.
- [141] J. Masci, U. Meier, D. Cireşan, and J. Schmidhuber. Stacked convolutional auto-encoders for hierarchical feature extraction. In T. Honkela, W. Duch, M. Girolami, and S. Kaski, editors, *Artificial Neural Networks and Machine Learning – ICANN 2011*, pages 52–59, Berlin, Heidelberg, 2011. Springer Berlin Heidelberg. ISBN 978-3-642-21735-7.
- [142] A. M. Massone, M. Piana, and F. Consortium. Chapter 14 - machine learning for flare forecasting. In E. Camporeale, J. Johnson, and S. Wing, editors, *Machine Learning Techniques for Space Weather*, pages 355 – 364. Elsevier, 2018. ISBN 978-0-12-811788-0. doi: <https://doi.org/10.1016/B978-0-12-811788-0.00014-7>.
- [143] W. H. Matthaeus and M. L. Goldstein. Measurement of the rugged invariants of magnetohydrodynamic turbulence in the solar wind. *Journal of Geophysical Research: Space Physics*, 87(A8):6011–6028, 1982. doi: <https://doi.org/10.1029/JA087iA08p06011>.

- [144] W. H. Matthaeus, M. Wan, S. Servidio, A. Greco, K. T. Osman, S. Oughton, and P. Dmitruk. Intermittency, nonlinear dynamics and dissipation in the solar wind and astrophysical plasmas. *Philosophical Transactions of the Royal Society of London Series A*, 373:20140154–20140154, Apr. 2015. doi: 10.1098/rsta.2014.0154.
- [145] W. D. McComb and M. Q. May. The effect of kolmogorov (1962) scaling on the universality of turbulence energy spectra. *arXiv: Fluid Dynamics*, 2018.
- [146] F. W. Menk, I. R. Mann, A. J. Smith, C. L. Waters, M. A. Clilverd, and D. K. Milling. Monitoring the plasmopause using geomagnetic field line resonances. *Journal of Geophysical Research: Space Physics*, 109:A04216, 2004. doi: <https://doi.org/10.1029/2003JA010097>.
- [147] D. K. Milling, I. R. Mann, and F. W. Menk. Diagnosing the plasmopause with a network of closely spaced ground-based magnetometers. *Geophysical Research Letters*, 28(1):115–118, 2001. doi: <https://doi.org/10.1029/2000GL011935>.
- [148] P. D. Mininni. Scale interactions in magnetohydrodynamic turbulence. *Annual Review of Fluid Mechanics*, 43(1):377–397, 2011. doi: 10.1146/annurev-fluid-122109-160748.
- [149] P. D. Mininni, D. O. Gómez, and S. M. Mahajan. Dynamo action in hall magnetohydrodynamics. *The Astrophysical Journal*, 567(1):L81–L83, feb 2002. doi: 10.1086/339850.
- [150] P. D. Mininni, D. O. Gomez, and S. M. Mahajan. Dynamo action in magneto-hydrodynamics and hall-magnetohydrodynamics. *The Astrophysical Journal*, 587(1):472–481, apr 2003. doi: 10.1086/368181.
- [151] P. D. Mininni, D. O. Gomez, and S. M. Mahajan. Direct simulations of helical hall-MHD turbulence and dynamo action. *The Astrophysical Journal*, 619(2): 1019–1027, feb 2005. doi: 10.1086/426534.
- [152] P. D. Mininni, A. Alexakis, and A. Pouquet. Energy transfer in hall-mhd

- turbulence: cascades, backscatter, and dynamo action. *Journal of Plasma Physics*, 73(3):377–401, 2007. doi: 10.1017/S0022377806004624.
- [153] P. D. Mininni, D. Rosenberg, R. Reddy, and A. Pouquet. A hybrid mpi–openmp scheme for scalable parallel pseudospectral computations for fluid turbulence. *Parallel Computing*, 37(6):316–326, 2011. ISSN 0167-8191. doi: <https://doi.org/10.1016/j.parco.2011.05.004>. URL <https://www.sciencedirect.com/science/article/pii/S0167819111000512>.
- [154] M. Momenifar, E. Diao, V. Tarokh, and A. D. Bragg. Dimension reduced turbulent flow data from deep vector quantisers. *Journal of Turbulence*, 23(4-5):232–264, 2022. doi: 10.1080/14685248.2022.2060508.
- [155] A. S. Monin and A. M. Yaglom. *Statistical fluid mechanics, volume II: mechanics of turbulence*, volume 2. Courier Corporation, 2013.
- [156] L. Morales, S. Dasso, and D. Gómez. Hall effect in incompressible magnetic reconnection. *Journal of Geophysical Research*, 110, 04 2005. doi: 10.1029/2004JA010675.
- [157] Y. Motoori and S. Goto. Hierarchy of coherent structures and real-space energy transfer in turbulent channel flow. *Journal of Fluid Mechanics*, 911:A27, 2021. doi: 10.1017/jfm.2020.1025.
- [158] D. Müller, O. C. St. Cyr, I. Zouganelis, H. R. Gilbert, R. Marsden, T. Nieves-Chinchilla, E. Antonucci, F. Auchère, D. Berghmans, T. S. Horbury, R. A. Howard, S. Krucker, M. Maksimovic, C. J. Owen, P. Rochus, J. Rodriguez-Pacheco, M. Romoli, S. K. Solanki, R. Bruno, M. Carlsson, A. Fludra, L. Harra, D. M. Hassler, S. Livi, P. Louarn, H. Peter, U. Schühle, L. Teriaca, J. C. del Toro Iniesta, R. F. Wimmer-Schweingruber, E. Marsch, M. Velli, A. De Groof, A. Walsh, and D. Williams. The Solar Orbiter mission. Science overview. *Astronomy & Astrophysics*, 642:A1, Oct. 2020. doi: 10.1051/0004-6361/202038467.
- [159] O. Métais and J. R. Herring. Numerical simulations of freely evolving turbu-

- lence in stably stratified fluids. *Journal of Fluid Mechanics*, 202:117–148, 1989. doi: 10.1017/S0022112089001126.
- [160] O. Métais and M. Lesieur. Spectral large-eddy simulation of isotropic and stably stratified turbulence. *Journal of Fluid Mechanics*, 239:157–194, 1992. doi: 10.1017/S0022112092004361.
- [161] M. M. N. B. Erichson and M. Mahoney. Physics-informed autoencoders for lyapunov-stable fluid flow prediction. In *Machine Learning and the Physical Sciences Workshop, Conference on Neural Information Processing Systems*, 2019. URL <https://arxiv.org/abs/1905.10866>.
- [162] G. D. Nastrom, W. H. Jasperson, and K. S. Gage. Kinetic energy spectrum of large- and mesoscale atmospheric processes. *Nature*, 310:36–38, July 1984. doi: 10.1038/310036a0.
- [163] M. Nikurashin, G. Vallis, and A. Adcroft. Routes to energy dissipation for geostrophic flows in the southern ocean. *Nature Geoscience*, 6:48–51, 12 2012. doi: 10.1038/ngeo1657.
- [164] C. Norman and J. Heyvaerts. Anomalous magnetic field diffusion during star formation. *Astronomy & Astrophysics*, 147(2):247–256, June 1985.
- [165] W. Obayashi, H. Aono, T. Tatsukawa, and K. Fujii. Feature extraction of fields of fluid dynamics data using sparse convolutional autoencoder. *AIP Advances*, 11(10):105211, 2021. doi: 10.1063/5.0065637.
- [166] K. T. Osman, W. H. Matthaeus, M. Wan, and A. F. Rappazzo. Intermittency and Local Heating in the Solar Wind. *Physics Review Letters*, 108(26):261102, June 2012. doi: 10.1103/PhysRevLett.108.261102.
- [167] E. Ott and J. C. Sommerer. Blowout bifurcations: the occurrence of riddled basins and on-off intermittency. *Physics Letters A*, 188(1):39–47, May 1994. doi: 10.1016/0375-9601(94)90114-7.
- [168] B. P. Pandey and M. Wardle. Hall magnetohydrodynamics of partially ionized

- plasmas. *Monthly Notices of the Royal Astronomical Society*, 385(4):2269–2278, 2008. doi: <https://doi.org/10.1111/j.1365-2966.2008.12998.x>.
- [169] P. Pant, R. Doshi, P. Bahl, and A. Barati Farimani. Deep learning for reduced order modelling and efficient temporal evolution of fluid simulations. *Physics of Fluids*, 33(10):107101, 2021. doi: 10.1063/5.0062546.
- [170] E. Papini, L. Franci, S. Landi, A. Verdini, L. Matteini, and P. Hellinger. Can Hall Magnetohydrodynamics Explain Plasma Turbulence at Sub-ion Scales? *The Astrophysical Journal*, 870:52, Jan. 2019. doi: 10.3847/1538-4357/aaf003.
- [171] T. N. Parashar and W. H. Matthaeus. Propinquity of Current and Vortex Structures: Effects on Collisionless Plasma Heating. *The Astrophysical Journal*, 832:57, Nov. 2016. doi: 10.3847/0004-637X/832/1/57.
- [172] T. N. Parashar and W. H. Matthaeus. Observations of cross scale energy transfer in the inner heliosphere by Parker Solar Probe. *Reviews of Modern Plasma Physics*, 6(1):41, Dec. 2022. doi: 10.1007/s41614-022-00097-x.
- [173] G. S. Patterson and S. A. Orszag. Spectral calculations of isotropic turbulence: Efficient removal of aliasing interactions. *The Physics of Fluids*, 14(11):2538–2541, 1971. doi: 10.1063/1.1693365.
- [174] B. Pearson and B. Fox-Kemper. Log-normal turbulence dissipation in global ocean models. *Phys. Rev. Lett.*, 120:094501, Feb 2018. doi: 10.1103/PhysRevLett.120.094501. URL <https://link.aps.org/doi/10.1103/PhysRevLett.120.094501>.
- [175] J. Pedlosky. *Geophysical fluid dynamics*. Springer New York, NY, 1990. doi: <http://adsabs.harvard.edu/abs/1973ppp..book.....K>.
- [176] D. Perrone, O. Alexandrova, A. Mangeney, M. Maksimovic, C. Lacombe, V. Rakoto, J. C. Kasper, and D. Jovanovic. Compressive Coherent Structures at Ion Scales in the Slow Solar Wind. *The Astrophysical Journal*, 826:196, Aug. 2016. doi: 10.3847/0004-637X/826/2/196.

- [177] D. Perrone, O. Alexandrova, O. W. Roberts, S. Lion, C. Lacombe, A. Walsh, M. Maksimovic, and I. Zouganelis. Coherent Structures at Ion Scales in Fast Solar Wind: Cluster Observations. *The Astrophysical Journal*, 849:49, Nov. 2017. doi: 10.3847/1538-4357/aa9022.
- [178] H. Politano and A. Pouquet. Dynamical length scales for turbulent magnetized flows. *Geophysical Research Letters*, 25(3):273–276, Jan. 1998. doi: 10.1029/97GL03642.
- [179] Y. Pomeau and P. Manneville. Intermittent transition to turbulence in dissipative dynamical systems. *Communications in Mathematical Physics*, 74(2): 189–197, June 1980. doi: 10.1007/BF01197757.
- [180] A. Pouquet and R. Marino. Geophysical turbulence and the duality of the energy flow across scales. *Phys. Rev. Lett.*, 111:234501, Dec 2013. doi: 10.1103/PhysRevLett.111.234501. URL <https://link.aps.org/doi/10.1103/PhysRevLett.111.234501>.
- [181] A. Pouquet, D. Rosenberg, R. Marino, and C. Herbert. Scaling laws for mixing and dissipation in unforced rotating stratified turbulence. *J. Fluid Mech.*, 844: 519–545, 2018.
- [182] A. Pouquet, D. Rosenberg, and R. Marino. Linking dissipation, anisotropy, and intermittency in rotating stratified turbulence at the threshold of linear shear instabilities. *Physics of Fluids*, 31(10):105116, 2019. doi: 10.1063/1.5114633. URL <https://doi.org/10.1063/1.5114633>.
- [183] A. Pumir, B. I. Shraiman, and E. D. Siggia. Exponential tails and random advection. *Phys. Rev. Lett.*, 66:2984–2987, Jun 1991. doi: 10.1103/PhysRevLett.66.2984. URL <https://link.aps.org/doi/10.1103/PhysRevLett.66.2984>.
- [184] S. Rai, M. Hecht, M. Maltrud, and H. Aluie. Scale of oceanic eddy killing by wind from global satellite observations. *Science Advances*, 7(28):eabf4920, 2021. doi: 10.1126/sciadv.abf4920.

- [185] M. Raissi, P. Perdikaris, and G. E. Karniadakis. Machine learning of linear differential equations using gaussian processes. *Journal of Computational Physics*, 348:683–693, 2017. ISSN 0021-9991. doi: <https://doi.org/10.1016/j.jcp.2017.07.050>.
- [186] M. Raissi, A. Yazdani, and G. Karniadakis. Hidden fluid mechanics: Learning velocity and pressure fields from flow visualizations. *Science*, 367:eaaw4741, 01 2020. doi: [10.1126/science.aaw4741](https://doi.org/10.1126/science.aaw4741).
- [187] K. Riemann-Campe, K. Fraedrich, and F. Lunkeit. Global climatology of convective available potential energy (cape) and convective inhibition (cin) in era-40 reanalysis. *Atmospheric Research*, 93(1):534–545, 2009. ISSN 0169-8095. doi: <https://doi.org/10.1016/j.atmosres.2008.09.037>. 4th European Conference on Severe Storms.
- [188] C. Rorai, P. D. Mininni, and A. Pouquet. Turbulence comes in bursts in stably stratified flows. *Phys. Review E*, 89(4):043002, Apr. 2014. doi: [10.1103/PhysRevE.89.043002](https://doi.org/10.1103/PhysRevE.89.043002).
- [189] D. Rosenberg, P. D. Mininni, R. Reddy, and A. Pouquet. Gpu parallelization of a hybrid pseudospectral geophysical turbulence framework using cuda. *Atmosphere*, 11(2), 2020. ISSN 2073-4433. doi: [10.3390/atmos11020178](https://doi.org/10.3390/atmos11020178). URL <https://www.mdpi.com/2073-4433/11/2/178>.
- [190] M. Sadek and H. Aluie. Extracting the spectrum of a flow by spatial filtering. *Phys. Rev. Fluids*, 3:124610, Dec 2018. doi: [10.1103/PhysRevFluids.3.124610](https://doi.org/10.1103/PhysRevFluids.3.124610). URL <https://link.aps.org/doi/10.1103/PhysRevFluids.3.124610>.
- [191] A. Saha and U. Feudel. Riddled basins of attraction in systems exhibiting extreme events. *Chaos*, 28(3):033610, Mar. 2018. doi: [10.1063/1.5012134](https://doi.org/10.1063/1.5012134).
- [192] F. Sahraoui, M. L. Goldstein, P. Robert, and Y. V. Khotyaintsev. Evidence of a Cascade and Dissipation of Solar-Wind Turbulence at the Electron Gyroscale. *PhRvL*, 102(23):231102, June 2009. doi: [10.1103/PhysRevLett.102.231102](https://doi.org/10.1103/PhysRevLett.102.231102).

- [193] A. A. Schekochihin, S. C. Cowley, W. Dorland, G. W. Hammett, G. G. Howes, E. Quataert, and T. Tatsuno. Astrophysical Gyrokinetics: Kinetic and Fluid Turbulent Cascades in Magnetized Weakly Collisional Plasmas. *Astrophysical Journals*, 182:310–377, May 2009. doi: 10.1088/0067-0049/182/1/310.
- [194] S. Servidio, P. Dmitruk, A. Greco, M. Wan, S. Donato, P. A. Cassak, M. A. Shay, V. Carbone, and W. H. Matthaeus. Magnetic reconnection as an element of turbulence. *Nonlin. Processes Geophys.*, 18:675–695, Oct. 2011. doi: 10.5194/npg-18-675-2011.
- [195] Z.-S. She and E. Leveque. Universal scaling laws in fully developed turbulence. *Phys. Rev. Lett.*, 72:336–339, Jan 1994. doi: 10.1103/PhysRevLett.72.336. URL <https://link.aps.org/doi/10.1103/PhysRevLett.72.336>.
- [196] H. Singer, D. Southwood, R. Walker, and M. Kivelson. Alfvén wave resonances in a realistic magnetospheric magnetic field geometry. *Journal of Geophysical Research: Space Physics*, 86(A6):4589–4596, 1981. doi: <https://doi.org/10.1029/JA086iA06p04589>.
- [197] L. Sorriso-Valvo, D. Perrone, O. Pezzi, F. Valentini, S. Servidio, I. Zouganelis, and P. Veltri. Local energy transfer rate and kinetic processes: the fate of turbulent energy in two-dimensional hybrid Vlasov-Maxwell numerical simulations. *Journal of Plasma Physics*, 84(2):725840201, Apr. 2018. doi: 10.1017/S0022377818000302.
- [198] C. Staquet and F. S. Godeferd. Statistical modelling and direct numerical simulations of decaying stably stratified turbulence. part 1. flow energetics. *Journal of Fluid Mechanics*, 360:295–340, 1998. doi: 10.1017/S0022112097008641.
- [199] O. Stawicki, S. P. Gary, and H. Li. Solar wind magnetic fluctuation spectra: Dispersion versus damping. *Journal of Geophysical Research: Space Physics*, 106(A5):8273–8281, 2001. doi: <https://doi.org/10.1029/2000JA000446>.
- [200] K. Stengel, A. Glaws, D. Hettinger, and R. N. King. Adversarial super-resolution of climatological wind and solar data. *Proceedings of the Na-*

- tional Academy of Sciences*, 117(29):16805–16815, 2020. doi: 10.1073/pnas.1918964117.
- [201] N. E. Sujovolsky and P. D. Mininni. From waves to convection and back again: The phase space of stably stratified turbulence. *Phys. Rev. Fluids*, 5:064802, Jun 2020. doi: 10.1103/PhysRevFluids.5.064802.
- [202] N. E. Sujovolsky, P. D. Mininni, and A. Pouquet. Generation of turbulence through frontogenesis in sheared stratified flows. *Physics of Fluids*, 30(8):086601, Aug. 2018. doi: 10.1063/1.5043293.
- [203] N. E. Sujovolsky, G. B. Mindlin, and P. D. Mininni. Invariant manifolds in stratified turbulence. *Phys. Rev. Fluids*, 4:052402, May 2019. doi: 10.1103/PhysRevFluids.4.052402.
- [204] D. Telloni, L. Sorriso-Valvo, L. D. Woodham, O. Panasenco, M. Velli, F. Carbone, G. P. Zank, R. Bruno, D. Perrone, M. Nakanotani, C. Shi, R. D’Amicis, R. De Marco, V. K. Jagarlamudi, K. Steinvall, R. Marino, L. Adhikari, L. Zhao, H. Liang, A. Tenerani, R. Laker, T. S. Horbury, S. D. Bale, M. Pulupa, D. M. Malaspina, R. J. MacDowall, K. Goetz, T. D. de Wit, P. R. Harvey, J. C. Kasper, K. E. Korreck, D. Larson, A. W. Case, M. L. Stevens, P. Whittlesey, R. Livi, C. J. Owen, S. Livi, P. Louarn, E. Antonucci, M. Romoli, H. O’Brien, V. Evans, and V. Angelini. Evolution of Solar Wind Turbulence from 0.1 to 1 au during the First Parker Solar Probe-Solar Orbiter Radial Alignment. *Astrophys. J., Lett.*, 912(2):L21, May 2021. doi: 10.3847/2041-8213/abf7d1.
- [205] D. Telloni, G. Zank, M. Stangalini, C. Downs, H. Liang, M. Nakanotani, V. Andretta, E. Antonucci, L. Sorriso-Valvo, L. Adhikari, L. Zhao, R. Marino, R. Susino, C. Grimani, M. Fabi, R. D’Amicis, D. Perrone, R. Bruno, F. Carbone, and A. Zhukov. Observation of a magnetic switchback in the solar corona. *The Astrophysical Journal Letters*, 936:L25, 09 2022. doi: 10.3847/2041-8213/ac8104.
- [206] J. M. TenBarge and G. G. Howes. Current Sheets and Collisionless Damping

- in Kinetic Plasma Turbulence. *The Astrophysical Journal*, 771:L27, July 2013. doi: 10.1088/2041-8205/771/2/L27.
- [207] R. M. Thorne. Radiation belt dynamics: The importance of wave-particle interactions. *Geophysical Research Letters*, 37:L22107, 2010. doi: <https://doi.org/10.1029/2010GL044990>.
- [208] N. A. Tsyganenko and M. I. Sitnov. Modeling the dynamics of the inner magnetosphere during strong geomagnetic storms. *Journal of Geophysical Research: Space Physics*, 110(A3), 2005. doi: <https://doi.org/10.1029/2004JA010798>.
- [209] G. Tóth, Y. Ma, and T. I. Gombosi. Hall magnetohydrodynamics on block-adaptive grids. *Journal of Computational Physics*, 227(14):6967–6984, 2008. ISSN 0021-9991. doi: <https://doi.org/10.1016/j.jcp.2008.04.010>.
- [210] G. Tóth, X. Jia, S. Markidis, I. B. Peng, Y. Chen, L. K. S. Daldorff, V. M. Tennishev, D. Borovikov, J. D. Haiducek, T. I. Gombosi, A. Gloer, and J. C. Dorelli. Extended magnetohydrodynamics with embedded particle-in-cell simulation of ganymede’s magnetosphere. *Journal of Geophysical Research: Space Physics*, 121(2):1273–1293, 2016. doi: <https://doi.org/10.1002/2015JA021997>.
- [211] F. Valentini, P. Trávníček, F. Califano, P. Hellinger, and A. Mangeney. A hybrid-Vlasov model based on the current advance method for the simulation of collisionless magnetized plasma. *Journal of Computational Physics*, 225: 753–770, July 2007. doi: 10.1016/j.jcp.2007.01.001.
- [212] F. Valentini, D. Perrone, S. Stabile, O. Pezzi, S. Servidio, R. De Marco, F. Marcucci, R. Bruno, B. Lavraud, J. De Keyser, G. Consolini, D. Brienza, L. Sorriso-Valvo, A. Retinò, A. Vaivads, M. Salatti, and P. Veltri. Differential kinetic dynamics and heating of ions in the turbulent solar wind. *New Journal of Physics*, 18(12):125001, Dec. 2016. doi: 10.1088/1367-2630/18/12/125001.
- [213] A. Vallgren, E. Deusebio, and E. Lindborg. Possible explanation of the atmospheric kinetic and potential energy spectra. *Physical review letters*, 107: 268501, 12 2011. doi: 10.1103/PhysRevLett.107.268501.

- [214] E. P. van der Poel, R. Ostilla-Mónico, J. Donners, and R. Verzicco. A pencil distributed finite difference code for strongly turbulent wall-bounded flows. *Computers & Fluids*, 116:10–16, 2015. ISSN 0045-7930. doi: <https://doi.org/10.1016/j.compfluid.2015.04.007>.
- [215] D. Vech, A. Mallet, K. G. Klein, and J. C. Kasper. Magnetic Reconnection May Control the Ion-scale Spectral Break of Solar Wind Turbulence. *The Astrophysical Journal*, 855:L27, Mar. 2018. doi: 10.3847/2041-8213/aab351.
- [216] D. Veleda, R. Montagne, and M. Araujo. Cross-Wavelet Bias Corrected by Normalizing Scales. *Journal of Atmospheric and Oceanic Technology*, 29(9): 1401–1408, Sept. 2012. doi: 10.1175/JTECH-D-11-00140.1.
- [217] M. K. Verma. Statistical theory of magnetohydrodynamic turbulence: recent results. *Physics Reports*, 401(5):229–380, 2004. ISSN 0370-1573. doi: <https://doi.org/10.1016/j.physrep.2004.07.007>. URL <https://www.sciencedirect.com/science/article/pii/S0370157304003163>.
- [218] P. Vieillefosse. Local interaction between vorticity and shear in a perfect incompressible fluid. *J. Physique*, 43:837–842, 1982.
- [219] P. Vieillefosse. Internal motion of a small element of fluid in an inviscid flow. *Physica A*, 125:150–162, 1984.
- [220] F. Waleffe. Non-linear interactions in homogeneous turbulence with and without background rotation. In *Annual Research Briefs, 1991*, pages 31–43, 1991.
- [221] M. Wan, W. H. Matthaeus, V. Roytershteyn, T. N. Parashar, P. Wu, and H. Karimabadi. Intermittency, coherent structures and dissipation in plasma turbulence. *Phys. Plasmas*, 23(4):042307, Apr. 2016. doi: 10.1063/1.4945631.
- [222] Z. Y. Wan, P. Vlachas, P. Koumoutsakos, and T. Sapsis. Data-assisted reduced-order modeling of extreme events in complex dynamical systems. *PLOS ONE*, 13(5):1–22, 05 2018. doi: 10.1371/journal.pone.0197704.

- [223] T. Wang, O. Alexandrova, D. Perrone, M. Dunlop, X. Dong, R. Bingham, Y. V. Khotyaintsev, C. T. Russell, B. L. Giles, R. B. Torbert, R. E. Ergun, and J. L. Burch. Magnetospheric Multiscale Observation of Kinetic Signatures in the Alfvén Vortex. *Astrophys. J. Lett.*, 871:L22, Feb. 2019. doi: 10.3847/2041-8213/aafe0d.
- [224] T. Wang, J. He, O. Alexandrova, M. Dunlop, and D. Perrone. Observational Quantification of Three-dimensional Anisotropies and Scalings of Space Plasma Turbulence at Kinetic Scales. *The Astrophysical Journal*, 898(1):91, July 2020. doi: 10.3847/1538-4357/ab99ca.
- [225] X. Wang, A. Bhattacharjee, and Z. W. Ma. Scaling of collisionless forced reconnection. *Phys. Rev. Lett.*, 87:265003, Dec 2001. doi: 10.1103/PhysRevLett.87.265003.
- [226] C. L. Waters, F. W. Menk, and B. J. Fraser. The resonance structure of low latitude Pc3 geomagnetic pulsations. *Geophysical Research Letters*, 18(12):2293–2296, 1991. doi: <https://doi.org/10.1029/91GL02550>.
- [227] R. T. Wicks, T. S. Horbury, C. H. K. Chen, and A. A. Schekochihin. Power and spectral index anisotropy of the entire inertial range of turbulence in the fast solar wind. *Monthly Notices of the Royal Astronomical Society: Letters*, 407(1):L31–L35, 2010. doi: <https://doi.org/10.1111/j.1745-3933.2010.00898.x>. URL <https://onlinelibrary.wiley.com/doi/abs/10.1111/j.1745-3933.2010.00898.x>.
- [228] S. Wing, J. R. Johnson, E. Camporeale, and G. D. Reeves. Chapter 6 - untangling the solar wind drivers of the radiation belt: An information theoretical approach. In E. Camporeale, J. Johnson, and S. Wing, editors, *Machine Learning Techniques for Space Weather*, pages 149 – 175. Elsevier, 2018. ISBN 978-0-12-811788-0. doi: <https://doi.org/10.1016/B978-0-12-811788-0.00006-8>.
- [229] P. Wu, S. Perri, K. Osman, M. Wan, W. H. Matthaeus, M. A. Shay, M. L. Goldstein, H. Karimabadi, and S. Chapman. Intermittent Heating in Solar

- Wind and Kinetic Simulations. *The Astrophysical Journal*, 763:L30, Feb. 2013. doi: 10.1088/2041-8205/763/2/L30.
- [230] P. Wu, S. Gong, K. Pan, F. Qiu, W. Feng, and C. Pain. Reduced order model using convolutional auto-encoder with self-attention. *Physics of Fluids*, 33(7):077107, 2021. doi: 10.1063/5.0051155.
- [231] J. Wurster, M. R. Bate, and I. A. Bonnell. The impact of non-ideal magnetohydrodynamic processes on discs, outflows, counter-rotation, and magnetic walls during the early stages of star formation. *Monthly Notices of the Royal Astronomical Society*, 507(2):2354–2372, Oct. 2021. doi: 10.1093/mnras/stab2296.
- [232] Z. Xia and W. Yang. Exact solutions of the incompressible dissipative hall magnetohydrodynamics. *Physics of Plasmas*, 22(3):032306, 2015. doi: 10.1063/1.4914931.
- [233] L. Xie, L. Li, Y. Zhang, Y. Feng, X. Wang, A. Zhang, and L. Kong. Three-dimensional Hall MHD simulation of lunar minimagnetosphere: General characteristics and comparison with Chang'E-2 observations. *Journal of Geophysical Research: Space Physics*, 120(8):6559–6568, 2015. doi: <https://doi.org/10.1002/2015JA021647>.
- [234] A. Yaglom. On the local structure of a temperature field in turbulent flows. *Dokl Akad Nauk SSSR*, 69:743–746, 1949.
- [235] Y. Yang. *Energy Transfer and Dissipation in Collisionless Plasma Turbulence*, chapter 1. Springer, 05 2019. ISBN 978-981-13-8148-5. doi: 10.1007/978-981-13-8149-2_5.
- [236] Y. Yang, W. H. Matthaeus, T. N. Parashar, C. C. Haggerty, V. Roytershteyn, W. Daughton, M. Wan, Y. Shi, and S. Chen. Energy transfer, pressure tensor, and heating of kinetic plasma. *Physics of Plasmas*, 24(7):072306, July 2017. doi: 10.1063/1.4990421.
- [237] Y. Yang, W. H. Matthaeus, Y. Shi, M. Wan, and S. Chen. Compressibility effect

- on coherent structures, energy transfer, and scaling in magnetohydrodynamic turbulence. *Physics of Fluids*, 29(3):035105, Mar. 2017. doi: 10.1063/1.4979068.
- [238] Y. Yang, M. Wan, W. H. Matthaeus, L. Sorriso-Valvo, T. N. Parashar, Q. Lu, Y. Shi, and S. Chen. Scale dependence of energy transfer in turbulent plasma. *Mon. Not. Royal Astron. Soc.*, 482(4):4933–4940, Feb. 2019. doi: 10.1093/mnras/sty2977.
- [239] G. V. Zasko, A. V. Glazunov, E. V. Mortikov, and Y. M. Nechepurenko. Large-scale structures in stratified turbulent couette flow and optimal disturbances. *Russian Journal of Numerical Analysis and Mathematical Modelling*, 35(1): 37–53, 2020. doi: doi:10.1515/rnam-2020-0004. URL <https://doi.org/10.1515/rnam-2020-0004>.
- [240] V. Zhdankin, S. Boldyrev, J. C. Perez, and S. M. Tobias. Energy Dissipation in Magnetohydrodynamic Turbulence: Coherent Structures or “Nanoflares”? *The Astrophysical Journal*, 795:127, Nov. 2014. doi: 10.1088/0004-637X/795/2/127.